Wintertime Stable Boundary-Layer Processes in Alpine Valleys

Gabriele Arduini

Communauté UNIVERSITÉ Grenoble Alpes

University of Hertfordshire UH

THÈSE

Pour obtenir le grade de

DOCTEUR DE LA COMMUNAUTE UNIVERSITE GRENOBLE ALPES

préparée dans le cadre d'une cotutelle *entre la Communauté Université Grenoble Alpes* et *University of Hertfordshire*

Spécialité : **Océan, Atmosphère, Hydrologie**

Arrêté ministériel : le 6 janvier 2005 - 7 août 2006

Présentée par

Gabriele ARDUINI

Thèse dirigée par **Chantal STAQUET** et **Charles CHEMEL**

préparée au sein des **Laboratoire des Ecoulements Géophysiques et Industriels (LEGI)** dans **les Écoles Doctorales Terre Univers Environnement**

et du **Centre for Atmospheric and Instrumentation Research, University of Hertfordshire, UK**

Processus de la Couche Limite Atmosphérique Stable Hivernale en Vallée Alpine

Thèse soutenue publiquement le **06/06/2017**,
devant le jury composé de :

M. Philippe DROBINSKI
Directeur de recherche, CNRS, Président
M. Simon VOSPER
Research scientist, UK Met Office, Rapporteur
M. Juan CUXART Rodamilans
Professeur, Universitat de les Illes Balears, Rapporteur
M. Martin HARDCASTLE
Professeur, University of Hertfordshire, Examinateur
Mme Chantal STAQUET
Professeur, Université Grenoble Alpes, Directeur de thèse
M. Charles CHEMEL
Senior Lecturer, University of Hertfordshire, Directeur de thèse

To my mother, to her love.

Abstract

Alpine valleys are rarely closed systems, implying that the atmospheric boundary layer of a particular valley section is influenced by the surrounding terrain and large-scale flows. A detailed characterisation and quantification of these effects is required in order to design appropriate parameterisation schemes for complex terrains. The focus of this work is to improve the understanding of the effects of surrounding terrain (plains, valleys or tributaries) on the heat and mass budgets of the stable boundary layer of a valley section, under dry and weak large-scale wind conditions. Numerical simulations using idealised and real frameworks are performed to meet this goal.

Several idealised terrains (configurations) were considered: an infinitely long valley (i.e. two-dimensional), and upstream valleys opening either on a plain (valley-plain), on a wider valley (draining) or on a narrower valley (pooling). In three-dimensional valleys, two main regimes can be identified for all configurations: a transient regime, before the down-valley flow develops, followed by a quasi-steady regime, when the down-valley flow is fully developed. The presence of a downstream valley reduces the along-valley temperature difference, therefore leading to weaker down-valley flows. As a result, the duration of the transient regime increases compared to the respective valley-plain configuration. Its duration is longest for the pooling configuration. For strong pooling the along-valley temperature difference can reverse, forcing up-valley flows from the narrower towards the wider valley. In this regime, the average cooling rate at the valley-scale is found to be a maximum and its magnitude is dependent on the configuration considered. Therefore pooling and draining induce colder and deeper boundary layers than the respective valley-plain configurations. In the quasi-steady regime the cooling rate is smaller than during the transient regime, and almost independent of the configuration considered. Indeed, as the pooling character is more pronounced, the warming contribution from advection to the heat budget decreases because of weaker down-valley flows, and so does the cooling contribution from the surface sensible heat flux. The mass budget of the valley boundary layer was found to be controlled by a balance between the convergence of downslope flows at the top of the boundary layer and the divergence of the down-valley flow along the valley axis, with negligible contributions of subsidence far from the valley sidewalls. The mass budget highlighted the importance of the return current above the down-valley flow, which may contribute significantly to the inflow of air at the top of the boundary layer.

A case-study of a persistent cold-air pool event which occurred in February 2015 in the Arve River Valley during the intensive observation period 1 (IOP1) of the PASSY-2015 field campaign, allowed us to quantify the effects of neighbouring valleys on the heat and mass budgets of a real valley atmosphere. The cold-air pool persisted as a result of warm air advection at the valley top, associated with the passage of an upper-level ridge over Europe. The contributions from each tributary valley to the mass and heat budgets of the valley atmosphere were found to vary from day to day within the persistent stage of the cold-air pool, depending on the large-scale flow. Tributary flows had significant impact on the height of the inversion layer and the strength of the cold-air pool, transporting a significant amount of mass within the valley atmosphere throughout the night. The strong stratification of the near-surface atmosphere prevented the tributary flows from penetrating down to the valley floor. The evolution of the large-scale flow during the episode had a profound impact on the near-surface circulation of the valley. The channelling of the large-scale flow at night, can lead to the decrease of the horizontal temperature difference driving the near-surface down-valley flow, favouring the stagnation of the air close to the ground.

Résumé

Une vallée alpine constitue rarement un système fermé et, de ce fait, la dynamique de sa couche limite atmosphérique est influencée par le relief environnant et par l'écoulement de grande échelle qui surmonte la vallée. La paramétrisation de la circulation atmosphérique d'une vallée alpine requiert donc de caractériser finement ces effets, ce qui est l'objectif de ce travail de thèse. Plus précisément, notre objectif est de comprendre l'influence du relief environnant une vallée (une plaine ou une autre vallée, de même axe ou tributaire) sur les bilans de masse et de chaleur au travers d'une section de cette vallée ; on suppose que les conditions atmosphériques sont stables et sèches et que le vent synoptique est faible mais non négligeable. Le travail s'appuie sur des simulations numériques menées dans un contexte idéalisé puis réaliste.

Plusieurs vallées idéalisées ont tout d'abord été considérées: une vallée infiniment longue (c'est-à-dire que cette vallée est bidimensionnelle) et une vallée tridimensionnelle, qualifiée de supérieure, ouvrant soit sur une plaine (configuration dite de "vallée-plaine"), sur une vallée plus large (configuration de type "drainage") ou sur une vallée plus étroite (configuration de type "quasi-stagnation") ; la vallée plus large ou plus étroite est qualifiée d'inférieure.

Dans les vallées tridimensionnelles, deux régimes principaux ont été identifiés, quelle que soit la configuration : un régime transitoire, avant que le vent de vallée (descendant) ne se développe, puis un régime quasi-stationnaire, quand le vent de vallée est complètement développé. La présence d'une vallée inférieure réduit la variation de température le long de la vallée, de sorte que le vent de vallée qui se développe est plus faible que dans la configuration vallée-plaine. En conséquence, la durée du régime transitoire augmente par rapport à cette dernière configuration, et est maximum pour la configuration quasi-stagnation. Lorsque la vallée inférieure est très étroite, la variation de température peut même changer de signe, conduisant à un vent de vallée montant, de la vallée inférieure vers la vallée supérieure. Durant ce régime transitoire, le taux de refroidissement moyenné sur le volume de la vallée est maximum, sa valeur dépendant de la configuration considérée. En conclusion, les configurations de drainage et quasi-stagnation conduisent à une couche limite dans la vallée supérieure plus froide et plus profonde que dans la configuration vallée-plaine.

Dans le régime quasi-stationnaire, le taux de refroidissement moyenné sur le volume de la vallée est plus faible que dans le régime transitoire et varie peu en fonction de la

configuration considérée. En effet, lorsque la vallée inférieure devient plus étroite, le réchauffement lié aux effets advectifs diminue car la vitesse du vent de vallée diminue, de sorte que la contribution (refroidissante) du flux de chaleur sensible diminue également. La conservation de la masse dans la couche limite de la vallée supérieure est assurée par un équilibre entre la convergence des vents de pente au sommet de la couche limite et la divergence du vent de vallée, les effets de subsidence loin des parois de la vallée jouant un rôle négligeable. L'analyse de la conservation de la masse a également mis en évidence la contribution majeure à l'entrée d'air au sommet de la couche limite du courant de retour au-dessus (et en sens inverse) du vent de vallée descendant.

La dernière partie du travail de thèse aborde le cas réaliste de la vallée de l'Arve autour de Passy – dénommée ci-après "vallée de Passy"– durant une période d'observation intensive de la campagne de mesures PASSY-2015, en février 2015. Une couche d'air froid persistante se forme en fond de vallée, liée à l'advection d'air chaud associée au passage d'une crête anticyclonique au-dessus de l'Europe. L'impact des vallées débouchant dans la vallée de Passy sur les bilans de masse et de chaleur dans cette vallée a été quantifiée précisément. Les écoulements le long des vallées tributaires présentent ainsi une grande variabilité durant la phase persistante de l'épisode, dépendant de la variabilité de l'écoulement de grande échelle. Ces écoulements ont un impact majeur sur l'intensité de la couche d'air froid et la hauteur de l'inversion qui la surmonte, au travers des flux de masse associés. La forte stratification présente près du sol conduit à leur décollement au-dessus du fond de vallée, laissant l'air s'y trouvant non affecté par leur présence. L'évolution de l'écoulement de grande échelle durant l'épisode a un profond impact sur la dynamique proche du fond de vallée. Durant la nuit en effet, la canalisation de cet écoulement réduit la variation de température le long de la vallée contrôlant le vent de vallée, favorisant la stagnation de l'air.

Acknowledgements

"The PhD is a long journey. You know where you start and where you would like to go, maybe, but you don't know the itinerary. " That's why it is better to have good travelling companions in order not to loose the track along the way.

Firstly, I would like to acknowledge my supervisors Charles Chemel and Chantal Staquet. Thank you for your never-ending availability and support. When something was going wrong, I knew that I could knock at your door (Chantal), turn my chair towards your desk (Charles), and discuss about it. You taught me a lot about how to make science. But more important, you transmitted to me the passion for the mountain meteorology. This will never go away. Thank you.

I would like to acknowledge my examiners and jury members, that reviewed this work. Thank you for the invaluable discussion that we had. It had been stressing and tough, but at the same time I really appreciated all of your comments and your sometimes different perspectives.

The PhD experience gave me the opportunity to travel, live in different places, and meet so many different people that influenced me, in a way or another. Thank you all, you helped me to keep on track. In particular, thank you Natalia, you had been the perfect travelling companion!

Finally, I would like to acknowledge Letizia. When I was along this travel, you came and never left me. Your love has been like these bright stars that enlighten the track to the sailors. Thank you Leti.

...tra la partenza e il traguardo
nel mezzo c'é tutto il resto
e tutto il resto é giorno dopo giorno
e giorno dopo giorno é
silenziosamente costruire
e costruire é potere e sapere
rinunciare alla perfezione.

Table of contents

"Se tu parlar sapessi, io chiederei:
Dimmi: perché giacendo
A bell'agio, ozioso,
S'appaga ogni animale;
Me, s'io giaccio in riposo, il tedio assale? "
Giacomo Leopardi,
Canto notturno d'un pastore errante dell' Asia

I

General Introduction

"Quand' la brujana a l'á el capelo,
pose la vanga, e pidje l'ombrelo"

I.1 Motivations

The short verse opening this thesis is a proverb in the local dialect of my home town, stating that when the top of the mountain Brugiana is covered by clouds (it has a 'hat'), most likely it is going to rain ('put down the spade, and pick up your umbrella!'). The proverb simply describes the correlation between low-level cloud cover (the height of mount Brugiana is about 1000 m) and rain event in the town of Massa. Many proverbs exist in the folk's culture that link meteorological phenomena and mountains, which express the impact that mountains and weather have on everyday life.

Broadly speaking, more than 50% of the earth's surface is in the form of mountains, hills and plateau and 26% of the global population lives in mountainous terrains [Meybeck et al., 2001]. Taking Europe as an example, there are more than 14 million people living in the Alpine chain, with a population density of 74.6 inhabitants per km^2 (calculated over the entire territory encompassed by the mountain range), which makes the Alps one of the most densely inhabited mountainous regions in the world [Permanent Secretariat of the Alpine Convention, 2015]. More specifically the highest population densities are found in valleys and pre-alpine regions. The valley floors are characterised by a population density similar to other non-Alpine regions in Europe [Permanent Secretariat of the Alpine Convention, 2015]. Moreover, the Alps, and mountainous regions in general, attract a huge number of tourists throughout the year, because of sport resorts and outstanding natural beauties (see Fig. I.1).

From a geographical point of view, the major mountain chains are a natural topographic barrier separating countries and economic centres. The Rocky mountains in North America are more than 4800 km long and oriented north-south, dividing the western United States and Canada from the Occidental part. The Alps in Europe divide some of the major countries of the continent, Italy, France, Germany, Switzerland

Figure I.1: The natural beauty of the Alps attracts tourists, and also the author, throughout the year. Photographs by G. Arduini.

and Austria. The main transport infrastructures are found in valleys and main gaps (like the Brenner Pass between Italy and Austria), where also most of the population in the region is concentrated.

Mountains have a profound impact on weather, climate and generally on atmospheric circulation at all scales. Historically, before orographic gravity wave drag was represented in numerical weather prediction models (NWP), significant systematic errors were found after a few days of numerical forecast [see for instance Palmer et al., 1986]. The simulated surface westerly wind was too strong at mid-latitude ("westerly bias") and excessive low-pressure systems formed at high latitude. This was affecting not only the regional weather forecasts but also global climate simulations, therefore a sound understanding of the response of the climate system to variations in the forcing parameters, like global carbon dioxide (CO_2) concentrations, was compromised. More recently Rotach et al. [2014] argued that the deficiencies of current global models in accurately simulate the global CO_2 budget can be due to the poor representation of exchange processes between complex terrains and the free atmosphere. Indeed, these exchanges are based on theories and parameterisations formally valid only on flat terrains, and the effects of terrain-induced flows and processes are poorly taken into account [Rotach et al., 2014, 2015]. This is not only true for quantities like momentum or CO_2 but also for heat, humidity and mass. As an illustration, Fig. I.2 shows clouds resulting from a transport of humidity due to daytime terrain-induced flows over the Apuan Alps, in Tuscany, a phenomenon called "mountain venting" [see for instance De Wekker and Kossmann, 2016].

Focussing on smaller spatial and temporal scales, the effect of mountains and complex terrains on the atmospheric flows impacts on the everyday life of people living in the surrounding areas. A detailed forecast in terms of timing, location and intensity of all phenomena associated with orographic precipitation (for instance rainfalls or,

Figure I.2: Clouds forming as a result of transport of humidity over the Apuan Alps associated with daytime terrain-induced flows (mountain venting). Photograph by G. Arduini.

during wintertime, snowfalls), requires a thorough understanding of the modification induced on the approaching flow by the complex topography [see for instance Rotunno and Houze, 2007]. Fog and low-level clouds in valley are another important aspect of the weather in mountainous regions.

During wintertime, a major issue for many urbanised mountainous areas around the world are cold-air pools and the associated poor air quality. Cold-air pools are usually referred to as an "accumulation" of cold-air within a valley or a basin caused by the confined topography. More precisely, atmospheric inversion layers characterized by temperature increasing with height form frequently at the valley floor during nighttime, reducing the dispersion of atmospheric pollution in the atmosphere. During wintertime, these conditions can last for multiple days when anticyclonic conditions persist over the region and the synoptic flow is weak (see Fig. I.3).

As a result of cold-air pools in valleys and basins the daily-averaged concentration of particulate pollution very often exceeds threshold values imposed by national/international directives [see for instance Whiteman et al., 2014]. Among these substances, airborne particulate matter with aerodynamic diameter less than 10 μm (PM_{10}) can cause severe health problems. As an example of the problem for the Alpine region, Largeron and Staquet [2016b] reported several episodes during the winter of 2006-2007 for which the threshold value of daily-averaged PM_{10} concentration imposed by the national directive (French Decree 2010-1250 of 21 October 2010) was exceeded for more than three consecutive days in the Grenoble Valley. In their study single days characterized by values of daily-average PM_{10} concentration that was almost twice the national threshold were also reported. Emissions and valley-scale circulation are the primary factors responsible for these high particulate pollution episodes. Major episodes of poor air quality are reported also in smaller urbanised valleys, like the Cache Valley in the United States [Malek et al., 2006], or the Arve River Valley,

Figure I.3: The Arve River Valley (in the French Alps) during the cold-air pool event that occurred at the beginning of January 2015, which caused a major episode of particulate pollution in the valley. Photograph by G. Arduini.

located at the foothills of Mount Blanc.

I.2 Scope of this thesis

While the main ingredients required for the development of stable boundary layer in complex terrains are reasonably well-known, the boundary-layer processes involved and their interactions are complex. The main ingredients/factors can be schematically identified as the nighttime radiative cooling of the ground, a weak synoptic forcing and clear sky conditions. However, using the words of Rotunno and Houze [2007] as regards to orographic convection, *"these factors constitute the general framework, for viewing a very complicated problem"* (p. 811). The complex orography may lead to terrain-induced flows affecting the dynamics and thermodynamics of the valley atmosphere; radiative cooling of the ground depends on land properties and on the thermal structure of the valley atmosphere; the role of synoptic flows can be different depending on the stratification within the valley and the direction of the flow with respect to the valley orientation; as a result of cooling, fog may form at the valley floor and transported by terrain-induced flows, modifying radiative cooling processes. These (and other) elements and the interactions among them depend on the geometry of the valley, small-scale terrain features or the surrounding terrains, modifying the structure and evolution of the boundary layer of the valley. For these reasons the characteristics of the atmospheric boundary layer in complex terrain are poorly represented in current numerical weather prediction models. The problem is important not only for the representation of the boundary layer, but also for the representation of the large-scale circulation, as shown by Sandu et al. [2013].

To date, the study of exchange processes in complex terrain has focused more on daytime conditions than nighttime conditions. Several works have shown how

the boundary-layer structure and its interactions with the surrounding atmosphere is modified by the complex orography during daytime [see for instance Weissmann et al., 2005; Weigel et al., 2007; Wagner et al., 2015a,b; Rotach et al., 2015]. During nighttime, as a consequence of the stable stratification which builds up in a valley, turbulent mixing in the atmosphere is reduced [see for instance Mahrt, 2014]. In such conditions, terrain-induced flows are essential mechanisms for transport (exchange) processes between the valley atmosphere and the surrounding.

This thesis focusses on the study of the stable boundary layer of deep valleys during nighttime and dry conditions under weak synoptic winds. This allows us to consider the essential elements of the problem, leaving the complexities due to micro-physical processes for further studies. The scientific background on the topic of this thesis is reported in Chapter II. The thesis examines the links between terrain-induced flows within the valley and surrounding terrains, and their effects on heat and mass transports within the valley atmosphere. This is addressed by means of numerical simulations in idealised and real frameworks.

II

Scientific Background

II.1 The atmospheric boundary layer in complex terrains

The atmospheric boundary layer (ABL) is usually defined as the lowest part of the atmosphere influenced by the presence of the Earth's surface [Garratt, 1992]. Most of past research on the ABL focused on relatively flat and homogeneous terrain [see for instance Garratt, 1992; Stull, 1988, for reviews]. In such conditions, turbulent mixing (induced for instance by friction and/or convection) is the main process controlling the transport of heat/momentum/mass within the boundary-layer. In a complex mountainous terrain terrain-induced flows affect the structure and evolution of the ABL. Terrain-induced flows are characterized by a wide range of spatial scales, from the microscale [<2 km, Orlanski, 1975] to the mesoscale [ranging from 2 to 200 km, Orlanski, 1975]. A schematic division of the ABL over mountainous terrain based on the spatial scale of the main atmospheric phenomena and processes involved can be drawn, following Zardi and Whiteman [2013] (see Fig. II.1): the atmospheric layer close to the slope (slope atmosphere) is associated with slope flows, characterised by spatial scales of the order of tens to hundreds of metres, nonetheless having an important impact on the evolution of the ABL at the valley scale. The valley atmosphere is affected by along-valley flows, acting at a spatial scale comparable with the valley atmosphere (1 to 100 km). Finally, following Ekhart [1948], a mountain atmosphere can be associated with the effect of the multitude of valleys and ridges forming a mountain range [De Wekker, 2002]. Atmospheric processes controlling the boundary layer of a valley (the Valley Boundary Layer, VBL) may be affected by those in the neighbouring valleys, and also interact with the synoptic (external) flow, making a simple and general description of the structure and evolution of the VBL a difficult task.

Perhaps a general question regarding the ABL over complex terrains can be formulated as follows:

"How are the atmospheric processes in a particular valley determined by the local and

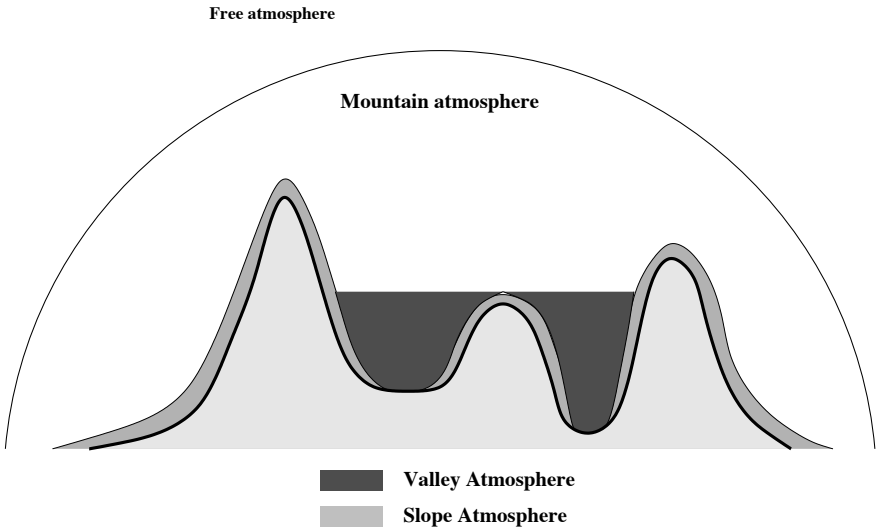

Figure II.1: The schematic division of the ABL in mountainous regions, adapted from Ekhart [1948].

surrounding orography and how do they respond to external conditions?"

In the following, the contributions from previous studies to this broad question are presented. A schematic division has been adopted: firstly the stable boundary layer in valleys is presented and secondly the mechanisms controlling the dynamics within a valley are described, followed by a discussion on the mechanisms controlling the cooling of the valley atmosphere. At the end of the chapter, the research objectives of the thesis are outlined.

II.2 Stable boundary layers in valleys

During nighttime, with clear sky and dry conditions, the ABL is usually characterised by a stably stratified atmosphere (i.e. the *potential* temperature increases with height) and it is referred to as the stable boundary layer [SBL, Garratt, 1992]. A cold-air pool (CAP) is commonly defined as an atmospheric layer confined in a valley characterised by a positive vertical temperature gradient (i.e. an inversion layer), that is *"a confined and stagnant layer of air colder than the air above"* [Whiteman et al., 2001a]. However, cold-air pools can be *"most generally defined as a surface-based atmospheric layer with high static stability (not necessarily a temperature inversion)"* [Zängl, 2005]. Burns [2014] pointed out that in a deep valley an inversion layer can be confined in the lower atmospheric layer of the valley, while the stable boundary layer of the valley (SVBL) can be much higher, reaching the valley top [a ground based inversion layer surmounted by a region of enhanced cooling, Burns, 2014]. In these conditions, the air within a valley at a given height can be found at a lower temperature than the air

outside of the valley at the same height, for instance over an adjacent relatively flat region [Vergeiner and Dreiseitl, 1987; Whiteman, 1990]. This difference stems from the influence of terrain-induced flows and other mechanisms on the structure and evolution of the SVBL, as will be discussed in more details in Sect. II.4.

Several projects and field campaigns were held in the past, motivated by the need for a better understanding of the underlying physical processes controlling the SBL in complex terrain. The Atmospheric Studies in Complex Terrain [ASCOT, Clements et al., 1989a] was conducted between the 70s and 80s, involving several field studies in multiple valleys in the United States. The overall aim of the project was to improve the understanding of transport processes associated with nocturnal valley flows in deep valleys. A similar aim motivated the Vertical Transport and Mixing project [VTMX, Doran et al., 2002], which took place in the Salt Lake Valley (USA), with a specific focus on vertical transport processes in the stable boundary layer. Vertical transport processes between the Alps and the foreland were the focus of the Vertical Exchange and Orography project [VERTIKATOR, Lugauer and Coauthors, 2003]. The Terrain-induced Rotor Experiment [T-REX, Grubišić et al., 2008], held in the southern Sierra Nevada (USA), was dedicated to atmospheric rotors, and had a complementary scientific objective to investigate the structure and evolution of the SBL under quiescent conditions.

The Meteor Crater Experiment [METCRAX, Whiteman et al., 2008] specifically aimed at investigating SBL processes and cold-air pools in a shallow ($\sim$ 100 m deep) and almost 'idealised' environment of the Arizona's Meteor Crater (USA). However, the frequent occurrence of regional drainage currents in the Meteor Crater motivated a second field campaign [Lehner et al., 2016], in order to better characterise downslope windstorm-type flows and their interactions with the SBL within the crater. The Cold-air pool Experiment [COLPEX, Price et al., 2011] aimed at improving the understanding on cold-air pooling processes in shallow ($\sim$ 100 m deep) valleys at the border between England and Wales, with the objective of developing parameterisations to represent such processes in coarser-resolution numerical models. The atmospheric processes governing multi-day persistent cold-air pools and their link to air pollution were studied during the Persistent Cold Air Pool Study [PCAPS, Lareau et al., 2013b], in the Salt Lake Valley (USA). As regards the Alps, the PASSY-2015 field campaign [Paci et al., 2016], aimed at studying persistent cold-air pooling processes in the truly complex terrain of the Arve River Valley, located on the foothills of Mont-Blanc. The project was motivated by the high level of particulate pollution commonly measured during wintertime in this valley. Understanding the link between severe particulate pollution events along Alpine transport routes and the link with meteorological processes was also the aim of the ALPNAP project [Heimann et al., 2007; de Franceschi and Zardi, 2009].

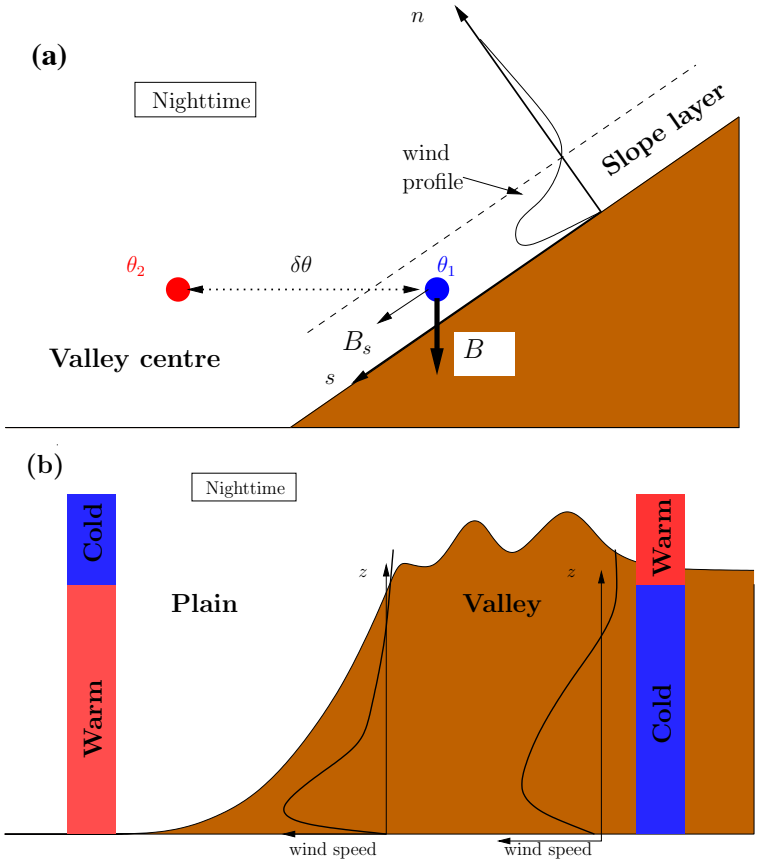

Figure II.2: Schematics of thermally-driven **(a)** downslope flows and **(b)** down-valley flows during nighttime; in **(a)** θ_1 is the potential temperature of a parcel of air close to the slope that is colder than a parcel at the same height far from the slope, of potential temperature θ_2; B is the buoyancy force on the parcel and B_s is the component of B along the slope s; a typical jet profile of a downslope flow is sketched; in **(b)** the blue-coloured columns represent relatively cold air while red-coloured columns represent relatively warm air; the air in a valley is generally colder than the air in the equivalent column on an adjacent plain, hence forcing a down-valley flow from the valley to the plain. The down-valley flow accelerates towards the valley exit forming a valley-exit jet. Adapted from Zardi and Whiteman [2013].

II.3 Dynamics of the valley boundary layer

II.3.1 The nighttime valley-wind system

The valley-wind system is a characteristic of mountainous terrain, for instance having a significant signature in climatic time-series of these regions [as reported by Martinez et al., 2008]. The local valley-wind system also has an important impact on the temporal and spatial variability of pollutant concentration within the valley, as showed by several studies [Panday and Prinn, 2009; Gohm et al., 2009; de Franceschi and Zardi, 2009].

The basic physical mechanisms beyond the formation of the valley-wind system rely on spatial temperature gradients [Zardi and Whiteman, 2013]. Because of the

sloping surfaces on the side of the mountain, a horizontal temperature gradient develops between the air close to the sloping surface and the air at the same altitude far from the surface. The air close to the slope is then negatively buoyant, forcing the air to flow down the slope during nighttime (downslope flows, see Fig. II.2a).

Thermally-driven along-valley flows are triggered by a temperature difference which forms along the valley axis. Generally, along-valley flows form because of the differential cooling between the valley atmosphere and the atmosphere of an adjacent plain [Vergeiner and Dreiseitl, 1987], or different sections of the same valley [McKee and O'Neal, 1989]. As a result, the along-valley flow direction is independent from the large-scale flow at the valley top, pointing from the low temperature region to the high temperature region (see Fig. II.2b).

It is worth noting that downslope flows are triggered by the cooling of the surface, while along-valley flows are closely related to temperature differences which arise from spatial differences of the thermal structure of the atmosphere. This aspect will be discussed in details in Sect. II.4.1. In the following analytical descriptions and typical features of these flows are discussed.

II.3.1.a Downslope flows

Most of the understanding on downslope flows relies on numerical and analytical models, with a smaller number of observations [Whiteman and Zhong, 2008].

Several models have been proposed to describe these flows. Broadly speaking, conceptual models for downslope flows can be divided into two categories:

(i) profile models, which describe the vertical structure of the flow;

(ii) parcel (or hydraulic) models, which describe the temporal evolution of the integrated (bulk) structure in the vertical of downslope flows.

The Prandtl [1952] model is a paradigm of the type **(i)**. This model describes the steady state of a flow in which there is a balance between the acceleration due to buoyancy and vertical diffusion of momentum, and the along-slope advection of heat and vertical diffusion of heat. Despite its simplicity, the model reproduces (after appropriate tuning of the constants of the model) the main feature of steady downslope flows, comparing well with observations and numerical simulations [Axelsen and van Dop, 2009]. Refinements to this analytical model have been made by Grisogono and Oerlemans [2001], to include a slowly varying eddy diffusivity, Stiperski et al. [2007] to include the Coriolis effects and Serafin and Zardi [2015] to develop an unsteady (periodic in time) solution for the Prandtl model.

The McNider [1982] model is a paradigm of type **(ii)**. The model predicts a quasi-steady regime of the downslope flow characterized by oscillatory motions with char-

acteristic frequency set by the Brünt-Väisäla frequency N and the slope angle. Physically, the oscillation of the downslope flow is due to the reduced buoyancy forcing on a fluid particle as it is advected downward (because the background flow is stably stratified). As the fluid particle decelerates, it cools due to the radiative cooling of the ground, which again accelerates the parcel down the slope. The oscillations described by the McNider [1982] model are pure oscillations in time, with no phase propagation in space. Oscillations of downslope flows are a well-documented feature from observations [see for instance Stone and Hoard, 1989; Monti et al., 2002; Princevac et al., 2008].

An unsteady downslope flow may also emit internal gravity waves as it travels in a stably stratified flows. Chemel et al. [2009] studied the internal gravity wave field generated by a downslope flow by means of numerical simulations of three-dimensional idealised valleys, and found that the wave field is characterized by a nearly constant frequency of $0.85N$. Their work was extended by Largeron et al. [2013] to consider the sensitivity to the valley geometry and initial background stratification. The authors found that the gravity wave field is generated by a hydraulic jump experienced by the downslope flow as it reaches the bottom of the slope.

Downslope flows properties also depend on surface characteristics. Numerical simulations of cold-air pools in two-dimensional idealised valleys with forest canopy on the sidewalls by Kiefer and Zhong [2013] show that downslope flows are generally weaker in valleys with forested sidewalls. This stems from weaker surface cooling on the near-surface slope atmosphere and increased drag on downslope flows.

II.3.1.b Along-valley flows

The structure of the down-valley flow was studied in detail during ASCOT [Clements et al., 1989b]. The vertical profile of this flow is usually characterized by a jet shape, with wind speeds in the range of 1 to 10 m s^{-1} [Clements et al., 1989b; Neff and King, 1989; Banta et al., 2004]. Empirically, the vertical profile of these flows can be described (best-fit) using a Prandtl-type mathematical expression as for slope flows (see Sect. II.3.1.a), even though it must be clearly stated that this functional form has not been derived formally from an analytical model [Clements et al., 1989b]. Observations of Chrust et al. [2013] in the Weber Canyon (Utah, USA) have shown that the down-valley flow develops in a few hours after the evening transition, reaching a steady state for the rest of the night. The depth of the down-valley flow layer is bounded by the actual depth of the terrain surrounding the valley, but observations of shallower (with respect to the depth of the terrain) down-valley flows have been reported.

Approaching the valley exit, down-valley flows can decrease in depth and accelerate forming a valley-exit jet [Whiteman, 2000, see also Fig. II.2]. Banta et al. [1995] reported Doppler-lidar measurements at the exit of the Eldorado canyon (Colorado,

USA), showing that the wind speed of the valley-exit jet was maximum under weak synoptic conditions, penetrating for more than 20 km over the adjacent plain. The doppler-lidar measurements indicated that the spatial structure of the valley-exit jet is complicated, with horizontal and vertical spatial heterogeneity. Zängl [2004] examined the valley-exit jet of the Inn Valley (Austria), considering the role of the narrowing of the valley in the formation of the jet. Numerical model results have shown that this valley exit-jet may be dynamically described as a transition from a subcritical to supercritical state due to the constriction at the exit of the valley [see for instance Pan and Smith, 1999]. However, a return to the subcritical state through a hydraulic jump was not observed afterwards over the foreland. Because the down-valley flow accelerates towards the valley end, divergence of the flow may occur along the valley axis [Whiteman and Barr, 1986], causing vertical motions at the valley top as required by mass conservation. This has a large impact on the heat and mass budget of the valley atmosphere as will be discussed in Sect. II.3.3 and Sect. II.4.2.

Oscillations in down-valley flows have been reported in the past, even though similar conceptual models used for downslope flows were difficult to apply. Porch et al. [1991] report regular down-valley flow oscillations in the Kimball Creek Valley (Colorado, USA) with a period of about 20 minutes. In that case the oscillations were hypothesised to be due to the interaction between the down-valley flow and the flow through the tributary valleys. Oscillations of the down-valley flow were also observed by Pinto et al. [2006] in the Salt Lake Valley as part of VTMX.

Down-valley flows extend up to the top of the SBL within the valley. Anti-winds (a wind flowing in the opposite direction with respect to the down-valley flow, i.e. up-valley) may co-exist above the down-valley flow layer. Anti-winds can be interpreted as the residual part of the daytime up-valley flows [Whiteman, 1986]. However, anti-winds may also form during nighttime, being the closing branch of the along-valley circulation, or because of a local thermal imbalance in the upper-layers of the valley atmosphere, as discussed by Serafin and Zardi [2011a]. Features such as the height of the maximum wind speed and the depth of the down-valley flow layer have been observed to be related to the intensity of the anti-wind above the down-valley flow layer [Clements et al., 1989b; Sakiyama, 1990], even though the exact nature of the upper-level anti-wind is not discussed in these studies.

Conceptual models for down-valley flows have been developed only for very simplified conditions. A linear solution for a single-layer flow within a valley with a prescribed forcing term was developed by Egger [1990]. The solution has the form of a propagating front, from the valley end towards the valley centre, with a "speed of propagation" $c = 0.5\,H\,N$, where H is the depth of the valley. The simple model established that the amplitude of the down-valley flow is inversely proportional to the background stratification N, so that as N increases, the down-valley wind speed

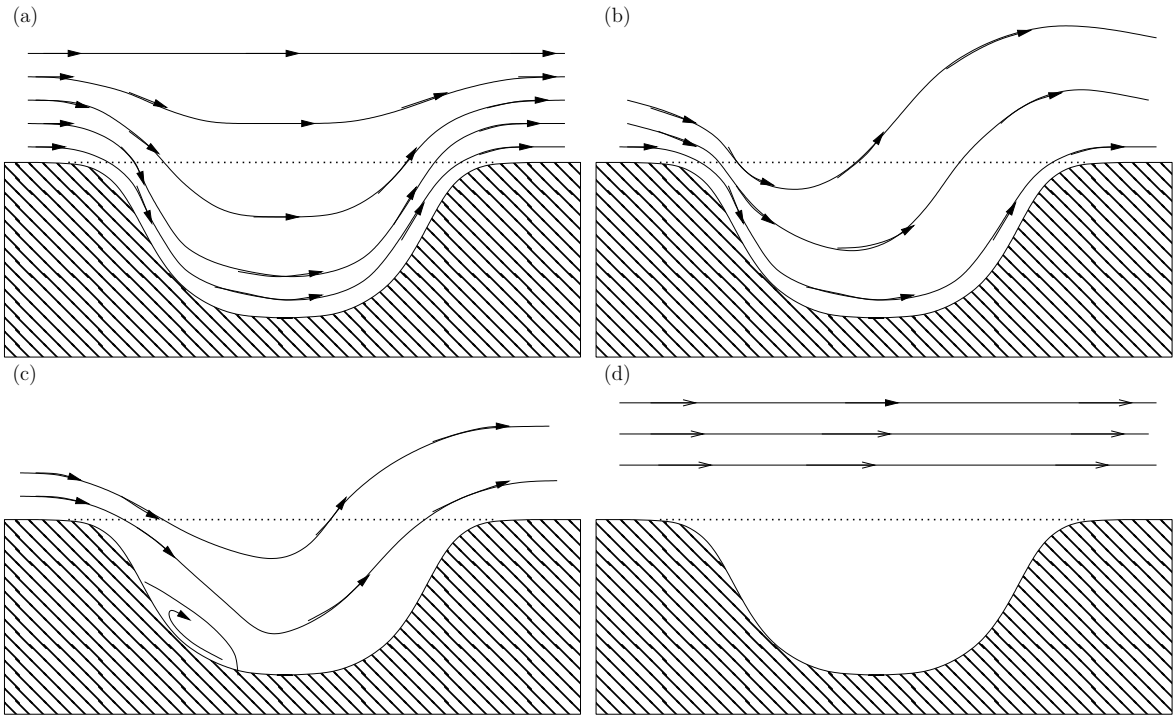

Figure II.3: Schematics of the possible regimes for an external flow passing over a valley distinguished by Holden et al. [2000]: **(a)** flow following the terrain, **(b)** phase shifting and gravity wave radiation, **(c)** flow separation and **(d)** dynamically-decoupled flow. Adapted from Holden et al. [2000].

decreases.

II.3.2 Effects of large-scale flows on valley-scale dynamics

II.3.2.a Froude number and non-dimensional mountain height

Holden et al. [2000] distinguished four possible situations that may occur when a large-scale (external) flow passes over a valley:

(1) the flow is following the terrain height, and the disturbances induced by the presence of the valley quickly decay with height (see Fig. II.3a);

(2) the flow experiences a phase-shift with height due to the generation and radiation of gravity waves (see Fig. II.3b);

(3) the flow penetrates within the valley but separates somewhere from the upstream sidewalls, leading to a region of stagnation within the valley (see Fig. II.3c);

(4) the flow aloft continues undisturbed above the valley (see Fig. II.3d).

Condition **(4)** leads to the concept of a dynamical decoupling of the valley atmosphere from the flow aloft. In such conditions, the valley dynamics is mostly controlled by the

local thermally-driven flows discussed in Sect. II.3.1. This situation may occur under ideal synoptic conditions, characterised by a "flat" pressure distribution and a weak anticyclonic circulation, as shown by Largeron and Staquet [2016a] for the Grenoble Valley.

From a dynamical point of view, making an analogy with a flow passing over a hill/mountain, the flow is able to penetrate within a valley if inertial forces dominate over the buoyancy forces, that is if the *Froude* number

$$Fr = \frac{U}{N\,H}, \tag{II.1}$$

is larger than a critical value, as specified below [Bell and Thompson, 1980]. In Eq. II.1 U is usually taken as the external large-scale wind speed above the valley and H is the depth of the valley.

Most studies in the past considered the situation of a flow transverse (or perpendicular) to the valley (cross-valley flow). Laboratory and numerical experiments performed by Bell and Thompson [1980] indicated a critical value for Fr of 1.3, hence if $Fr > 1.3$ the external flow penetrates within the valley [regime **(1)**], which otherwise remains dynamically-decoupled from the air above [regime **(4)**]. This condition can be also reported in terms of the non-dimensional mountain height

$$\hat{H} = N\,H/U = Fr^{-1}. \tag{II.2}$$

Vosper and Brown [2008] showed that for idealised shallow two-dimensional valleys ($H < 150$ m), the valley is decoupled ("sheltered") from the external flow for values of $\hat{H}$ above a critical value in the range $0.35 - 0.64$, depending on the depth H of the valley. In this work the values of U and N were computed from idealised one-dimensional simulations (i.e. single-column vertical models), in order to use "undisturbed" values of these quantities for the calculation of $\hat{H}$. Holden et al. [2000] using observations taken in a moderately deep (400-m deep) valley in Wales, indicated a critical value of $\hat{H}$ of about 2. Above this threshold turbulent production due to dynamical instabilities maintains the coupling of the ground surface with the atmosphere above. Similar conclusions were reported by Lareau and Horel [2015b], by means of numerical simulations of idealised deep two-dimensional valleys.

Rotunno and Lehner [2016] studied systematically the possible regimes of a flow passing over a valley by means of numerical simulations of idealised two-dimensional valleys, in the light of the measurements done during METCRAX II [Lehner et al., 2016]. The authors showed that the behaviour of the flow can depend generally on three non-dimensional parameters, which were chosen as the non-dimensional valley depth and width, $\hat{H}$ and $N\,L/U$, respectively, and the Froude number of the approach-

ing flow upstream of the valley, defined as $Fr_D = \pi U/2\,N\,D$, with D the depth of the approaching flow. Numerical results showed that the air within a valley is completely stagnant for values of $Fr_D < 1$ and $\hat{H}$, $N\,L/U$ much larger than one [regime **(4)**]. Conversely, for $Fr_D > 1$ and $0 < \hat{H} < 1$ the flow is symmetrical around the valley, "sweeping" the entire valley atmosphere for a large range of $N\,L/U$ [regime **(1)**]. In between these regimes, the interaction between the external flow and the valley atmosphere may result in a number of possible phenomena, like partial stagnation, internal wave generation, wave breaking and hydraulic jumps, which can describe the nighttime warm-air intrusions observed sometimes in the Arizona Meteor Crater [Adler et al., 2012; Lehner et al., 2016].

Finally, it is worth stressing that all of the studies reported have considered the case of a large-scale (external) flow transverse to a valley. In the case of a large-scale flow aligned with the valley axis, in order to have a dynamically-decoupled condition it is reasonable to expect a critical value for $\hat{H}$ larger than for the case of a flow transverse to the valley axis. Largeron [2010] analysed, by means of numerical simulations of the Grenoble valleys, the conditions for which the valley atmosphere was dynamically-decoupled from the synoptic flow aligned with the valley axis. The valley atmosphere was found to be decoupled from the large-scale flow if $\hat{H}$ was above a critical value in the range $3.3 - 16.7$, that is a range of values larger than the ones reported by other studies that consider flows transverse to the valley axis.

II.3.2.b Effects of large-scale flows on downslope flows

A large-scale flow transverse to a mountain barrier can lead to strong flows down the lee side of the mountain, with low-level wind speeds which may exceed 60 m s^{-1} [Durran, 1990]. Downslope windstorms are well-known phenomena occurring in many mountain ranges around the world. They can be associated with cold-air advection within the valley, such as the Bora in the oriental Alps, or warm-air advection, such as the Föehn in the Alps or the Chinook in the western United States. The mechanisms behind the formation of downslope windstorms have been the subject of extensive study in the past [see for instance Durran, 1990; Jackson et al., 2013].

According to Jackson et al. [2013], the mechanisms which can explain the formation of downslope windstorm-type flows are essentially:

(a) a transition from sub-critical to super-critical flow as the flow moves over the mountain barrier, in analogy with hydraulic theory [Long, 1954; Smith, 1985];

(b) amplification of vertically-propagating waves due to wave reflection at a pre-existing critical layer followed by constructive interference [Klemp and Lilly, 1975];

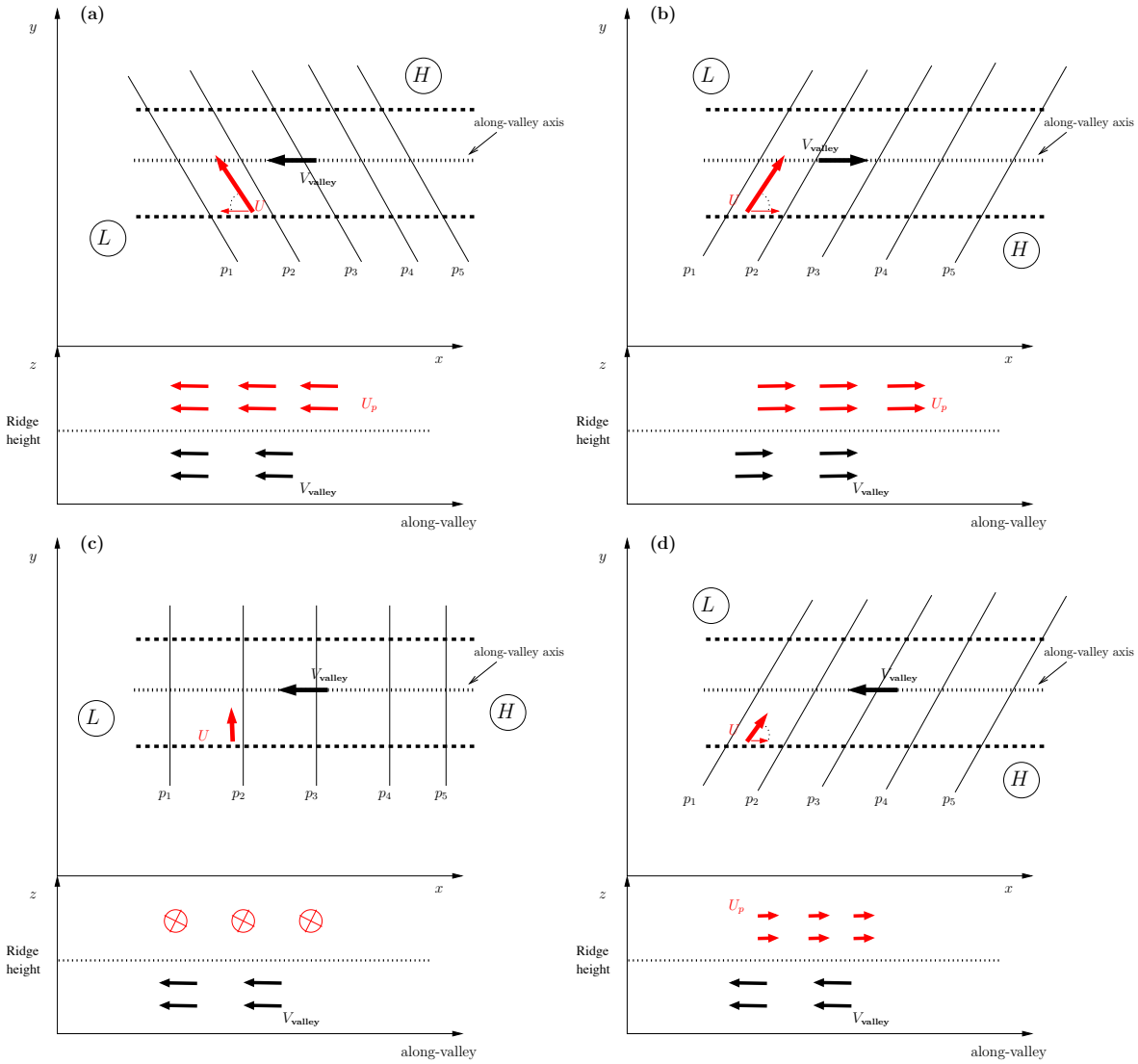

Figure II.4: Schematics of **(a)**, **(b)** forced channelling and **(c)**, **(d)** pressure-driven channelling mechanisms in a straight valley in the northern hemisphere. Not all the possible configurations are illustrated but only selected examples for a large-scale geostrophic flow U that is **(a)** south-easterly, **(b)** south-westerly, **(c)** southerly and **(d)** south-westerly. V_{valley} is the along-valley flow within the valley, continuous black lines indicate isobar of pressure p_i $(i = 1, 2...5)$ at the valley top, increasing from L (low-pressure) to H (high-pressure), U_p is the projection of U along the valley axis, and dashed lines identify the valley sidewalls. Each frame illustrates a top-view in a horizontal x-y plane (where x indicates the west-east direction and y the south-north direction) in the upper part, and a vertical cross-section along the valley axis in the bottom part. Adapted from Kossmann and Sturman [2003].

(c) amplification of vertically-propagating waves due to wave reflection at a self-induced critical layer created by wave-breaking at a certain height [Peltier and Clark, 1979].

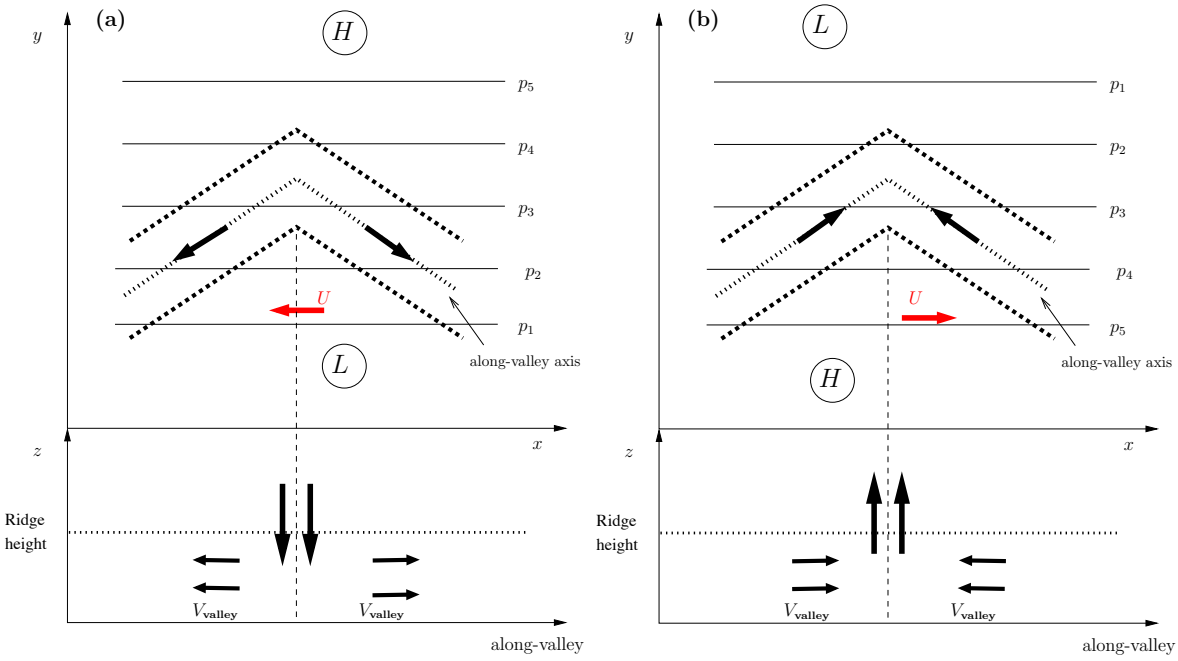

Figure II.5: Schematics of the pressure-driven forcing mechanism in a bent valley with angle $\alpha = 120°$ for a large-scale flow U that is **(a)** easterly and **(b)** westerly; V_{valley} is the resulting valley flow within the valley (black arrows), continuous lines indicate isobar of pressure p_i ($i = 1, 2...5$) at the valley top, increasing from L (low-pressure) to H (high-pressure), and dashed lines identify the valley sidewalls. Each frame illustrates a top-view in a horizontal x-y plane (where x indicates the west-east direction and y the south-north direction) in the upper part, and a vertical cross-section along the valley axis in the bottom part; regions of convergence/divergence are identified with vertical black arrows in the bottom part of each frame. Adapted from Kossmann and Sturman [2003].

II.3.2.c Effects of large-scale flows on valley flows

As shown by Whiteman and Doran [1993], the main mechanisms of valley flows due to the effect of large-scale (external) flows are downward momentum transport, forced channelling and pressure driven channelling (see Fig. II.4).

If the valley atmosphere is not dynamically-decoupled from the external flow above the valley (see Sect. II.3.2.a), momentum can be transported downward within the valley atmosphere, as a result of vertical mixing at the top of the valley, or gravity waves on the lee side of a valley sidewall. In wide and shallow valleys, this may lead to a valley flow in the same direction of the large-scale flow aloft.

The term "channelling" is more appropriately used when the valley flow is aligned with the valley axis, so that the variety of possible wind directions are essentially two (i.e. up-valley and down-valley). In deep and narrow valleys, forced channelling usually refers to a downward transport of horizontal momentum from the large-scale flow aloft [see also Whiteman, 2000], for which the resulting along-valley flow is in the direction of the component of the external flow projected along the valley axis (see

Fig. II.4a and Fig. II.4b).

The pressure-driven channelling mechanism refers to a valley flow forced by the geostrophic pressure gradient along the valley axis (see Fig. II.4c and Fig. II.4d). This mechanism is most efficient when the synoptic wind is perpendicular to the valley axis (see Fig. II.4c), hence the large-scale pressure gradient is oriented along the valley axis. This mechanism can be efficient also during periods of decoupling of the valley atmosphere from the flow aloft, depending only on the orientation and intensity of the large-scale pressure gradient at the valley top with respect to the valley orientation. Pressure-driven channelling (similarly to the thermally-driven forcing) may lead to "counter-currents", a situation in which the direction of the near-surface valley flows is opposite to the wind direction at the valley top [Gross and Wippermann, 1987]. Kossmann and Sturman [2003] proposed a conceptual model which indicates that in a curved valley, pressure-driven channelling may lead to convergence or divergence of the along-valley flow, hence forming regions of compensatory upward or downward motions where the valley bends (see Fig. II.5). Zängl [2005b] showed that the preferred direction of a thermally-driven down-valley flow can be controlled by the direction of the synoptic pressure gradient imposed at the top of the valley.

A climatological study in the upper Rhine Valley by Weber and Kaufmann [1998] showed that all the mechanisms developing along-valley flows within the valley (i.e. forced channelling, pressure-driven channelling and thermally-driven forcing) can occur simultaneously in some locations, because of the multitude of orientations of valleys surrounding the observation site, hence making it difficult to classify valley flows based only on the synoptic conditions.

Schmidli et al. [2009] studied the interplay between large-scale upper-level pressure forcing, mid-level pressure forcing ($\sim$ 2 km above sea level, below the crest height) and locally-induced thermal forcing on the along-valley flow observed in the Owen Valley (California, USA). The authors observed two different down-valley flows during two episodes characterised by anticyclonic large-scale conditions, which are supposed to be ideal to have thermally-driven along-valley flows near the surface. Numerical model simulations for these two episodes, showed that the large-scale flow may induce a different mid-level pressure forcing, which can act either to reinforce or weaken the near-surface down-valley flow, thereby leading to the observed differences during the two episodes.

II.3.3 Transport of mass at the valley-scale

Horizontal and vertical transport of mass in and out of the valley atmosphere, using an expression of Porch et al. [1989], "though (...) may appear academic, it could be very important for air pollutant source siting and receptor determination" [Porch et al.,

1989, pp. 579].

Chemel and Burns [2015a] using a numerical model studied the dispersion of a scalar tracer continuously emitted in an idealised deep (1 km) pseudo two-dimensional valley (i.e. invariant along the valley axis). In this case, the effect of down-valley transport was neglected. Numerical model results showed that, despite the fact that compensatory vertical motions induced by downslope flow convergence can mix efficiently tracers emitted from different locations within the valley, most of the tracers were trapped within the valley atmosphere below the capping inversion. Moreover, the induced compensatory vertical motions were able to replenish the tracer concentration within the strongly stratified near-surface inversion layer. A similar mechanism was proposed by Panday and Prinn [2009] to explain the pollutant dispersion in the Kathmandu valley, Nepal, and confirmed by Panday et al. [2009] using a numerical model of the dispersion within the same valley.

Down-valley flows promote the horizontal transport of mass (and any scalar) between a valley and the foreland, and hence are an efficient mechanism of ventilation along the valley axis [Gudiksen and Shearer, 1989]. Whiteman et al. [1996] computed the mass flux out of the Salt Wash canyon in the Sinbad basin (Colorado, USA) by means of single-point measurements of the vertical structure of the flow. The calculated mass flux out of the Salt Wash canyon was about 1.7 kton s^{-1} during the late evening. This number can be physically interpreted if it is compared with the total mass contained within the volume used for the calculation of the mass budget (control volume), that is computing a mass turnover time for the basin [Whiteman et al., 1996]. The mass turnover time quantifies the time required to fully transport the air within a valley volume, through a given surface of the control volume. This can be defined as

$$t_M = \frac{[\text{Mass}]}{M} \,, \tag{II.3}$$

where [Mass] is the total mass of the control volume and M is the mass flux through the Salt Wash canyon. Whiteman et al. [1996] found that $t_M = 3.8$ hours for the Sinbad basin, a value that is very similar to the one computed for the Brush Creek valley (Colorado, USA) using data of mass fluxes reported by Whiteman and Barr [1986]. This is rather surprising, given that the former is a basin-like depression with a narrow exit canyon while the latter is a wide and well-drained valley. As reported already in Sect. II.3.1.b, along-valley divergence of down-valley flows induces compensatory motions as required by mass conservation. The source of the compensatory air has been received little attention in the past. Whiteman and Barr [1986] assumed a horizontally homogeneous subsidence at the valley top in order to balance the along-valley divergence of the down-valley flow, neglecting influences from slope flows and tributaries because of the lack of data. A more refined calculation was performed during the 1984

ASCOT experiment by Porch et al. [1989] in the Brush Creek Valley (Colorado, USA), taking into account the contribution to the mass flux from one tributary valley. The analysis showed that a single tributary valley may contribute up to 15% of the entire mass exported out of the valley. A similar analysis performed by Coulter et al. [1989] for the same tributary valley of Brush Creek indicated that the mass flux through the tributary is extremely sensitive to the external flow. In a successive study, Coulter et al. [1991] studied three tributaries of Kimball Creek (Colorado, USA), indicating that the mass flux through a tributary is also sensitive to the orientation of the tributary with respect to the main valley. Specifically, the computed mass flux was the greatest for the tributary most closely aligned with the main valley axis. A numerical experiment of an idealised valley-tributary system of similar spatial scales of Brush Creek Valley was performed by O'Steen [2000]. Numerical results suggested that a single tributary can increase the along-valley mass flux within the main valley by 5 to 10%, in agreement with the conclusions drawn by Porch et al. [1989]. However, many flow features, such as the interactions between the tributary flow and the main valley flow, were not captured by the idealised numerical model setup.

II.4 Thermodynamic processes of the valley boundary layer

The physical processes contributing to the change of temperature of any parcel of air in the atmosphere are formally described by the equation for the potential temperature tendency

$$\frac{\partial \theta}{\partial t} = -u_i \frac{\partial \theta}{\partial x_i} - \frac{\partial s_i}{\partial x_i} - \frac{\theta}{\rho\, c_p T} \frac{\partial R_i}{\partial x_i}, \tag{II.4}$$

where ρ, θ, T are the resolved density, potential temperature and temperature fields, respectively, c_p is the specific heat capacity at constant pressure and the Einstein notation is used. The terms on the right-hand side (RHS) of Eq. II.4 represent the advection of heat associated with the resolved motions, the divergence of turbulent heat (temperature) fluxes s and the heat loss/input associated to the divergence of radiative fluxes R, respectively.

It is worth noting that the form of Eq. II.4 is similar in the Reynolds averaging (RANS) or Large Eddy Simulation (LES) formalisms. However, the two techniques are fundamentally different as the former implies ensemble (temporal) averages while the latter spatial filtering [see also Zhong and Chow, 2013]. The difference stems from the turbulent heat flux term: using the LES technique, this represents the non-resolved sub-filter turbulent fluxes; in the RANS, it represents the turbulent fluxes associated to the entire turbulent part of the spectrum. Whilst the LES technique can generally be used to parametrise sub-grid-scale motions, a "proper" LES must resolve the most

energetic part of the energy spectrum, down to the inertial sub-range [see for instance Wyngaard, 2004; Cuxart, 2015].

A better physical insight into Eq. II.4 can be obtained by integrating Eq. II.4 over an atmospheric volume within the valley which considers the sloping ground as bottom surface (see Fig. II.6). Invoking Gauss' theorem and assuming incompressibility, Eq. II.4 yields

$$\int_V \frac{\partial \theta}{\partial t}\, dV = \int_{\Sigma_i} -u_i\, \theta\, n_i\, d\Sigma + \int_{\Sigma_i} -s_i\, n_i\, d\Sigma + \int_{\Sigma_s} \tau_g\, d\Sigma + \int_V -\left[\frac{\theta}{\rho\, c_p T}\right] \frac{\partial R_i}{\partial x_i}\, dV, \quad \text{(II.5)}$$

In this form, the volume integral of the advection contribution is decomposed into the heat fluxes through the top and lateral surfaces Σ_i (first term on the RHS of Eq. II.5), n_i being the unit vector normal to the surfaces Σ_i. The volume integral of the turbulent heat fluxes is decomposed in the turbulent heat fluxes s_i through the surfaces Σ_i, and the surface heat (temperature) flux τ_g through the ground surface Σ_s. The last term on the RHS of Eq. II.5 defines the contribution within the volume due to radiative processes. This term can be rewritten as, integrating by parts,

$$\begin{aligned}\int_V \left[\frac{\theta}{\rho\, c_p T}\right] \frac{\partial R_i}{\partial x_i}\, dV = \int_{\Sigma_s} \left[\frac{\theta}{\rho\, c_p T}\right] R_i\, n_i\, d\Sigma + \int_{\Sigma_i} \left[\frac{\theta}{\rho\, c_p T}\right] R_i\, n_i\, d\Sigma - \\ - \int_V R_i \frac{\partial}{\partial x_i}\left[\frac{\theta}{\rho\, c_p T}\right] dV.\end{aligned} \quad \text{(II.6)}$$

The first and second terms on the RHS of Eq. II.6 represent the cooling due to radiative flux through the surfaces of the control volume V, and the third term describes the dependency of the radiative cooling term on the temperature gradients. As shown by Hoch et al. [2011], strong near-surface temperature gradients can significantly increase the longwave radiative cooling. Substituting the RHS of Eq. II.6 in Eq. II.5 yields

$$\begin{aligned}\int_V \frac{\partial \theta}{\partial t}\, dV = \\ + \int_{\Sigma_i} -u_i\, \theta\, n_i\, d\Sigma + \int_{\Sigma_i} -s_i\, n_i\, d\Sigma + \int_{\Sigma_i} \left[\frac{\theta}{\rho\, c_p T}\right] R_i\, n_i\, d\Sigma + \\ + \int_{\Sigma_s} \tau_g\, d\Sigma + \int_{\Sigma_s} \left[\frac{\theta}{\rho\, c_p T}\right] R_i\, n_i\, d\Sigma - \\ - \int_V R_i \frac{\partial}{\partial x_i}\left[\frac{\theta}{\rho\, c_p T}\right] dV\end{aligned} \quad \text{(II.7)}$$

Eq. II.7 states that the cooling of a given volume of air [left-hand-side (LHS) of Eq. II.7] results from the heat export due to advective, turbulent and radiative heat fluxes through the lateral and top surfaces of the control volume (second line of Eq. II.7), the heat loss at the ground surface due to the surface sensible heat and radiative heat flux (third line of Eq. II.7), and the volume integral of the term representing the dependency

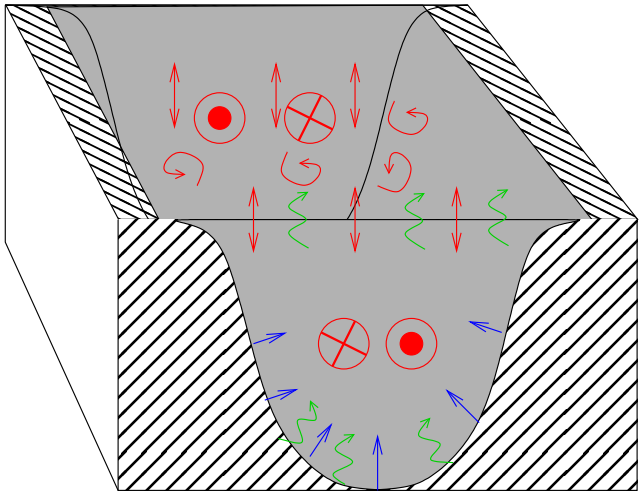

Figure II.6: Schematic of the cooling processes acting within an atmospheric volume encompassing the ground up to the top of the valley. Surface sensible heat flux at the ground surface (blue arrows), divergence of radiative heat fluxes (green arrows) and heat import/export due to advective and turbulent heat fluxes through the lateral and top surfaces (red arrows and eddies); see Eq. II.7.

of the radiative cooling on temperature gradients (fourth line of Eq. II.7), respectively (see Fig. II.6). The interplay between the different processes is highly dependent on the geometry of the terrain (i.e. depth, width and shape of the depression), on the effect of thermally-driven valley flows and on large-scale flows influences.

Even though it is clear that thermally-driven flows are related to terrain features, the following discussion about the mechanisms affecting the physical processes governing the valley boundary layer structure and evolution is schematically divided into the ones due to the topographic characteristics of the valley, the local thermally-driven flows and finally the ones due to large-scale flows.

II.4.1 Effects of terrain features

The valley-volume argument [Wagner, 1932; Whiteman, 1990] is usually one of the main mechanisms to explain the larger amplitude of the diurnal cycle of temperature within a valley [Vergeiner and Dreiseitl, 1987]. The argument can be derived from thermodynamic principles, so that "a given increment of heat Q added to or subtracted from an atmospheric volume will produce a potential temperature change in proportion to... volume V" [Whiteman, 1990, p. 10]. Because valleys are usually U-shaped or V-shaped, the volume of air within a valley embedded by the valley sidewalls up to ridge top (V_v), is smaller than the equivalent volume over a flat terrain (V_p) (see Fig. II.7). Hence, the volume argument states that given the same amount of heat loss during nighttime, the valley volume experiences a larger cooling than the equivalent volume over a flat terrain. The volume-argument can be used to explain the larger cooling

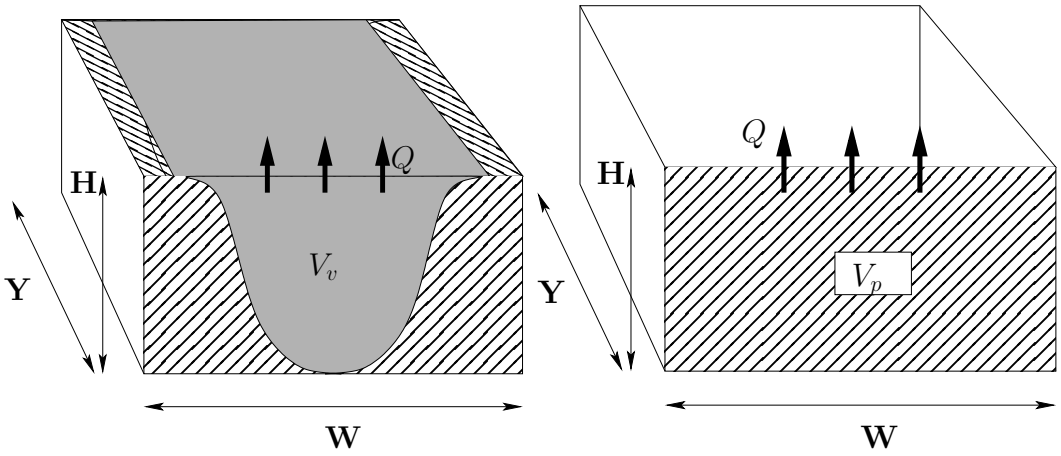

Figure II.7: Schematics illustrating the valley-volume argument. The volume of air embedded between the valley sidewalls up to the valley top (V_v) is smaller than the equivalent volume if the terrain was flat (V_p), that is a volume of same width W, length Y and depth H. Given the same amount of heat loss Q in the two volumes, the volume of air in the valley will cool more than the one on the plain.

at nighttime within a valley than on a plain region nearby, as well as temperature differences between different sections along the valley axis [McKee and O'Neal, 1989]. The value of the volume argument to explain the temperature differences between the atmosphere in a valley and the atmosphere in an adjacent plain has been investigated by several authors, in particular for daytime conditions [Weigel et al., 2006; Schmidli and Rotunno, 2010; Serafin and Zardi, 2011a; Schmidli, 2013]. Schmidli and Rotunno [2010] showed by means of numerical simulations of an idealised valley opening on a plain that the volume argument explains in part the larger cooling at nighttime within the valley than on a plain. However, the analysis also highlights its limitations because of the non-negligible effects of thermally-driven flows.

Other topographic parameters directly affect the cooling processes within the VBL, in particular if the near-surface atmosphere is considered. Those are related essentially to radiative processes within the VBL. Indeed a sloping topography has a reduced view of the sky compared to a flat terrain, so that downward long-wave radiation at the valley floor is both contributed by the atmosphere and by the surrounding terrain (see Fig. II.8). This effect is quantified by the sky-view factor, which ranges from 0 (no sky visible) to 1 (360° view of the sky, i.e. on a flat terrain) [see for instance Whiteman et al., 1989]. Whiteman et al. [2004b] analysed temperature data from various small-scale basins (few tens to hundred meters depth) characterized by different orographic characteristics, and found that the sky-view factor better explains the observed temperature at the floor of the basins than the valley-volume argument. Hoch et al. [2011] showed that the counterradiation from the valley sidewalls can change the cooling rate within a valley. For instance, counterradiation can decrease the volume-averaged radiative cooling by about 44 to 58 %, compared to a flat terrain

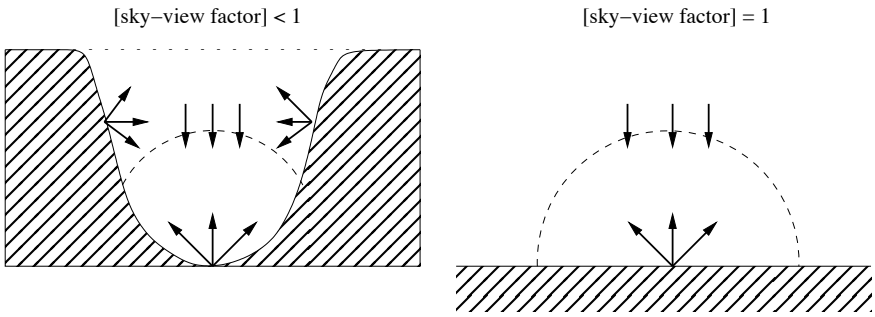

Figure II.8: Schematics of the reduced view of the sky within a valley. Arrows show long-wave radiation emitted by the ground or by the atmosphere. In a valley, because of the sloping surfaces, the downward long-wave radiation received at the valley floor is contributed from the atmosphere and by the surrounding terrain obstructing the sky; in a flat terrain only the air in the atmosphere contributes to downward long-wave radiation and the sky-view factor is one. Modified after Oke [1987].

during the early night. However, it was shown that above the valley centre, this effect rapidly vanishes as soon as the distance from the sidewalls is larger than 2 km.

Another mechanism affecting near-surface cooling processes is the sheltering effect of the valley from the flow aloft [Gustavsson, 1995; Vosper and Brown, 2008], even though this is more linked to the non-dimensional terrain depth than to the terrain itself. As discussed in Sect. II.3.2.a, the sheltering of the valley leads to a dynamical decoupling of the valley with the flow aloft, and so turbulent mixing processes are significantly reduced within the valley atmosphere. Hence the near-surface air is not mixed vertically with warmer air, cooling continuously throughout the night. Vosper and Brown [2008] showed that for idealised two-dimensional valleys, as the non-dimensional valley depth increases above its critical value (see also Sect. II.3.2.a), the maximum temperature difference between the air outside the valley and the air at the valley floor becomes independent of the valley depth. In such conditions, the temperature at the valley floor is only controlled by radiative cooling of the ground. However this mechanism seems to be most effective in hilly areas (characterised by a depth $H \sim 100$ m) where local thermally-driven flows are unlikely to play a major role. Numerical real-case simulations of the shallow Clun valley in Shropshire, England, by Vosper et al. [2014], confirmed the importance of such a mechanism for the cooling of air adjacent to the ground. Turbulent heat flux divergence was found to dominate the near-surface heat budget.

Land cover heterogeneities are also an important factor. Zangl [2005] showed that snow cover strongly affects the minimum temperature observed in closed basins. By means of idealised three-dimensional simulations of a basin-like depression, the author found that snow cover reduces the heat flux within the soil, hence increasing the cooling rate of the near-surface air. Extremely low temperatures can then trigger a drying mechanism preventing the formation of fog, thereby cooling can continue

throughout the night.

II.4.2 Effects of thermally-driven flows

In deep valleys, SBLs and cold-air pools are usually associated with the drainage of cold air from the valley sidewalls towards the valley bottom, which accumulates with time [Geiger, 1965]. From a physical point of view, the convergence of downslope flows at the valley bottom induces compensatory upward vertical motions because of mass conservation, which transport cooled air at the valley bottom into the upper-layer of the valley atmosphere [see Fig. II.9 and Whiteman, 1986; Fast and Darby, 2004; Burns and Chemel, 2015]. Observations by Whiteman [1986] in the Eagle valley (Colorado, USA) confirmed the existence of such transport process within the valley, showing that the capping inversion at the top of the boundary layer moves upward with time as a result of the compensatory vertical motions (see Fig. II.9). After the evening transition, the upward displacement of the capping inversion ceases, and the layer of air above the ground-based-inversion stabilises slowly with time. It should be noted that this downslope flow-induced circulation only affects the vertical thermal structure of the valley atmosphere if the compensatory vertical motions vary with height or, as for the case observed by Whiteman [1986], if there is a layer where the potential temperature gradient varies with height [Whiteman et al., 2010]. Following Whiteman et al. [2010], this can be shown by taking the partial derivative along the vertical of Eq. II.4 and only considering the vertical component of the advection term on the RHS, that is

$$\frac{\partial}{\partial t}\left[\frac{\partial \theta}{\partial z}\right] = -\left[\frac{\partial \theta}{\partial z}\right]\frac{\partial w}{\partial z} - w\frac{\partial}{\partial z}\left[\frac{\partial \theta}{\partial z}\right]. \tag{II.8}$$

The first term on the RHS of Eq. II.8 contributes to variation of stability only if the vertical velocity varies with height, while the second term on the RHS of Eq. II.8 only contributes if the stability varies with height (see Fig. II.9).

Downslope flows in deep valleys respond to the developing stable stratification decreasing their speed and progressively retreating "back up the slope" [Burns and Chemel, 2015]. Burns and Chemel [2015] showed that in such deep valleys, the detrainment of downslope flows towards the valley centre is maximum not far above the ground-based inversion layer. However, the weakening of the downslope flow with time leads to progressively weaker compensatory vertical motions over the valley centre [Catalano and Cenedese, 2010; Burns and Chemel, 2015].

If this detrainment is associated with a horizontal advection of colder air into the valley, the vertical stratification of the valley atmosphere may decrease throughout the night [Whiteman et al., 2010]. This argument was proposed by Whiteman et al. [2010]

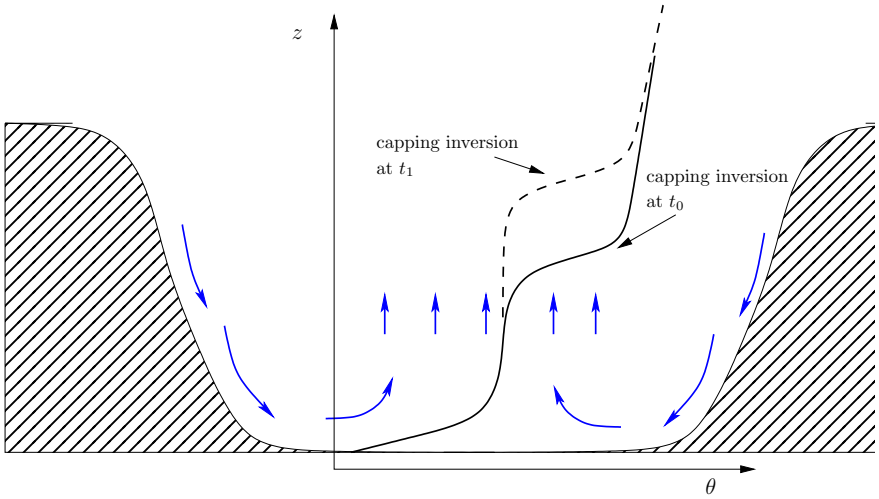

Figure II.9: Schematic of the structure of the stable boundary layer in a valley during the development period, at time t_1 and at time $t_2 > t_1$, with the main features highlighted. Adapted from Whiteman [1986].

and Haiden et al. [2011] in order to explain the near-isothermal layer above the strongly stratified ground-based-inversion in the Meteor Crater (Arizona, USA): air cools at the top of the basin, over the elevated plateaux, then it is advected into the basin, hence detraining at the height corresponding to its level of neutral buoyancy. This leads to a differential vertical cooling which weakens the stability of the upper part of the basin atmosphere. This mechanism was confirmed by Kiefer and Zhong [2011] in a numerical simulation of an idealised two-dimensional valley with similar geometrical parameters of the Meteor Crater (Arizona, USA). A similar two-layer vertical thermal structure of the boundary layer (namely a strong ground-based inversion surmounted by a near-isothermal layer) was also observed by other authors in deeper valleys. Clements et al. [1989b] observed a strong ground-based inversion layer surmounted by a nearly isothermal region up to the valley top for the Brush Creek Valley (Colorado, USA). Neff and King [1989] reported a similar structure for the De Beque basin (Colorado, USA).

The vertical thermal structure of the valley boundary layer can be also affected by mixing processes associated with the vertical shear of a down-valley flow. As showed by Pinto et al. [2006] the development of a down-valley flow at the southern terminus of the Salt Lake Valley (Utah, USA) was followed by a warming of the near-surface atmosphere and a cooling of the atmospheric layer just above it. Gravity and Kelvin-Helmholtz waves were identified and associated with the interaction of the down-valley flow with the SBL within the valley. Moreover, interactions between downslope and down-valley flows may create regions of local convergence/divergence of the flow so that local vertical transport of heat and mass can occur within a valley [Banta et al., 2004].

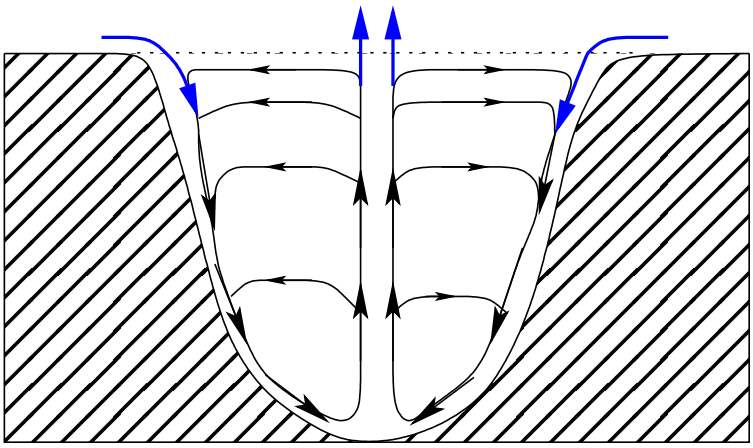

Figure II.10: Schematic of the circulation induced by downslope flow convergence over the valley centre at the beginning of the night, i.e. when a strongly stable stratified ground-based inversion layer has not developed yet. Arrows indicates the direction of the flow. Note that possible detrainment of downslope flows is not considered here. After Wagner [1932].

II.4.3 Evaluation of heat budget terms

Budgets of heat calculated over valley volumes have been studied extensively to quantify the role of the different atmospheric processes in the cooling of the nocturnal VBL (see Eq. II.5). In basin-like environments advective processes associated with thermally-driven flows are only due to downslope flows. The heat budget of a certain valley volume varies (i.e. the averaged temperature of the volume varies) only if heat (positive temperature fluctuation) is exported through one of the boundaries. Therefore, in this case, cooling of the valley volume occurs only if the downslope flow induced circulation (i.e. convergence of downslope over the valley centre and compensatory rising motions) exports heat out of the valley volume (see Fig. II.10). This can be accomplished either if relatively colder air is imported within the valley volume by downslope flows at the valley top, or if relatively warmer air is exported by the compensatory rising motions (see Fig. II.10). Noppler and Fiedler [2002] based on the idea that thermally-driven slope flows modify the vertical exchanges of heat between the surface and the free atmosphere, developed a conceptual model in order to take into account such effects. Their results point for a strong need of parameterisations in coarse-resolution global models.

Kondo et al. [1989] analysed the heat budget in the Aizu basin (Japan), a 1-km deep basin, by means of observations. The cooling rate averaged over the volume encompassing the centre of the valley (the atmospheric layer above the valley floor far from the valley sidewalls, see Fig. II.6) and over four nights was found to be mainly contributed by advection and radiative cooling close to the ground. However, when the heat budget terms were averaged over the entire basin atmosphere (see

Fig. II.6) the volume-averaged cooling rate was mainly driven by the surface sensible heat flux divergence, with minor influence of radiative processes. The contribution to the heat budget from advection was found to be negligible. This result indicates that the downslope-flow-induced-circulation for this particular case did not export heat through the top surface of the basin atmosphere (see Fig. II.10). Burns and Chemel [2014] showed in a numerical simulation of a deep (1 km) idealised two-dimensional valley (i.e. invariant along the valley axis) that the contribution from advection and turbulent heat flux divergence together contributes half of the volume-averaged cooling throughout the first part of the night. However, the repartition between advection, turbulent fluxes and surface sensible heat flux was not reported. Katurji and Zhong [2012] analysed the sensitivity of nocturnal VBL structure and cooling processes to the valley topography and ambient stability. The idealised simulations consisted of an extensive set of two-dimensional valleys of different width and slope angles. Two different values for the initial stability profiles were used, one corresponding to an isothermal atmosphere and one to a strongly stratified atmosphere. Numerical results indicated that the upper-layer of the valley atmosphere above the valley floor (for $z > 200$ m above ground level for the authors) was mainly controlled by vertical advection, while the lower layer by radiative heat flux divergence. In the upper-layer, the cooling rate was found to be larger for the narrower valley than for wider valleys, because of a stronger effect of vertical advection in the former.

As soon as down-valley flows can develop, for instance in a valley which opens on a plain further downstream, the picture presented above changes. Down-valley flow divergence in the along-valley direction (see Sect. II.3.1.b) has to be compensated by vertical motions at the valley top as required by mass conservation. In a stably stratified atmosphere this means that potentially warmer air is transported downward within the valley by vertical motions during nighttime. Fast et al. [1996] showed in a high-resolution numerical simulation ($\Delta x = 250$ m) of the Sinbad depression (Colorado, USA), that the volume-averaged contribution of advection to the heat budget does indeed warm the valley atmosphere. This is because the terrain surrounding the depression is only partially closed, opening on one side on the narrow Salt Wash canyon, allowing a down-valley flow to develop. The volume-averaged heat budget terms computed by the numerical model were found to be a few times smaller than the respective terms computed from the observations by Whiteman et al. [1996]. However, the simulated relative contributions of each term to the total cooling rate were more in accord with the ones computed from the observations. Schmidli and Rotunno [2010] in an idealised numerical simulation of a three-dimensional valley corroborate the idea that advection contributes to a warming of the valley atmosphere during nighttime because of the divergence of down-valley flows in the along-valley direction. Pinto et al. [2006] computed vertical profiles of the potential temperature tendency

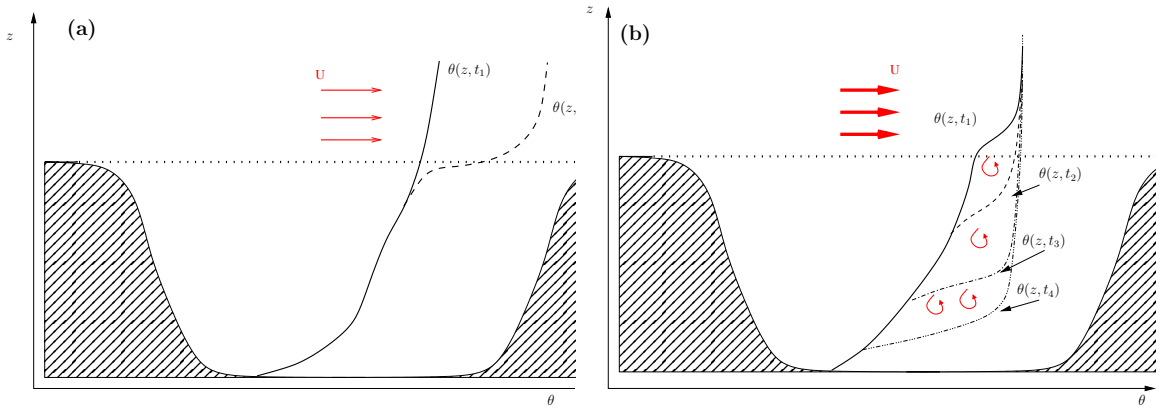

Figure II.11: Schematics of **(a)** advection of warm air at the top of the valley, leading to the formation of a strong capping inversion layer at the valley top and **(b)** turbulent erosion of the stable valley boundary layer; U is the large-scale (external) flow and different dash patterns identify different times of the vertical profile of potential temperature $\theta(z, t_i)$ $(i = 1, 2...)$.

(see Eq. II.4) from observations and vertical profiles of radiative cooling rate using a radiative transfer model to infer the contribution from advection and turbulent heat flux divergence as a residual. The computed profiles of the cooling processes showed that during the time period associated with the development of the down-valley flow (evening transition), the cooling of the near-surface inversion layer stems from the radiative flux divergence, with a warming contribution from the residual (i.e. the sum of advection and turbulent heat flux divergence). During the mature stage of the down-valley flow, the averaged cooling rate over the lowest 500 m above ground level was contributed by radiative cooling by only 30%, meaning that most of the cooling stems from advection or turbulent heat flux divergence. However, a clear quantification of the relative importance of these two processes was not performed. The numerical simulations of cold-air pools in the shallow (100-m deep) Clun Valley (UK) performed by Vosper et al. [2014] indicated that for $z > 5$ m above ground level, the cooling of the valley atmosphere far from the valley sidewalls was controlled by advection of cold air, associated with downslope flows during the early night, and down-valley flows during the late night.

II.4.4 Effects of large-scale flows

Large-scale flows have been recognised widely as a key factor affecting the thermal structure and evolution of the SBL of deep valleys. Advection of warm air in the upper layer of the valley atmosphere leads to the creation or intensification of elevated stable layers (a capping inversion) at the top of the valley atmosphere (see Fig. II.11a) which favours the dynamical decoupling between the air in the valley and the atmosphere aloft [Whiteman et al., 1999c].

This type of advection is usually associated with anticyclonic conditions and the movement of synoptic upper-level ridges over the region [Reeves and Stensrud, 2009]. These conditions had been shown to be strongly linked with the formation of persistent cold-air pools (PCAPs), which are stable boundary layers characterised by an inversion layer at the valley-scale which persists for multiple days within the valley [Reeves and Stensrud, 2009; Lareau et al., 2013b; Largeron and Staquet, 2016b]. Reeves and Stensrud [2009] showed that, based on a 3-year climatology study in the Western United States, the motion over the region of a large-scale ridge corresponds with the simultaneous formation of persistent cold-air pools in various valleys. All the valleys analysed were characterized by a mid-level warm air advection during the onset of the persistent cold-air pool event. The end of the event was linked to the approach of an upper-level trough that was responsible of the advection of cold air at the mid-levels. These findings confirm the results from previous case studies of persistent cold-air pools by Whiteman et al. [2001a] and Zhong et al. [2001]. Numerical simulations of a persistent (multi-day) cold-air pool event in the Salt Lake Valley (Utah, USA) performed by Lu and Zhong [2014] showed that large-scale warm air advection controls the tendency of potential temperature in the upper layer of the valley atmosphere ($3000 < z < 4000$ m above sea level for the Salt Lake Valley) throughout the core of the episode. The cold-air pool was then removed by cold-air advection in the upper layer of the valley atmosphere. The same behaviour was observed in the Grenoble Valley (France) in the work by Largeron and Staquet [2016a], in which several multi-day persistent cold-air pools episodes were simulated during the winter of 2006-2007, all episodes being initiated by a advection of warm air at mid-levels (about 1500 m above sea level for the Grenoble Valley).

Even though large-scale cold-air advection is the main mechanism accounting for the destruction of cold-air pools within a valley, other mechanisms can influence the thermal structure of the valley boundary layer. When a capping inversion is present at the top of the boundary layer, strong large-scale flows above the valley top can be prevented from penetrating within the valley (see Sect. II.3.2.a). However, the shear associated with the flow aloft can favour the entrainment of relatively warmer air from upper levels into the valley atmosphere, thereby progressively reducing its stability because of vertical mixing (see Fig. II.11b). This mechanism is usually referred to as a turbulent erosion of a cold-air pool [see for instance Lareau and Horel, 2015b]. Petkovšek [1992] developed an analytical model for this turbulent erosion mechanism. The model showed that the speed of the flow above the cold-air pool has to be "large enough" in order for turbulent production to be large enough to initiate the erosion process, and then it must increases continuously with time in order to fully mix the air within the valley. The first condition can be expressed quantitatively using the bulk Richardson number Ri_b for the capping inversion at the top of the valley boundary

layer, as done by Zhong et al. [2003]. For Ri_b smaller than its critical value $Ri_c = 0.25$ turbulent erosion at the top of the capping inversion initiates, that is if

$$U \geq 2\,N\,CI_h, \tag{II.9}$$

where U is the wind speed of the flow above the valley, N the Brünt-Väisäla frequency of the capping inversion of depth CI_h. Analogously, Eq. II.9 can be expressed as a condition for the Froude number (see Sect. II.3.2.a) for the capping inversion layer. The second condition is necessary because as the depth of the boundary-layer decreases, the stability of the capping inversion at its top increases (see Fig. II.11b). Using a semi-analytical model Zhong et al. [2003] concluded that turbulent erosion cannot mix the stably stratified air within a deep valley in a time-scale of the order of a day. A similar conclusion was drawn by Zhong et al. [2001] by means of numerical simulations of a cold-air pool event in the Columbia basin. However, other studies pointed towards different conclusions. Zängl [2005b] in a series of numerical simulations of the shallow Danube basin showed that turbulent erosion can be of moderate importance for the removal of the stably stratified air from the valley. High-resolution numerical simulation of idealised two-dimensional valleys (of spatial scales similar to the Salt Lake Valley) by Lareau and Horel [2015b] showed that if the speed of the flow aloft linearly increases with time, turbulent erosion can be a suitable mechanism for mixing the stably stratified air within the valley on a daily time-scale. The dynamical description stems from a continuous interplay between breaking Kelvin-Helmhotz waves, subsequent mixing, and horizontal advection.

Air in a valley can be also "displaced" horizontally by an impinging external flow so that the stably stratified cold-air is replaced by "new" air characterised by a weaker stability [see Fig. II.12, Lareau and Horel, 2015a]. This mechanism is usually associated with descending air on the lee side of one of the valley sidewalls. The flow accelerates as it flows down the slope before plunging into the capping inversion at the top of the boundary layer and, as a result, the air in the valley is displaced downstream and warm air is advected into the valley atmosphere (see Fig. II.12).This mechanism can lead to a full removal of cold-air from the valley atmosphere when the impinging flow is strong enough. Flamant et al. [2006] studied the interactions between a Föhn and a cold-air pool in the lower Rhine valley during IOP15 of MAP using a comprehensive set of observations. Analysis of data showed that the dynamical displacement of the cold-air pool by the Föhn flow was the primary mechanism accounting for the complete removal of the stably stratified air from the valley, with a negligible contribution of turbulent erosion at the top of the cold-air pool. Lareau and Horel [2015a] by means of the set of measurements collected during IOP1 of PCAPS, showed that internal gravity waves formed on the upstream sidewalls, accelerating the flow down the slope.

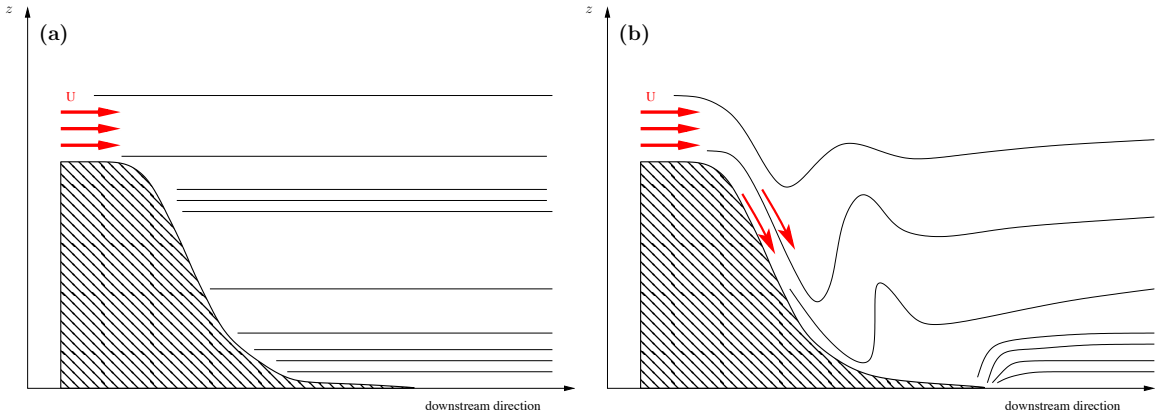

Figure II.12: Schematics of the displacement of a cold-air pool in a vertical cross-section along the downstream direction of the valley, **(a)** before that mountain waves form and the flow accelerates down the slope and **(b)** after that the accelerated flow displaced the cold-air pool downstream; red arrows represent the external flow and continuous black lines are lines of constant potential temperature (isentropes). Adapted from Lareau and Horel [2015a].

This leads to the displacement and tilting of the cold-air pool upward in the downstream direction. The cold-air pool can then eventually be displaced again upstream as soon as the balance of forces, which was maintaining the tilting, is destroyed.

II.5 Research objectives

Most of the process-level studies on cold-air pools and SBLs in complex terrains have considered idealised valleys invariant in the along-valley direction, in which thermally-driven along-valley flows are prevented. However Alpine valleys generally present a three-dimensional valley-wind system, because of terrain heterogeneities along the valley axis. The simplest modelling of this system consists of a valley opening on a plain region in the along-valley direction. A detailed mechanistic understanding of the interactions between the three-dimensional valley-wind system and the thermal structure of the stable valley boundary layer is still missing: what are the interactions between downslope and down-valley flows? What is the effect of these interactions on the boundary-layer thermal structure? What are the mechanisms controlling the conservation of mass within the valley? Chapter III aims to answer these questions, using high-resolution numerical modelling of an idealized, straight valley opening on a plain, without considering the effect of external (synoptic) flows. The numerical results are compared with the results from an idealised valley invariant in the along-valley direction. This allows a quantitative investigation of the effects of the thermally-driven down-valley flow.

A very idealised shape of the terrain is used in Chapter III. However, straight valleys opening directly on plain regions rarely exist in nature. Most valleys show complex

terrain features like heterogeneities in the along-valley direction, asymmetries in the cross-valley terrain (i.e. one slope steeper than the other), curved or inclined along-valley terrains, etc. All these aspects have been barely investigated. Among others, along-valley orographic variations are a key feature common to all Alpine valleys: valleys usually widen or narrow in the along-valley direction, a terrain feature which can be modelled schematically as a system of multiple valleys. In Chapter IV the SBL of a system of two valleys of different widths is analysed. Particular emphasis is given to the analysis of the effect that the along-valley terrain heterogeneity has on heat and mass transport processes.

Thus far, this discussion tacitly assumes that the orography is the main *local* factor affecting the evolution of the valley atmosphere, at least in deep valleys. Previous studies showed that other factors may be important, but those would probably *modulate* the response of the atmospheric processes to the terrain features (for instance surface heterogeneity, canopies...). More complex system of valleys can be studied, to further our understanding of the multiple interactions that may occur between atmospheric processes in a given valley and the ones in neighbouring valleys (the "mountain atmosphere" as it was called in Sect. II.1). In particular, the role of side (tributary) valleys on the heat and mass budgets of a given valley has received little attention, especially from a modelling perspective. This question is considered for a real terrain landscape under a weak synoptic forcing, in order to study the influence of surrounding valleys and tributaries on the boundary layer of a valley, in the light of the process-level understanding developed in the idealised framework. The link between the idealised and real worlds is given by semi-idealised numerical simulations, namely numerical simulations with well-controlled initial and boundary conditions (idealised), but using a real orography. The contrast between semi-idealised and real-case studies allows to quantify the impact of the thermally-driven circulation in the evolution of heat and mass budgets of a cold-air pool, compared to the large-scale (synoptic) forcing. Also, some of the mechanisms put forward in the idealised process-level studies of Chapter III and Chapter IV may be evaluated in such analysis. These aspects will be the objective of Chapter V. The investigation relies on the dataset collected during the PASSY-2015 field campaign, a field experiment that was held in a section of the Arve River Valley, near the town of Passy, during the winter of 2014-2015. The area often experiences severe air pollution episodes during wintertime.

To summarise, this thesis aims to advance the understanding of the physical processes controlling the evolution of heat and mass budget of the stable boundary layer in deep Alpine valleys, with the following scientific objectives:

O1 Characterise the influence of the thermally-driven valley-wind system on the mass and heat budgets of the stable valley boundary layer;

O2 Quantify the influence of along-valley orographic variations on the physical processes governing the heat budget of the valley atmosphere;

O3 Quantify the role of the flows from confluent valleys and tributaries to the mass and heat budget of a real valley;

O4 Determine how the synoptic forcing control or modulate the dynamical and thermal characteristics of the atmosphere in a real valley.

The next chapters are organized as follows: Objective **O1** will be considered in Chapter III; Chapter IV aims at addressing objective **O2**; Chapter V focusses on objectives **O3** and **O4** using a dataset collected during IOP1 of the PASSY-2015 field campaign; more details about the PASSY-2015 field campaign are reported in Appendix A. Chapter VI draws general conclusions from this work and gives indications for future research in the field.

III

Interactions between the Nighttime Valley-Wind System and a Developing Cold-Air Pool

---

The simplest modelling of the valley-wind system consists of a valley opening on a plain. In this chapter the influence of thermally-driven downslope and down-valley flows on the mass and heat budgets of the valley atmosphere is characterised, by contrasting the valley-plain system with a two-dimensional valley where down-valley flows are non-existent.

This chapter is a reproduction of Arduini et al. [2016]. Note that few minor points on the model setup and the computation of the heat budget have been clarified in the thesis.

Abstract The Weather Research and Forecast (WRF) numerical model is used to characterize the influence of a thermally-driven down-valley flow on a developing cold-air pool in an idealized alpine valley decoupled from the atmosphere above. Results for a three-dimensional (3D) valley, which allows for the formation of a down-valley flow, and for a two-dimensional (2D) valley, where the formation of a down-valley flow is inhibited, are analyzed and compared. A key result is that advection leads to a net cooling in the 2D valley and to a warming in the 3D valley, once the down-valley flow is fully developed. This difference stems from the suppression of the slope-flow induced upward motions over the valley centre in the 3D valley. As a result, the downslope flows develop a cross-valley circulation within the cold-air pool, the growth of the cold-air pool is reduced and the valley atmosphere is generally warmer than in the 2D valley. A quasi-steady state is reached for which the divergence of the down-valley flow along the valley is balanced by the convergence of the downslope flows at the top of the cold-air pool, with no net contribution of subsiding motions far from the slope

layer. More precisely, the inflow of air at the top of the cold-air pool is found to be driven by an interplay between the return flow from the plain region and subsidence over the plateaux. Finally, the mechanisms that control the structure of the cold-air pool and its evolution are found to be independent of the valley length as soon as the quasi-steady state is reached and the down-valley flow is fully developed.

III.1 Introduction

The representation of the stable atmospheric boundary layer in complex terrain, ranging from rugged lowlands with valley incisions to the highest mountains, constitutes a significant forecasting challenge. Small-scale processes in such complex terrain remain largely unresolved by current numerical weather prediction models and so are their impacts on weather, climate and air quality [see for instance Zardi and Whiteman, 2013]. Specifically, large temperature variations may occur over short distances, especially during clear nights when radiative cooling of the surface leads to a strong ground-based inversion (GBI). In areas sheltered from the atmosphere above, particularly from flow where high wind speeds and consequent intense turbulent mixing conspire to reduce vertical temperature gradients towards zero [e.g. Vosper and Brown, 2008; Lareau and Horel, 2015a], or under quiescent synoptic conditions, cold-air pools (CAPs) form. CAPs are associated with a strong GBI, and so weather hazards and pollution episodes are more likely in CAPs than over flat terrain in the same region, especially when they are intense, shallow and long lasting as this may occur in winter.

Under these conditions, thermally-driven slope and valley winds are key to maintaining some degree of ventilation [e.g. Largeron, 2010; Nadeau et al., 2013]. Slope flows develop as a result of the horizontal thermal imbalance between the layer of air adjacent to the slope and the air at the same altitude far from the slope. At night, the radiative cooling of the ground produces downslope flows. Along-valley flows are also thermally driven and are triggered by the thermal imbalance in the down-valley direction, for instance between the valley interior and an adjacent plain.

The role of downslope flows in CAP formation under decoupled conditions depends on the scales of the terrain. Burns and Chemel [2014, 2015] and Vosper et al. [2014] discussed results from numerical model simulations of the formation of a CAP in valleys of very different depths. Vosper et al. [2014] considered the Clun Valley, England, a narrow valley with depth between 75 and 150 m. In such a shallow valley, the sheltering provided by surrounding terrain allowed a CAP to form. The strong atmospheric static stability of the simulated developing CAP rapidly suppressed downslope flows. The cooling of the air adjacent to the ground was dominated by the parametrized subgrid-scale (SGS) turbulent mixing, while the cooling above was dominated by the transport of cold air from the valley sides or from down-valley drainage. By contrast, Burns and

Chemel [2014, 2015] considered an idealized 1-km deep narrow valley, not subject to down-valley winds. In such a deep valley, downslope flows were found to play a major role in the development of a CAP. As the cold-air region engulfed the slopes, a 100-m deep strongly stratified GBI was left above the valley floor. The downslope flows then detrained largely above the GBI layer, thereby mixing the upper part of the CAP. The valley-atmosphere instantaneous cooling was eventually driven by a complex interplay between radiative cooling and dynamical cooling.

Although widely observed [e.g. Neff and King, 1987; Banta et al., 2004; Pinto et al., 2006; Schmidli et al., 2009], the influence of down-valley flows on the evolution of CAPs under decoupled conditions is not well characterized, presumably owing to the challenges in simulating CAPs [Baker et al., 2011] and collecting extensive observations. Numerical modelling studies investigating CAP processes have generally considered two-dimensional (2D) valley geometries that are invariant in the down-valley direction (referred to as 2D valleys hereafter), thereby preventing any thermally-driven down-valley flow from developing [e.g. Vosper and Brown, 2008; Catalano and Cenedese, 2010; Katurji and Zhong, 2012; Burns and Chemel, 2014, 2015]. Numerical simulations considering valleys with a three-dimensional (3D) geometry that is varying in the down-valley direction (referred to as 3D valleys hereafter) have generally focussed on convective situations [e.g. Rampanelli et al., 2004a; Schmidli et al., 2011]. Only a few studies have examined pooling and draining processes in 3D valleys. Zangl [2005] investigated processes promoting the formation of extreme CAPs in an idealized elevated sinkhole (i.e., closed basin). O'Steen [2000] examined the impact of tributaries on the nighttime down-valley flow and on the associated mass transport outside idealized valleys. Schmidli and Rotunno [2010] examined the mechanisms leading to the formation of a thermally-driven along-valley flow in a 3D valley. The importance of the geometry of the valley with respect to the other mechanisms in the development of a valley–plain temperature difference, was quantified using the concept of a topographic amplification factor [see, for instance, Whiteman, 1990]. Results indicated that the along-valley flow induces a heating of the valley atmosphere during the night and a cooling of the valley atmosphere during the day. Similar conclusions were reported during daytime by Rampanelli et al. [2004a] in a study of an idealized valley, and by Weigel et al. [2006] in a real-case study of the Riviera Valley in southern Switzerland. For nocturnal conditions, the heating of the valley atmosphere was explained by subsidence motions from the atmosphere above the valley, due to the divergence of the down-valley flow.

The overall aim of the present work is to characterize the influence of a thermally-driven down-valley flow on a developing CAP in an idealized alpine valley under decoupled conditions. For this purpose, we analyze and compare results from numerical model simulations of a developing CAP in a 3D valley and in the counterpart 2D

valley. The set-up of the numerical simulations is presented in Sect. III.2, and the development of the thermally-driven down-valley flow is discussed in Sect. III.3. In Sect. III.4, the influence of the down-valley flow is quantified by contrasting the 3D and 2D valley cases, and in Sect. III.5 we investigate the sensitivity of the results to the valley length. Finally, conclusions are given in Sect. III.6.

III.2 Design of the numerical simulations

III.2.1 The numerical model

The numerical simulations were performed with the Weather Research and Forecasting (WRF) model, in its version 3.4.1 of the Advanced Research core formulation [Skamarock et al., 2008]. The WRF model is a compressible non-hydrostatic model, appropriate for scales ranging from metres to global scales. The governing equations are formulated using a terrain-following hydrostatic-pressure coordinate and discretized on a staggered Arakawa-C grid. For the present work, time integration was performed with a third-order Runge–Kutta scheme using a time-splitting technique to integrate the fast acoustic mode [Wicker and Skamarock, 2002]. The advection terms were discretized using a fifth-order Weighted Essentially Non-Oscillatory (WENO) scheme with positive definite filter. The planetary boundary layer was not parametrized and SGS motions were modelled with a turbulent kinetic energy 1.5-order closure scheme, which accounts for the stability dependence of the SGS length scale in stably stratified conditions and with the Smagorinsky coefficient C_s set to 0.1 [Moeng et al., 2007]. We note that in a stably stratified atmosphere, C_s may vary with height [Smith and Porté-Agel, 2014], limiting or enhancing SGS mixing. Dynamical models [see for instance Bou-Zeid et al., 2004; Smith and Porté-Agel, 2014] allow the variation of C_s with height, depending on the instantaneous flow characteristics. The effect of these variations on the motion at the resolved scales need to be quantified in future work. Radiative transfer was taken into account using the Rapid Radiative Transfer Model for longwave radiation [Mlawer et al., 1997] and the scheme proposed by Dudhia [1989] for shortwave radiation. Shadowing effects were not included, as in Burns and Chemel [2014]. The interactions with the ground surface were modelled using the community Noah Land Surface Model [Chen and Dudhia, 2001] using four soil layers.

III.2.2 The topography of the valley

A valley similar to the one used by Schmidli et al. [2011] is considered. It is symmetric about the origin at $x = 0$ and $y = 0$ (see Fig. III.1), and the analytical expression for

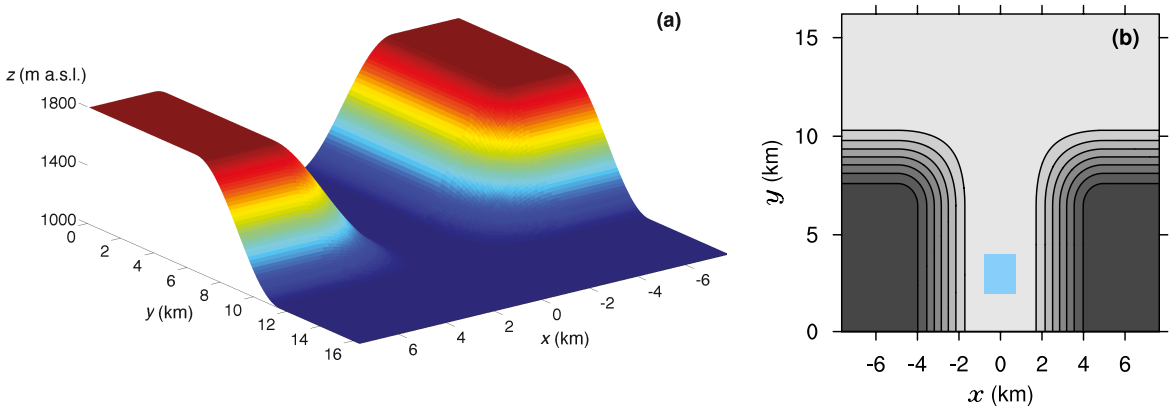

Figure III.1: **(a)** Terrain height for the control case. The topography is symmetric about the origin $(x, y) = (0, 0)$, where the cross-valley direction x is oriented west-east and the down-valley direction y is oriented south-north. **(b)** Contours of the terrain height (with intervals of 100 m) for the control case; the light blue box denotes the *valley centre* area, i.e. the area within the valley defined by $2 < y < 4$ km and $|x| \leq L_x$; see Sect. III.2.6 for details. Note that half of the topography along the y-direction is displayed.

the height of the terrain is given by

$$h\left(x, y\right) = H\, h_x\left(x\right)\, h_y\left(y\right) + h_0, \tag{III.1}$$

where

$$h_x\left(x\right) = \begin{cases} \left[1 - \cos\left(\pi\ \left(|x| - L_x\right)/S_x\right)\right]/2 & \text{for} \quad L_x \leq |x| \leq S_x + L_x \\ 0 & \text{for} \quad |x| < L_x \\ 1 & \text{for} \quad |x| > S_x + L_x \end{cases} \tag{III.2}$$

and

$$h_y\left(y\right) = \begin{cases} \left[1 + \cos\left(\pi\ \left(|y| - L_y\right)/S_y\right)\right]/2 & \text{for} \quad L_y < |y| \leq S_y + L_y \\ 0 & \text{for} \quad |y| > L_y + S_y \\ 1 & \text{for} \quad |y| \leq L_y \end{cases} . \tag{III.3}$$

The topography considered is characterized by a valley depth $H = 800$ m, a width of the sloping sidewalls $S_x = 4200$ m (in the cross-valley direction x) and $S_y = 5000$ m (in the down-valley direction y) and a half-width of the valley floor $L_x = 750$ m (in the cross-valley direction x). The reference height is set to $h_0 = 1000$ m. With this setup, the maximum angle α of the slope is about 17°. The length of the valley L_y (as displayed in Fig. III.1) is varied from 6 to 10 km, with $L_y = 6$ km for the control case. The total valley length $L_{\text{tot}} = L_y + S_y$ for the control case is then equal to 11 km. All the model points were assigned the latitude and longitude of the centre of the Chamonix valley located in the French Alps.

III.2.3 Grid design

Burns and Chemel [2014] have shown that a vertical resolution smaller than a few metres is needed to capture the downslope flows and the structure of the valley boundary layer. Furthermore, the modelling studies by Rampanelli et al. [2004a] and Schmidli et al. [2011] have shown that the domain should be large enough for the flow dynamics not to be influenced by the lateral boundary conditions. To satisfy these constraints, we relied on the nesting capability of the WRF model. Two domains were used: an outer domain (D1) discretized with $114 \times 334 \times 101$ grid points in the x-, y- and z-direction, respectively, with a horizontal resolution $\Delta x|_{\mathrm{D1}} = \Delta y|_{\mathrm{D1}} = 270$ m, and an inner domain (D2) discretized with $172 \times 361 \times 101$ grid points in the x-, y- and z-direction, respectively, with a horizontal resolution $\Delta x|_{\mathrm{D2}} = \Delta y|_{\mathrm{D2}} = 90$ m, both centered on the origin. The nesting between the two domains is one-way, in the sense that the boundary conditions of the inner domain are updated from the outer domain solution every outer-domain timestep, with no feedback from the inner domain on the outer domain.

The vertical coordinate was stretched along the vertical direction using a hyperbolic tangent function [Vinokur, 1980], providing a vertical resolution $\Delta z \approx 1.7$ m for the first level above the ground surface, and 10 levels in the first 20 m above the ground surface. In order to obtain numerically stable results, the vertical grid resolution demanded a timestep $\Delta t|_{\mathrm{D2}} = 0.15$ s for the inner domain, and a timestep $\Delta t|_{\mathrm{D1}} = 0.45$ s for the outer domain.

It is acknowledged that the grid resolution is too coarse to resolve the full range of turbulent motions acting in stable boundary layers and the numerical simulation performed in this work should be referred to as high-resolution mesoscale simulations [Cuxart, 2015].

III.2.4 Initial conditions

The simulations were initialized 1 h before sunset, and were run for a 6-h period. Decoupled conditions were considered and so no flow was prescribed at the initial time ($t = 0$). The atmosphere was initialized to be in hydrostatic balance. The vertical lapse rate of virtual potential temperature $\partial\theta_v/\partial z$ at $t = 0$ was set to 1.5 K km^{-1}, yielding a temperature profile typical of post-convective conditions. For simplicity, θ_v is referred to as potential temperature thereafter. The Brunt–Väisäla frequency $N = \sqrt{(g/\theta_v)\,\partial\theta_v/\partial z}$, where g is the acceleration due to gravity, has then an initial value $N_0 \approx 0.71\ 10^{-2}$ s^{-1} within the valley. The potential temperature of the first air layer at the valley floor was set to $\theta_0 = 288$ K, and the skin temperature was initialized by extrapolating the temperature of the first three air layers above the ground surface. The soil temperature of the deepest soil layer (at a depth of 8m) at the valley floor

was set to the annual mean surface air temperature of 281.4 K [Chen and Dudhia, 2001], and a constant temperature gradient of 2 K km^{-1} was used across the idealized terrain in order to account for the variation with height of the deep soil temperature [Burns and Chemel, 2014]. The soil temperature profile was initialized assuming an exponential increase of temperature with depth between the skin temperature and the deep soil temperature. A detailed discussion of the soil initialization is given in Burns and Chemel [2014]. The atmosphere was initialized with a relative humidity of 40 %.

III.2.5 Boundary conditions

Lateral boundary conditions for the outer domain were set to periodic boundary conditions in the x-direction and to open boundary conditions in the y-direction. The total height of the domain is 12 km. A 4-km deep implicit Rayleigh sponge layer [Klemp et al., 2008] was used at the top of the domain to damp upward propagating gravity waves; the damping coefficient was set to 0.2 s^{-1}. At the ground the usual impermeability condition was used, together with the Monin-Obukhov similarity theory, which was applied as the bottom boundary condition for the turbulent fluxes [Jimenez et al., 2012]. An alternative formulation for the stably stratified surface layer proposed by Zilitinkevich et al. [2013] was also tested, which did not affect significantly the numerical results. We note that a slope-modified similarity theory [see for instance Łobocki, 2014] may be more appropriate to represent the surface layer of a sloping surface. The aerodynamic roughness length was set to 0.1 m.

III.2.6 Definition of control volumes

Since the valley boundary layer coincides with the CAP, it will be referred to as CAP thereafter. Following Burns and Chemel [2015], the CAP is decomposed in two parts: the GBI, defined as the layer of atmosphere above the ground surface where a temperature inversion develops (that is $\partial T/\partial z > 0$, where T is the absolute temperature), and the part of the CAP above the GBI, which will be referred to as CAP↑.

The height of the GBI, denoted by z_{GBI}, is defined as the height where the absolute temperature ceases to increase with height. When the atmosphere is not dry, Burns and Chemel [2015] have shown that the height of the top of the humid layer can be used to track accurately the top of the CAP, denoted by z_{CAP}; we use this definition hereafter. Note that a more standard definition of the height of the CAP, based on the height where the vertical gradient of potential temperature reaches a maximum, will also be used; this definition can be equivalently expressed in terms of the height where the Brunt–Väisäla frequency reaches a maximum value.

Different spatial averages will be considered below. We consider the average over

the area defined by $|x| \leq L_x$ (i.e. the width of the valley floor) and $2 \leq y \leq 4$ km (where the plateaux are flat and the slope angle does not change along the down-valley direction, see Fig. III.1b), which will be referred to as the *valley centre* area hereafter and, for clarity, will be written in italics when referring to this area. Volume averages will be performed over along-valley sections defined by $2 \leq y \leq 4$ km and of height range corresponding to the GBI or CAP↑. These volumes will be referred to as the GBI volume and the CAP↑ volume, respectively.

III.2.7 Definition of a counterpart two-dimensional valley

The atmospheric circulation in the 3D valley will be compared to that developing in a 2D valley. The topography of the 2D valley is defined by Eq. III.1 with $h_y(y) = 1$. The 2D simulation was set up as the 3D ones except that no grid nesting was used, and periodic boundary conditions were applied at all lateral boundaries. We recall that the formation of an along-valley flow is inhibited in the 2D valley.

III.3 Mechanism of down-valley winds

III.3.1 Differential cooling between the valley and the plain

Vertical profiles of the potential temperature above the valley floor and the plain are displayed at different times in Fig. III.2. During the first 30 min of simulation, the vertical temperature structure in the valley is the same as over the plain (see Fig. III.2a). After 90 min (i.e., 30 min after sunset), a shallow stable boundary layer typical of flat terrain develops over the plain; in the valley, by contrast, the boundary layer is deeper and, for a given height, displays lower temperatures than over the plain. This differential cooling is linked to the downslope flows, which develop about 30 min after sunset, as follows. The air advected by the downslope flow, together with the cold air layer over the valley floor due to longwave radiative heat loss, are mixed in the vertical by the rising motions resulting from mass conservation [see Burns and Chemel, 2015, and Sect. 4.1], since the down-valley flow has hardly formed at this time.

After 330 min, the differential cooling between the valley and the plain is maintained, except over a thin layer of 10 m or so, where the near-surface air temperature is lower over the plain than over the valley floor (see Fig. III.2c, d). This feature is closely linked to the dynamics of the downslope and down-valley flows, which are fully developed at this time, as will be discussed in the next sections.

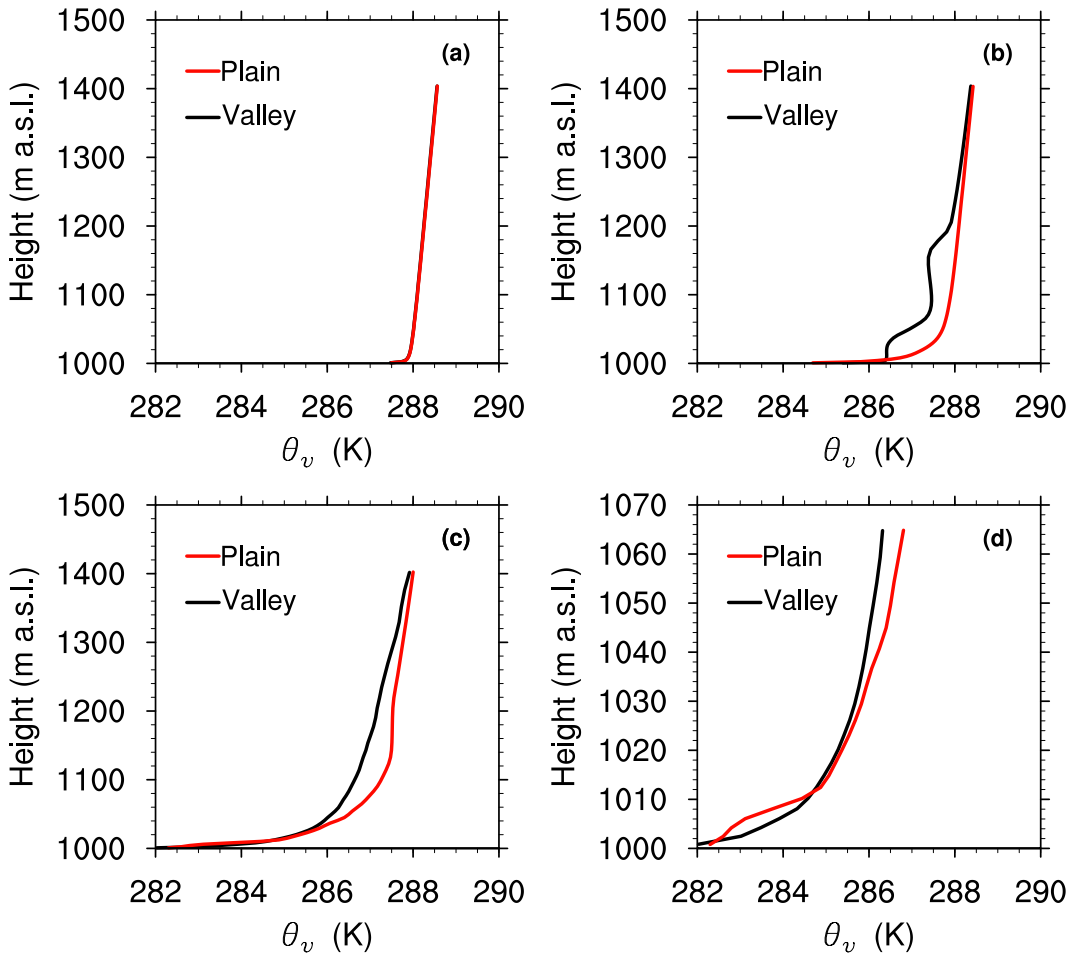

Figure III.2: Vertical profiles of potential temperature θ_v, averaged over the *valley centre* (black line, see Sect. III.2.6) and over the plain for $12.4 \leq y \leq 14.4$ km (red line) at **(a)** $t = 30$ min, **(b)** $t = 90$ min, and **(c)** and **(d)** $t = 330$ min. **(d)** is a zoom of **(c)** over the first 70 m above the ground surface.

III.3.2 Development of the down-valley flow

The valley atmosphere far from the slope layer may be assumed to be in hydrostatic balance as discussed for example by Rampanelli et al. [2004a] and Serafin and Zardi [2011a]. The boundary layer being deeper and colder in the valley than over the plain (except, as already discussed, over the first 10 m above ground level, see Fig. III.2c, d), the resulting pressure difference drives a down-valley flow from the valley to the plain. Schmidli and Rotunno [2010] showed that this pressure difference can be in part explained by the topographic amplification factor of the valley. In the next two sections, we investigate the role of the valley-wind system on the formation of this pressure difference.

Figure III.3a displays the height of the CAP z_{CAP} versus time for different positions in the along-valley direction y. Since the CAP height is partly controlled by the vertical motions induced by the downslope flows, the maximum value of the downslope flow speed $u_{\mathrm{s,max}}$ computed at the same y-positions is displayed versus time in Fig. III.3b.

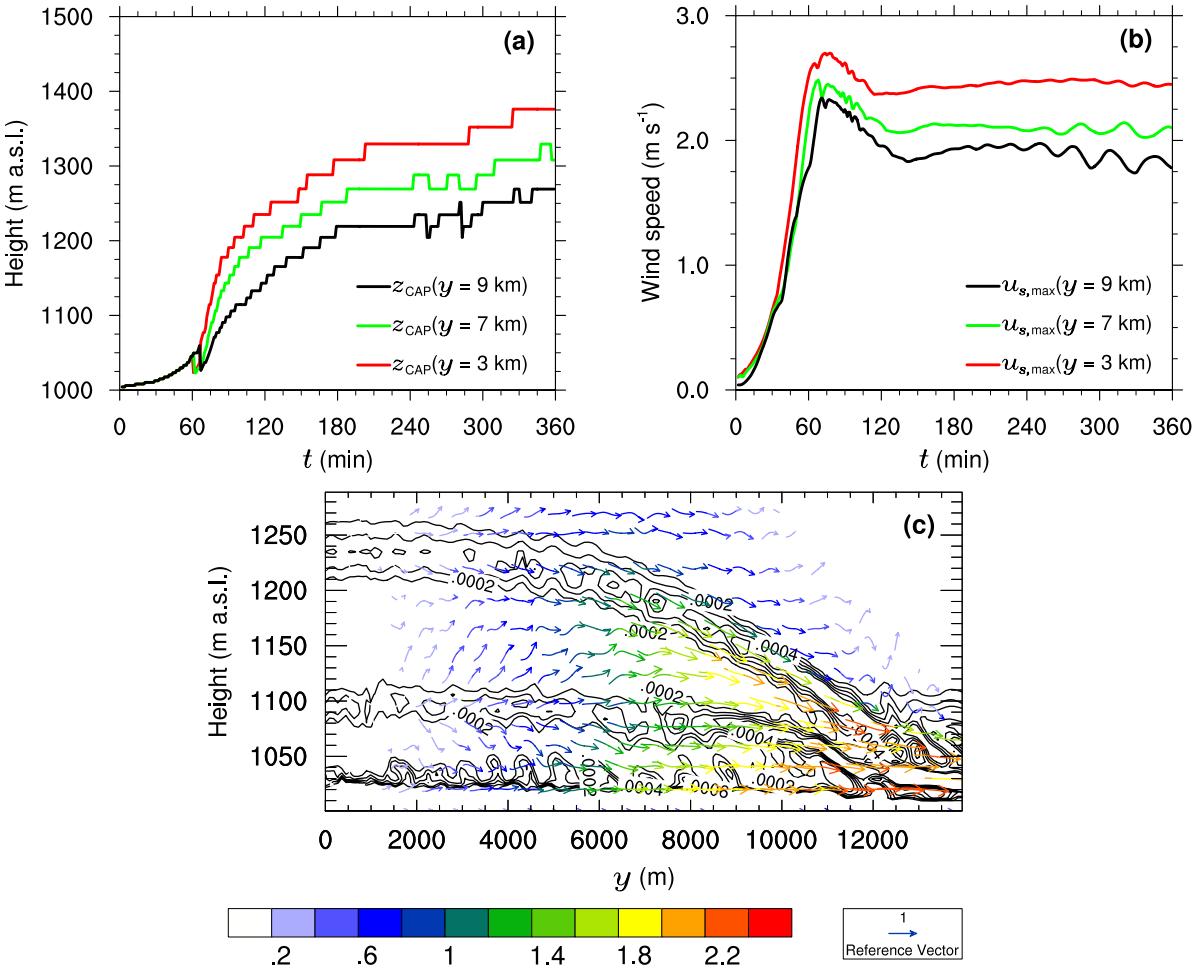

Figure III.3: Time series of **(a)** the height of the CAP z_{CAP} and **(b)** the maximum downslope wind speed $u_{s,\max}$ at different positions in the along-valley direction y [$y =$ 3 km (red lines), $y = 7$ km (green lines) and $y = 9$ km (black lines)]. **(c)** Along-valley cross-section of the down-valley wind vectors at $t = 150$ min averaged over the width of the valley floor. The reference wind vector corresponds to 1 m s^{-1}. Iso-contours of the square of the Brunt-Väisälä frequency N^2 averaged over the width of the valley floor are superimposed, with intervals of 10^{-4} s^{-2}.

Figure III.3b shows that, until 60 min or so, $u_{\mathrm{s,max}}$ hardly varies in the y-direction. The downslope wind speed decreases from this time on, more so as the y-value is closer to the valley exit. This is associated with the development of the down-valley flow after 1 h into the simulation (see Fig. III.4). Figure III.3b indicates that the downslope flows reach a quasi-steady regime after about 3 h into the simulation. This is also the time when the along-valley flow becomes quasi-steady (see Fig. III.4).

Analyzing now the evolution of the CAP height, three regimes can be distinguished (see Fig. III.3a). Until the time $u_{\mathrm{s,max}}$ reaches a maximum value, at about 60 min, z_{CAP} hardly increases or varies in the y-direction. The CAP height increases sharply from this time on, due to the vertical motions induced by the downslope flows, which are more vigorous as the valley exit is farther. From $t \approx 180$ min, when the down-valley

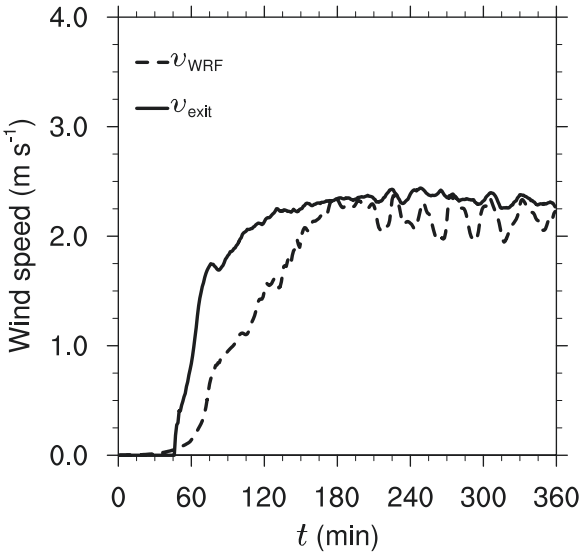

Figure III.4: Down-valley component v of the wind field (dashed line) at $y = 9$ km and a height of 20 m above ground level, averaged over the width of the valley floor, compared to an estimate of v from the Bernoulli equation (solid line, see text for details).

flow is fully developed (i.e. a quasi-steady state is reached), the growth rate of the CAP becomes linear and nearly y-independent. As indicated above, $u_{s,\max}$ decreases as one moves from the valley to the plain and so does the air mass flux that contributes to the build-up of the CAP. As a result, the value reached by z_{CAP} after 6 h decreases toward the plain. This is attested by contours of the square of the Brunt–Väisäla frequency N^2 averaged over the width of the valley floor (see Fig. III.3c).

Hence, the flow behaves as 'a flow in a pipe', with the cross-sectional area of the pipe set by the height of the CAP. The reduction in pressure towards the plain leads to an increase in the speed of the down-valley flow, eventually creating a jet at the valley exit. This is attested by vectors of the velocity field displayed in Fig. III.3c. This result is consistent with the observations that a down-valley wind jet can persist for several km [e.g. Vergeiner and Dreiseitl, 1987; Zängl, 2004], eventually reaching a quasi-steady state [Neff and King, 1989].

III.3.3 A simple model for the down-valley flow

A model for the down-valley wind component v once a quasi-steady regime has been reached can be obtained from Bernoulli's equation for a steady, frictionless and irrotational fluid, viz.

$$v_2 = \sqrt{v_1^2 + 2\left(\frac{p_1}{\rho_1} - \frac{p_2}{\rho_2}\right)}, \tag{III.4}$$

where p is the pressure, ρ is the air density, and the subscripts 1 and 2 refer to two positions in the along-valley direction, y_1 and y_2, respectively. Equation III.4 expresses

that a steady state is reached with the pressure force balanced by the advection. For a position y_2 close to the valley exit, we denote v_2 by v_{exit}.

We computed the value of v_{exit} from Eq. III.4 and the WRF model outputs. For v_1, p_1 and ρ_1 we used the values of these fields averaged over the width of the valley floor, at a height of 20 m above ground level and for $y_1 = 3$ km. For ρ_2 and p_2, values at $y = 9$ km are used. The value of v_{exit} is displayed in Fig. III.4 versus time and compared with the numerical prediction of the down-valley wind speed at $y = 9$ km (using the same average along x and for $z = 20$ m), denoted by v_{WRF}. Since a steady assumption is used to compute v_{exit}, this theoretical prediction should be compared to the numerical finding once the quasi-steady state is reached (after 180 min). Figure III.4 shows that both values agree well, v_{exit} overestimating the mean (temporally averaged) value of v_{WRF} by about 10 %. Thus, Eq. III.4 is a good model for the down-valley wind speed at the valley exit.

III.3.4 Along-valley variation of the downslope flows

As shown in Fig. III.3b, the speed of the downslope flows decreases towards the plain. Figure III.5 displays time series of the height of the maximum speed of the downslope flows $z\,(u_{\text{s,max}})$ along with those of z_{CAP} at two positions in the along-valley direction. There is a general retreat of the downslope flows up the slopes as the CAP engulfs the slopes. This is consistent with the findings of Burns and Chemel [2015] for a 2D valley case. However, $z\,(u_{s,\text{max}})$ is always lower than z_{CAP} for $y = 9$ km (i.e., towards the valley exit). This can be explained as follows: towards the valley exit, the depth of the valley is significantly shallower (about 360 m at $y = 9$ km), and the downslope flows penetrate well below the height of the CAP. They reach their level of neutral buoyancy and detrain just above the GBI, located at about 100 m above the valley floor towards the valley exit.

III.4 Impact of the down-valley flow on cold-air-pooling processes

In the following we compare results from the 3D valley section defined by $2 \leq y \leq 4$ km to those from the counterpart 2D valley.

III.4.1 Changes in the vertical structure of the cold air pool

Figure III.6 displays, for different times, vertical cross-valley sections of potential temperature θ_v and wind vectors $\mathbf{u}_{\text{cr}} \equiv (u, w)$, where u and w are the components of the wind in the cross-valley direction x and vertical direction z, respectively. Both

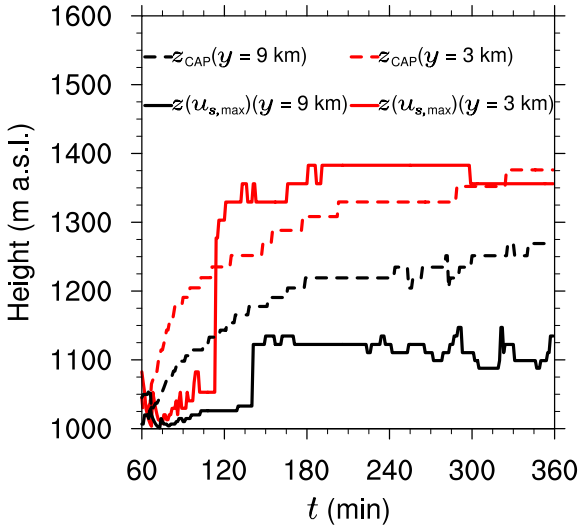

Figure III.5: Time series of the height of the maximum downslope wind speed $z\,(u_{s,\max})$ (dashed lines) and the height of the CAP z_{CAP} (solid lines) at two positions in the along-valley direction y [$y = 3$ km (red lines) and $y = 9$ km (black lines)].

fields are averaged over the along-valley section defined above. We recall that the down-valley flow is fully developed and reaches a quasi-steady state about 3 h into the simulation, that is 2 h after sunset (see Fig. III.4). Before this time, the thermodynamics of the valley atmosphere is qualitatively the same (see Fig. III.6a, b for $t = 120$ min). At $t = 360$ min, the valley atmosphere is significantly cooler in the 2D valley than in the 3D valley (see Fig. III.6c, d). This difference is closely connected to the dynamics of the valley-wind system, as discussed below.

Figure III.6 suggests that, in the 3D valley, the circulation induced by the downslope flows may be subdivided in two regimes, depending on the presence of a down-valley flow or not. Before the down-valley flow is fully developed, there is a circulation within the CAP↑, with rising motions in the centre of the valley (see Fig. III.6a, b for $1200 \leq z \leq 1400$ m). After the down-valley flow is fully developed, a cross-valley circulation develops within the CAP↑ (see Fig. III.6c). This cross-valley circulation is not present in the 2D valley.

Close inspection of the flow features in Fig. III.6c reveals that the cross-valley circulation is the result of the downslope flows overshooting their level of neutral buoyancy. This corresponds to the plume regime described by Baines [2008]. In this regime, the downslope flows penetrate below their level of neutral buoyancy, transporting warmer air inside the CAP. This creates an unstable layer immediately above the downslope flows (see the potential temperature contours in Fig. III.6c, for $x \approx 2100$ m and $z \approx 1300$ m), which forces upward motions, and mass conservation constrains the flow to move toward the centre of the valley.

After the valley-wind system is fully developed (after $t = 180$ min) the downslope flows oscillate (see Fig. III.7a). These oscillations result from stratification effects and

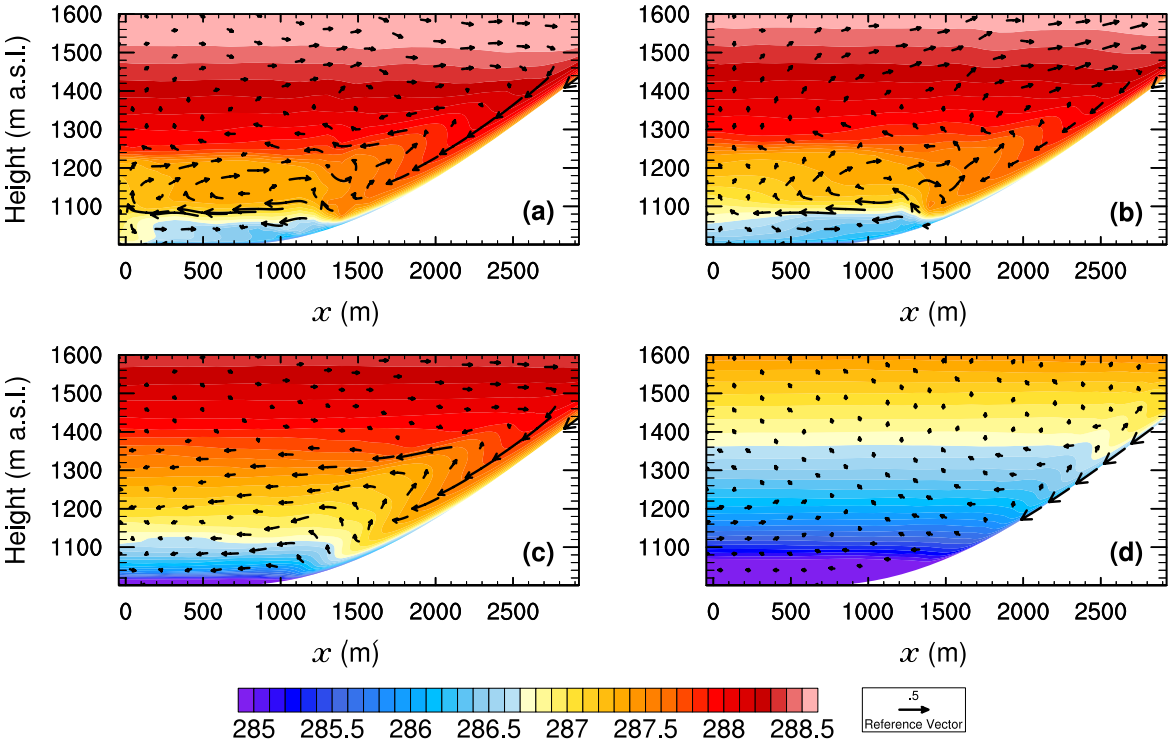

Figure III.6: Cross-valley sections (along the cross-valley direction x) of potential temperature θ_v averaged over the along-valley section defined by $2 \leq y \leq 4$ km at $t = 120$ min [**(a)** and **(b)**] and $t = 360$ min [**(c)** and **(d)**] in the 3D (left) and 2D (right) valleys. The wind vectors $\mathbf{u_{cr}} \equiv (u, w)$, where u and w are the components of the wind in the cross-valley direction x and vertical direction z, respectively, averaged over the same along-valley section are superimposed. The reference wind vector is 0.5 m s^{-1}.

the slope-surface cooling [McNider, 1982]. Such oscillations are not as clear in the 2D valley [see also Burns and Chemel, 2015], where the speed of the downslope flows decrease as the CAP deepens. The frequency spectrum of the downslope wind speed u_s at 10 m above ground level for the 3D valley shows a clear peak for a frequency $f = 0.4\ 10^{-3}$ s^{-1} (see Fig. III.7b), corresponding to a period $T \approx 40$ min. This frequency is close to that predicted by the model of McNider [1982], namely $f_{\mathrm{McNider}} = N \sin\alpha / (2\,\pi)$. Indeed, using $N = N_0 \approx 0.71\ 10^{-2}$ s^{-1} and the maximum slope angle $\alpha = \alpha_{\max} \approx 17°$, one gets $f_{\mathrm{McNider}} \approx 0.33\ 10^{-3}$ s^{-1}. This result is consistent with the findings of Largeron et al. [2013] for a 3D valley.

Times series of the heights of the GBI and of the CAP are displayed in Fig. III.8. The heights of the CAP in the 2D and 3D valleys diverge from one another already after 1 h or so into the simulation, when the down-valley flow develops (see Fig. III.4). It is worth noting that the growth of the CAP in the 3D valley is significantly reduced, when compared to that in the 2D valley, after this time, that is when vertical motions over the centre of the valley are suppressed. This result suggests that vertical advection due to slope-flow induced mass convergence over the centre of the valley is the key

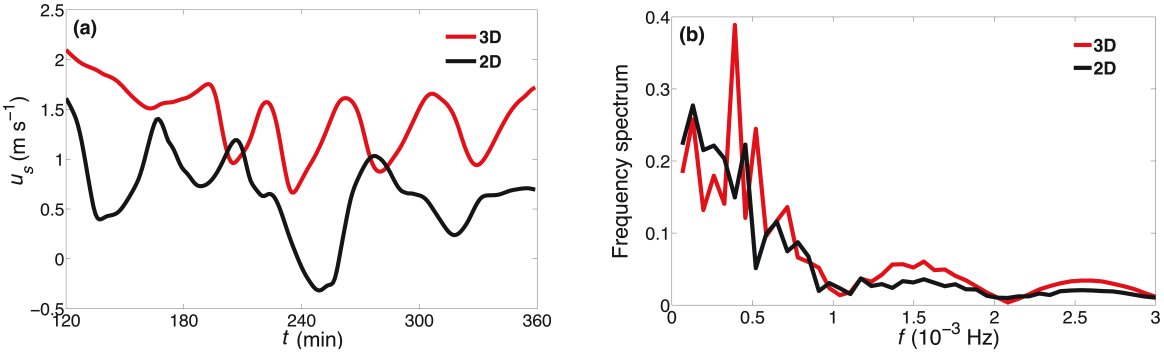

Figure III.7: **(a)** Time series of the downslope wind speed u_s at 10 m above ground level, for $x = -1500$ m and $y = 3000$ m, for $120 \leq t \leq 360$ min (i.e. when the downslope flows oscillate), in the 3D (red) and 2D (black) valleys. **(b)** Spectra $|F|$ of u_s at the same location, in the 3D (red) and 2D (black) valleys.

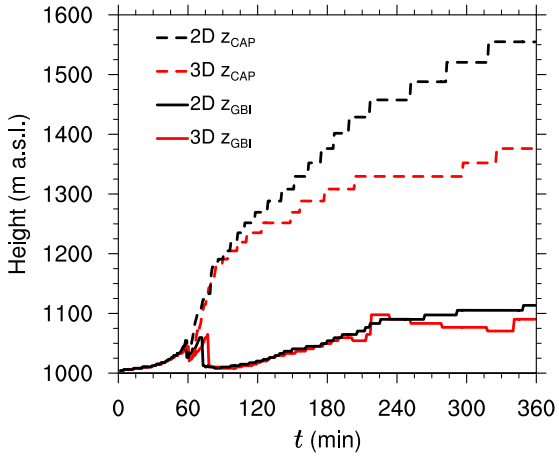

Figure III.8: Time series of the height of the ground-based inversion z_{GBI} (solid line) and cold-air pool z_{CAP} (dashed line) in the 3D (red) and 2D (black) valleys, averaged over the over the x and y ranges of the *valley centre*.

process controlling the growth of the CAP. The height of the GBI z_{GBI}, is similar in the 2D and 3D valleys before the down-valley flow is fully developed (after $t = 180$ min). Later on, z_{GBI} decreases with time in the 3D valley, as a result of advective processes associated with the down-valley flow development. This will be discussed in the next subsections.

Figure III.9 displays vertical profiles of $\overline{N^2}$, where the overbar indicates an average over the x and y ranges of the *valley centre* and over time intervals of 40 min (corresponding to that of the oscillations of the downslope flows). The stratification in the GBI is similar for both the 2D and 3D valleys with a stratification two orders of magnitude larger than the initial stratification by the end of the simulated time period (not visible on Fig. III.9a, b). However, the temporal evolution of the stratification above the GBI is more complex for the 3D valley (see Fig. III.9a) than for the 2D valley (see Fig. III.9b). For the 3D valley, prior to $t = 180$ min $\overline{N^2}$ presents two local maxima at $z \approx$ 1100 m and $z \approx 1250$ m, which are associated with the strong shear

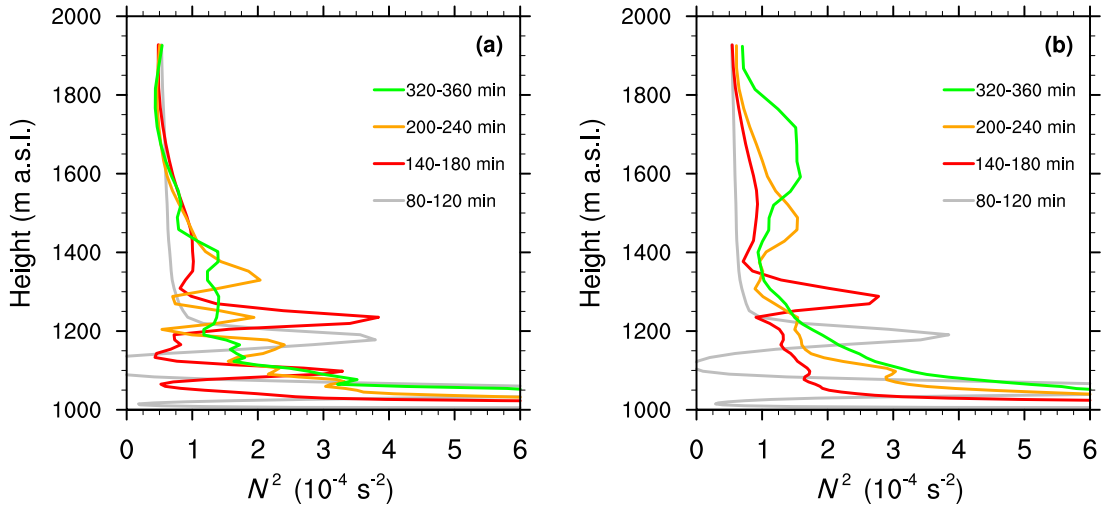

Figure III.9: Vertical profiles of the Brunt-Väisäla frequency N^2, averaged over the x and y ranges of the *valley centre* and over time intervals of 40 min for the 3D **(a)** and 2D **(b)** valleys.

that develops over the centre of the valley because of the detrainment of the downslope flows above the GBI. After $t = 180$ min, the vertical profile of $\overline{N^2}$ is layerized as a result of the interaction between the cross-valley circulation and the down-valley flow, which generates locally shear mixing, thereby decreasing atmospheric stability.

At the top of the CAP, a capping inversion develops in the 2D valley, largely as a result of the continuous upward transport within the CAP of air colder than the air above, and continuously increases in height with time (see Fig. III.8, III.9b). This inversion is not as marked in the 3D valley by the end of the simulated time period, because it is destroyed by local shear mixing and the advection of potentially warmer air by the cross-valley circulation.

III.4.2 Analysis of the time rate of change of potential temperature

In the absence of any phase change, as is the case here, the equation for the potential temperature tendency is:

$$\frac{\partial \theta_v}{\partial t} = -u_i \frac{\partial \theta_v}{\partial x_i} - \frac{\partial F_i}{\partial x_i} - \frac{\theta_v}{\rho c_\mathrm{p} T} \frac{\partial R_i}{\partial x_i}, \tag{III.5}$$

where the common summation notation is used. The terms on the right-hand side (r.h.s.) represent the contributions from advection, the divergence of the SGS turbulent heat flux $\vec{F}$ and the divergence of the radiative flux $\vec{R}$, c_p is the specific heat capacity at constant pressure. All terms of Eq. III.5 are output of the numerical simulation computed on the model grid, in order to avoid any error due to the calculation

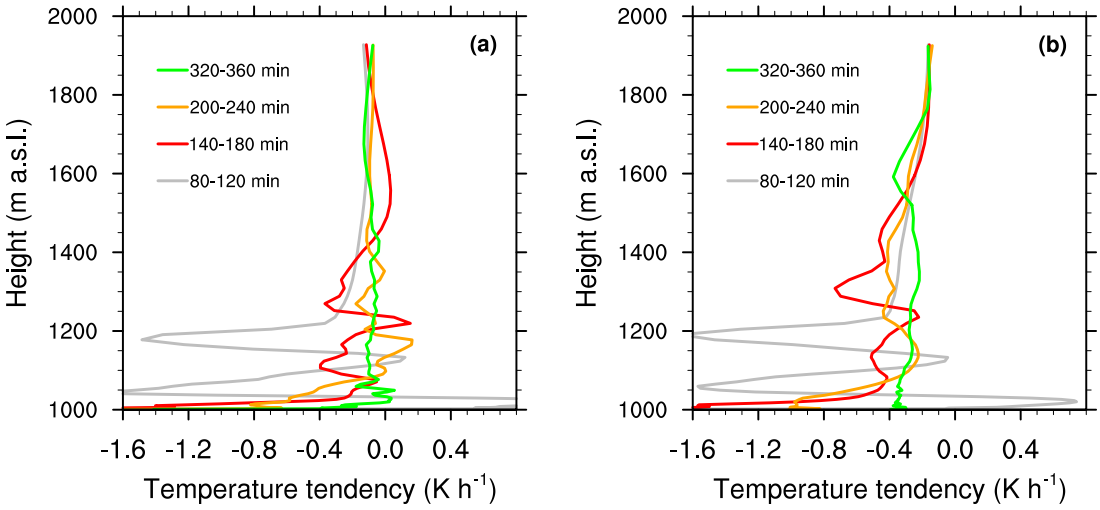

Figure III.10: Vertical profiles of potential temperature tendency $\partial\theta_v/\partial t$, averaged over the x and y ranges of the *valley centre* and over time intervals of 40 min, for the 3D **(a)** and 2D **(b)** valleys.

of spatial derivatives. This ensures that the budget balance, i.e. the sum of all terms of Eq. III.5 is equal to zero (not shown).

Figure III.10 displays vertical profiles of the potential temperature tendency $\partial\theta_v/\partial t$, averaged over the x and y ranges of the *valley centre* and over time intervals of 40 min, for the 2D and 3D valleys. A striking feature is the near uniformity of the profiles with height after $t = 240$ min, for both the 3D and 2D valleys. By contrast, there are large variations along the vertical before that time, which calls for an examination of the different terms contributing to the potential temperature tendency.

Vertical profiles of the different terms contributing to the potential temperature tendency (see Eq. III.5), averaged in the same way as $\partial\theta_v/\partial t$, are presented in Fig. III.11 for two time intervals. Before $t = 180$ min, the advection and SGS turbulent heat flux divergence terms dominate the cooling rate (see Fig. III.11a, b). The contributions of advection in the 2D and 3D valleys are similar, as was already qualitatively described from Fig. III.6a, b. After $t = 180$ min, the advection contribution in the 3D valley changes from a cooling to a warming as the circulation induced by the downslope flows changes (see Fig. III.6c). The near uniformity of the advection contribution with height, above the GBI (of height ≈ 1100 m) in the 3D valley may be explained as follows: the downslope flows become positively buoyant over the slope as they overshoot their level of neutral buoyancy, resulting in a spreading of the relatively warmer air vertically by convection. This relatively warmer air is then advected horizontally by the cross-valley circulation over the entire CAP. In the 2D valley, vertical motions in the centre of the valley are eventually reduced, but not suppressed (see Fig. III.6d). This vertical transport produces a homogeneous cooling for $1100 \leq z \leq 1500$ m, with the contributions from advection and radiation being almost equal. Hence, the

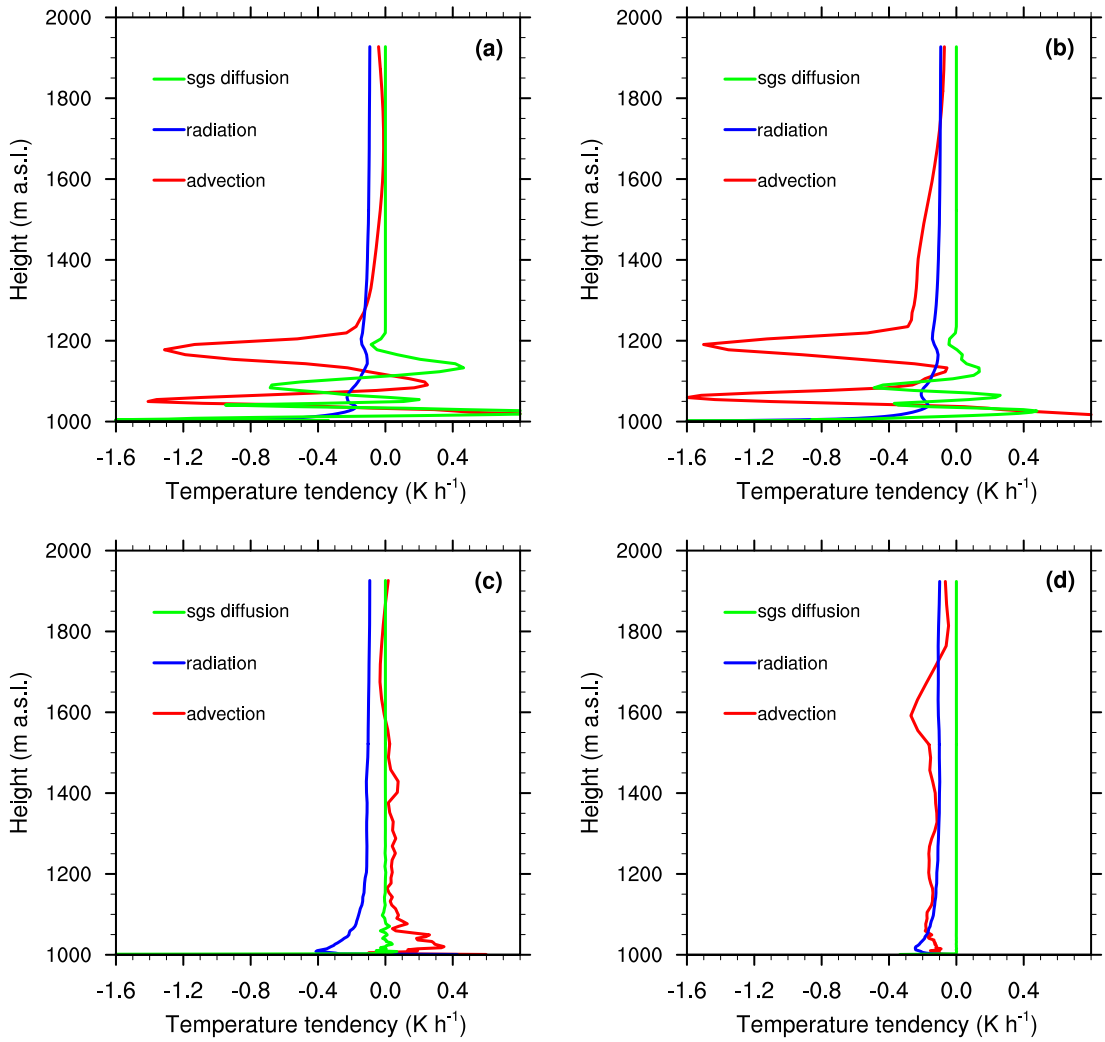

Figure III.11: Vertical profiles of the terms of the r.h.s. of Eq. III.5 for the 3D (left) and 2D (right) valleys: advection (red line), radiative flux divergence (blue line) and SGS turbulent heat flux divergence (green line), averaged over the x and y ranges of the *valley centre* and over the time periods 80–120 min [**(a)** and **(b)**] and 320–360 min [**(c)** and **(d)**].

uniform cooling rate observed within the 3D and 2D valleys (above the near-surface layer) is the result of the circulations induced by the downslope flows for both valleys. Interestingly, a similar conclusion was reported for daytime conditions by Weigel et al. [2006] for the Riviera valley, and by Schmidli [2013] for a 2D idealized valley. This suggests that the effect of the thermally-driven slope flows on the vertical structure of the potential temperature tendency is similar during daytime and nighttime conditions.

Figure III.11a, b indicate that, until $t \approx 120$ min, the magnitude of the contribution from the SGS turbulent heat flux divergence is comparable to that of the (resolved) advection contribution up to 1250 m (that is the height of the CAP at $t = 120$ min). By the end of the simulated time period, for the 3D valley, the SGS turbulent heat flux divergence contribution at the valley floor is -2.7 K h^{-1}, that is larger than the

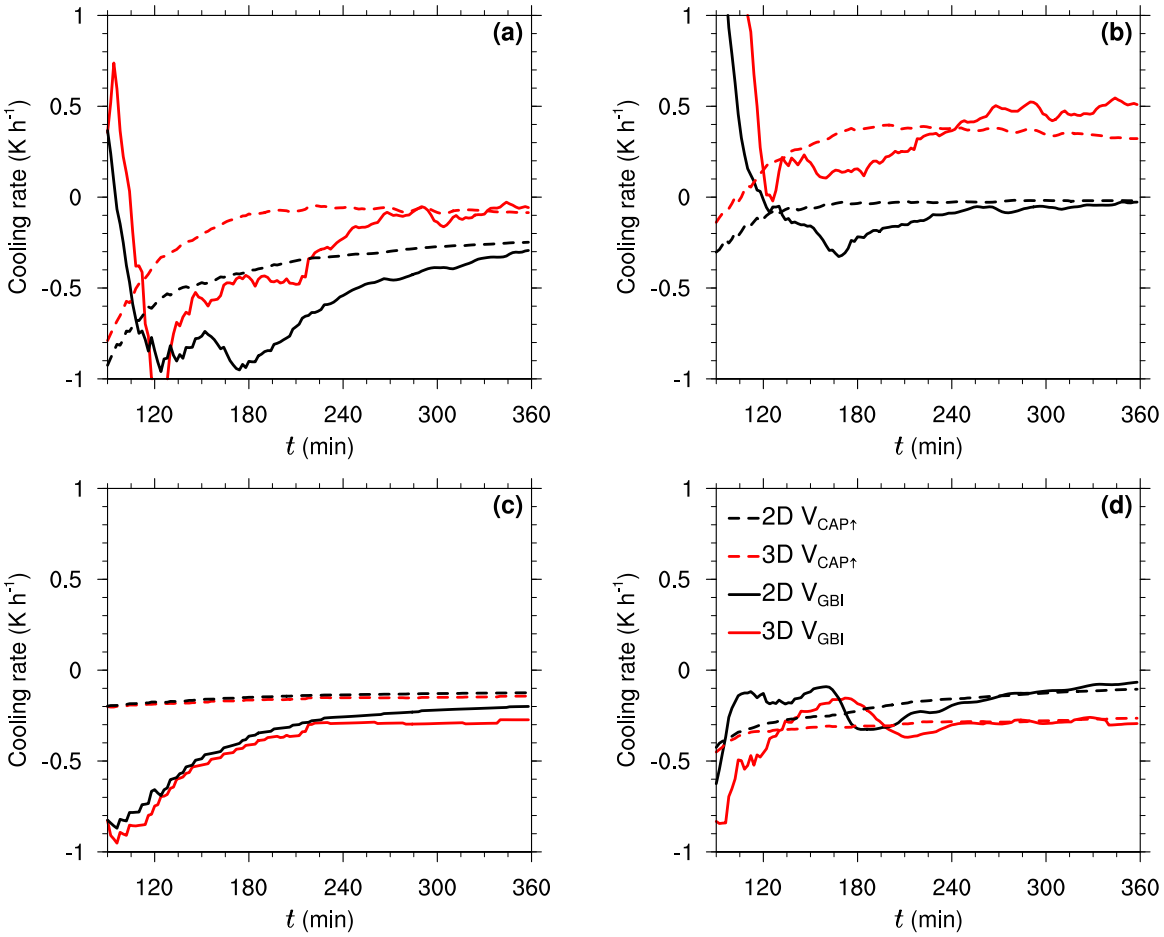

Figure III.12: Time series of the terms of the heat budget Eq. III.5, volume-averaged over the GBI (solid line) or over the CAP↑ (dashed line), for the 3D (red) and the 2D (black) valleys: **(a)** potential temperature tendency $\partial\theta_v/\partial t$, **(b)** advection, **(c)** radiative flux divergence, and **(d)** SGS turbulent heat flux divergence; see Sect. III.2.6 for the definition of the control volumes.

contributions from the other terms and larger than that for the 2D valley, for which the value at the valley floor is -0.4 K h^{-1}. This result is due to the friction induced by the down-valley wind at the ground surface. However, apart from the near-surface region, the SGS turbulent heat flux divergence contribution after $t \approx 120$ min is very small compared to the contributions from the other terms for both the 2D and 3D valleys, over the x and y ranges of the *valley centre* (see Fig. III.11c, d).

It should be stressed that, by considering vertical profiles horizontally averaged over the *valley centre*, we ignore the atmosphere above the slopes. This important point is discussed in the next section.

III.4.3 Changes in the heat budget

In this section, we examine the processes that control the evolution of the GBI layer and upper part of the valley boundary layer. Figure III.12 compares time series of the

different terms of Eq. III.5 averaged over the GBI or CAP↑ volumes (see Sect. III.2.6 for the definition of the control volumes). Before $t \approx 120$ min, the atmosphere within the CAP↑ experiences a rapid cooling (see Fig.III.12a). After this time, a transient regime develops between 120 and 270 min into the simulations, which is characterized by a higher cooling of the GBI compared to the CAP↑. For the 3D valley, this transient regime is followed by an equilibrium regime characterized by an equal cooling rate within the GBI and the CAP↑. By the end of the simulated time period, the cooling rates within the GBI and CAP↑ for the 2D valley are 3 times larger and 4 times larger, respectively, than for the 3D valley.

The presence of the down-valley flow in the 3D valley changes the relative importance of the processes contributing to the cooling of the valley, when compared to the 2D valley, as already discussed. Figure III.12b displays the time series of the advection contribution. For the 2D valley the magnitude of the advection contribution to the cooling rate decreases with time and tends to zero by the end of the simulated period within both the GBI and CAP↑. For the 3D valley, by contrast, the down-valley flow development leads to a warming within both the GBI and the CAP↑; this warming is higher within the GBI than within the CAP↑ by the end of the simulated time period.

Radiative cooling is comparable for both valleys for the entire simulated time period and within the CAP↑ is approximately half that within the GBI (see Fig. III.12c). Figure III.12d displays the time series of the contribution from SGS turbulent heat flux divergence, which is mostly due to the surface turbulent heat flux. After $t \approx 180$ min, because of the slow down of the downslope flows as the CAP grows up, its magnitude decreases with time for the 2D valley and is almost the same within the GBI and CAP↑. For the 3D valley, friction is maintained over the valley surface by the fully developed downslope and down-valley flows (after $t = 180$ min). As a result, the contributions from SGS turbulent heat flux divergence within the GBI and CAP↑ are almost equal and nearly constant with time, and about 3 times larger than for the 2D valley. For the 3D valley, the contribution from SGS turbulent heat flux divergence within the GBI by the end of the simulated time period is of the same order of magnitude as the radiative cooling. By contrast, it is less than half the radiative cooling for the 2D valley. When considering the CAP↑ rather than the GBI, it is about twice the radiative cooling for the 3D valley and is of the same order of magnitude as the radiative cooling for the 2D valley.

III.4.4 Changes in the mass budget

Figure III.13 shows vertical cross-sections of the vertical velocity w, with the along-valley velocity component v superimposed at $t = 300$ min for the 3D and 2D valleys. The fields are averaged over the along-valley section defined by $2 < y < 4$ km. The

vertical velocity is a proxy for the vertical mass flux, as long as the flow is approximately incompressible (as it is in the present case). Figure III.13a, b suggest that the vertical mass flux is associated with the downslope flow advection for both the 2D and 3D valleys. The major difference between the 2D and 3D cases stems from the suppression of homogeneous vertical motions in the valley regions far from the slope for the 3D case. More precisely, no vertical motions are observed in the atmospheric region above the CAP ($z > 1350$ m) for the 3D case. This suggests that pure downward vertical motions far from the slope layer, i.e. subsidence, play a minor role in the mass conservation within the CAP atmosphere for the 3D valley, for this particular setup. The importance of subsiding motions far from the slope layer with respect to the cross-valley advection in the mass budget of the CAP, can be quantified by computing the mass budget in the control volume defined horizontally by the *valley centre*, and of height equal to that of the CAP. Figure III.14 displays time series of the net mass fluxes (defined positively outwards) associated with the three velocity components u, v and w across the surfaces of this volume, scaled by the mass of the CAP, for the 2D and the 3D valleys. The contribution of the vertical mass flux far from the slope layer (M_w) to the mass budget of the 3D valley is much smaller than that of the cross-valley circulation (M_u), confirming that downward vertical motions far from the slope do not play any major role in the conservation of mass within the CAP. As a consequence, the horizontal mass fluxes M_u and M_v have opposite (and nearly constant) values from $t = 180$ min. This result also confirms that the growth of the CAP is driven by vertical advection (due to slope-flow induced mass convergence over the centre of the valley). Indeed, for the 3D valley, when M_w becomes negative the CAP stops growing, while for the 2D valley the growth rate decreases with time as M_w is reduced (see also Fig. III.8).

While M_w approaches zero by the end of the simulated time period for both the 2D and 3D valleys, the vertical mass flux across the entire CAP upper surface (from slope to slope, denoted by $\hat{M}_w$) for the 3D valley does not vanish (see the grey line in Fig. III.14a), due to the advection of air along the slopes. This air must be replenished by air coming from other regions. Figure III.13a shows that an upper-level return flow [see also Rampanelli et al., 2004a] develops above the CAP for the 3D valley (see Fig. III.8 for the height of the CAP). This return flow transports air from the plain to the valley, as opposed to the down-valley flow underneath. Hence, for the 3D case the inflow of air into the slope layer, is driven by a combination of the return flow, the subsidence above the plateaux and the horizontal (cross-valley) advection from the plateaux.

The relative contributions of these processes to the mass budget of the 3D valley can be quantified by considering the mass budget for a control volume encompassing the upper part of the valley atmosphere and part of the plateaux, defined by $z_{\mathrm{CAP}} <$

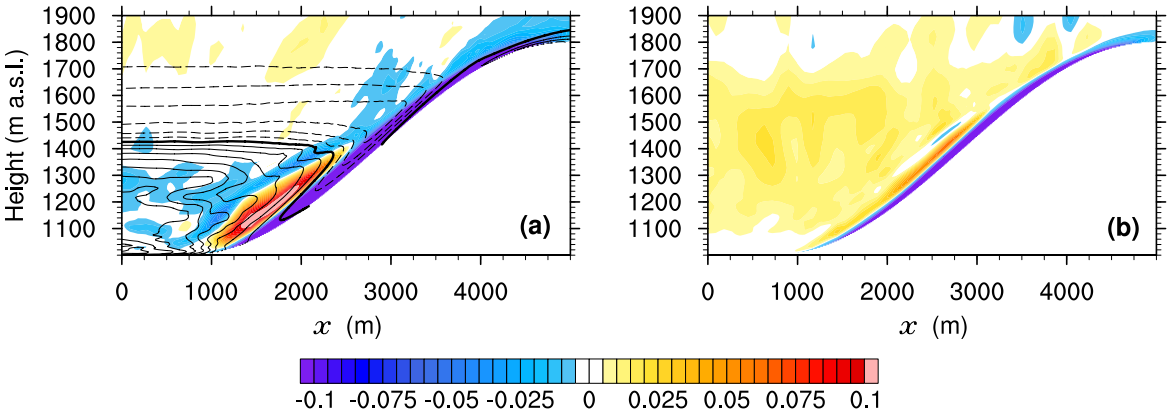

Figure III.13: Cross-valley section (along the cross-valley direction x) of the vertical velocity (colour contours) at $t = 300$ min, averaged over the along-valley section defined by $2 < y < 4$ km for **(a)** the 3D valley and **(b)** the 2D valley. The along-valley wind component v (contour lines, with intervals of 0.1 m s^{-1}) averaged over the same along-valley section is superimposed. Continuous lines correspond to positive values (i.e. down-valley flow), dashed lines to negative values (i.e. up-valley flow) and the thick black line corresponds to $v = 0$.

$z < (h_0+H+100\text{ m})$, $-(S_x+L_x+1000\text{ m}) < x < (S_x+L_x+1000\text{ m})$ and $2 < y < 4$ km. Figure III.15 displays time series of the net mass fluxes associated with the horizontal velocity components u and v, and the mass fluxes associated with the vertical velocity w across the top and bottom surfaces of this control volume, denoted by $\hat{M}_u$, $\hat{M}_v$, $\hat{M}_{w,t}$ and $\hat{M}_w$, respectively. We quantify the importance of each of these terms in the mass budget with respect to $\hat{M}_w$ by normalizing them by $\hat{M}_w$. Before $t = 285$ min, the subsidence from the free atmosphere ($\hat{M}_{w,t}$) decreases monotonically in absolute value with time. The along-valley mass flux ($\hat{M}_v$) decreases continuously and becomes negative from about $t = 160$ min, as the return flow intensifies. After $t = 160$ min, $\hat{M}_v$ increases monotonically in absolute value with a value of $-0.75\,\hat{M}_w$ at $t = 285$ min. At this time, the advection of air along the slopes, across the upper surface of the CAP, is mainly replenished by the air from the plain, due to the return flow. After this time, $\hat{M}_{w,t}$ increases in absolute value, which is associated with a decrease in absolute value of $\hat{M}_v$. By the end of the simulated time period, $\hat{M}_{w,t}$ is equal to $-0.35\,\hat{M}_w$ and $\hat{M}_u$ to $-0.15\,\hat{M}_w$, while $\hat{M}_v$ is equal to $-0.50\,\hat{M}_w$. Hence, we conclude that, by the end of the simulated time period, the vertical mass flux in the slope layer is driven by a complex interplay between the along-valley mass flux from the plain to the valley, resulting from the return flow, and the subsidence and horizontal advection from the plateaux.

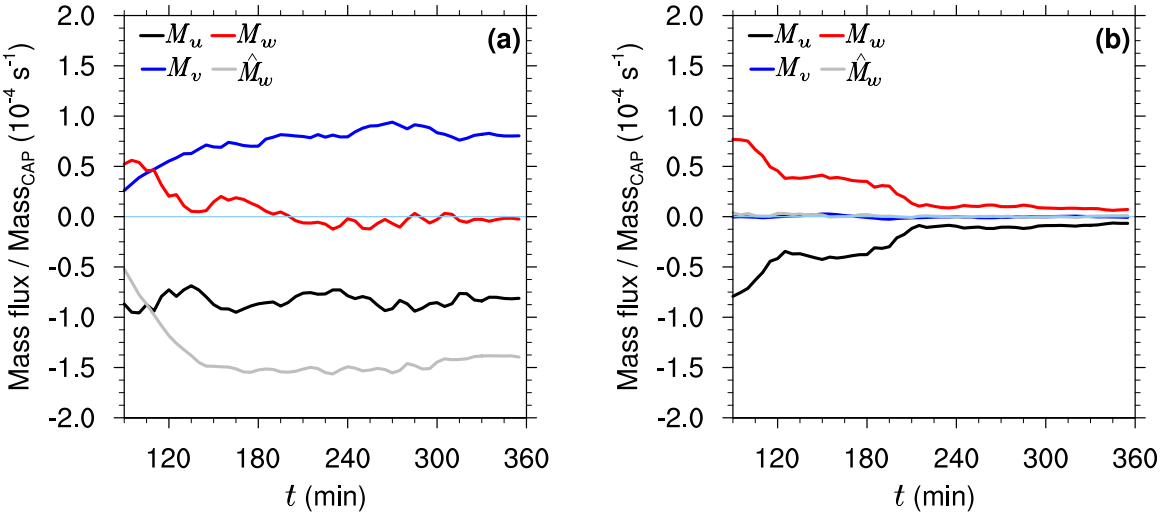

Figure III.14: Net mass fluxes across the surfaces of the control volume defined horizontally by the *valley centre* and of height equal to that of the CAP, scaled by the mass of the CAP: vertical flux M_w (red), along-valley flux M_v (blue) and cross-valley flux M_u (black) for **(a)** the 3D valley and **(b)** the 2D valley. The grey line shows the vertical mass flux across the entire upper surface of the CAP (from slope to slope), denoted by $\hat{M}_w$.

III.5 Sensitivity to the length of the valley

The previous discussion shows that the flow characteristics depend on the time when the quasi-steady state is reached and the down-valley flow is fully developed, denoted by T_{ss}. By changing the length of the valley, we expect T_{ss} to vary. Schmidli and Rotunno [2015] suggested that, assuming constant forcing (i.e. a constant surface sensible heat flux), T_{ss} is proportional to $T_\ell = 2\,L_{tot}/\,(H\,N_0)$, with a coefficient of proportionality of about 3. T_ℓ is the timescale associated with the linear wave solution of the along-valley wind equations derived by Egger [1990]. To examine this proportionality and the sensitivity of the flow characteristics to the valley length, an additional simulation was performed by changing L_{tot} only, from 11 to 15 km. Table III.1 summarizes the main variables analyzed for the different valley lengths L_{tot}, including that of the 2D valley, which is infinite.

The coefficient of proportionality between T_{ss} and T_ℓ is 2.8 for the two valley lengths considered, and therefore is about 3 as was suggested by Schmidli and Rotunno [2015]. Since for the simulations considered H and N_0 are constant as is the ratio T_{ss}/T_ℓ, T_{ss} should vary in proportion to L_{tot}, as confirmed from Table III.1. This shows that T_ℓ is the relevant timescale for the approach to the quasi-steady state. The longer is the valley, the longer is the time before the quasi-steady state is reached and a cross-valley circulation is established. This results in a more gradual transition from the 2D regime and the 3D regime and therefore a deeper CAP. Note however that the change of the valley length has no significant effect on z_{GBI}, $u_{s,max}$ and the volume-averaged

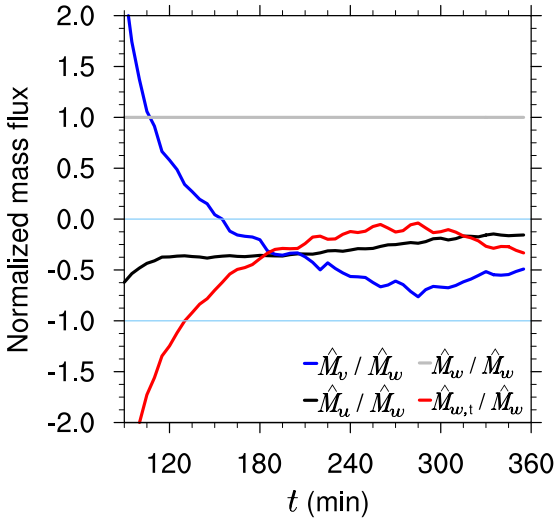

Figure III.15: Mass fluxes across the surfaces of the upper control volume defined by $z_{\mathrm{CAP}} < z < (h_0 + H + 100\ \mathrm{m})$, $-(S_x + L_x + 1000\ \mathrm{m}) < x < (S_x + L_x + 1000\ \mathrm{m})$, $2 < y < 4$ km, normalized by the vertical mass flux across the bottom surface, denoted $\hat{M}_w$: net along-valley flux $\hat{M}_v/\hat{M}_w$ (blue), net cross-valley flux from the plateaux $\hat{M}_u/\hat{M}_w$ (black), vertical flux across the bottom surface (within the CAP) $\hat{M}_w/\hat{M}_w$ (grey), vertical flux across the top surface (subsidence) $\hat{M}_{w,t}/\hat{M}_w$ (red), for the 3D valley.

temperatures ($\langle\theta_v\rangle_{\mathrm{GBI}}$ and $\langle\theta_v\rangle_{\mathrm{CAP}\uparrow}$ in Table III.1).

Table III.1 also shows that the deeper the valley boundary layer, the stronger the down-valley wind jet at the same distance from the valley exit. This can be explained by the Bernoulli model discussed in Sect. III.3.3 and using hydrostatic balance. Writing each of the flow variable as the sum of a reference value (denoted by a subscript r), and a deviation from this reference value (denoted by a prime), hydrostatic balance within the CAP can be written as

$$\partial p'/\partial z = (\rho_{\mathrm{r}}/\theta_{\mathrm{r}})\theta'_v\, g, \tag{III.6}$$

where ρ_{r} and θ_{r} are the reference density and potential temperature, respectively, outside of the CAP, and the usual approximation $-\rho'/\rho_{\mathrm{r}} = \theta'_v/\theta_{\mathrm{r}}$ is used since density variations due to pressure changes are small compared to those due to potential temperature changes [see for instance Holton, 2004, pp. 198–199]. Integrating Eq. III.6 from the valley floor altitude, h_0, to the height of the CAP, z_{CAP}, yields

$$p' = -\rho_{\mathrm{r}} \int_{h_0}^{z_{\mathrm{CAP}}} \frac{g}{\theta_{\mathrm{r}}}\,\theta'_v\,\mathrm{d}z + p'\left(z = z_{\mathrm{CAP}}\right) = -\rho_{\mathrm{r}}\,\frac{g}{\theta_{\mathrm{r}}}\,\overline{\theta'_v}\,d_{\mathrm{CAP}} + p'\left(z = z_{\mathrm{CAP}}\right), \tag{III.7}$$

where $\overline{\theta'_v}$ is the layer-averaged potential temperature deficit across the depth of the CAP $d_{\mathrm{CAP}} = z_{\mathrm{CAP}} - h_0$. We now consider Eq. III.4; by assuming that $\rho_1 \approx \rho_2 \approx \rho_{\mathrm{r}}$ (that is density variations are only important in the buoyancy term, i.e. the fluid is

Table III.1: Effect of the valley length on the variables discussed in Sect. III.5, namely: the total valley length $L_{\rm tot}$; the time when the quasi-steady state is reached $T_{\rm ss}$; the ratio $T_{\rm ss}/T_\ell$, where T_ℓ is the timescale associated with the along-valley wind (see text for details); the along-valley wind speed at the distance $y = L_{\rm tot} - 2$ km from the valley exit, for $z = 20$ m and averaged over $[-L_x, L_x]$ in the cross-valley direction, denoted by v_2; the maximum downslope wind component $u_{s,\rm max}$ at $y = 3$ km; the height of the ground-based inversion $z_{\rm GBI}$ and of the cold-air pool $z_{\rm CAP}$, calculated as in Fig. III.8; and the volume-averaged potential temperature within the GBI and CAP↑, denoted by $\langle\theta_v\rangle_{\rm GBI}$ and $\langle\theta_v\rangle_{\rm CAP\uparrow}$, respectively. The values of the last six variables were computed at $t = 360$ min.

$L_{\rm tot}$ (km)	$T_{\rm ss}$ (min)	$T_{\rm ss}/T_\ell$	v_2 (m s^{-1})	$u_{\rm s,max}$ (m s^{-1})	$z_{\rm GBI}$ (m)	$z_{\rm CAP}$ (m)	$\langle\theta_v\rangle_{\rm GBI}$ (K)	$\langle\theta_v\rangle_{\rm CAP\uparrow}$ (K)
11	180	2.8	2.2	2.45	1090	1376	285.8	287.2
15	250	2.8	3.4	2.48	1098	1430	285.6	287.2
∞	∞	∞	0	1.60	1113	1554	284.6	286.6

Boussinesq), Eq. III.4 becomes

$$v_2^2 - v_1^2 = \frac{2}{\rho_{\rm r}}\,(p_1' - p_2')\,, \tag{III.8}$$

where the subscripts 1 and 2 refer to a position within the valley and at the valley exit. As in Sect. III.3.3 v_2 will be denoted as $v_{\rm exit}$. Using hydrostatic balance written in the form of Eq. III.7, the difference between the squared down-valley wind speed for two valleys of different length may be computed by subtracting Eq. III.8 for the two valleys. Assuming that the pressure at the valley exit is the same in the two valleys and that the down-valley wind speed within the valley is almost the same (as it is in the present case), we obtain

$$\Delta v_{\rm exit}^2 = -2\,\frac{g}{\theta_{\rm r}}\,\overline{\theta_v'}\,\Delta z_{\rm CAP}, \tag{III.9}$$

where we have also assumed that the potential temperature variations averaged over the depth of the CAP ($\overline{\theta_v'}$) and the pressure perturbations at the top of the CAP $[p'(z = z_{\rm CAP})]$ are the same within the two valleys (as is the case here, not shown). $\Delta v_{\rm exit}^2$ and $\Delta z_{\rm CAP}$ are the differences in the squared along-valley speed at the valley exit and in the height of the CAP between the two valleys, respectively.

Figure III.16 shows the comparison between the squared wind speed difference computed using Eq. III.9 (denoted by $\Delta v_{\rm exit}^2$) with the variables averaged in the range $2 < y < 4$ km, and from the WRF model outputs (denoted by $\Delta v_{\rm WRF}^2$) at the valley exit ($y = 9$ km and $y = 13$ km for the shorter and longer valley, respectively). The comparison is made between 150 and 360 min. Despite the assumptions made to derive Eq. III.9, the expression gives a correct order-of-magnitude of the squared along-

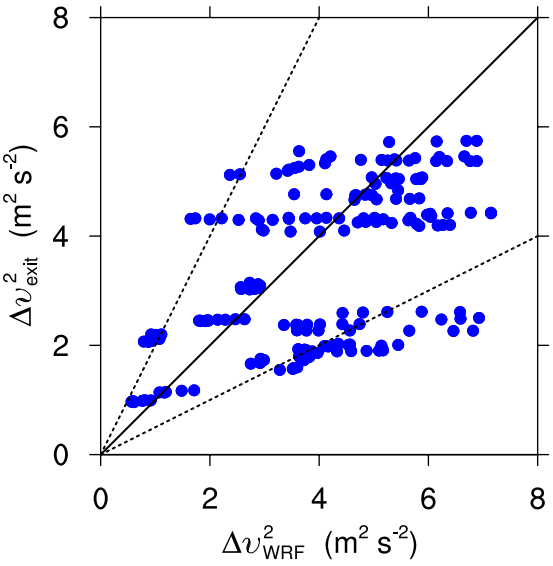

Figure III.16: Scatter plot of the difference in the squared along-valley wind speed between the two finite length valleys displayed in Table III.1, computed from the WRF model outputs (x-axis, $\Delta v^2_{\mathrm{WRF}}$) versus its estimate, using Eq. III.9 (y-axis, $\Delta v^2_{\mathrm{exit}}$), between 150 and 360 min. The dashed lines indicate the range within a factor 2 and the solid line is the one-to-one line.

valley wind difference: 74 % of the values for $\Delta v^2_{\mathrm{WRF}}$ are within a factor of 2 of the counterpart values for $\Delta\, v^2_{\mathrm{exit}}$. It should be noted that Eq. III.9 provides an expression for the difference in the squared along-valley wind speed between two finite length valleys, provided that Δz_{CAP} is known. This means that an equation for Δz_{CAP} is still required.

Even though the CAP is deeper in the longer valley, the maximum speed of the downslope flows at the end of the simulation hardly varies, and a steady state is reached, after T_{ss}. Furthermore the cross-valley circulation and the structure of the CAP present the same characteristics. To conclude, the mechanisms that control the structure of the CAP and its evolution are independent of the valley length as soon as the down-valley flow is fully developed.

III.6 Conclusions

We have characterized the influence of a thermally-driven down-valley flow on a developing cold-air pool in an idealized alpine valley under decoupled conditions. Results from numerical model simulations of a developing cold-air pool in a 3D valley, which allows for the formation of a down-valley flow, and in a 2D valley, where the formation of a down-valley flow is inhibited, were analyzed and compared. The main conclusions, along with some discussion, are given below.

- Before the development of the down-valley flow, the thermodynamics of the valley atmosphere in the 3D valley is similar to that in the 2D valley. The downslope flows induce upward motions in the centre of the valley, which are responsible for the growth of the cold-air pool (CAP). As shown by Catalano and Cenedese [2010] and Katurji and Zhong [2012], the depth of the valley is also a key factor controlling the growth of the CAP. Shallower valleys will be 'filled' more rapidly by the developing CAP, suppressing the effect of the downslope flows on the valley atmosphere.

- The down-valley flow, which forms as a result of the differential cooling between the valley and the plain, is fully developed after a time period that increases with the valley length. After this time, the down-valley flow reaches a quasi-steady state characterized by a balance between the pressure force and advection in the along-valley direction. It then behaves as 'a flow in a pipe', with the cross-sectional area of the pipe set by the depth of the CAP. The value of the down-valley wind speed at the valley exit during the steady-state appears to be well predicted by the Bernoulli equation. The time when the quasi-steady state is reached is found to be about $3\,T_\ell$, where $T_\ell = 2\,L_{\text{tot}}/\left(H\,N_0\right)$, L_{tot} is the total valley length, H is the valley depth, and N_0 is the initial Brunt–Väisäla frequency [see also Schmidli and Rotunno, 2015].

- In the 2D valley, as the CAP deepens and engulfs the slopes, the downslope flows retreat back up the slopes and slow down. This is not the case in the 3D valley. When the down-valley flow forms, vertical motions induced by the downslope flows cease, and a cross-valley circulation develops as a result of the downslope flow advection within the CAP. Hence, the growth of the CAP is reduced in the 3D valley, the capping inversion at its top is not as marked as in the 2D valley and the valley atmosphere is warmer than that for the 2D valley. This result has implications for the dilution of pollutants. Indeed, pollutants emitted at the valley floor will be spread in the horizontal by the down-valley flow, as was observed for instance by Gudiksen and Shearer [1989] from field measurements, instead of being diluted throughout the CAP as for a 2D valley configuration [e.g. Chemel and Burns, 2015b].

- Even though the 2D valley atmosphere is cooler than that of the 3D valley, the stability of the CAP is similar for both valleys. By the end of the simulated time period, the net cooling rate is uniform in the vertical throughout the upper part of the CAP, above the near-surface layer, for both the 3D and 2D valleys. This prevents the stability of the upper part of the CAP from increasing with time for both valleys. However, the processes involved are different. While radiative flux divergence leads to a cooling in both valleys, advection leads to a cooling

in the 2D valley and a warming in the 3D valley. These processes are found to be uniform in the vertical throughout the upper part of the CAP for both the 3D and 2D valleys, thereby explaining the uniformity of the net cooling rate in the vertical. Near-surface cooling from subgrid-scale turbulence flux divergence is greatly enhanced for the 3D valley (by more than a factor 6 over the *valley centre*). Our results may explain the findings of De Wekker and Whiteman [2006] as regards the time scale for nocturnal cooling, defined as the time when $\approx$ 63 % (namely $1 - e^{-1}$) of the total cumulative nocturnal cooling over one night has occurred, assuming an exponential decay for this quantity. It was found by these authors that, for different basins, valleys and plains, this time scale is in the range 3–6 h, depending on the geometry of the basin or valley being considered. This range may be related to the time when cooling by advection is suppressed by the developing down-valley flow, or is gradually being suppressed by the developing CAP (as for the 2D valley).

- When considering the CAP volume, the mass budget of the 3D valley is largely driven by a balance between the divergence of the down-valley flow in the along-valley direction and the convergence of the downslope flows at the top of the CAP. The net contribution from downward vertical motions to the mass budget far from the slopes is found negligible for the 3D valley. When considering the entire valley scale, the return flow above the CAP (flowing from the plain to the valley) plays a non-negligible role in the mass budget. Indeed, the vertical mass flux at the top of the CAP is driven by an interplay between the along-valley convergence of the return flow and the subsiding or horizontal convergent motions from the plateau regions. It should be noted that the computation of the mass budget in previous work relied on the hypothesis of horizontally-homogeneous subsidence from the free atmosphere above the CAP, therefore neglecting the feedback of the down-valley flow on the downslope flows [Whiteman and Barr, 1986]. The results of the present paper suggest that unlike daytime situations [Rampanelli et al., 2004a; Weigel et al., 2006], mass conservation does not imply subsidence over the valley centre during the night.

- The mechanisms that control the structure of the CAP and its evolution are independent of the valley length as soon as the quasi-steady state is reached and the down-valley flow is fully developed.

This work has described the interactions that take place between the nighttime valley-wind system and a developing cold-air pool. Even though the physical mechanisms presented above are found to be independent of the length of the valley, there are a number of other parameters that may affect the results (e.g., the geometry of the valley, the land cover, the stratification) and remain to be examined.

Acknowledgments

This work has been supported by a PhD grant provided by the LabEx Osug@2020 (Investissements d'avenir – ANR10LABX56) in Grenoble and by the University of Hertfordshire. Numerical simulations were run on the French national HPC facilities at CINES. Finally, the authors thank the referees for valuable comments, which led to substantial improvements in this paper.

IV

Energetics of Deep Alpine Valleys in Pooling and Draining Configurations

In Chapter III the interactions between downslope and down-valley flows have been described and the influence of these flows on heat and mass budgets of the valley boundary layer has been quantified. However, a very idealised terrain shape was considered, that is a straight valley opening on a plain. These valleys rarely exist in the Alpine chain. Usually valleys widen or narrow in the along-valley direction. As a step towards modelling the complexities of real-world valleys, a system of two valleys characterised by different valley widths is considered in this chapter. The influence of the neighbouring valley on the heat and mass budgets of a given valley section is quantified and compared to the respective valley opening on a plain. Particular emphasis is given to the variations of heat and mass transport processes.

This chapter is a reproduction of Arduini et al. [2017].

Abstract The Weather Research and Forecast numerical model is used to investigate the nocturnal atmospheric boundary layer in a valley that opens either on a wider valley (draining configuration) or on a narrower valley (pooling configuration). One draining case and three weak to strong pooling cases are considered. Results show that the structure of the nocturnal boundary layer is substantially different for the draining and pooling configurations. The greater the pooling, the deeper and colder is the boundary layer. Down-valley winds are weaker for pooling and draining configurations than in an equivalent valley opening directly on a plain. For the strong pooling case, an up-valley flow develops from the narrower to the wider valley during the evening transition, affecting the mass budget of the wider valley during that period. Considering the heat budget of the valley system, the contribution of the

diabatic processes, when appropriately weighted, hardly varies along the valley axis. Conversely, the contribution of advection varies along the valley axis: it decreases for a pooling configuration and increases for a draining configuration. Consequently, for a pooling configuration, the heat transfer between the valley and the plain is reduced, thereby increasing the temperature difference between them. For the strong pooling case, this temperature difference can be explained by the valley-volume effect once the down-valley flow has developed. This occurs in a valley when the 'extra' heat loss within the valley due to the surface sensible heat flux balances the heat input due to advection.

IV.1 Introduction

The characteristics of the boundary layer in complex terrain are often tightly coupled with the variations of the underlying orography. The valley to plain temperature differences are primarily explained by the valley-volume effect, which can be quantified by the topographic amplification factor (TAF), a purely geometrical factor characterizing the reduction in the air volume within a valley compared to the equivalent volume if the terrain were flat [Wagner, 1932; Vergeiner and Dreiseitl, 1987; Muller and Whiteman, 1988; Sakiyama, 1990; Whiteman, 1990]. McKee and O'Neal [1989] considered the intra-valley variations of the TAF, thereby characterizing temperature gradients along the valley axis. In valleys characterized by a decreasing TAF (i.e. the valley widens) in the down-valley direction, the along-valley variation of the valley geometry induces a horizontal temperature gradient that promotes the development of a down-valley flow. Such valleys are defined as 'draining' valleys. Conversely, when the TAF increases (i.e. the valley narrows) in the down-valley direction, the horizontal temperature gradient changes sign, hindering the development of a down-valley flow and promoting stagnation of the air in the valley. Such valleys are defined as 'pooling' valleys. This classification was used by Lundquist et al. [2008] in the development of an algorithm to map mountainous regions sensitive to cold-air-pooling processes.

The use of the TAF to characterize along-valley variations in temperature holds when diabatic effects only are considered. When the valley atmosphere is decoupled from the free atmosphere above this is equivalent to neglecting the contribution of advection by thermally-driven flows (along-slope and along-valley flows) to the valley heat (energy) budget, so that the temperature variations are due to radiative, sensible and latent heat flux divergences only. The role of the thermally-driven flows on the volume-averaged (bulk) valley heat budget has been debated in several modelling studies, most of them focusing on daytime conditions. Rampanelli et al. [2004a] studied an idealized valley-plain configuration, highlighting the importance of the valley-scale circulation induced by thermally-driven flows in the warming of the valley atmosphere

during daytime. Schmidli and Rotunno [2010] studied a valley-plain configuration similar to that of Rampanelli et al. [2004a], using a diagnostic framework providing the means to disentangle the valley-volume effect from the processes controlling the valley heat budget. The authors concluded that, despite the importance of the valley-scale circulation, the valley-plain temperature difference can be qualitatively explained by the valley-volume effect. Further work on the respective roles of the valley-scale circulation and the volume effect on the warming of the valley atmosphere during daytime was performed by Schmidli [2013], who considered an idealized set of two-dimensional and three-dimensional valleys. The author demonstrated that the net effect of the valley-scale circulation, when integrated over the scale of the valley, is to cool the valley atmosphere. Hence, the valley-volume effect is the main cause of the enhanced warming of a valley with respect to an adjacent plain region during daytime.

The effects of the along-slope (i.e. upslope or downslope) flows on the thermal structure of the valley atmosphere were studied by Catalano and Cenedese [2010] for a set of two-dimensional idealized valleys characterized by different volumes. Numerical simulations for a diurnal cycle indicated that the volume of the valley is a parameter key to controlling the growth of the nocturnal valley boundary layer (VBL), which, in turn, affects the evolution of downslope flows. Kiefer and Zhong [2011] investigated the impact of downslope flows on the atmospheric static stability of the nocturnal VBL of shallow, idealized valleys of varying widths. The authors found that the valley-averaged cooling rate is reduced in wider valleys because of the reduced impact of downslope flows on the valley heat budget. Similar conclusions were drawn by Katurji and Zhong [2012] in a more systematic sensitivity study, exploring a larger set of the parameter space. While most of these studies considered the effects of thermally-driven flows on the structure of the VBL, the interplay between the two has received less attention. Burns and Chemel [2015] explored the two-way interactions taking place between downslope flows and the thermal structure of the nocturnal VBL in a two-dimensional idealized deep valley. Numerical model results indicated that the deepening of the nocturnal VBL above the ground-based inversion leads to a deceleration of downslope flows with time, because of the reduction of the near-slope horizontal buoyancy deficit that ultimately drives downslope flows. Their work was extended by Arduini et al. [2016] by considering the interactions between the nocturnal valley-wind system (i.e. downslope and down-valley flows) and the thermal structure of the nocturnal VBL. The formation of down-valley flows was found to reduce the growth of the VBL, leading to downslope flows reaching a quasi-steady state. An analysis of the heat and mass budgets indicated that the air evacuating the VBL as a result of the down-valley flow is replenished by the advection of warmer air from downslope flows, with a small contribution from subsidence of air above the valley centre.

Quantifying the effect of the thermally-driven flows on the mass transport in and out of the valley atmosphere is key to understanding the atmospheric circulation at all scales [Rotach et al., 2014]. The impact of the valley geometry on the structure of the VBL and its evolution was studied by Wagner et al. [2015a] for daytime conditions, for a set of idealized valley-plain systems. The authors showed that the valley-scale circulation is more sensitive to the valley width and depth than the valley length. The same conclusion holds for the associated mass transport processes. Wagner et al. [2015b] investigated more systematically the effect of along-valley orographic variations on transport processes during daytime. For a set of idealized valleys, the authors showed that a gradual narrowing of the valley cross-section along the valley axis, leads to an increase of the vertical mass flux out of the valley, when compared to that out of a valley of same volume but constant cross-sectional area.

The typical alpine landscape is not formed by single isolated valleys opening directly on plains. Valleys are usually connected to one another, and are characterized by different geometries and land covers. The effects of neighbouring valleys on the structure of the nocturnal VBL and its evolution in a single valley section have received little attention to date. The overall aim of the present work is to quantify the impact of along-valley orographic variations (in a system of valleys) on the structure of the nocturnal VBL and its evolution in pooling and draining configurations. To meet this aim, high-resolution numerical simulations of idealized valleys in such configurations are performed.

This work is organized as follows: Sect. IV.2 introduces the valley geometry, the definition of pooling and draining valleys, and the methodology used to compare valleys of different geometries; Sect. IV.3 presents the design of the numerical simulations; the structure of the nocturnal VBL and its evolution are analyzed in Sect. IV.4; the analysis of the valley heat budget is reported in Sect. IV.5 and Sect. IV.6; conclusions are given in Sect. IV.7.

IV.2 Methodology

IV.2.1 The idealized terrain

The idealized terrain considered in the present work can be thought as a system of two valleys of different cross-valley widths, connected to one another by a 'junction', with one of the valleys opening on a plain ($\mathcal{P}$). For the purpose of the discussion, the along-valley direction of the valley system is defined in this work as follows: because we consider nocturnal conditions, when the along-valley wind normally blows from the valley to the plain (that is down-valley), the valley adjacent to the plain will be referred to as the *downstream* valley ($\mathcal{V}_d$) and the valley farther from the plain will

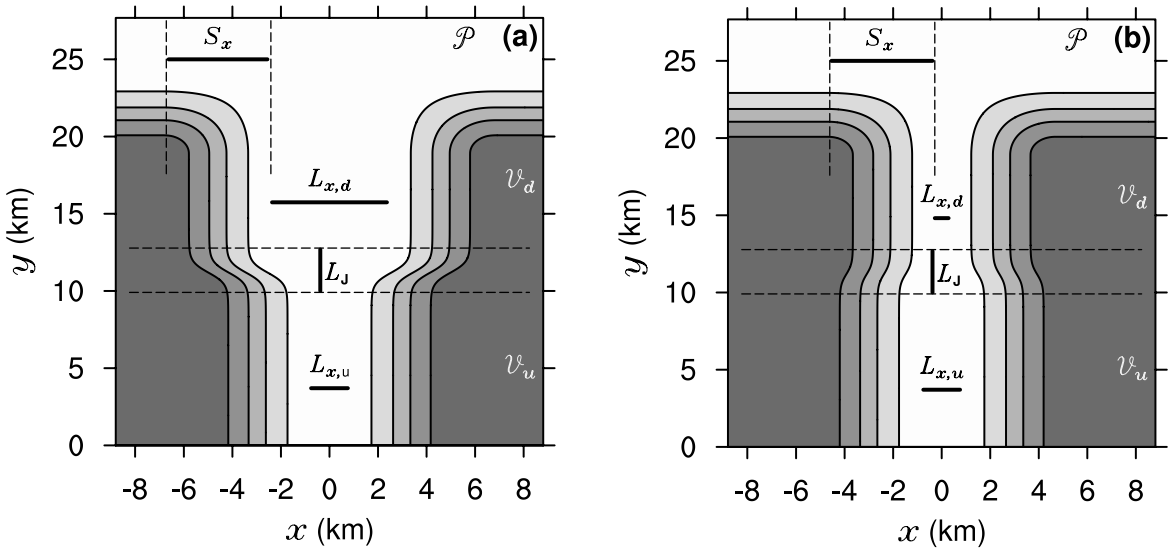

Figure IV.1: Contours of the terrain height h (with intervals of 100 m) defined by Eq. IV.1. The cross-valley direction x is oriented west-east and the along-valley direction y is oriented south-north. The terrain is symmetric about the plane $y = 0$. **(a)** Draining case D1 in Table IV.1; upstream valley ($\mathcal{V}_u$, $0 < y < 10$ km) with half-width valley floor $L_{x,u}$, connected by a junction of length L_J to the downstream valley ($\mathcal{V}_d$, $13 < y < 19$ km) with half-width valley floor $L_{x,d} = 2.875\, L_{x,u}$, which opens on a plain $\mathcal{P}$. The cross-valley slope width S_x is the same for the downstream and upstream valleys. **(b)** Pooling case P1 in Table IV.1; same as **(a)**, but considering a downstream valley with half-width valley floor $L_{x,d} = 0.25\, L_{x,u}$.

be referred to as the *upstream* valley ($\mathcal{V}_u$). We restrict our attention to a system of valleys with flat valley floor. The system of valleys is made symmetric about the origin $(x, y) = (0, 0)$, where the cross-valley direction x is oriented west-east, and the along-valley direction y is oriented south-north. The analytical expression for the terrain height h is given by

$$h\,(x, y) = H\, h_x\,(x, y)\; h_y\,(y) + h_0, \tag{IV.1}$$

where H is the height of the surrounding plateaux, set to 800 m, and h_0 is a reference height, set to 1000 m.

The terrain height in the cross-valley direction x, denoted by h_x, is given by

$$h_x\,(x, y) = \begin{cases} \frac{1}{2} - \frac{1}{2}\cos\left(\pi \frac{|x| - L_x(y)}{S_x}\right) & L_x(y) \le |x| \le S_x + L_x(y) \\ 0 & |x| < L_x(y) \\ 1 & |x| > S_x + L_x(y) \end{cases}, \tag{IV.2}$$

where S_x is the cross-valley slope width and L_x is the half-width of the valley floor. h_x is made to vary continuously in the along-valley direction y by varying the half-width

of the valley floor (along y) such that

$$L_x(y) = \frac{(L_{x,u} + L_{x,d})}{4 \tanh\left(\frac{\alpha}{2}\right)} \left\{ \tanh\left[\alpha \left(\frac{|y| - L_{y,\mathrm{u}}}{L_\mathrm{J}} - \frac{1}{2}\right)\right] + \tanh\left(\frac{\alpha}{2}\right)\right\}, \tag{IV.3}$$

where $L_{y,\mathrm{u}} = 10$ km is the length of $\mathcal{V}_u$, $L_\mathrm{J} = 3$ km is the length of the junction that connects $\mathcal{V}_u$ to $\mathcal{V}_d$ and $L_{x,u}$ and $L_{x,d}$ are the half-width of the $\mathcal{V}_u$ floor and $\mathcal{V}_d$ floor, respectively. We set $\alpha = 5$, so that the half-width L_x in the $\mathcal{V}_u$ and $\mathcal{V}_d$ sections is approximately equal to $L_{x,u}$ and $L_{x,d}$, respectively.

The terrain height in the along-valley direction y, denoted by h_y, is defined as

$$h_y(y) = \begin{cases} \frac{1}{2} + \frac{1}{2}\cos\left(\pi \frac{|y| - L_{y,\mathrm{tot}}}{S_y}\right) & L_{y,\mathrm{tot}} < |y| \leq S_y + L_{y,\mathrm{tot}} \\ 0 & |y| > L_{y,\mathrm{tot}} + S_y \\ 1 & |y| \leq L_{y,\mathrm{tot}} \end{cases}, \tag{IV.4}$$

where $L_{y,\mathrm{tot}} = 24$ km is the total length of the valley system, $L_{y,\mathrm{d}} = 6$ km is the length of $\mathcal{V}_d$, and $S_y = 5$ km is the along-valley slope width of $\mathcal{V}_d$.

This formulation for the terrain height can describe a valley opening or narrowing on another valley, which opens on a plain, as illustrated in Fig. IV.1. Fig. IV.1a and Fig. IV.1b show contours of the terrain height h defined by Eq. IV.1 for $L_{x,d} = 2.875\, L_{x,u}$ and $L_{x,d} = 0.25\, L_{x,u}$, respectively.

IV.2.2 Definition of the pooling and draining configurations

Following McKee and O'Neal [1989] and Whiteman [1990], the topographic amplification factor (TAF) of a cross-valley section with respect to the equivalent plain section is defined by the ratio

$$\Gamma = \frac{W_v\, H}{A_v}, \tag{IV.5}$$

where W_v is the width of the valley at the height of the plateaux H and A_v is the cross-sectional area at fixed along-valley position y. The TAF can be calculated for different valley sections along the valley axis. If Γ decreases (i.e. the valley widens) in the down-valley direction, the valley is defined as a draining valley (see Fig. IV.1a); if Γ increases (i.e. the valley narrows) in the down-valley direction, the valley is defined as a pooling valley (see Fig. IV.1b). Hence, the ratio of the TAF between two cross-valley sections, termed the intra-valley TAF and denoted by γ hereafter, characterizes the draining or pooling character of a valley; for instance for $\mathcal{V}_u$ and $\mathcal{V}_d$, we get

$$\gamma = \frac{\Gamma_u}{\Gamma_d}, \tag{IV.6}$$

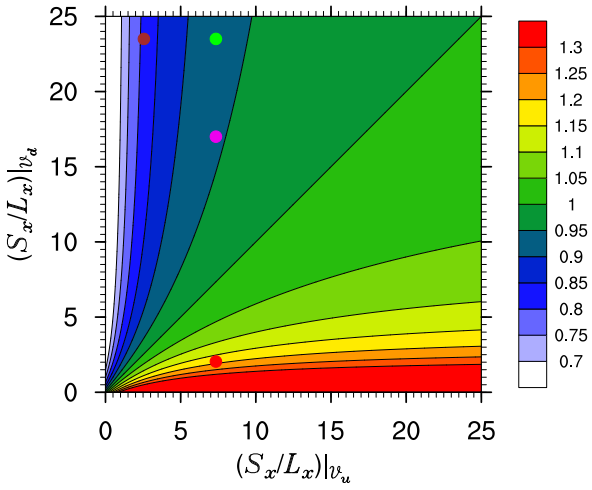

Figure IV.2: Contours of $\gamma = \Gamma_u/\Gamma_d$, as a function of $(S_x/L_x)|_{\mathcal{V}_u}$ and $(S_x/L_x)|_{\mathcal{V}_d}$, where S_x is the slope length and L_x is the half-width of the valley floor; Γ_u, Γ_d are the topographic amplification factors for $\mathcal{V}_u$ and $\mathcal{V}_d$, respectively, with $\Gamma = W_v\, H/A_v$. W_v is the width of the valley at the height of the plateaux H and A_v is the cross-sectional area at a fixed position in the along-valley direction. The color dots correspond to the cases considered in this work: D1 (red), P1 (green), P1b (magenta), and P2 (brown).

where Γ_u, Γ_d are the topographic amplification factors for $\mathcal{V}_u$ and $\mathcal{V}_d$, respectively. Thus, we have $\gamma > 1$ for a draining valley and $\gamma < 1$ for a pooling valley.

With the parameters characterizing the valley geometry used in the present work, introduced in Sect. IV.3, the width W_v of the valley at the height of the plateaux H is given by $W_v(y) = 2\,[L_x(y) + S_x]$. The cross-sectional area A_v, at fixed along-valley position y, can be computed from the analytical expression for the terrain height in the cross-valley direction x (see Eq. IV.2). Integrating h for $-(S_x + L_x) < x < (S_x + L_x)$, and a fixed along-valley position y, where $h_y\,(y) = 1$, we get $A_v = H\ (2\,L_x + S_x)$. Hence, for the terrain geometry considered herein, Γ can be written explicitly as a function of L_x and S_x : $\Gamma = 2\,(1 + S_x/L_x)\,(2 + S_x/L_x)^{-1}$. Γ is therefore between 1 and 2, corresponding to the two limits $S_x/L_x \ll 1$ and $S_x/L_x \gg 1$, respectively.

For the valley geometry considered herein γ is between 0.5 and 2. Contours of γ displayed in a $[(S_x/L_x)|_{\mathcal{V}_u}, (S_x/L_x)|_{\mathcal{V}_d}]$ diagram, are shown in Fig. IV.2. For a deep and narrow (alpine) valley model, S_x/L_x should be larger than about 2 leading to γ between about 0.75 and 1.33. This shows that only a limited range of values for γ can be explored.

The geometrical parameters for the numerical simulations presented in this work are listed in Table IV.1. A symbolic notation is used to differentiate the simulations: a capital letter $X = I, D, P$ defines the type of valley system [isolated valley-plain (I), draining (D), pooling (P)]; a number $n = 1, 2$ defines the geometry of the upstream and reference valleys considered. The subscripts u and d are used to indicate the valley section considered (u for $\mathcal{V}_u$ and d for $\mathcal{V}_d$). For instance $\mathrm{P1}_d$ refers to $\mathcal{V}_d$ for the P1

Table IV.1: List of the numerical simulations performed in this study. A symbolic notation is used to differentiate the simulations, in which a capital letter $X = I, D, P$ defines the type of valley system [isolated valley-plain (I), draining (D), pooling (P)]; a number $n = 1, 2$ defines the geometry of the upstream and reference valleys considered. $L_{x,u}$ is the half-width floor of the upstream valley $\mathcal{V}_u$; $L_{x,d}$ is the half-width floor of the downstream valley $\mathcal{V}_d$; $S_{x,d}$ is the cross-valley slope width of the downstream valley; R_V is the ratio of the cross-sectional area of $\mathcal{V}_d$ to that of $\mathcal{V}_u$; Γ_u and Γ_d are the topographic amplification factor (TAF) of $\mathcal{V}_u$ and $\mathcal{V}_d$, respectively, and γ is the intra-valley TAF between the two valley sections, e.g. the ratio of Γ_u to Γ_d. For all cases, $S_{x,u} = 4230$ m and $H = 800$ m.

Case	$L_{x,u}$ (m)	$L_{x,d}$ (m)	$S_{x,d}$ (m)	R_V	Γ_u	Γ_d	γ
I1	720	∞	4230	NA*	1.74	1	1.74
D1	720	2070	4230	1.48	1.74	1.50	1.16
P1	720	180	4230	0.81	1.74	1.92	0.91
P1b	720	180	3060	0.60	1.74	1.89	0.92
I2	2070	∞	4230	NA*	1.50	1	1.50
P2	2070	180	4230	0.55	1.50	1.92	0.78

*NA stands for non appropriate.

case. A draining case (D1) and a pooling case (P1) will be compared to the isolated valley-plain I1 case. An additional case was simulated, referred to as P1b in Table IV.1, for which the parameters are the same as for the P1 case, except for $S_{x,d} = 3060$ m. The comparison between the P1 and the P1b cases elucidates the sensitivity of the $\mathcal{V}_u$ atmosphere to the ratio of the cross-sectional area of $\mathcal{V}_d$ to that of $\mathcal{V}_u$, denoted by R_V, while keeping γ almost constant (see Table IV.1). A limited range of pooling cases can be explored when considering the geometry for the I1 case. Therefore, another reference case (I2) is considered, for which $L_{x,u}$ is increased, allowing a pooling case characterized by a smaller value of γ. This pooling case will be referred to as the strong pooling case and denoted by P2. The along-valley variation of the cross-valley slope width S_x for the P1b case is obtained by applying a tanh function to S_x as is done for the half-width L_x, thereby leading to steeper slopes.

IV.2.3 Heat budget

When examining the differential cooling along the valley, we consider the volume-averaged heat budget equation over a volume V_j (either in $\mathcal{V}_u$, $\mathcal{V}_d$ or $\mathcal{P}$), that is

$$\frac{1}{V_j}\int_{V_j}\frac{\partial\theta}{\partial t}\,dV = \frac{1}{V_j}\int_{V_j} -u_i\frac{\partial\theta}{\partial x_i}\,dV + \frac{1}{V_j}\int_{V_j} -\frac{\partial s_i}{\partial x_i}\,dV + \frac{1}{V_j}\int_{V_j} -f\,dV. \qquad \text{(IV.7)}$$

The term on the left-hand-side (l.h.s.) of Eq. IV.8 is the volume-averaged potential temperature tendency, and the forcing terms on its right-hand-side (r.h.s.) are the volume-averaged potential temperature advection, divergence of the sub-grid-scale (SGS) turbulent fluxes and divergence of the radiative flux, respectively. Using Gauss' theorem and assuming incompressibility, the volume integrals of the advection and SGS turbulent flux divergence terms can be expressed as surface integrals, yielding

$$\underbrace{\frac{1}{V_j}\int_{V_j}\frac{\partial\theta}{\partial t}\,dV}_{T_j} = \frac{1}{V_j}\Bigg(\underbrace{\int_{\Sigma_{j,i}} -a_i\,n_i\,d\Sigma + \int_{\Sigma_{j,i}} -\tau_i\,n_i\,d\Sigma}_{A_j} + \underbrace{\int_{\Sigma_{j,s}}\tau_s\,d\Sigma}_{S_j} + \underbrace{\int_{V_j} -f\,dV}_{F_j}\Bigg), \tag{IV.8}$$

where a_i and τ_i are the advective and SGS turbulent heat fluxes through the top and lateral surfaces $\Sigma_{j,i}$ of the volume V_j, respectively, n_i is the unit vector normal to the surfaces $\Sigma_{j,i}$ (defined positively outwards), and τ_s is the sensible heat flux at the ground surface $\Sigma_{j,s}$.

We collect on the r.h.s. the radiative flux divergence and surface sensible heat flux terms, which are responsible for the heat loss in the valley atmosphere. The sum of these two terms will be referred to as the diabatic term.

Hereafter the following notation is used

$$X_{j,V_i} = \frac{1}{V_i}X_j, \quad \overline{X_j} = \int_{t_0}^{t_1} X_j\,dt,$$

where $X_j = T_j,\ A_j,\ S_j,\ F_j$ and the volume V_i can be different from V_j.

Following Whiteman et al. [1996], we introduce a simple non-dimensional form of the heat budget Eq. IV.8, based on the balance between T_{j,V_j} and A_{j,V_j} normalized by the diabatic term that is

$$\frac{T_{j,V_j}}{\left(S_{j,V_j}+F_{j,V_j}\right)} - \frac{A_{j,V_j}}{\left(S_{j,V_j}+F_{j,V_j}\right)} = 1. \tag{IV.9}$$

This equation can be interpreted physically as

$$[\text{cooling efficiency}] + [\text{draining efficiency}] = 1. \tag{IV.10}$$

Indeed, the larger is the first term on the l.h.s. of Eq. IV.9 when compared to the second term in absolute value, the larger is the fraction of the diabatic heat loss that contributes to cool the valley atmosphere. The first term on the l.h.s. of Eq. IV.9 can thus be thought as a term measuring the 'cooling efficiency' of the valley. By contrast, when the ratio of the advection terms to the diabatic term is equal to -1 for instance, the cooling within a valley section ceases even though the heat loss resulting from the diabatic term is non zero. The second term on the l.h.s. of Eq. IV.9, will be referred

to as the 'draining efficiency'; it is maximum when equal to -1.

When the cooling efficiency is larger than the draining efficiency in a valley, the valley is referred to as a trapper [Whiteman et al., 1996; Fast et al., 1996]. If the reverse holds, the valley atmosphere is affected by advective warming, so reducing its overall cooling. This type of valley is referred to as a drainer. It is worth noting that Eq. IV.9 characterizes the behaviour of valleys with internal variables (the heat budget terms), rather than with the geometry of the valley.

IV.2.4 Comparison of the cumulative heat budget terms for different valley sections

In the following, we use the diagnostic framework introduced by Schmidli and Rotunno [2010], which separates the valley-volume effect from the thermodynamical processes controlling the valley heat budget when examining the differential cooling between an isolated valley and an adjacent plain.

Introducing the volume $P = W_v\, H\, Y$ of the equivalent plain volume, the r.h.s. of Eq. IV.8 can be rewritten as

$$T_{j,V_j} = \Gamma_j \left[A_{j,P} + S_{j,P} + F_{j,P}\right], \tag{IV.11}$$

where Γ_j is the TAF of the upstream (for $j = u$) or downstream (for $j = d$) valley-section of length Y in the along-valley direction, with respect to the equivalent plain section. Integrating Eq. IV.11, from a time t_0 to t yields $\overline{\mathrm{T}_{j,V_j}} = \Gamma_j \left(\overline{\mathrm{A}_{j,P}} + \overline{\mathrm{S}_{j,P}} + \overline{\mathrm{F}_{j,P}}\right)$. The ratio of this latter expression for $\mathcal{V}_u$ to that for $\mathcal{V}_d$ for Y constant is a measure of the difference of the temperature changes from t_0 between $\mathcal{V}_u$ and $\mathcal{V}_d$. Collecting the diabatic term on the r.h.s. yields

$$\frac{\overline{\mathrm{T}_{u,V_u}}}{\overline{\mathrm{T}_{d,V_d}}} = \gamma \frac{\left(\overline{\mathrm{S}_{u,P_u}} + \overline{\mathrm{F}_{u,P_u}}\right)}{\left(\overline{\mathrm{S}_{d,P_d}} + \overline{\mathrm{F}_{d,P_d}}\right)} \frac{\left[1 + \dfrac{\overline{\mathrm{A}_{u,P_u}}}{\left(\overline{\mathrm{S}_{u,P_u}} + \overline{\mathrm{F}_{u,P_u}}\right)}\right]}{\left[1 + \dfrac{\overline{\mathrm{A}_{d,P_d}}}{\left(\overline{\mathrm{S}_{d,P_d}} + \overline{\mathrm{F}_{d,P_d}}\right)}\right]}. \tag{IV.12}$$

In order to simplify the notation, Eq. IV.12 is rewritten as

$$\mathrm{R}_T = \gamma\, \mathrm{R}_C\, \mathrm{R}_A\,, \tag{IV.13}$$

where R_T is the ratio of the net temperature changes and R_C and R_A are the ratios of the temperature changes due to the diabatic processes and advection, respectively, appropriately weighted by the respective plain volumes. Eq. IV.13 allows the compari-

son of the heat budgets of different valley sections, separating the valley-volume effect from the differences in the thermodynamical processes. If the comparison is made between a valley-section of volume V_j and an adjacent plain, Eq. IV.13 is equivalent to the one used by Schmidli and Rotunno [2010], that is

$$\mathrm{R}_T = \Gamma_j \, \mathrm{R}_C \, \mathrm{R}_A \, . \tag{IV.14}$$

IV.2.5 Definition of the control volumes and averaging

We set the length Y to 2 km. All the vertical profiles of the different fields shown in the next sections, if not specified otherwise, are horizontally averaged between $-180 < x < 180$ m and $2 < y < 4$ km and $14 < y < 16$ km for the upstream and downstream valleys, respectively. These regions are termed the 'valley centre' areas (of $\mathcal{V}_u$ and $\mathcal{V}_d$, respectively). We shall also consider control volumes defined by $-(L_x+S_x) < x < (L_x+S_x)$, y in the ranges above, and $h_0 < z < H+h_0$. These volumes are denoted by V_u and V_d and will be termed 'valley volume' regions. An average over such a control volume will be referred to as a valley-volume average. Control volumes for the isolated valley-plain configurations (I1 and I2) are defined as for V_u and V_d, and will be termed V_I. Finally, a plain volume is defined by: $-(L_x + S_x) < x < (L_x + S_x)$, $30 < y < 32$ km and $h_0 < z < H + h_0$ and denoted by $\mathcal{P}$.

IV.3 Numerical model set-up

IV.3.1 Numerical method

The numerical simulations reported in Table IV.1 were performed with the Weather Research and Forecasting (WRF) model, version 3.4.1, using the ARW core [Skamarock et al., 2008]. The WRF model is a compressible, non-hydrostatic model, appropriate for scales ranging from meters to global scales. The governing equations are formulated using a terrain following hydrostatic-pressure coordinates and discretized on a staggered Arakawa-C grid. Advection terms were discretized using a fifth-order Weighted Essentially Non Oscillatory (WENO) scheme with positive definite filter. The time integration was performed with a third-order Runge-Kutta scheme, using the time-splitting technique described by Wicker and Skamarock [2002] for the acoustic mode. The sub-grid scales were parametrized using a 1.5-order Turbulent Kinetic Energy (TKE) scheme [Deardorff, 1980]. The Rapid Radiative Transfer model [Mlawer et al., 1997] was used to parametrize the longwave radiation, and the Dudhia [1989] scheme for the shortwave radiation. The surface forcing was simulated explicitly by coupling the atmospheric model to the Noah Land Surface Model [Chen and Dudhia,

2001] using the Monin-Obukhov similarity theory [the "MM5 revised" scheme, Jimenez et al., 2012]. Shadowing effects were not taken into account in the present work.

IV.3.2 Grid design

To prevent spurious numerical effects at the lateral boundaries a large domain in the horizontal directions is needed. Two nested domains were used, with the inner domain covering the full valley system and part of the plain regions. Both domains were centered on the valley-system region. To minimize the errors at the lateral boundaries between the two domains, the ratio between the horizontal grid resolutions of the two domains was set to 3, and the number of grid points in the relaxation layer at the lateral boundaries of the inner domain was increased to 5 according to Moeng et al. [2007]. The outer domain was discretized using 120 grid points in the x-direction and 336 grid points in the y-direction with a grid resolution $\Delta x|_{\mathrm{D1}} = \Delta y|_{\mathrm{D1}} = 270$ m. For the inner domain, 196 and 610 grid points were used in the x- and y- directions, respectively, with a grid resolution $\Delta x|_{\mathrm{D2}} = \Delta y|_{\mathrm{D2}} = 90$ m. The height of the domain was 12 km and 100 grid points were used along the vertical direction z for both domains. The vertical coordinate was stretched along the vertical using an hyperbolic tangent function, resulting in a resolution close to the ground of about 2 m, and vertical grid spacings continuously increasing with height. The time-steps were 0.45 and 0.15 s for the outer and inner domains, respectively.

IV.3.3 Initial conditions

The design of the initial conditions follows the setup of Burns and Chemel [2014]. All the model runs were initialized 1 hour before sunset, simulating a 6-h time period after that time, during wintertime. Because this study focuses on the development of stable boundary layers, post-convective conditions were considered for the initial base-state, with the vertical gradient of virtual potential temperature θ set to 1.5 K km^{-1}. Even though highly idealized, such value of the lapse rate has been observed in mountainous region at sunset [e.g. Whiteman and Zhong, 2008]. For simplicity, θ will be referred as potential temperature thereafter. Its value at the valley floor was initialized to 288 K. The skin temperature was initialized by an extrapolation from the air temperature of the first three layers above ground level, and a random temperature perturbation with a minimum value of -0.05 K was applied to the skin temperature to reduce the spin-up time of the simulation. In order to focus on the effects of the valley geometry on the circulation within the valley, the valley atmosphere was dynamically decoupled from the free atmosphere above by setting the wind speed to zero at the initial time across the domains. We restrict our attention to a relatively dry atmosphere, and so relative humidity was set to 40 % across the domains, following previous setup of

idealized cases [e.g. Schmidli, 2013; Chemel and Burns, 2015a].

The soil properties and the land-use were homogeneous in order to focus on the effects of the valley geometry. The land-use type was set to 'grassland', which corresponds to short grass, a reasonable assumption for an alpine valley. The soil type was set to 'silty clay loam'; the soil moisture was initialized so that it is 90 % of the soil moisture content at field capacity. This is a value typical of conditions a few days after rainfall, which is a reasonable assumption given that wintertime is considered. The details of the soil initialization are reported in Burns and Chemel [2014].

IV.3.4 Boundary conditions

Periodic boundary conditions were imposed for the outer domain in the x-direction. This is equivalent to having an infinite repetition of the same valley in this direction. Open boundary conditions were imposed in the y-direction; because of the idealized setup and the duration of the simulations, only outflow at the boundaries in the y-direction can be simulated. By increasing the number of grid points along y from 336 to 436 we verified that the flow in the region of interest is not affected by the open boundaries for this particular setup. The lateral boundaries of the inner domain were updated every outer domain time-step. A sponge layer was introduced across the top 4 km of the domain to avoid any spurious effect of wave reflection on the numerical solution.

IV.4 Thermal structure and flow evolution

The development of the down-valley flow depends on the differential cooling along the valley axis. In principle, the valley sections should cool differently because of the change of Γ along the valley axis. Because the valley sections are communicating, the down-valley flow transports mass and heat from $\mathcal{V}_u$ to $\mathcal{V}_d$ and to the plain, modifying this picture.

IV.4.1 Thermal structure of the valley boundary layer

Figure IV.3 displays vertical profiles of potential temperature change from $t = 0$ in $\mathcal{V}_u$ and $\mathcal{V}_d$, denoted by $\Delta\theta$, for the different cases at $t = 150$ min and $t = 360$ min. The top height of the VBL is diagnosed here by the top height of the elevated inversion layer. Figure IV.3a show that the near-surface atmosphere experiences a strong cooling during the first part of the night (θ decreases by 5 K from $t = 0$ to $t = 150$ min) for all the cases. The pooling cases P1 and P1b present a colder and deeper VBL than the respective reference case I1 and draining case D1; this result also holds for P2 and I2. As shown by Arduini et al. [2016], before the down-valley flow is fully developed, the

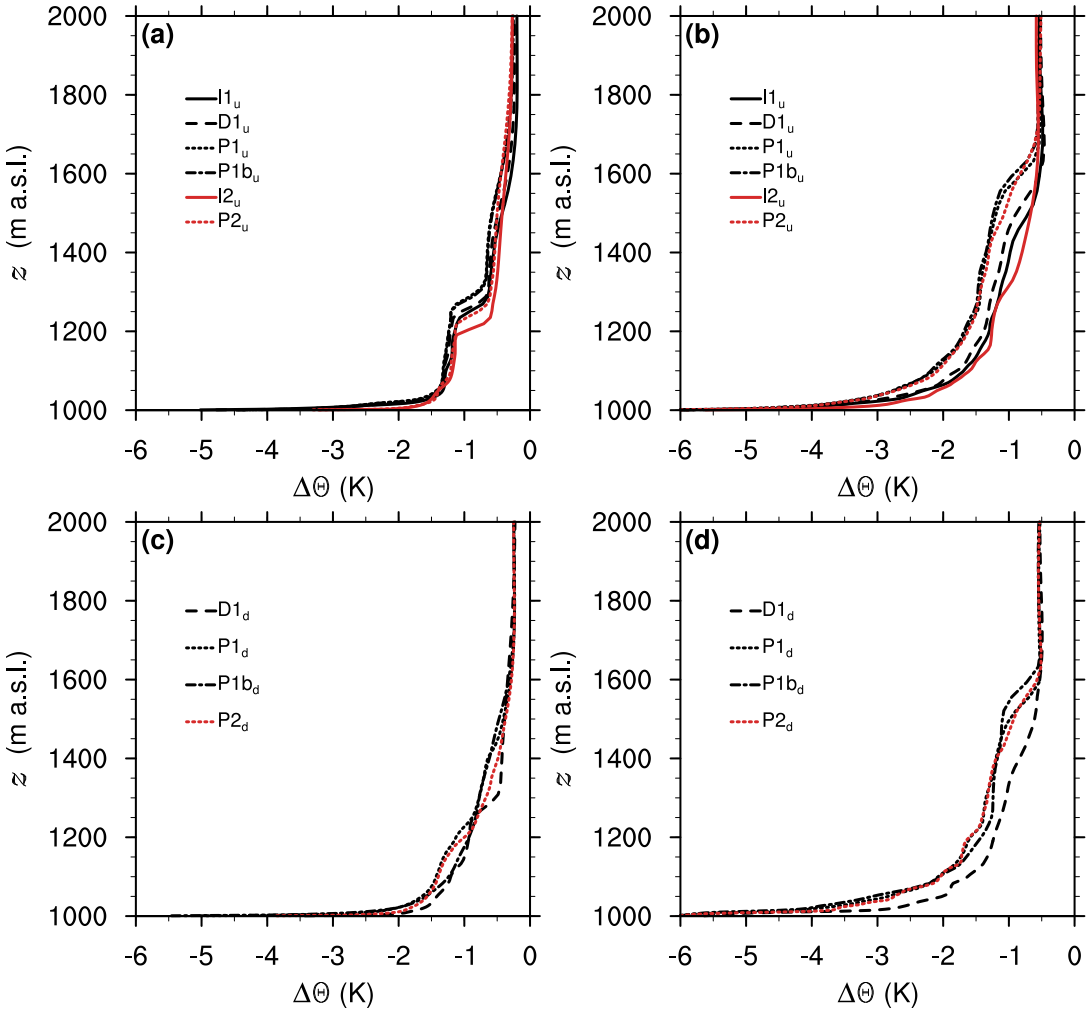

Figure IV.3: **(a)** Vertical profiles of potential temperature change $\Delta\theta$ from $t = 0$ in the upstream valley, horizontally averaged in the range $-180 < x < 180$ m and $2 < y < 4$ km (in $\mathcal{V}_u$), at $t = 150$ min for the I1 (*black solid line*), D1 (*black dashed line*), P1 (*black dotted line*), I2 (*red solid line*), and P2 (*red dotted line*) cases; **(b)** same as **(a)**, but at $t = 360$ min. **(c)** Same as **(a)**, but in the downstream valley, horizontally averaged in the range $-180 < x < 180$ m and $14 < y < 16$ km (in $\mathcal{V}_d$); **(d)** same as **(c)**, but at $t = 360$ min; see Table IV.1 and Sect. IV.2.2 for the definition of the simulations.

depth of the VBL is controlled by the upward vertical transport induced by downslope flow convergence over the valley centre. This vertical transport is suppressed by the development of the down-valley flow. As will be shown in Sect. IV.4.2, the development of the down-valley flow is delayed for the pooling cases with respect to the respective reference cases, and with respect to the D1 case for the P1 and P1b cases. Hence, the vertical transport induced by the downslope flow convergence persists for a longer time in the pooling valleys, leading to a deeper VBL.

For the P1 and P2 cases, $\mathcal{V}_d$ presents a colder VBL than $\mathcal{V}_u$ for $z < 200$ m a.g.l. (see Fig. IV.3a and Fig. IV.3c). Figure IV.3c also shows that the temperature difference between $\mathcal{V}_d$ and $\mathcal{V}_u$ is different for the P1 and P1b cases. For the P1b case the

atmosphere of $\mathcal{V}_d$ below $z = 200$ m a.g.l. is slightly warmer than that for the P1 case, because the downslope flows that develop in $\mathcal{V}_d$ for the P1b case are weaker than those for the P1 case. Weaker downslope flows lead to a reduced sensible heat flux (since it is proportional to the near-surface wind speed), and so to a reduced cooling.

At $t = 360$ min, for $z > 100$ m a.g.l., $\mathcal{V}_d$ presents a warmer VBL than $\mathcal{V}_u$ for all the cases considered (see Fig. IV.3d). $\mathcal{V}_u$ for the D1, P1, P1b and P2 cases generally presents a colder and deeper VBL than that for the respective reference cases (see Fig. IV.3b). Nonetheless, the degree of deviation from the reference cases changes between the draining and pooling cases. The thermal structure of $\mathcal{V}_u$ for the D1 case presents only small differences with that for the I1 case. Much deeper and colder boundary layers develop for the pooling cases. The case with the smallest value of γ (P2) presents the largest differences with the respective reference case (I2), with an increase of the boundary-layer depth of 85%. The thermal structure of $\mathcal{V}_u$ is similar for the valley systems characterized by different geometries downstream but similar values of γ (the P1 and P1b cases), suggesting that the thermal structure of $\mathcal{V}_u$ is independent of the volume of $\mathcal{V}_d$, as long as the TAF of $\mathcal{V}_d$ is unchanged.

Finally, it is worth noting that the atmosphere of $\mathcal{V}_u$ presents approximately the same vertical gradient of potential temperature in the upper part of the VBL (above the ground-based inversion) for all the cases by the end of the simulated time period, even though the atmosphere is generally colder for the valley-system cases. This suggests that the pooling or draining character of a valley does not substantially modify the atmospheric stability of the valley atmosphere above the ground-based inversion.

IV.4.2 Down-valley flow

The differences in cooling of the valley atmosphere between the different configurations, shown in Sect. IV.4.1, have a substantial effect on the along-valley pressure gradient that ultimately drives the down-valley flow and, therefore, on the structure of the flow itself. Time series of the horizontally-averaged near-surface down-valley wind speed at the exit of $\mathcal{V}_u$ and along-valley near-surface pressure difference between $\mathcal{V}_u$ and $\mathcal{V}_d$ are shown in Fig. IV.4a and Fig. IV.4b, respectively.

A low-level up-valley flow (i.e. negative values of the wind speed resulting from a negative pressure difference between $\mathcal{V}_u$ and $\mathcal{V}_d$) develops for the P1 and P2 cases during the first part of the night, while the thermally-driven along-valley flow is normally down-valley during the night [see for instance Zardi and Whiteman, 2013]. A similar unexpected behaviour of the along-valley flow was observed by Whiteman et al. [1999c] in sub-basins of the Colorado River valley. The low-level up-valley wind is stronger as γ decreases and lasts until $t \simeq 105$ min for the P1 case and until $t \simeq 210$ min for

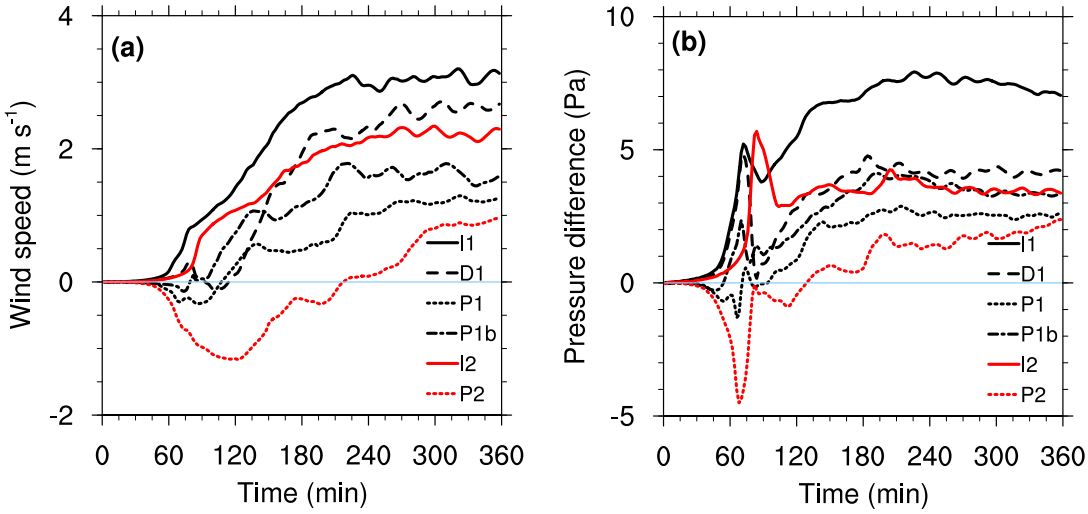

Figure IV.4: **(a)** Time series of the down-valley wind speed at $z = 25$ m a.g.l., averaged in the range $-180 < x < 180$ and $11 < y < 13$ km (i.e. $\mathcal{V}_u$ exit) and **(b)** horizontal pressure gradient between $\mathcal{V}_u$ and $\mathcal{V}_d$, computed along the valley axis at $y = 3$ km for $\mathcal{V}_u$ and $y = 13$ km for $\mathcal{V}_d$, at $z = 25$ m a.g.l., horizontally averaged in the range $-180 < x < 180$ m, for the I1 (*black solid line*), D1 (*black dashed line*), P1 (*black dotted line*), P1b (*black dashed-dotted line*), I2 (*red solid line*), and P2 (*red dotted line*) cases; see Table IV.1 and Sect. IV.2.2 for the definition of the simulations.

the P2 case (see Fig. IV.4a). This is explained by the colder VBL for $z < 1200$ m in $\mathcal{V}_d$ than in $\mathcal{V}_u$ during these periods (see Fig. IV.3a and Fig. IV.3c). The near-surface down-valley flow for the P1b case does not present the same feature as for the P1 case during the early night; the near-surface pressure gradient barely changes sign and so an up-valley flow barely forms in this case. This is explained by the slightly warmer VBL in $\mathcal{V}_d$ for the P1b case than for the P1 case (see Fig. IV.3a and Fig. IV.3c).

The down-valley flow reaches a dynamical steady state by the end of the simulated time period for all the cases considered. When that steady state is reached, the near-surface down-valley wind speed is lower by at least a factor of 2 for the pooling and draining cases than for the respective reference cases. This reduction of the down-valley wind speed results from a reduction of the along-valley pressure gradient. The down-valley wind speed is also significantly smaller (40% smaller) for the pooling cases P1 and P1b than for the draining case. It is worth noting that the valley-to-plain pressure difference is smaller (and so is the down-valley wind speed) for the I2 case than for the I1 and D1 cases, because the VBL is shallower (see Fig. IV.3a and IV.3b).

To investigate the characteristics of the down-valley wind speed along the vertical, vertical profiles of the wind speed at the same times as in Fig. IV.4 ($t = 150$ min and $t = 360$ min) are shown in Fig. IV.5. At $t = 150$ min the up-valley flow in $\mathcal{V}_u$ for the P2 case fills the valley atmosphere up to the top of the VBL at this time (cf. Fig. IV.3a), reversing above. The other cases present qualitatively the same down-valley wind profiles, with a general reduction of the low-level (below 200 m a.g.l.) wind speed

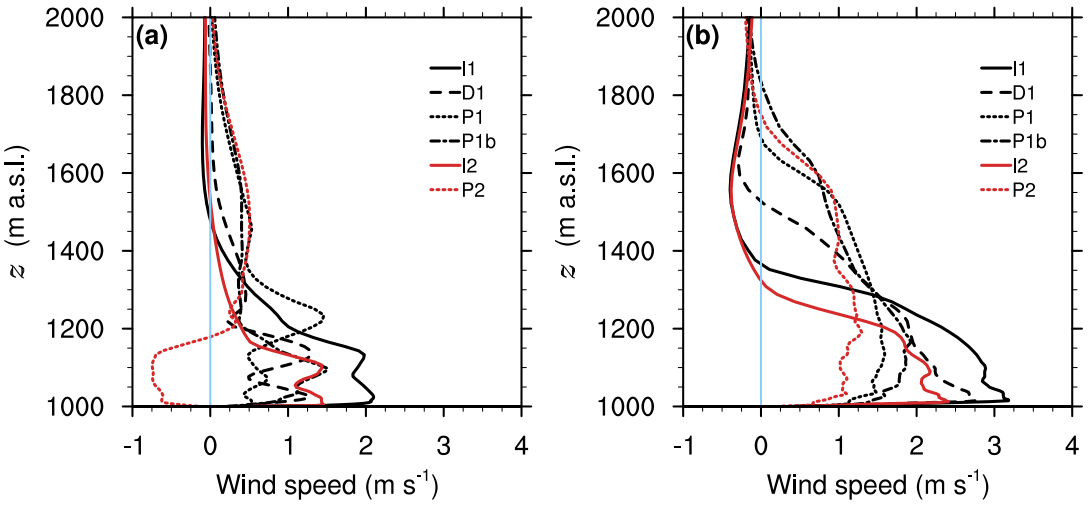

Figure IV.5: **(a)** Vertical profiles of the down-valley wind component v, horizontally averaged in the range $-180 < x < 180$ m and $11 < y < 13$ km (i.e. $\mathcal{V}_u$ exit), at $t = 150$ min for the I1 (*black solid line*), D1 (*black dashed line*), P1 (*black dotted line*), I2 (*red solid line*), and P2 (*red dotted line*) cases; see Table IV.1 and Sect. IV.2.2 for the definition of the simulations. **(b)** Same as **(a)**, but at $t = 360$ min.

when a downstream valley is present. At $t = 360$ min (see Fig. IV.5b), no up-valley flow is observed in the P2 case, in agreement with Fig. IV.4a. A distinction needs to be made between pooling and non-pooling cases. An anti-wind is indeed present for the reference cases (and to some extent for the D1 case). By contrast, no anti-wind forms for the pooling configurations within the valley, as the VBL is deeper in these cases and the down-valley flow fills the valley atmosphere almost up to the height of the plateaux. Hence, mass conservation should be ensured by weak anti-winds above the plateaux for these cases.

IV.4.3 Mass fluxes along the valley axis

The differences in the down-valley flow that develops in the different configurations have an impact on the mass budget of $\mathcal{V}_u$. Figure IV.6 shows time series of the net along-valley mass fluxes in $\mathcal{V}_u$ for the D1, P1, P1b and P2 cases, normalized by the net along-valley mass fluxes in the valleys for the respective reference cases (I1 and I2). All the mass fluxes are calculated across the along-valley surfaces of the volume V_u. Before $t = 150$ min, the mass fluxes are less than half those of the respective reference cases, indicating that the outflow of cold air from $\mathcal{V}_u$ is strongly reduced during the evening transition. The along-valley mass flux is negative in $\mathcal{V}_u$ until $t = 120$ min for the P2 case (the net mass flux being always positive for the I2 case), showing that there is a net flux of mass from $\mathcal{V}_d$ to $\mathcal{V}_u$ associated with the up-valley flow. It is worth noting that for the D1, P1 and P1b cases the values of the mass flux are similar after $t = 180$ min, despite the differences in the along-valley flow structure (see Fig. IV.5b).

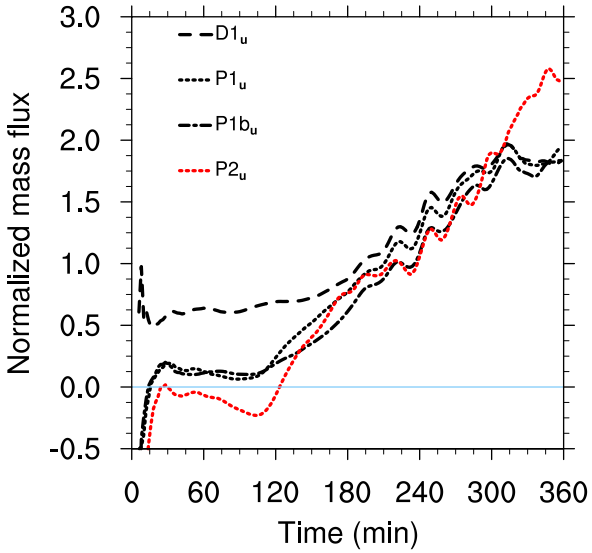

Figure IV.6: Time series of the normalized net along-valley mass fluxes across the surfaces of the $\mathcal{V}_u$ valley volumes (V_u), for the D1 (*black dashed line*), P1 (*black dotted line*), P1b (*black dashed-dotted line*), and P2 (*red dotted line*) cases; see Table IV.1 and Sect. IV.2.2 for the definition of the simulations. The mass fluxes are normalized by the mass fluxes in the valleys for the respective reference cases (I1 and I2).

Although the low-level down-valley wind speed is reduced by a factor of 2 between the reference cases and the pooling cases (I1 and P1,P1b; I2 and P2) by the end of the simulated time period, the net along-valley mass flux is larger than that of the reference case, by a factor of 2 for the P1 and P1b cases and by a factor of 2.5 for the P2 case. This is because of the presence of the return flow in the upper part of the valley atmosphere for the reference cases I1 and I2, which reduces the net along-valley mass flux out of V_u.

IV.5 Heat budget of the upstream valley atmosphere

The differences in the thermal structure of the VBL in $\mathcal{V}_u$ between the different configurations, described in Sect. IV.4.1, are driven by the competing cooling processes described in Sect. IV.2.3. Here, we analyze in detail the effects of the downstream valley on the cooling processes in the upstream valley, highlighting the differences with a reference valley opening directly on a plain.

IV.5.1 Instantaneous heat budget

Figure IV.7 displays time series of the V_u-averaged terms of the heat budget equation (Eq. IV.8), for the D1, P1, P1b and P2 cases and the respective reference cases (I1

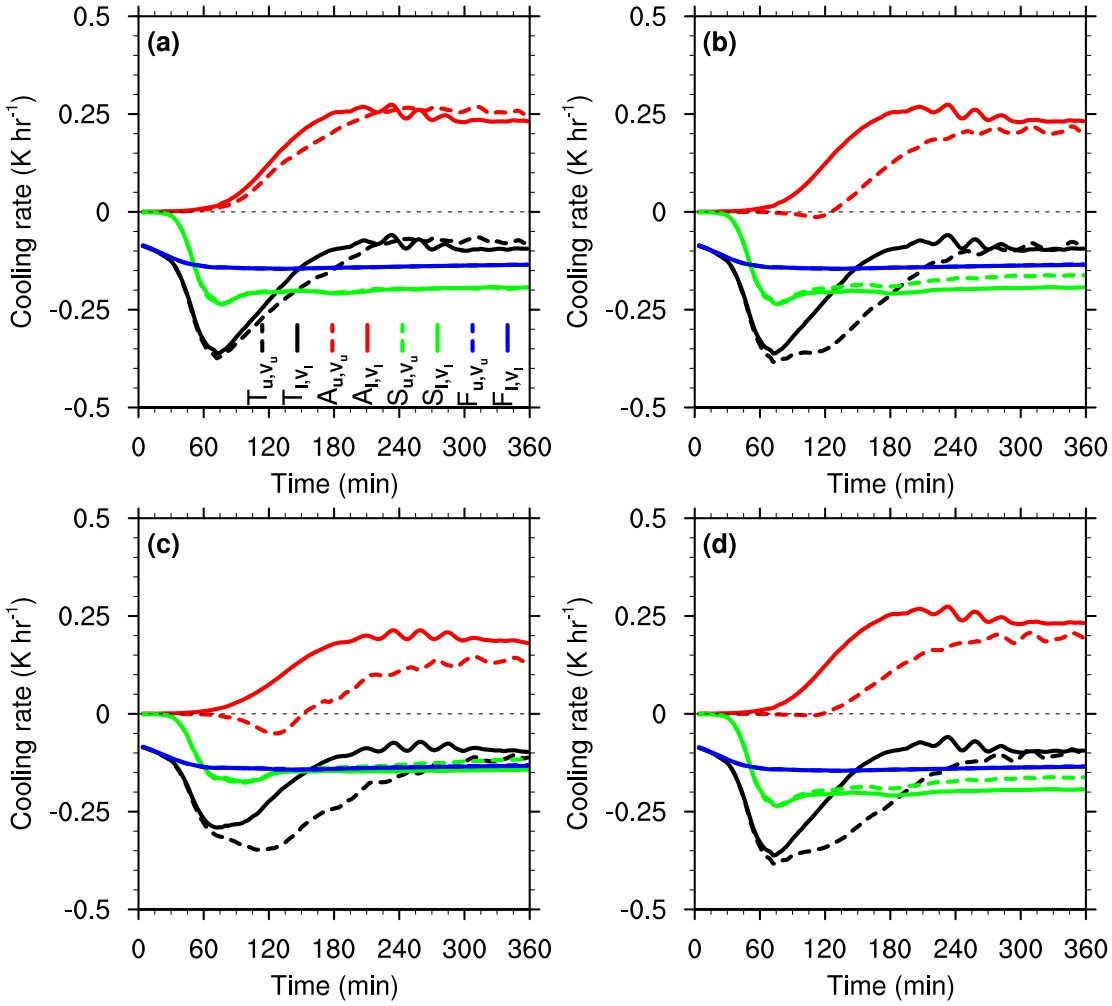

Figure IV.7: Time series of the valley-volume-averaged terms of the heat budget equation [T: (total) tendency; A: advection; S: surface sensible heat flux F: radiative flux divergence; see Eq. IV.8] for the upstream valley (*dashed line*) and the corresponding isolated valley opening directly on a plain (*continuous line*) for the **(a)** D1, I1; **(b)** P1, I1; **(c)** P2, I2; **(d)** P1b, I1 cases; see Table IV.1 and Sect. IV.2.2 for the definition of the simulations.

and I2). The control volumes over which the average is performed are defined in Sect. IV.2.5. The total cooling rate presents the same temporal evolution for all the cases: a transient regime characterized by a higher cooling rate, followed by a quasi-steady state with a lower cooling rate, which varies only slightly from case to case. As one would expect, the contribution of radiative flux divergence to the heat budget is not affected by the presence of the downstream valley, whatever the particular configuration considered. Hence, the differences in the temperature profiles observed in Fig. IV.3 are due to the differences in the advection and surface sensible heat flux contributions, which are affected by the orographic variations along the valley axis. The advection contribution from the SGS turbulent processes at the top of the valley atmosphere and lateral boundaries is found to be negligible compared to that from the resolved motions (not shown). The duration of the transient regime increases as γ

decreases (from the D1 to P2 cases; see Fig. IV.7a and Fig. IV.7c), thereby delaying the time when the advection contribution reaches a steady state. When the steady state is reached, the contributions from advection and surface sensible heat flux differ from case to case, but the sum of the two does not. This is because weaker down-valley flows lead to a reduction of the contributions from both advection and sensible heat flux (in absolute value). Hence, the cooling rate is almost equal for all the cases considered by the end of the simulated time period.

IV.5.2 Heat transport in and out of the valley

The heat fluxes that determine the heat transport in and out of $\mathcal{V}_u$ are those across the surfaces of V_u normal to the valley axis and across the upper surface of V_u. The calculation of the heat fluxes across the surfaces has to be done with respect to a physically-based reference temperature, in order to get a meaningful information [Lee et al., 2004]. Because the heat budget terms are averaged over the valley volume, the potential temperature averaged over that volume is used as the reference temperature.

Figure IV.8 displays time series of along-valley and vertical heat fluxes for $\mathcal{V}_u$, for the D1, P1, P1b, P2 cases and the respective reference cases (I1 and I2). For the I1 and I2 cases, the contribution from the net along-valley heat flux increases with time, and it is 82% and 88%, respectively, of the total advection contribution by the end of the simulated time period (see Fig. IV.8a and IV.8c). For the D1 case the along-valley heat flux is reduced, and it is 60% of the total advection contribution by the end of the simulated time period (see Fig. IV.8a). This indicates that the net export of colder air out of $\mathcal{V}_u$ by the down-valley flow is the most efficient heat transport mechanism for the draining and reference cases. However, the vertical heat flux plays a nonnegligible role for the D1 case, and it is increased by a factor of 2.4 compared to that for the respective reference case. For the pooling cases, the net along-valley heat flux accounts for 32% of the contribution from advection for the P1 and P1b cases and 15% for the P2 case at the end of the simulated time period (see Fig. IV.8b, Fig. IV.8c and Fig. IV.8d). This indicates that the import of warmer air at the valley top is the dominant heat transport mechanism for the pooling cases. Compared to those for the respective reference cases, the vertical heat flux is increased by a factor of 3.2 for the P1 and P1b cases, and by a factor of 5.3 for the P2 case.

The larger value of the vertical heat flux for the pooling and draining cases can be explained as follows: $\mathcal{V}_u$ for the pooling and to some extent the draining cases do not present significant anti-winds because of the deeper VBL. Hence, the mass in $\mathcal{V}_u$ for these cases is conserved only by downward vertical motions at the valley top. Using mass conservation in the upstream valley, it is inferred from Fig. IV.6 that the

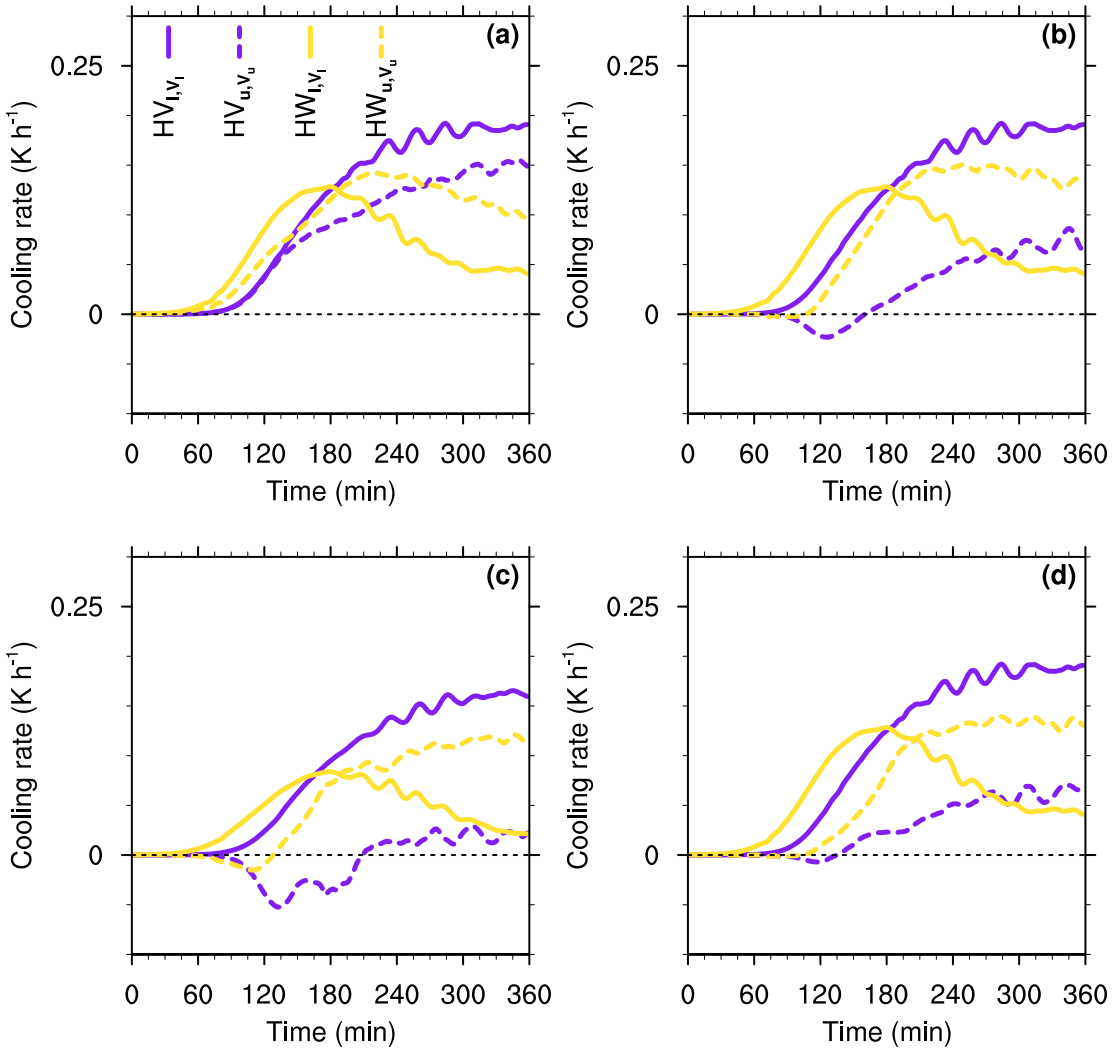

Figure IV.8: Time series of the horizontal and vertical heat fluxes across the surfaces of V_u [HV: horizontal (along-valley) heat flux; HW: vertical heat flux] for the upstream valley (*dashed line*) and the corresponding isolated valley opening directly on a plain (*continuous line*) for the **(a)** D1, I1; **(b)** P1, I1; **(c)** P2, I2; **(d)** P1b, I1 cases; see Table IV.1 and Sect. IV.2.2 for the definition of the simulations.

downward vertical mass flux is 1.8 times larger for the D1, P1 and P1b cases than for the I1 case and 2.5 times larger for the P2 case than for the I2 case. In addition, the V_u-averaged temperature is lower for the pooling and draining cases than that for the respective reference cases, hence the vertical heat flux calculated with respect to this reference temperature is larger, provided that the atmosphere is stably stratified and that the temperature at the valley top is the same for all the cases considered (as it is the case here; see Fig. IV.3). The increased downward vertical motions and larger temperature deficit combined, explain the larger vertical heat flux across the valley-top surface when compared with that of the respective reference cases. The same arguments can be used for the P2 case to account for the larger vertical heat flux relative to the net along-valley heat flux. In summary, when considering $\mathcal{V}_u$ for the

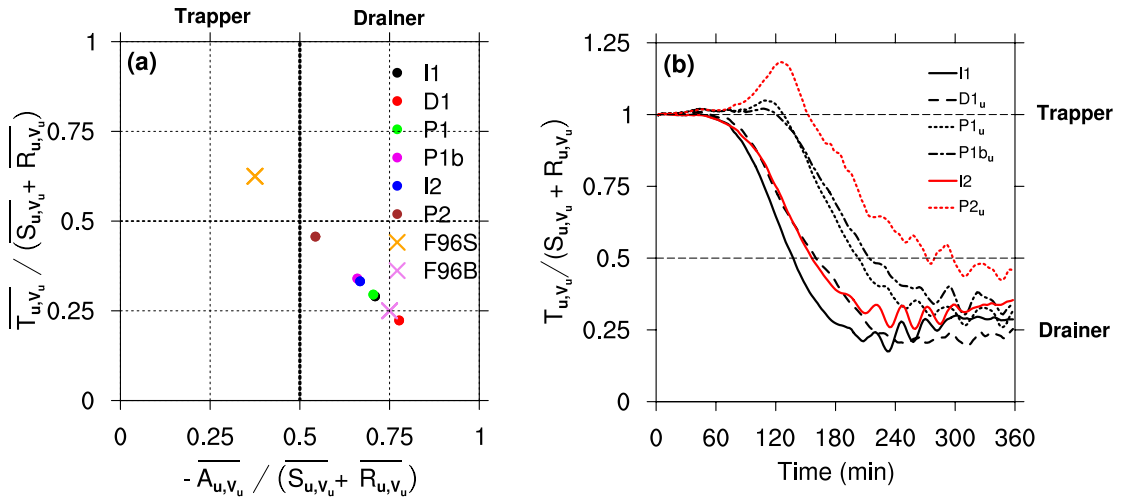

Figure IV.9: **(a)** Heat budget diagram based on Eq. IV.9 for the upstream valley, for all the configurations simulated; see Table IV.1 and Sect. IV.2.2 for the definition of the simulations. The terms of the heat budget are valley-volume- and time-averaged between $t = 300$ min and $t = 360$ min. For comparison, the values computed for the Colorado's Sinbad basin (F96S marker) and the Brush Creek valley (F96B marker) by Fast et al. [1996], averaged over the full nighttime period, are reported. **(b)** Time series of the ratio of the (total) tendency to the diabatic term for the upstream valley, with the terms of the heat budget averaged over the valley volume, for the I1 (*black solid line*), D1 (*black dashed line*), P1 (*black dotted line*), P1b (*black dashed-dotted line*), I2 (*red solid line*) and P2 (*red dotted line*) cases.

pooling and draining cases the net heat flux in the along-valley direction is reduced when compared to those for the respective reference cases, in particular during the transient regime, enhancing the V_u-averaged valley cooling during this time. This results in a stronger vertical heat flux at the valley top, which in turn advects warmer air diminishing the V_u-averaged valley cooling when a quasi-steady state is reached.

IV.5.3 Draining versus cooling efficiency

Further insight into the respective contributions of the diabatic and advective terms in the heat budget equation (Eq. IV.8) for $\mathcal{V}_u$ for the different cases considered can be obtained by comparing the cooling and draining efficiencies introduced in Eq. IV.9 and Eq. IV.10. Whiteman et al. [1996] proposed a comparison of draining efficiency versus cooling efficiency for the nighttime period, when a quasi-steady state is reached. This representation allows a direct and quantitative comparison with other valleys and basins. Figure IV.9a shows draining efficiency versus cooling efficiency with the terms of the heat budget valley-volume-averaged and time-averaged over the last hour of the simulations (i.e. between $t = 300$ min and $t = 360$ min), when the quasi-steady state is reached. As references, the nighttime values calculated for the Sinbad basin and the Brush Creek valley [Fast et al., 1996] are also displayed.

From Eq. IV.9, all cases are located on the main diagonal of Fig. IV.9a. $\mathcal{V}_u$ will be referred to as a drainer if the case belongs to the lower (right) quadrant, and as a trapper if it belongs to the upper (left) quadrant. The draining case D1 is characterized by a smaller value of the cooling efficiency than the I1 case during the quasi-steady state, indicating that the draining character of a valley is associated with a lower cooling efficiency. The value for the D1 case is very similar to the one computed for the Brush Creek valley, which was classified as a drainer by Whiteman et al. [1996]. Figure IV.9a indicates that the stronger the pooling character, the higher is the cooling efficiency of the valley. Yet, pooling configurations do not fall in the trapper quadrant, implying that a valley characterization based on the intra-valley TAF (γ) only can be misleading. For instance, the value of the cooling efficiency for $\gamma = 0.79$ (for the P2 case) is only 0.46 during the quasi-steady state, because the contribution from advection is still large compared to that from the diabatic term. It is worth reporting that the development of a down-valley flow does not prevent a valley from behaving as a trapper. Fast et al. [1996] indeed observed a considerable mass flux out of the Sinbad basin during the period of analysis, despite its trapper character.

The characterization of the valleys based on this diagram is valid strictly only when a steady-state is reached. Figure IV.9b shows time series of the cooling efficiency of $\mathcal{V}_u$ with the terms of the heat budget averaged over the valley volume. During the first two hours of the simulations (i.e. during the evening transition), all the valleys behave as a trapper, since the along-valley flow is not fully developed yet, then 'sliding down' on the diagram (as the cooling efficiency decreases), eventually reaching a position characterizing their quasi-steady state for the rest of the night. Once the cooling efficiency starts to decrease, the speed of the descent (the rate of change of the cooling efficiency) is remarkably independent of γ. However, a shift in time and a difference in amplitude are apparent between the different cases, which make both the position (on the diagram) of the steady state and the time to reach it, dependent on γ. It is worth noting that the I2 case presents a greater cooling efficiency than the I1 case during the entire simulated time period. However both cases behave as a drainer, implying that the valley width in the case of an isolated valley opening on a plain does not influence the drainer character of the valley. Finally, in this representation the P1b case hardly differs from the P1 case (taking into account that the ratio of the volumes of $\mathcal{V}_d$ and $\mathcal{V}_u$ for the P1b case is closer to that for the P2 case than that for the P1 case; see Table IV.1). Hence, for the range of values for γ considered, we can conclude that the intra-valley volume effect explains to a certain extent the influence of the downstream valley on the trapper or drainer character of the upstream valley.

IV.6 Along-valley variations of the heat budget

In the following sections, the cooling processes in the upstream and downstream valleys are compared, elucidating their impact on the heat budget of the valley system.

IV.6.1 Instantaneous heat budget of the upstream and downstream valleys

Figure IV.10 shows time series of the valley-volume-averaged terms of the heat budget (Eq. IV.8) and of the net along-valley and vertical heat fluxes across the surfaces of the volumes for $\mathcal{V}_u$ and $\mathcal{V}_d$, for the D1, P1 and P2 cases, and the total cooling (tendency term) averaged over the plain volume. For $t < 60$ min, Fig. IV.10c and Fig. IV.10e show that for the pooling cases (P1 and P2), $\mathcal{V}_d$ experiences a stronger cooling than $\mathcal{V}_u$. This stronger cooling stems from the cooling contribution from the surface sensible heat flux, which is larger in the narrower valley because of the smaller valley volume. During this time period, the warming effect from advection has not started yet (see Fig. IV.10c and Fig. IV.10e). Hence, the atmosphere is cooler in $\mathcal{V}_d$ than in $\mathcal{V}_u$, forcing the up-valley flow from $\mathcal{V}_d$ to $\mathcal{V}_u$ (most noticeable for the P2 case).

After this initial period and for the rest of the simulated time, the surface sensible heat flux contribution to the valley heat budget for $\mathcal{V}_u$ and $\mathcal{V}_d$ evolves similarly in time, whatever the case considered, with an almost constant offset between the two. The sign of this offset is reversed for the pooling and draining cases, because the surface sensible heat flux is larger in the narrower valleys.

With regard to the advection contribution, its temporal evolution differs from case to case. For the draining case D1, the advection contribution for $\mathcal{V}_d$ follows that for $\mathcal{V}_u$ (see Fig. IV.10a), with a slightly greater warming in $\mathcal{V}_u$ than in $\mathcal{V}_d$ after $t \simeq 90$ min. This can be explained as follows: the along-valley heat flux hardly varies between $\mathcal{V}_u$ and $\mathcal{V}_d$ (see Fig. IV.10b); by contrast, at the end of the simulated time period, the vertical heat flux at the valley top is about 2 times larger in $\mathcal{V}_u$ than in $\mathcal{V}_d$, these fluxes being smaller than their along-valley counterparts by a factor of 1.5 (in $\mathcal{V}_u$) and 3 (in $\mathcal{V}_d$).

For the pooling cases the advection contribution for $\mathcal{V}_d$ increases rapidly during the transient regime (after 60 min; see Fig. IV.10c for the P1 case and Fig. IV.10e for the P2 case), because of the transport of cold air out of $\mathcal{V}_d$ by the down-valley flow towards the plain and the up-valley flow towards $\mathcal{V}_u$, and the resulting downward transport of warm air at the valley top (see Fig. IV.10d and Fig. IV.10f). For $\mathcal{V}_u$, the advection contribution becomes positive and increases after $t \simeq 120$ min for the P1 case and $t \simeq 150$ min for the P2 case. This is due to the vertical heat flux that increases rapidly at those times, while the along-valley heat flux is negative. The difference between

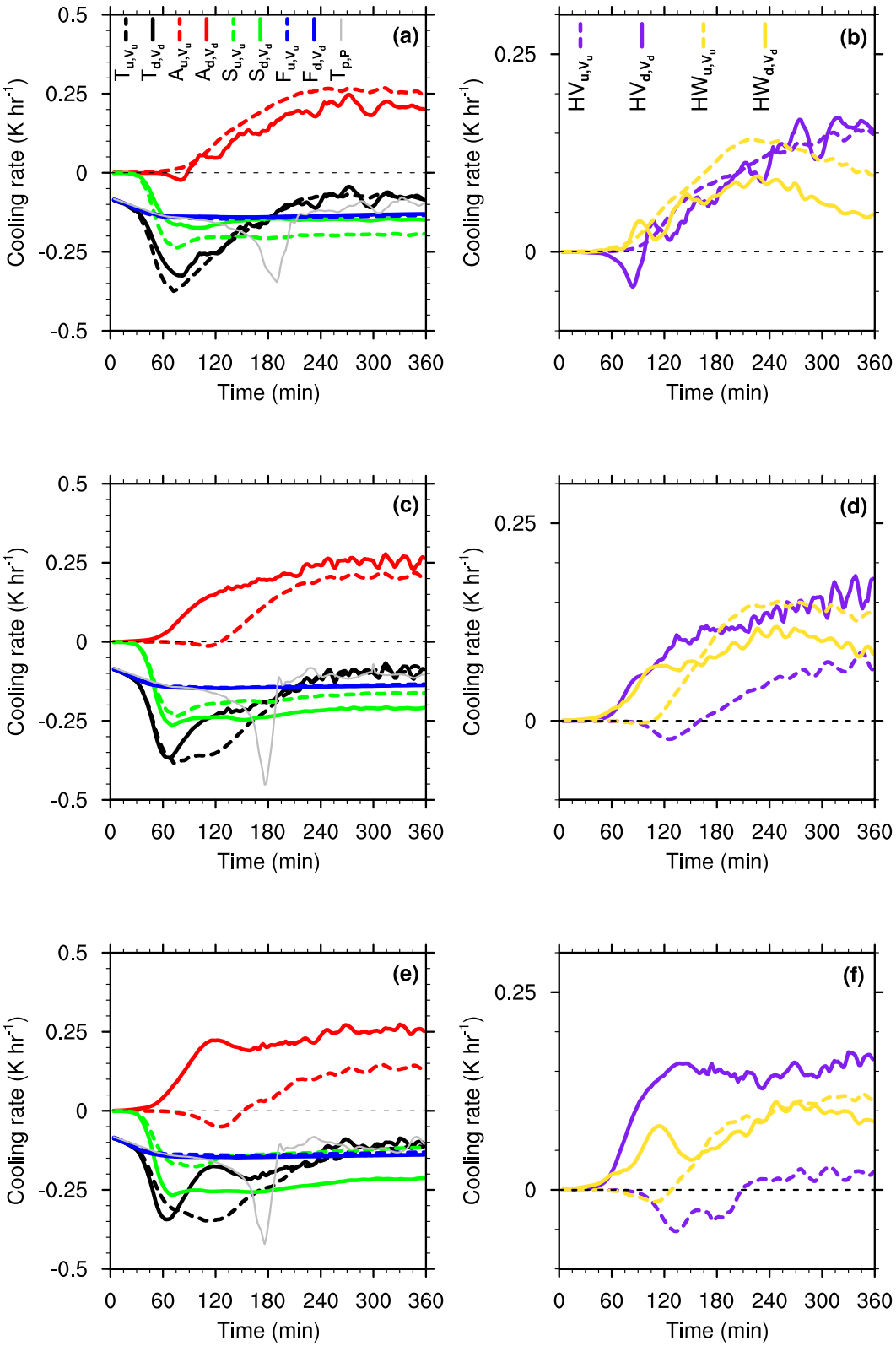

Figure IV.10: Time series of the terms of the valley heat budget (see Eq. IV.8) and horizontal and vertical heat fluxes across the surfaces of V_u and V_d [HV: horizontal (along-valley) heat flux; HW: vertical heat flux] for the upstream (*dashed line*) and downstream (*continuous line*) valleys, respectively, for the **(a)** D1, **(b)** P1 and **(c)** P2 cases; see Table IV.1 and Sect. IV.2.2 for the definition of the simulations. The grey line corresponds to the total cooling (tendency term) for the plain volume, defined by $-(L_{x,u} + S_{x,u}) < x < (L_{x,u} + S_{x,u})$, $30 < y < 32$ km and $h_0 < z < H + h_0$.

the advection contributions for $\mathcal{V}_u$ and $\mathcal{V}_d$ exceeds that between the surface sensible heat flux contributions for $60 < t < 185$ min for the P1 case and $70 < t < 210$ min for the P2 case, leading to a higher cooling rate in $\mathcal{V}_u$. This leads to a reversal of the pressure gradient and so a down-valley flow develops from $\mathcal{V}_u$ to $\mathcal{V}_d$.

When a quasi-steady state is reached, for the P1 case, the vertical heat flux is 50% larger in $\mathcal{V}_u$ than in $\mathcal{V}_d$, while the along-valley heat flux in $\mathcal{V}_u$ is about 2.5 smaller that in $\mathcal{V}_d$. For the P2 case the vertical heat flux is 30% larger in $\mathcal{V}_u$ than in $\mathcal{V}_d$, while the along-valley heat flux in $\mathcal{V}_u$ is about 8 times smaller that in $\mathcal{V}_d$. This shows that the difference between the advection contribution for $\mathcal{V}_u$ and $\mathcal{V}_d$ for the pooling cases is due largely to the reduction of the along-valley heat flux in $\mathcal{V}_u$.

The development of the down-valley flow leads to the homogenization of the cooling rate in the along-valley direction after 210 min, whatever the case considered. This homogenization of the cooling rate results from a balance between advection and surface sensible heat flux: a greater contribution from advection for $\mathcal{V}_u$ than for $\mathcal{V}_d$ (as for the D1 case) goes along with a greater (in absolute value) contribution from the surface sensible heat flux. Conversely, when the contribution from advection is smaller for $\mathcal{V}_u$ than for $\mathcal{V}_d$ (as for the P1 and P2 cases), the contribution from the surface sensible heat flux is also smaller (in absolute value). These aspects are discussed in the next section using volume arguments.

IV.6.2 Time-integrated valley heat budget

The left column of Fig. IV.11 shows the along-valley variability of the cooling processes, using the ratios of the time-integrated terms of the heat budget of $\mathcal{V}_u$ to those of $\mathcal{V}_d$ weighted by the plain volume (see Eq. IV.13), for the D1, P1 and the P2 cases. The time integration starts at the beginning of the simulation. For all the cases the ratio R_C of the sum of the diabatic forcing terms for $\mathcal{V}_u$ to that for $\mathcal{V}_d$ hardly differs from one after a rapid adjustment at the beginning of the simulations (first 30 min). This suggests that, for the range of parameters considered, the heat loss from the diabatic term, weighted by the volumes of the respective equivalent plains, is unchanged along the valley axis. The advection contribution to the heat budget is similar (and almost negligible) for $\mathcal{V}_u$ and $\mathcal{V}_d$ during the initial period ($t < 60$ min for the pooling cases, $t < 100$ min for the draining case; see Fig. IV.10). Hence, the lower (higher) cooling rate in $\mathcal{V}_u$ with respect to that in $\mathcal{V}_d$ for the pooling (draining) cases is in large part explained by the intra-valley volume effect. This result holds also for the P1b case (not shown). However, it should be noted that R_C decreases slightly with time for the pooling cases (see Fig. IV.11c and Fig. IV.11e) because of the weaker down-valley wind speed in $\mathcal{V}_u$, which reduces the surface sensible heat flux and so the surface sensible heat flux component of R_C. The importance of this process for values of γ smaller

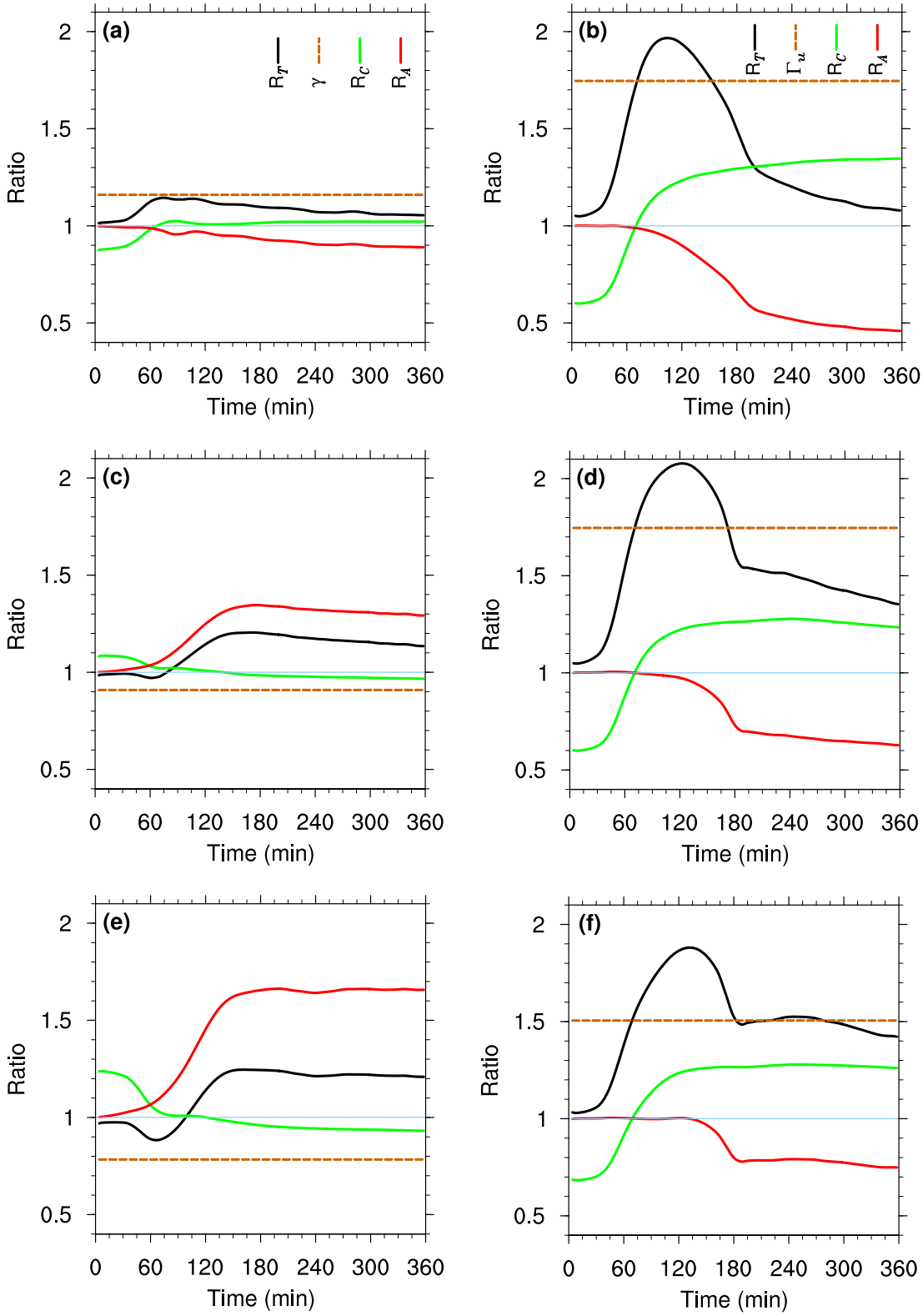

Figure IV.11: Left column: ratios of the time-integrated terms of the heat budget of the upstream valley to those of the downstream valley (see Eq. IV.13), for the **(a)** D1, **(c)** P1 and **(e)** P2 cases; see Table IV.1 and Sect. IV.2.2 for the definition of the simulations. Right column: the same ratios, but considering the upstream valley and the plain, (see Eq. IV.14), for the **(b)** D1, **(d)**P1 and **(f)** P2 cases. The plain volume is defined as in Fig. IV.10.

than the ones considered in this study needs to be evaluated in future work.

The ratio of the advection contributions to the valley heat budget for $\mathcal{V}_u$ and $\mathcal{V}_d$ (R_A) may be interpreted as follows: recalling the change in the cooling efficiency of valleys of different widths, wider valleys are characterized by a higher cooling efficiency when compared to narrower valleys, for the range of parameters studied (see the position of the I1 and I2 cases in Fig. IV.9a), yielding $R_A < 1$ for the D1 case (see Fig. IV.11a) and $R_A > 1$ for the P1 case (see Fig. IV.11c) and the P2 case (see Fig. IV.11e). It is worth noting that for the pooling cases the product $\gamma\, R_A$ is larger than 1; since $R_C \simeq 1$, this leads to a larger temperature change from $t = 0$ in $\mathcal{V}_u$ than in $\mathcal{V}_d$ (R_T), forcing the development of the down-valley flow from $\mathcal{V}_u$ to $\mathcal{V}_d$.

The right column of Fig. IV.11 shows the variability of the cooling processes in $\mathcal{V}_u$ with respect to the plain, using the same ratios used for the left column, but considering the plain volume instead of $\mathcal{V}_d$ (see Eq. IV.14), for the same cases (D1, P1 and P2). As already shown by Schmidli and Rotunno [2010] for a valley-plain configuration, the higher cooling experienced by the valley with respect to the plain during the transient regime can be in large part explained by the valley-volume effect. However, as opposed to the intra-valley analysis, R_C substantially differs from one. As shown by Arduini et al. [2016], downslope flows are the main driver of the surface sensible heat flux, so that the contribution of the surface sensible heat flux to the heat budget is necessarily different between the valley and the plain for quiescent synoptic conditions. After the down-valley flow has developed, the thermally-driven circulation acts in order to reduce the temperature contrast between the valley and the plain, through the advection term (R_A, smaller than one), which can be thought as the result of the transfer of cold air from the valley to the plain. This process is most efficient for the D1 case, where $R_A = 0.46$ by the end of the simulated time period (see Fig. IV.11b), leading to a nearly constant temperature difference between the valley and the plain of about 10%. This process is less effective as γ decreases (from the D1 to P2 cases; see Fig. IV.11c and Fig. IV.11e), because the heat transfer from $\mathcal{V}_u$ to the plain volume is reduced by the valley constriction. Interestingly, for the P2 case the temperature difference between $\mathcal{V}_u$ and the plain follows Γ once the down-valley flow has developed (that is after $t \simeq 180$ min); this is the result of the product $R_A\, R_C$ being almost equal to 1.

IV.7 Conclusions

The purpose of this work was to quantify the impact of along-valley variations of the valley width on the nocturnal boundary-layer structure of deep valleys, considering systems of two valleys, one upstream, one downstream, opening on a plain. The work shows that the dynamical and thermodynamical properties of the nocturnal valley

boundary layer of a valley section are strongly affected by the valley width of the neighbouring valleys. Three main configurations are considered: a draining case, a moderate pooling case and a strong pooling case, which are compared to reference cases for which the upstream valley opens directly on a plain. The key findings, for the range of parameters considered, are summarized below for the upstream valley, unless otherwise stated:

- Draining and pooling configurations induce deeper and colder valley boundary layers compared to valleys opening directly on a plain (see Fig. IV.3). This effect is more pronounced for the pooling configurations.

- The along-valley variations of the valley width lead to a general decrease of the low-level down-valley wind speed when compared to a valley-plain configuration. This reduction of the wind speed results from a reduction of the along-valley pressure gradient that ultimately drives the down-valley flow (see Fig. IV.4a and Fig. IV.4b). The deeper valley boundary layer in the pooling configurations leads to a deeper down-valley flow, with no anti-winds up to the plateaux, as opposed to the valley-plain configuration. Because of the absence of anti-winds, the net mass flux out of the valley is higher in pooling and draining configurations when compared to the corresponding valley-plain configurations (see Fig. IV.6), although the low-level down-valley wind is reduced by a factor of 2. For the strong pooling configuration, the mass flux is up-valley during the early night, leading to an inflow of air from the downstream to the upstream valley.

- For all the configurations considered, a steady state is reached, but the duration of the transient regime depends on the configuration. This duration is shortest for the draining and valley-plain configurations. For the pooling configurations, it increases as the valley becomes narrower in the down-valley direction (that is the intra-valley topographic factor γ decreases). As pointed out by previous studies [e.g. Burns and Chemel, 2015; Arduini et al., 2016], the growth of the valley boundary layer is mainly controlled by the vertical motions induced by downslope flows within the valley centre. Hence, the transient regime is responsible for the differences in the thermal structure of the atmosphere of the different valleys.

- For the draining configuration the cooling processes in the upstream valley are comparable to those of the corresponding valley-plain configuration, and so are hardly affected by the presence of the downstream valley (see Fig. IV.7a). For the pooling configurations the cooling rate is about 50% larger than that of the corresponding valley-plain configurations during the transient regime, because of the reduction of the along-valley and vertical heat fluxes during this time period (see Fig. IV.8b, Fig. IV.8c and Fig. IV.8d). When a steady state is reached, the

advection contribution to the valley heat budget leads to a warming of the valley atmosphere. It is dominated by the along-valley heat flux for the draining and valley-plain configurations and by the vertical heat flux at the valley top for the pooling configurations.

- By comparing the quasi-steady state for the upstream valleys, we conclude that a pooling valley is not necessarily a 'trapper' in the Whiteman et al. [1996] classification (see Fig. IV.9a), this classification being strictly valid only when a steady state is reached. In other words, $\gamma < 1$ is not a sufficient condition to have a trapper for the entire night. Note that, when examining the trapper or drainer character of the valley during the evening transition, namely before the steady-state is reached, all the valleys behave as trappers, then evolve towards a drainer state when the down-valley flow develops (see Fig. IV.9b). It is found that, as soon as the down-valley flow develops, the rate at which the steady state is reached is independent of γ, while the time when the down-valley wind develops and the cooling rate during the quasi-steady state are dependent on γ.

- The effect of the along-valley flow is to reduce the horizontal temperature gradients resulting from the variations of the valley width along the valley axis. Once the down-valley flow is fully developed, all valleys present a homogeneous cooling rate in the along-valley direction (see Fig. IV.10). The diabatic forcing term of the valley heat budget (defined as the sum of the radiative flux divergence and the surface sensible heat flux), when weighted by the volume of the respective equivalent plains, hardly varies between different valley sections [as was assumed in McKee and O'Neal, 1989], with minor differences resulting from the differences in the down-valley wind speed between the two adjacent valleys (see Fig. IV.11, left column). Therefore the difference in the temperature change from $t = 0$ between the two valley sections is driven by that during the transient regimes in the two valleys. Hence, it is driven by the value of γ and the ratio R_A of the advection contribution (to the valley heat budget) for $\mathcal{V}_u$ to that for $\mathcal{V}_d$: $\gamma > 1$ and $\mathrm{R}_A < 1$ for the draining configuration, and $\gamma < 1$ and $\mathrm{R}_A > 1$ for the pooling configurations. Since for the pooling configurations the product $\gamma\,\mathrm{R}_A$ is larger than 1, the valley boundary layer in the upstream valley is colder than that in the downstream valley (after the dynamics in the valleys are established) leading to the formation of the down-valley flow from the upstream to downstream valleys.

- For the considered quiescent synoptic conditions, the assumption that the diabatic forcing term has the same amplitude within the valley and over the plain is not valid during nighttime for the deep valley considered here. Indeed, the

diabatic forcing term is larger within the valley than over the plain, thus enhancing the temperature contrast between the valley and the plain (see Fig. IV.11, right column). The development of the down-valley flow reduces this temperature contrast. This reduction cannot be explained by the valley-volume effect. It is slowed down for the pooling configurations because of the reduced heat flux out of the valley. It is found that for the strong pooling configuration the valley-volume effect explains the differential cooling between the valley and the plain once the down-valley flow has developed. In the absence of significant dynamical processes, the valley-plain (bulk) temperature differences can possibly be quantified by the topographic amplification factor. Our results also suggest that this condition can be reached in a valley subject to dynamical processes, when the cooling resulting from the surface sensible heat flux within the valley compensates the warming due to advection; the along-valley constriction is key to reaching this balance.

The results reported here concern a small fraction of possible configurations. Other parameters of particular importance that have not been considered in this study include the shape of the cross-valley slopes along the valley axis and the height of the terrain, which would both affect the topographic amplification factor of the valley (valley-volume effect) and downslope flows (dynamical effects). A characterization of the effects of the full range of orographic variations along the valley axis is needed in order to understand and predict the evolution of the boundary layer of a particular valley section.

Acknowledgments

This work has been supported by a PhD grant provided by the LabEx Osug@2020 (Investissements d'avenir – ANR10LABX56) in Grenoble and by the University of Hertfordshire. Numerical simulations were run on the French national HPC facilities at CINES.

V

Local and non-local controls on a persistent cold-air pool in the Arve River Valley

---

Chapters III and IV demonstrated that the vertical and along-valley transport of mass and heat in a valley can be largely modified by the surrounding terrain under dynamically decoupled conditions. Building up on the process-level understanding developed in the idealised framework, a case-study of a persistent cold-air pool event in a section of the Arve River Valley, in the French Alps, is considered in this chapter. The objective is to quantify the effects of tributary valleys on the heat and mass budgets of the atmosphere of a real valley under weak synoptic winds. This section of Valley is characterised by three major tributaries and a variation of the valley floor width along the valley axis from about 2000 m upstream to approximately 200 m close to the valley exit, where the Valley opens on the southern part of the wide Swiss Plateau. The study relies on the dataset collected during the PASSY-2015 field campaign, a field experiment that was held in this section of the Valley during the winter of 2014-2015.

This chapter is a reproduction of a manuscript submitted to the *Quarterly Journal of the Royal Meteorology Society*.

Abstract A numerical model is used to simulate a persistent cold-air pool event that occurred in the section of the Arve River Valley around Passy in the French Alps. During this period, an upper-level ridge from the Atlantic moved over Europe, allowing a CAP to form and persist over time. The impact of the upper-level ridge on the cold-air pool and the dynamics within the valley section is quantified, by examining the mass and heat budgets of the valley atmosphere. During the persistent stage the flows through the tributary valleys together with subsiding motions at the valley top,

control by and large the nighttime valley-scale circulation and thermal structure of the cold-air pool, while thermally-driven valley flows play only a minor role. When the upper-level ridge passes over the Arve River Valley, warm air advection through the tributaries displace the upper-layer of the cold-air pool out of the valley during nighttime, thereby reducing the depth of the CAP. The near-surface atmosphere over the valley floor shows a variability from day to day during the persistent stage of the cold-air pool. When the upper-level ridge passes over the valley, down-valley flows export the air mass out of the valley. As the ridge moves away from the valley, the near-surface air is trapped within the valley. This trapping is the result of the channelling of the large-scale flow, which leads to a reduction of the near-surface horizontal pressure difference along the valley axis, thereby suppressing the near-surface down-valley flow. The study highlights the importance of the tributary valleys in the evolution of the persistent cold-air pool. In particular, the direction of the flow through one of the tributaries is found to be determined by the height of the cold-air pool with respect to that of the tributary above the valley floor.

V.1 Introduction

A cold-air pool (CAP) is a stably stratified layer of air confined towards the bottom of a valley or basin. Diurnal CAPs form frequently during nocturnal hours under clear-sky and weak synoptic wind conditions and are destroyed following sunrise by convection resulting from surface heating. When relatively warm air associated with anticyclonic conditions is transported immediately above deep terrain over multiple days [Reeves and Stensrud, 2009], convection is often insufficient to destroy the stable layer, particularly during wintertime [see for instance Vrhovec and Hrabar, 1996; Lu and Zhong, 2014], allowing a persistent cold-air pool (PCAP) to develop. Since a PCAP is characterised by a long-lasting (multi-day) valley inversion and weak winds, air pollutants and moisture emitted within the CAP are trapped and accumulate from day to day, thereby affecting air quality [Chemel et al., 2016; Largeron and Staquet, 2016a] and visibility when fog forms. The removal of the PCAP may occur because of the advection of a synoptic disturbance within the valley [Zhong et al., 2001], turbulent erosion of the CAP from the top [Lareau and Horel, 2015b] or the displacement of the cold-air layer out of the valley [Flamant et al., 2006]. While the formation, persistence and destruction stages are common to PCAP in many different regions and conditions [Zhong et al., 2001; Zängl, 2005; Lareau et al., 2013b; Lu and Zhong, 2014; Largeron and Staquet, 2016b], the characteristics of the CAP (depth and strength) during each stages depend largely on the characteristics of the surrounding terrain and variability of the synoptic conditions. Thereafter a distinction is made between the processes that control the characteristics of the CAP and are governed by those of the terrain at the

valley or basin scale, which are referred to as *local* controls, and processes affecting the CAP characteristics but occurring at scales larger than that of the valley (i.e. synoptic winds above the valley boundary layer or flow intrusion from neighbouring valleys and tributaries), which are referred to as *non-local* controls.

Previous work has considered local controls on CAPs. Vrhovec [1991] showed using results from numerical simulations of a diurnal CAP in the Slovenj Gradec basin that a dynamical decoupling can take place between the flow within the valley boundary layer and the synoptic flow aloft. As a result, at the top of the CAP an abrupt change in wind speed and direction was observed. In such decoupled condition thermally-driven along-slope and along-valley flows are the key dynamical features of the valley atmosphere [Largeron and Staquet, 2016a]. However, much remains to be understood on their role in the formation and evolution of CAPs [Bodine et al., 2009]. In a numerical modelling case study of the formation of a CAP in a $\sim$ 100-m deep narrow valley, Vosper et al. [2014] concluded that the principal mechanism responsible for the formation of the CAP was the sheltering effect of the valley. The sheltering was shown to increase the turbulent heat flux divergence close to the ground compared to a less sheltered region (i.e. hilltop sites), thereby increasing near-surface cooling and promoting the formation of a ground-based inversion. However, in such a shallow valley, thermally-driven flows are rapidly suppressed after the evening transition [Clements et al., 2003; Vosper et al., 2014]. In a deep and narrow valley dynamically decoupled from the atmosphere above, downslope flows can persist for a longer time, reaching a quasi-steady state if a down-valley flow can develop during the night [Burns and Chemel, 2015; Arduini et al., 2016]. Under these conditions, downslope winds are the main driver of the sensible heat flux divergence, which enhances the cooling of the valley atmosphere with respect to a flat region nearby. Downslope flows are also important in the evolution of the thermal structure of the upper-part of a CAP, through the vertical transport induced by the air flowing down the slopes [Whiteman, 1982; Kiefer and Zhong, 2011; Burns and Chemel, 2015; Arduini et al., 2016].

In addition to thermally-driven flows, the variations of the orography and surface properties affect the evolution of a CAP. Because of the reduction in the volume of atmosphere in a valley or basin when compared to that over a flat terrain, a valley or basin experiences a cooling stronger than if it were a flat terrain for the same amount of heat loss [Whiteman, 1990]. A differential cooling can also take place between different sections of the same valley because of along-valley geometrical variations [McKee and O'Neal, 1989]. This differential cooling can lead to along-valley flows that are up-valley instead of down-valley during the night [Arduini et al., 2017], affecting the mass and heat budgets of the valley atmosphere. If the ground is covered by snow (as is common in winter in alpine regions), surface albedo is increased and the heat conductivity to the ground is significantly decreased, leading to stronger ground-based

inversions [Zängl, 2005a; Billings et al., 2006; Neemann et al., 2015].

Non-local controls on CAPs have been examined for a number of case studies. Zhong et al. [2001] showed that the formation and maintenance of a PCAP event in the Columbia basin in the Pacific Northwest region of North America was primarily the result of the continuous advection of warm air immediately above the basin by strong westerly winds descending the lee slopes of the surrounding Cascade mountains. Similar results as regards the importance of large-scale advection of warm air above the terrain in the formation and maintenance of a PCAP in the Salt Lake Valley, Utah, USA, were reported by Wei et al. [2013]. Lu and Zhong [2014] quantified the respective contributions of the different terms determining the heat budget of the atmosphere during this PCAP event. Large-scale advection was found key to the formation, maintenance and destruction of the PCAP. While these studies have demonstrated the essential role of warm air advection in the formation and maintenance of a PCAP, the dynamical controls of large-scale flows on the temporal evolution of CAPs have received less attention.

In a numerical modelling case study Zängl [2005] showed the importance of the direction of the synoptic pressure gradient and of the along-valley terrain geometry, with respect to the Alpine foreland, in the maintenance of CAPs in a deep Alpine valley system. Model results indicated that the direction of the synoptic pressure gradient controlled the direction of the along-valley drainage flows. The author concluded that, for that particular case study, the ideal conditions for cold-air pooling are met when the synoptic pressure gradient is orientated down a constriction in the along-valley direction. In a following work based on semi-idealised numerical simulations and observations, Zängl [2005b] extended this analysis to the shallower Bavarian Danube basin. Model results showed that advection resulting from the synoptic pressure difference (pressure-driven channelling) and advection down the direction of the synoptic wind (forced-channelling) can both act to remove the PCAP, depending on the direction of the synoptic wind with respect to the orientation of the highest mountain range. Another dynamical mechanism that may affect the temporal evolution of CAPs is shear-induced turbulent mixing at the top of the CAP due to strong winds aloft. Some studies questioned the effectiveness of such turbulent erosion for the destruction of CAPs over time-scales shorter than one day [see for instance Zhong et al., 2001, 2003]. However, semi-idealised numerical simulations analysed by Zängl [2005b] suggested that this mechanism can contribute significantly to the destruction of a CAP in the relatively shallow Danube basin. In deep valleys, idealised simulations by Lareau and Horel [2015b] indicated that CAPs can be removed by turbulent erosion on a time-scale of less than a day, provided that the speed of the flow aloft increases continuously with time such that the Froude number exceeds a threshold value of about 2.

The contribution of tributary flows in the mass budget of a valley was studied

extensively as part of the Advanced Studies in Complex Terrain (ASCOT) programme [Clements et al., 1989a]. However, the computation of mass fluxes through tributaries relied solely on limited observations, and so several assumptions and approximations had to be made to estimate their contributions to the mass budget. Porch et al. [1989] calculated that the mass flux through a single tributary may account for 5 to 15% of the drainage out of Brush Creek Valley, Colorado, USA. Assuming a similar contribution from all the tributaries of Brush Creek Valley, the authors estimated that tributary flows control by and large the mass budget of the valley, and so that the contribution of slope flows and subsiding motions at the valley top are only minor. Numerical model simulations reported by O'Steen [2000] for an idealised valley-tributary system under dynamically decoupled conditions confirmed that the flow through the tributary can increase the along-valley mass flux by 5 to 10% compared to an idealised valley without a tributary. However, some of the complex interactions between the tributary flow and the down-valley flow were not captured with this idealised configuration. Coulter et al. [1989] showed that the mass flux through the tributary is extremely sensitive to the external flow. Under particular synoptic conditions the drainage from the tributary was found 20% larger than that expected if the mass flux was assumed proportional to the drainage area. Coulter et al. [1991] examined the mass fluxes through three tributaries of Kimball Creek, Colorado, and showed that the mass flux is largest for the tributary most closely aligned with the valley axis. Despite the efforts led in the ASCOT programme, large uncertainties remain about the effects of tributary flows on the heat and mass budget of a valley atmosphere.

In this paper, we investigate local and non-local controls on a PCAP that formed in the section of the Arve River Valley around Passy in the French Alps, in February 2015 using numerical model simulations. This PCAP event occurred during the first intensive observation period (IOP1) of the PASSY-2015 field campaign [Paci et al., 2015a; Staquet et al., 2015]. In Sect. V.2, we present the design of the numerical simulations. Sect. V.3 provides an overview of the synoptic conditions during IOP1. Model results are analysed in Sect V.4 to V.6. A summary and conclusions are presented in Sect. V.7.

V.2 Methodology

V.2.1 The Passy Valley

The Arve River Valley is located in the French Alps south of the Swiss Plateau, located between the Jura mountain range and the Swiss Alps (see Fig. V.1a). Thereafter the Passy Valley refers to the section of the Arve River Valley enclosed by the dashed black polygon in Fig. V.1b. The mean height of the terrain along the polygon defin-

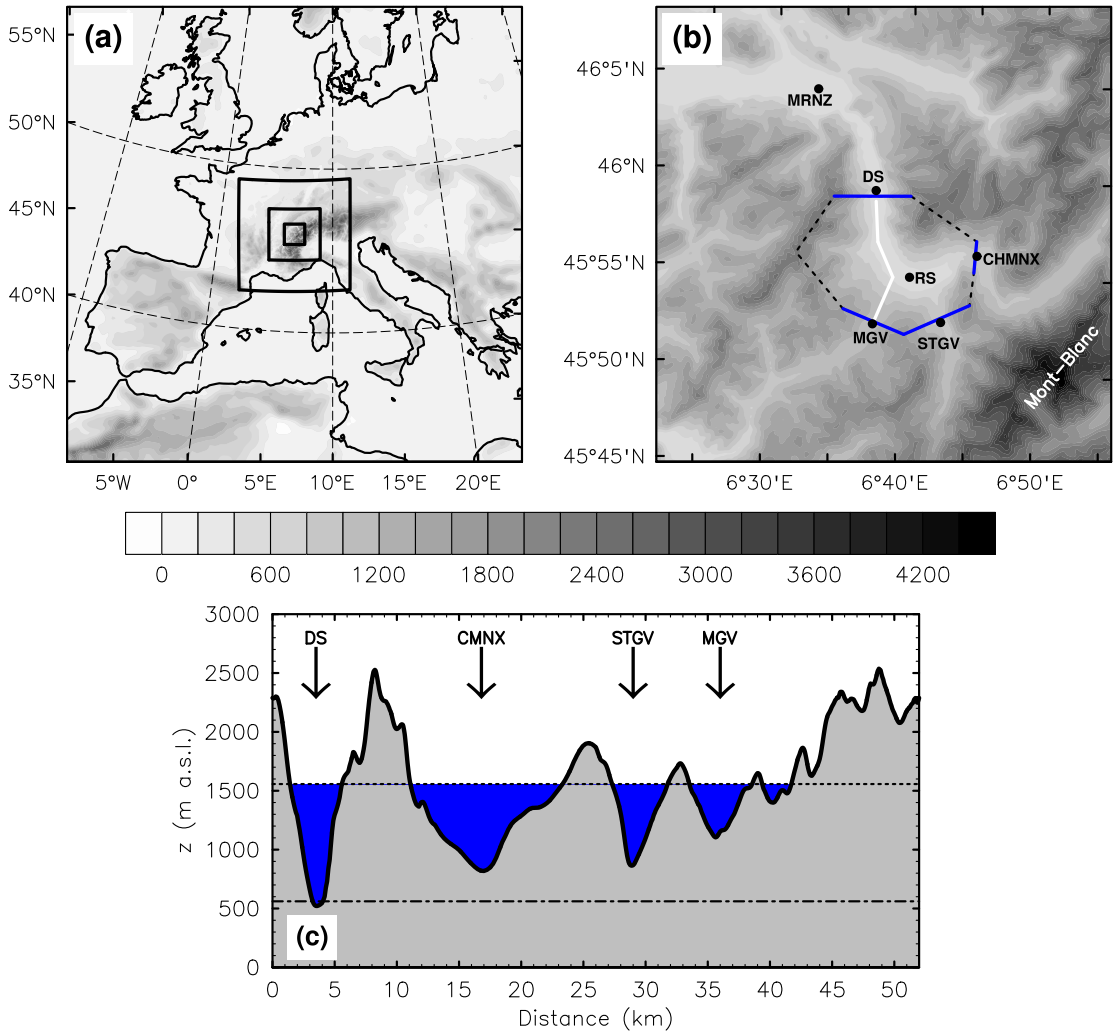

Figure V.1: (a) Topographic map of domain d01 with the positions of the nested domains d02, d03 and d04 represented by boxes. (b) Topographic map of the innermost domain d05; the dashed black polygon indicates the horizontal extent of the PASSY control volume, the white line indicates the path of cross-sections used in the paper; mass and heat fluxes are calculated across 'gates' represented by the blue lines; the position of selected sites are labelled in bold: radiosounding site (RS), downstream part of the valley (DS), Megève (MGV), Saint-Gervais-les-Bains (STGV), Chamonix (CHMNX) and Marnaz (MRNZ). (c) Terrain height along the polygon defining the PASSY control volume; the dotted line indicates the mean height of the terrain along the polygon; the dashed-dotted line is the height of the RS site; see text for details.

ing the PASSY control volume is $z_m = 1560$ m a.s.l. (see Fig. V.1c), and the highest massif surrounding the Arve River Valley is Mont-Blanc, culminating at 4808 m a.s.l. The valley-floor elevation decreases gradually down-valley from 588 m a.s.l. at Passy [upstream of the radiosounding site (RS)] to 488 m a.s.l. at Marnaz (MRNZ) over a distance of about 23 km. The width of the valley floor along this section of the valley increases gradually up-valley from just about 200 m upstream of MNRZ, where the valley presents a major constriction, to approximately 2000 m near the location of the RS site, and hardly decreases from there towards the escarpment leading to

Chamonix (CHMNX). The Passy valley presents three major tributaries leading to Megève (MGV), Saint-Gervais-les-Bains (STGV) and CHMNX (see Fig. V.1c).

V.2.2 Terrain representation and snow initialisation

An accurate representation of the terrain is essential to numerical modelling in truly complex terrain such as alpine valley systems. Most alpine valleys are characterised by steep slopes that are a challenge for numerical models formulated using terrain-following coordinates, as is the case for the Weather Research and Forecasting (WRF) model used here. Even at horizontal resolutions of the order of 3 km, slope angles exceed 25°across the Alpine chain of Western Europe. At a horizontal resolution of 100 m, the maximum slope angle in the Arve River Valley is about 75°. In the present work, 90-m terrain elevation data from the Shuttle Radar Topography Mission [SRTM, Farr et al., 2007] were carefully interpolated at the horizontal resolutions of the nested model domains (see Fig. V.1a). A smoothing filter was used to reduce the largest slope angles of the terrain to a maximum slope angle $\alpha_{\max} = 45°$ while minimising any changes in the overall shape and small-scale features of the valley geometry.

Several studies have pointed out that the presence of snow on the ground surface alters significantly surface–atmosphere interactions [Zängl, 2005a; Neemann et al., 2015; Tomasi et al., 2014]. The initialisation and modelling of the snow pack are difficult tasks. Numerical model reanalysis products are currently available at too coarse a resolution ($\sim$ 15 km) to be used to provide an appropriate representation of the snow cover at sub-kilometre scales. Furthermore, the initialisation of the snow density performed by the WRF Preprocessing System (WPS) assumes climatological values that are not representative for a specific case study. In the present work, MODIS/Terra (MOD10_L2) satellite products at a spatial resolution of 500 m [Hall et al., 2006], averaged in time between 5 and 10 February 2015 were used to initialise the snow fields. The snow mask was directly interpolated at the horizontal resolutions of the nested model domains. To initialise snow albedo, we followed the methodology outlined by Tomasi et al. [2014]. Snow albedo is a function of the age of the snow [see Livneh et al., 2010], which is initialized as fresh snow [i.e. with the greatest value of snow albedo, based on an analysis of climatological data, Robinson and Kukla, 1985]. A snow age corresponding to the satellite-retrieved albedo was calculated by inverting the functional relationship proposed by Livneh et al. [2010], which is implemented in the current version of the Noah land-surface model. The calculated snow age was then used as initial condition. The snow water equivalent was diagnosed by assuming that the density of the snow is, as a zero-order approximation, only a function of the age of the snow [Meløysund et al., 2007]. Hence, given the snow depth, the snow water equivalent can be specified at the initial time. Snow depth was assumed to depend

Table V.1: Spatial and temporal resolutions for the domains used for the real-case numerical simulations: number of points nx, ny and nz in the east, north and vertical directions, respectively, horizontal grid resolution $\Delta\mathrm{x} = \Delta\mathrm{y}$, vertical grid spacing near the ground surface $\Delta\mathrm{z}_{\mathrm{min}}$, time step Δt and frequency f_{bu} at which the lateral boundaries of the nested grids were updated.

Domain	nx, ny, nz	$\Delta x = \Delta\mathrm{y}$	Δz_{min}	Δt	f_{bu}
d01	202, 202, 46	15 km	42 m	30 s	6 h
d02	246, 246, 46	3 km	42 m	6 s	30 s
d03	340, 340, 46	1 km	42 m	2 s	6 s
d04	406, 406, 92	333 m	21 m	0.6 s	10 min
d05	382, 382, 92	111 m	21 m	0.1 s	5 min

only on the elevation of the underlying terrain, as in previous studies [e.g. Schmidli et al., 2009]. Snow depth was initialised to 0.05 m at sea level, to linearly increase above sea level to 0.15 m at 500 m above sea level (a.s.l.) and to linearly increase above 500 m a.s.l. to 1.5 m at 4500 m a.s.l.

V.2.3 Model setup for the real and semi-idealised cases

The numerical simulations were performed using the WRF model with the advanced research core [ARW, Skamarock et al., 2008], version 3.5.1. Five nested domains were used (see Table V.1 for the spatial and temporal resolutions that were used for the domains). The simulations were performed in three steps.

Firstly, a simulation for the three outermost domains (d01, d02 and d03) was performed using online one-way nesting and a grid aspect ratio of 5 and 3 for domains d02 and d03 respectively. The computations were made on 46 vertical layers. The grid was stretched along the vertical axis, with a vertical resolution of about 40 m near the ground surface (so that the first mass point above the surface is approximately 20 m above it). Lateral boundary conditions for d02 and d03 were updated every parent domain time step. Initial conditions other than those for the snow fields and lateral boundary conditions for the outermost domain d01 were derived from the European Centre for Medium-range Weather Forecasts (ECMWF) gridded analyses available every 6 h with a horizontal resolution of 0.25°. The simulation was run continuously for 7 days from 7 to 14 February 2015. Results from additional sensitivity simulations showed that the model results can drift with respect to the ECMWF analysis (not shown). Therefore the simulated fields in domains d01, d02 and d03 were relaxed towards the ECMWF analysis using spectral nudging. Only the upper-part of d03 (above 6000 m a.s.l.) was nudged towards the analyses. Compared to standard nudging techniques, spectral nudging allows to relax only the large-scale flow features

towards the analysis, maintaining the small-scale variability of the regional numerical simulation [see for instance Miguez-Macho et al., 2004].

Secondly, a simulation for domain d04 was performed using initial and lateral boundary conditions extracted from the results for d03 (i.e. using offline nesting). The extent of d04 was chosen to cover the main regional-scale orographic feature surrounding the Passy Valley (see Fig. V.1a). The horizontal grid resolution was set to 333 m and 92 vertical levels were used, with a vertical resolution of about 20 m near the ground surface (so that the first mass point above the surface is approximately 10 m above it) and 29 levels in the lowest 1000 m above the surface. The lateral boundary conditions were updated every 10 min. This simulation was run continuously from 8 to 14 February 2015.

Finally, a simulation for domain d05 was performed using the same methodology as that for d04 except that it was re-initialised every day at 1200 UTC to facilitate the comparison with semi-idealised simulations for selected days and that the lateral boundary conditions were updated every 5 min. The coverage of d05 is shown in Fig. V.1b. The number of vertical levels was the same as that of d04 but the horizontal grid resolution used was refined to 111 m. Results from additional sensitivity simulations revealed negligible differences when using a domain twice as large as d05 and the necessity of a horizontal grid resolution as fine as 111 m to resolve the constriction in the downstream part of the Passy Valley, which was found to significantly affect the (thermo-) dynamics of the near-surface valley atmosphere (not shown). The simulation for d05 is the reference simulation and is referred to as WRF-R hereafter.

All the nested domains were centred at the airport in Sallanches (45.935°N, 6.636°E) and shared the same 'dynamics' and 'physics' options, apart from that for the planetary boundary-layer (PBL) and subgrid-scale turbulence. A third-order Runge-Kutta scheme was used to integrate the model equations and a time-splitting technique was used to integrate the acoustic modes. The advection terms were discretised using a fifth-order Weighted Essentially Non-Oscillatory (WENO) scheme with positive definite filter. The PBL was parameterised for d01, d02 and d03 using the Yonsei University (YSU) parameterisation scheme [Hong, 2010], and explicitly simulated in the higher-resolution simulations for d04 and d05, using a turbulent kinetic energy (TKE) 1.5-order closure scheme with the Smagorinsky coefficient C_s set to 0.1. Surface–atmosphere exchanges were modelled using the Noah land surface model [Chen and Dudhia, 2001] using four soil layers. Shortwave and longwave radiation were parameterised using the Rapid Radiative Transfer Model [Mlawer et al., 1997]. Shadowing effects were included to take into account the effect of the mountains on the radiative fluxes. Microphysics was parameterised using the scheme developed by Morrison et al. [2005], modified for the treatment of ice fog following Neemann et al. [2015].

A set of semi-idealised numerical simulations were performed to extract the ef-

fects of the large-scale flow (simulation WRF-I). WRF-I differs from WRF-R in that the domain is twice as large in order to avoid spurious effects due to the symmetric boundary conditions imposed at the lateral boundaries and that at the initial time the temperature and humidity fields are horizontally homogeneous and the wind speed is set to zero. The initial temperature and humidity profiles for WRF-I were extracted from the real-case simulation for d04 at the centre of the domain. The skin temperature was initialised by extrapolating the temperature of the first three air layers above the ground surface. Hence, the main difference between WRF-I and WRF-R is that there is no large-scale flow for WRF-I. WRF-I was run for the period between 10 February 2015 at 1200 UTC and 12 February 2015 at 1200 UTC and re-initialised on 11 February 2015 at 1200 UTC.

V.3 Overview of the large-scale circulation during IOP1

The PCAP that formed in the Passy Valley during IOP1 was the result of the passage of a upper-level ridge over the region. A Rex block interested Europe between 4 and 8 February 2015. The upper-level ridge of the blocking pattern was located immediately to the east of the British Isles on 9 February 2015 at 0000 UTC (see Fig. V.2a). The CAP formed in the evening on 9 February 2015, when the upper-level ridge moved over Northwest Europe (see Fig. V.2b). This synoptic flow pattern led to the channelling of the large-scale north-easterly flow over the Swiss Plateau, bringing warm air above the Passy Valley. From 10 to 12 February 2015 the upper-level ridge continued to move across Europe and was centred over Central Europe on 12 February 2015. The displacement of the ridge resulted in a weakening of the wind speed and a rotation of the wind over the occidental Alps clockwise from north-easterly on 9 February 2015 to south-easterly on 12 February 2015 (see Fig. V.2b to d), allowing the CAP to persist over time. On 13 February 2015 the trailing upper-level trough cut across Northwest Europe, leading to a southerly flow and an increase in wind speed over the occidental Alps (see Fig. V.2e). On 14 February 2015 cold air brought by the large-scale perturbation reached the occidental Alps (see Fig. V.2f), thereby removing the PCAP and putting an end to IOP1.

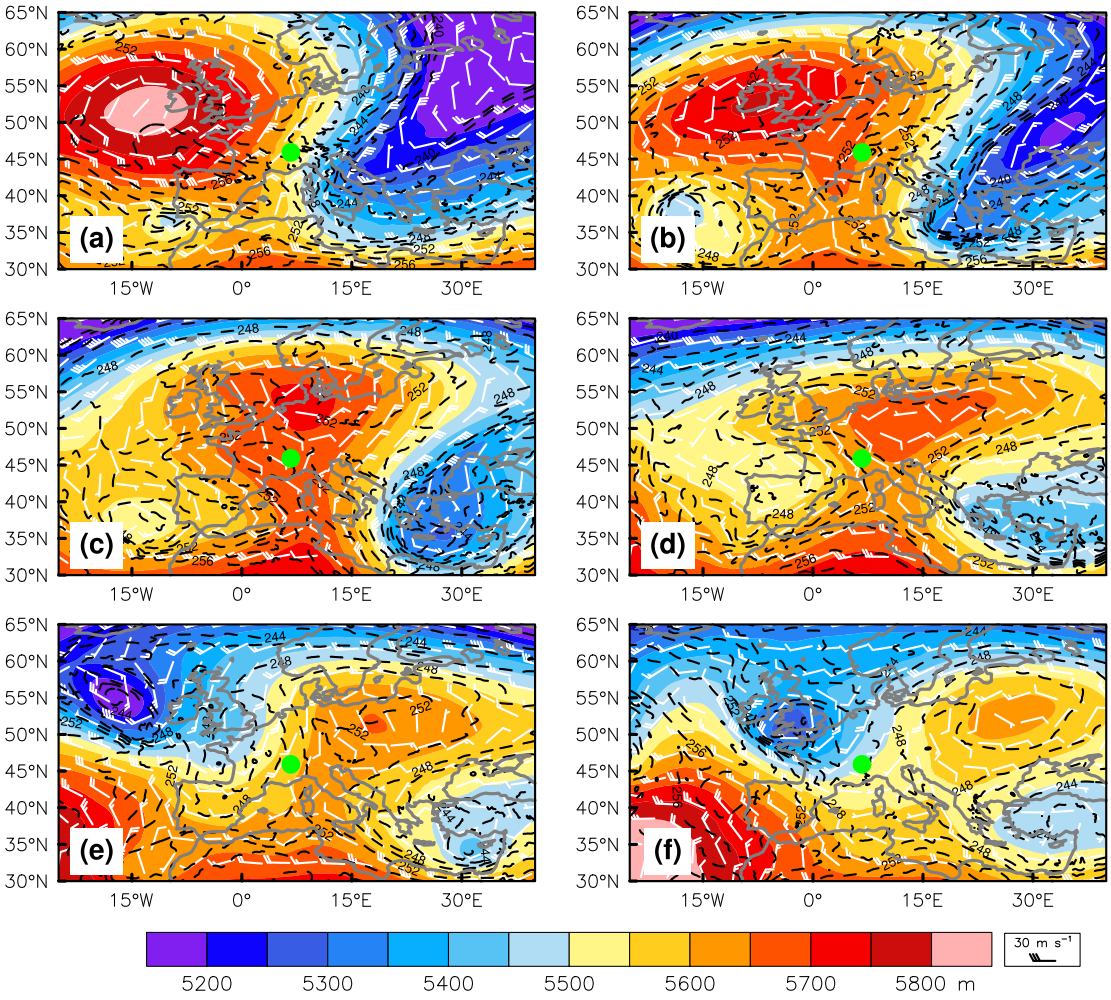

Figure V.2: Synoptic weather conditions at 500 hPa from 9 to 14 February 2015 at 0000 UTC (a) to (f) extracted from the European Centre for Medium-range Weather Forecasts (ECMWF) gridded analyses with a horizontal resolution of 0.25°. The colour and dashed contours indicates geopotential height and temperature (in K), respectively. The green dot in the centre of the weather charts indicates the position of the Passy Valley.

V.4 Life-cycle of the persistent cold-air pool during IOP1

V.4.1 Vertical structure of the cold-air pool

Figure V.3 shows the temporal evolution of the vertical structure of the CAP obtained by compiling potential temperature profiles from the radiosounding ascents and wind profiles retrieved from LiDAR and wind profiler data at the RS site during IOP1, and extracted from the WRF-R simulation. It is overall well captured in WRF-R, despite some discrepancies in particular before the PCAP event during the night from 8 to 9 February 2015 and the end of the episode on 14 February when simulated temperatures are slightly too warm and the transitions in the simulated wind regime occur a bit

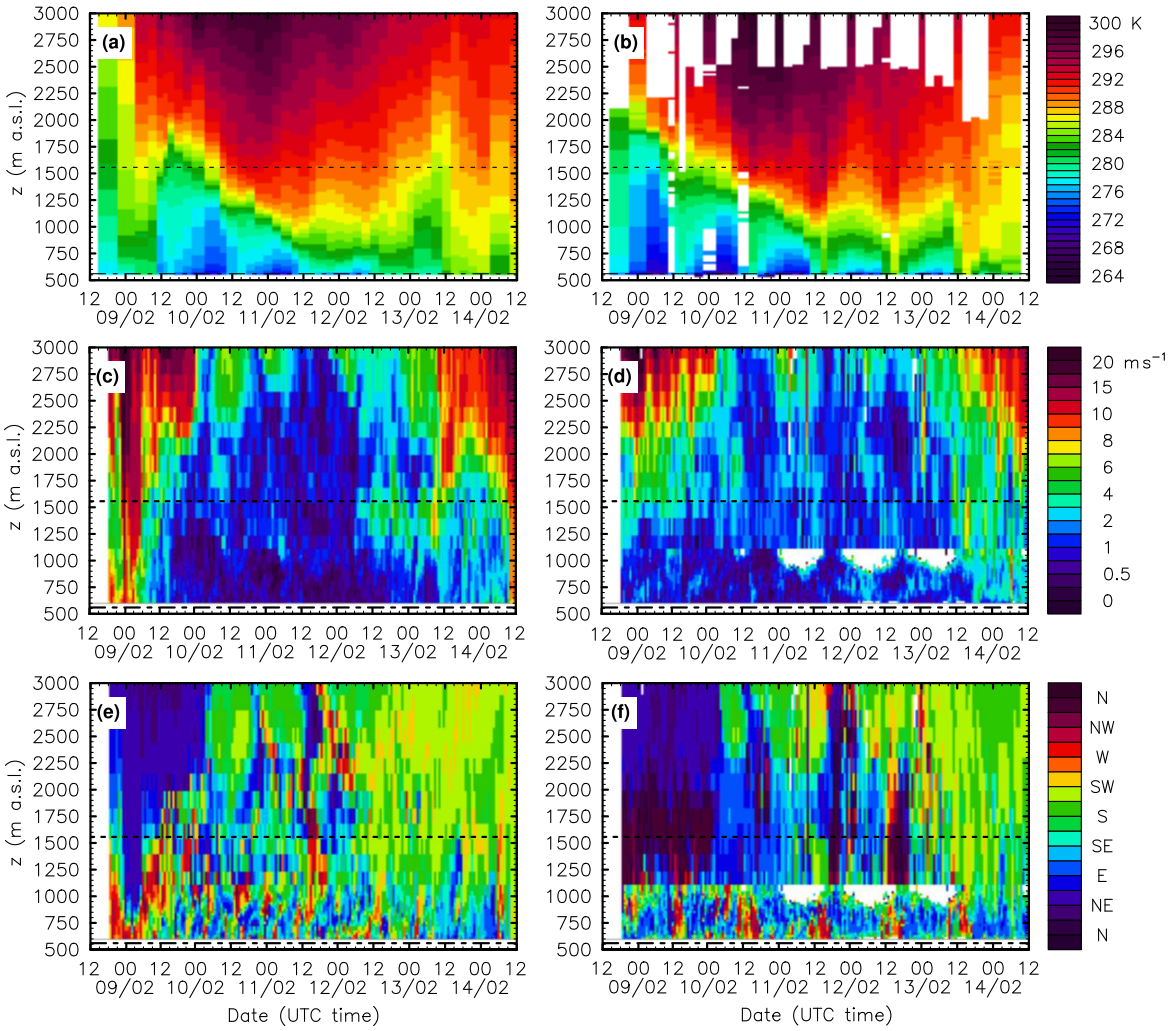

Figure V.3: Temporal evolution of the vertical structure of the cold-air pool as obtained from the WRF-R simulation (left column) and from observational data (right column). (a) and (b): potential temperature; (c) and (d): wind speed, (e) and (f): wind direction. The potential temperature data are obtained from the radiosounding (RS) ascents, the wind speed and wind direction are retrieved from the LiDAR (below 1050 m a.s.l.) and the wind profiler (above 1050 m a.s.l.) at the RS site during IOP1. The dashed lines indicates $z_m = 1560$ m a.s.l. (see Fig. V.1c). The RS site is shown in Fig. V.1b.

too early. The CAP formed in the evening on 9 February 2015, when warm air was advected above the Passy Valley as the upper-level ridge approached the occidental Alps (see Sect. V.3). Note the weakening and rotation of the flow associated with the passage of the ridge (see Fig. V.3c to f and Fig. V.2). The formation of the CAP led to a rapid increase of the vertically-integrated valley heat deficit [VHD, Whiteman et al., 1999a] from 3 to 12 MJ m^{-2}, which is well reproduced in WRF-R (see Fig. V.4a).

Between 9 February 2015 at 1200 UTC and 12 February 2015 at 1200 UTC, the structure of the CAP in the Passy Valley varied substantially, while the wind speed below 2500 m a.s.l. was in the order of a few metres per second. During this period

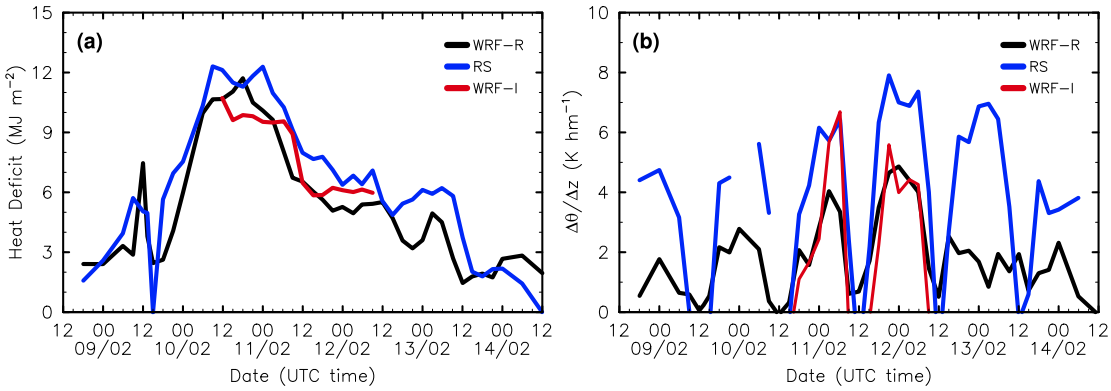

Figure V.4: Timeseries of the valley heat deficit, vertically integrated from the ground surface to the mean height of the terrain $z_m = 1560$ m a.s.l. (a), and of the near-surface potential temperature gradient over the lowest 100 m above the surface (b), at the RS site (see Fig. V.1b), derived from data from the radiosounding ascents and computed from the WRF-R and WRF-I outputs.

the height of the CAP decreased gradually with time. This decrease was most rapid during the night from 10 to 11 February 2015, leading to a decrease of the VHD by 4–5 MJ m^{-2}. Although the VHD decreased with time afterwards, the nighttime near-surface potential temperature gradient $\Delta\theta/\Delta z$ was found to increase from day to day (see Fig. V.4b), though its amplitude is underestimated in WRF-R. The maximum value of $\Delta\theta/\Delta z$ was found on 12 February 2015 at 0000 UTC, as a result of the change in wind direction in the height range $1000 < z < z_m = 1560$ m a.g.l.

On 13 February 2015 the wind speed in the valley atmosphere increased above 5 m s^{-1} as a large-scale perturbation approached the occidental Alps (see Sect. V.3). On 14 February 2015 the wind speed also increased at the valley bottom, leading to mixing and the full destruction of the CAP.

V.4.2 Regional-scale circulation

A more detailed account of the regional-scale flow at $z = z_m$, simulated in domain d04, is given in Fig. V.5. Timeseries of wind and temperature at selected sites in the Passy Valley, RS and DS, and in the main tributary valleys, MGV and CHMNX (see Fig. V.1b for the location of the sites), are displayed in Fig. V.6 to show the response of these fields (in WRF-R) to the large-scale flow. On 10 February 2015 at 0000 UTC, the large-scale flow was channelled through the downstream part of the Passy Valley, and split between CHMNX and MGV (see Fig. V.5a and V.6e), while the near-surface flow is down-valley at DS and CHMNX (see Fig. V.6k). At 1200 UTC, the large-scale flow rotated to a south-westerly direction, reaching a minimum wind speed of less than 1 m s^{-1} at the different sites (see Fig. V.6a and V.6b). A strong down-valley wind formed in the Sion Valley, upstream of the Chamonix Valley, which was channelled through the gap that connects the two valleys, strengthening the

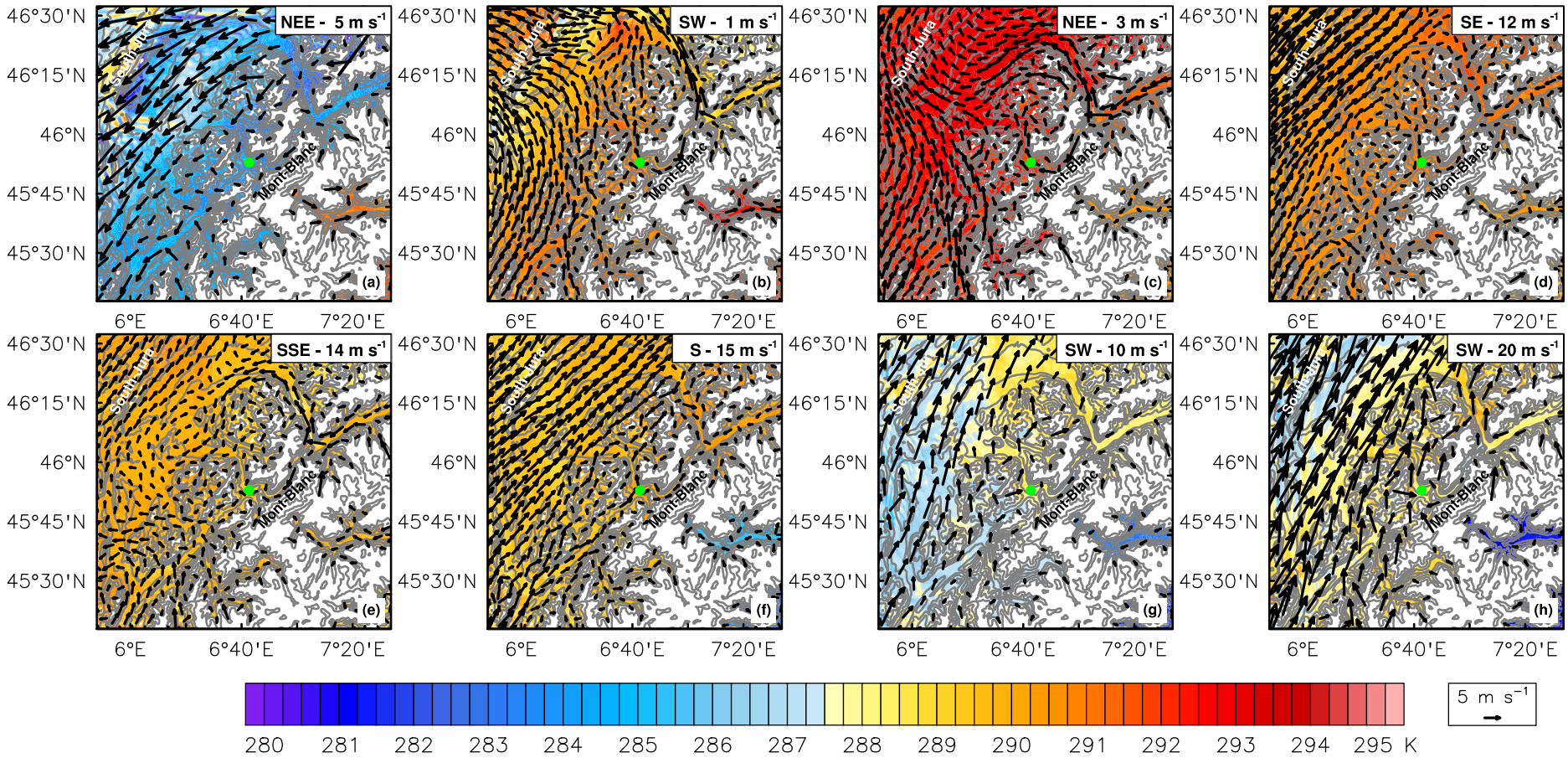

Figure V.5: Birdeye plots of the wind and potential temperature fields at $z = z_m = 1560$ m a.s.l. from 10 to 14 February 2015 at 0000 UTC (a), (c), (e), (g) and (h), respectively, and 1200 UTC (b), 1500 UTC (d), and 1200 UTC (f), respectively. The speed and direction of the large-scale flow at $z = 6000$ m a.s.l. are indicated on the top right corner of the plots. The green dot in the centre of the plots indicates the position of the Passy Valley.

down-valley flow in CHMNX (see Fig. V.5b). The flow at DS reversed to down-valley from the surface to $z = z_m$ and remained down-valley during nighttime until the end of the simulated time period. Up-valley flows were noticed at $z = 1000$ m a.s.l. at the different sites for a few hours around 1200 UTC every day (Fig. V.6h). Warm air advection occurred over night across the entire region, where θ at $z = z_m$ increased by 7 K in 12 hours (see Fig. V.6f), while it decreased by 2–3 K at $z = 1000$ m a.s.l. (see Fig. V.6i). This process, warming at mid levels and cooling at lower levels, led to the initial strengthening of the CAP within the Passy Valley (see Fig. V.4a).

Potential temperature θ at $z = z_m$ was maximum on 10 February 2015 at 2100 UTC (see Fig. V.6f), that is when the upper-level ridge just passed over the Passy Valley. This can be inferred by noticing the rotation of and weakening of the wind aloft (at $z = 6000$ m a.s.l., see Fig. V.6b and a, respectively). In the early night between 10 to 11 February 2015 the near-surface flow from MGV reversed to down-valley as the upper-level ridge moved away from the occidental Alps, and remained down-valley until the end of the simulated time period (see Fig. V.6k). During the night θ at $z = 1000$ m a.s.l. increased, while it stayed approximately constant at $z = z_m$ (see Fig. V.6f and i). The large-scale flow at this time was northeast-easterly, i.e. aligned with the Sion and Chamonix valleys, thereby favouring the channelling of the flow down these two valleys (see Fig. V.5c). Throughout the night the large-scale flow slowly rotated clockwise and strengthened as the upper-level ridge moved towards the north-east (see Fig. V.6a and V.6b). Later on, on 11 February 2015 at 1200 UTC, the large-scale flow became south-easterly, and the resulting channelling through the Swiss Plateau gave rise to a regional south-westerly flow at mid-level (see Fig, V.5d). This led to a channelling of the flow through the downstream part of the Passy Valley and the rapid change in the wind direction within the valley to south-west from 1200 UTC to 1800 UTC, a transition well captured in WRF-R. During the night between 11 and 12 February 2015 θ at $z = 1000$ m a.s.l. and $z = z_m$ hardly varied (Fig. V.6f and i), while the near-surface temperature dropped throughout the night, as during the previous night. The amplitude of the diurnal range of θ at $z = z_m$ is somewhat underestimated in WRF-R, but the overall temporal evolution is well captured during this night. From 10 to 12 February 2015 the near-surface temperature at night was non-homogeneous across the valley floor, as indicated by differences of 4–5 K between the DS and RS sites that are approximately at the same height (see Fig. V.6l), while the wind speed there was very weak (at maximum 1 m s^{-1}). It is worth noting that simulated near-surface temperatures are slightly underestimated at night, though they fall within the observed range when spatially averaged within a radius of a few hundred metres around the sites (not shown). A cold bias of about 3 K is also present in the afternoon. Such a bias in the afternoon under anticyclonic conditions is not atypical to numerical models and was reported in previous studies [e.g. Lu and Zhong, 2014].

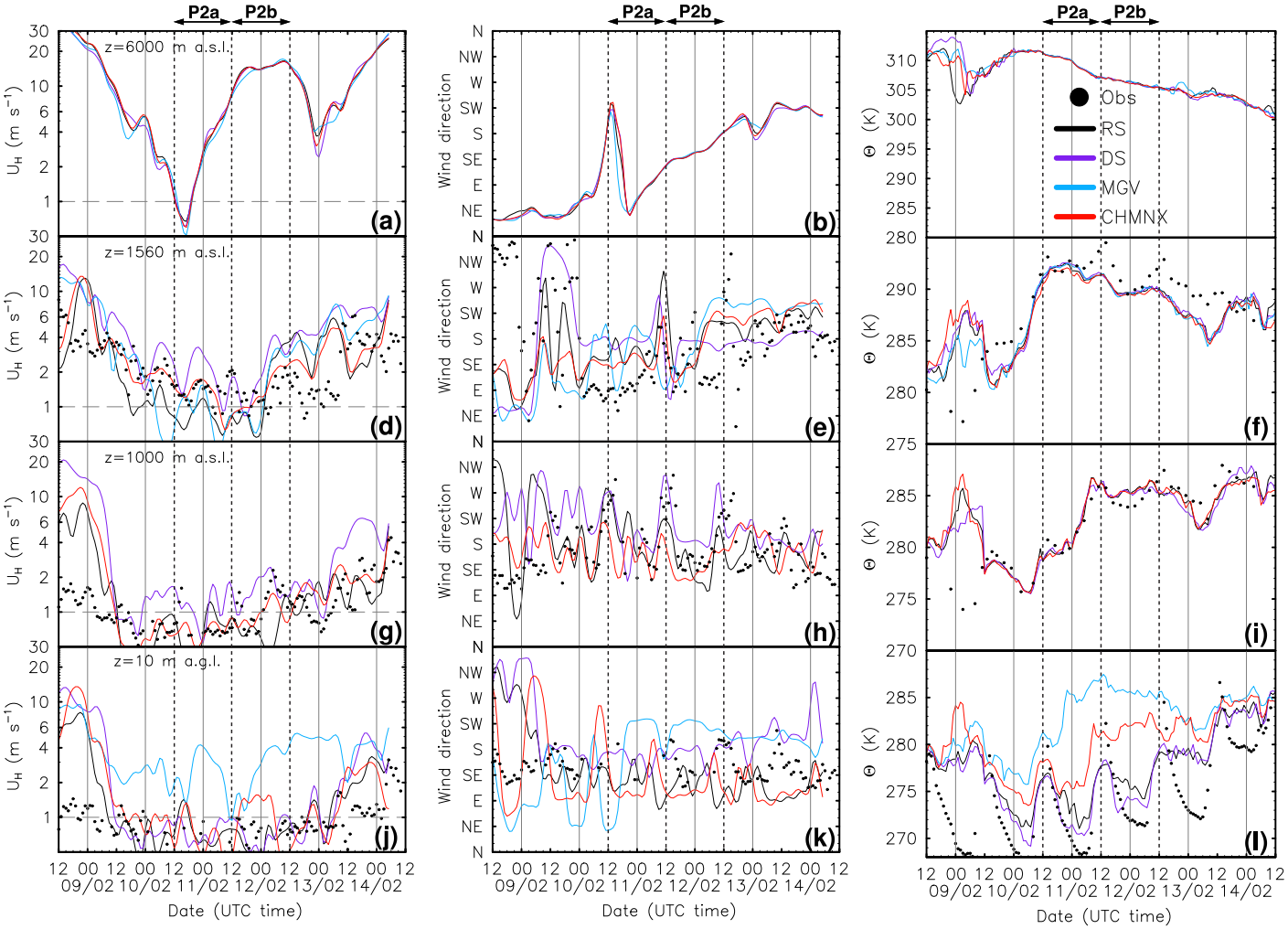

Figure V.6: Timeseries of the horizontal wind speed (left column) and direction (middle column), and potential temperature (right column) at $z = 6000$ m a.s.l., $z = z_m = 1560$ m a.s.l., $z = 1000$ m a.s.l. and $z = 10$ m a.g.l. (top to bottom rows, respectively), at the locations of the RS, DS, MGV and CHMNX sites (see Fig. V.1b for the location of the sites), in WRF-R during the simulated time period. Observational data at the RS site are superimposed: wind data derived from the wind profiler measurements at $z = z_m$ and $z = 1000$ m a.s.l. and from an instrumented meteorological mast at $z = 10$ m a.g.l., and potential temperature data at $z = z_m$ and $z = 1000$ m a.s.l. derived from the radiosounding measurements and from an instrumented meteorological mast at $z = 10$ m a.g.l.

During 13 and 14 February 2015, advection of cold air by the large-scale perturbation led to the destruction of the CAP, strengthening of the near-surface flow with prevalently southerly winds, and a homogenisation of the temperature across the valley floor (see Fig. V.5g, V.5h and V.6l).

The overview of the life-cycle of the CAP presented above identified three main time periods, which correspond to the three stages of a PCAP:

P1 The formation stage – from 8 to 10 February 2015, when the valley inversion formed in the Passy Valley and a change in wind direction was observed aloft;

P2 The persistent stage – from 10 to 13 February 2015, when the valley inversion persisted in the Passy Valley;

P3 The destruction stage – on 14 February 2015.

Since the large-scale flow deviated from that for 'standard' anticyclonic weather conditions in that it varied with time, the persistent stage is divided in two sub-periods:

P2a From 10 February 2015 at 1200 UTC to 11 February 2015 at 1200 UTC, when the upper-level ridge moved over the Passy Valley, and the wind speed at $z =$ 6000 m a.s.l. increased over night from a minimum value;

P2b From 11 February 2015 at 1200 UTC to 12 February 2015 at 1200 UTC, when the large-scale flow rotated continuously from south-easterly to southerly, and the wind speed at $z = 6000$ m a.s.l. continued to increase with time.

Because the formation and destruction stages of the CAP follow rather well-understood patterns, the focus of the subsequent analysis is on the persistent stage P2 and its sub-periods P2a and P2b.

V.4.3 Valley-scale circulation during the persistent stage

In this section the valley-scale circulation during the persistent stage P2 is analysed by comparing results from WRF-R and the semi-idealised simulation WRF-I.

V.4.3.a Sub-period P2a

Sub-period P2a (from 10 February 2015 at 1200 UTC to 11 February 2015 at 1200 UTC) is characterised by a maximum VHD at the valley scale around 1800 UTC, followed by a gradual decrease of the VHD during the course the night. The wind speed near the surface and at $z = 1000$ m a.s.l. was at maximum 1 m s^{-1} at the different sites considered in Fig. V.6, except MGV, where it was maximum and in the order 3–4 m s^{-1} near the surface. The non-local control of the large-scale flow on

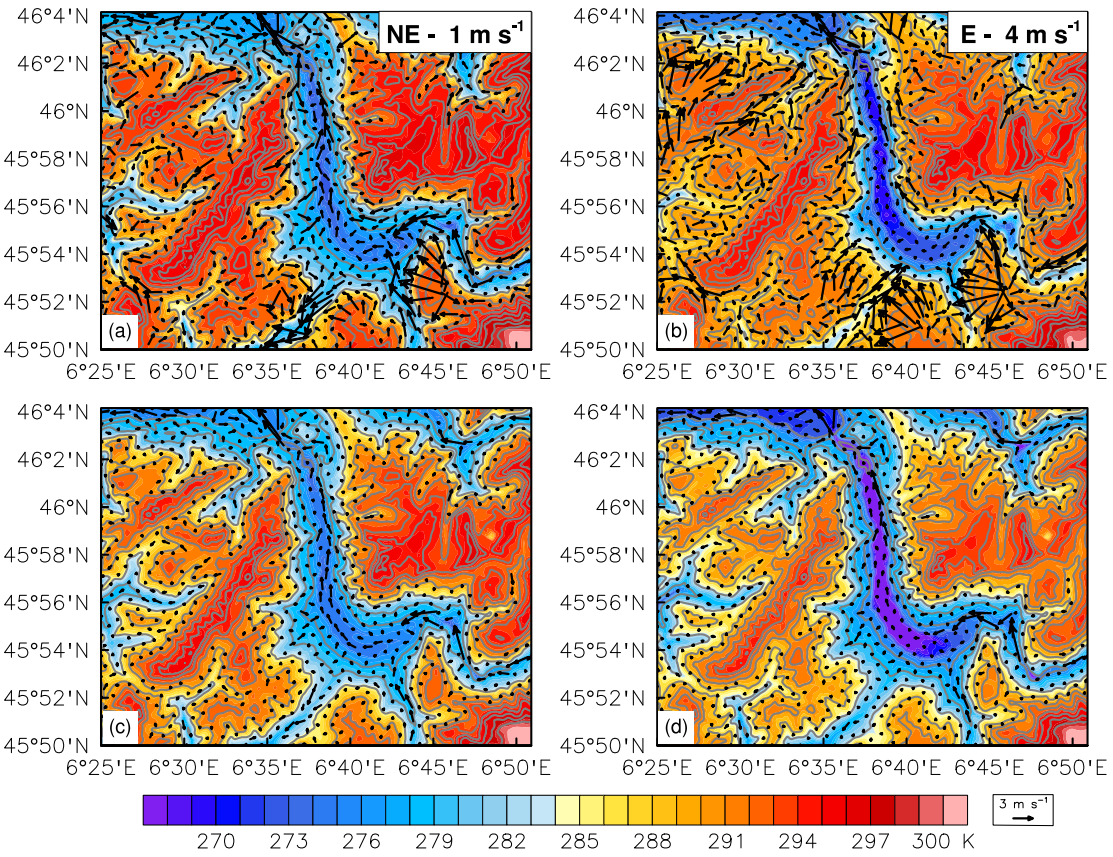

Figure V.7: Simulated wind and potential temperature fields at $z = 10$ m a.g.l. in WRF-R (top row) and WRF-I (bottom row) on 10 February 2015 at 1800 UTC (left column) and 11 February 2015 at 0600 UTC (right column). The speed and direction of the large-scale flow at $z = 6000$ m a.s.l. are indicated on the top right corner of the plots for WRF-R.

the near-surface circulation can be extracted by comparing results from WRF-R and WRF-I (see Fig. V.7). Between 1800 UTC and 0600 UTC on the following day, the circulation at the bottom of the Passy Valley is qualitatively similar in WRF-R and WRF-I. There is a clear down-valley flow in the downstream part of the valley and down-valley flows from CHMNX and STGV mostly detrain above the valley floor. At the valley exit the along-valley flow is found to accelerate because of the narrowing of the valley. The flow in MGV was up-valley until 2100 UTC (see Fig. V.6). This up-valley flow is weaker in WRF-I than in WRF-R (see Fig. V.7a and V.7d) and do not reverse to down-valley (see Fig. V.7d) at the surface.

The discontinuity in the magnitude of the wind vectors in Fig. V.7b where the air flows from MGV to the Passy Valley indicates that the flow detrains at a certain height within the valley because of the strong stratification of the CAP. This detrainment is clearly visible in the composite vertical cross-sections following the flow (along the white line in Fig. V.1b), shown in Fig. V.8. The capping inversion at the top of the CAP progressively descends and 'sharpens' (i.e. its depth decreases) as the

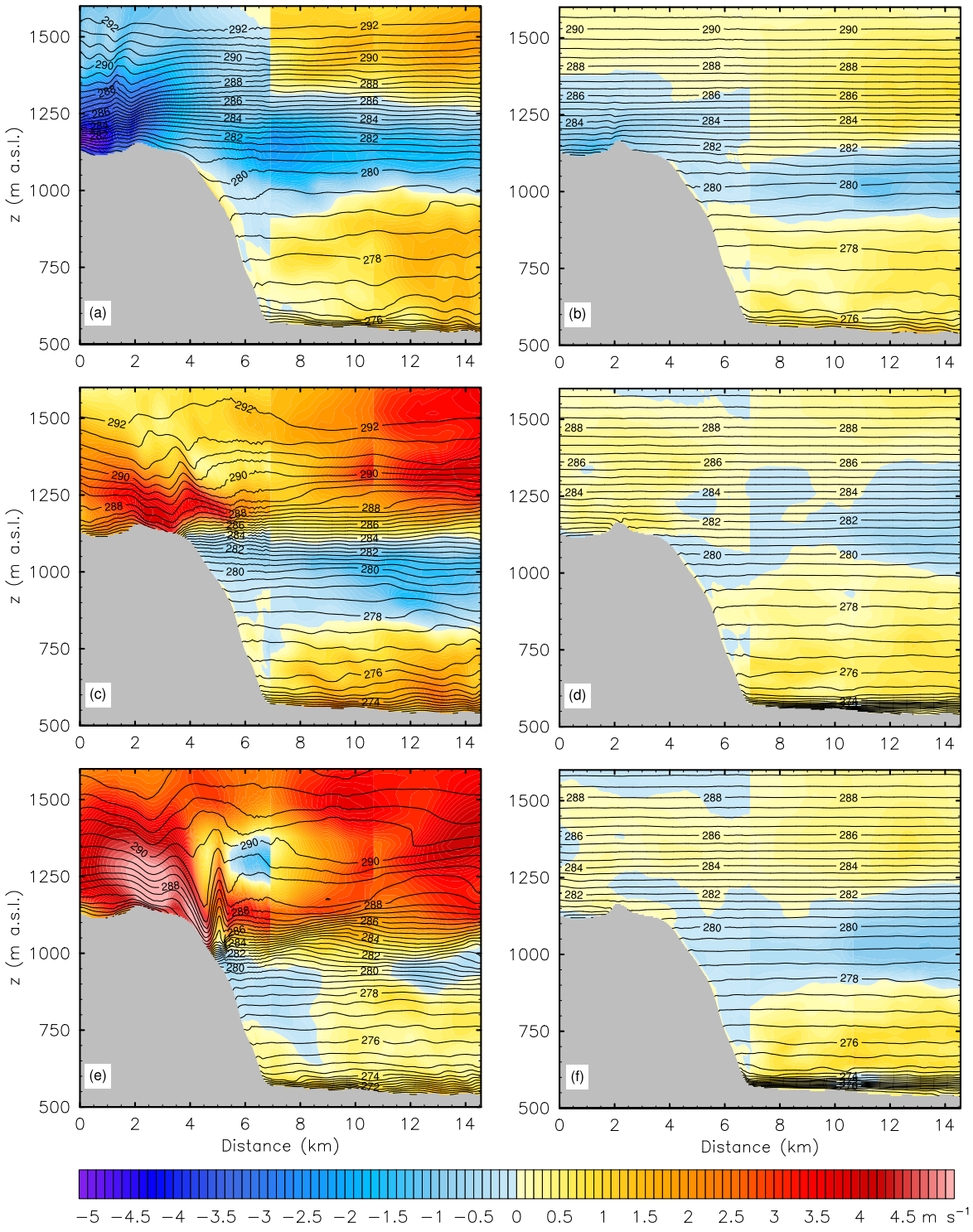

Figure V.8: Composite vertical cross-sections following the flow (along the white line in Fig. V.1b) of horizontal wind speed (in the plane of the cross-section) and potential temperature (K) in WRF-R (left column) and WRF-I (right column) on 10 February 2015 at 1800 UTC, and 11 February 2015 at 0000 and 0400 UTC (top to bottom rows, respectively).

flow through MGV strengthens during the course of the night (see Fig. V.8a,c,e). A hydraulic jump forms as the air descends into the Passy Valley (see Fig. V.8e). Con-

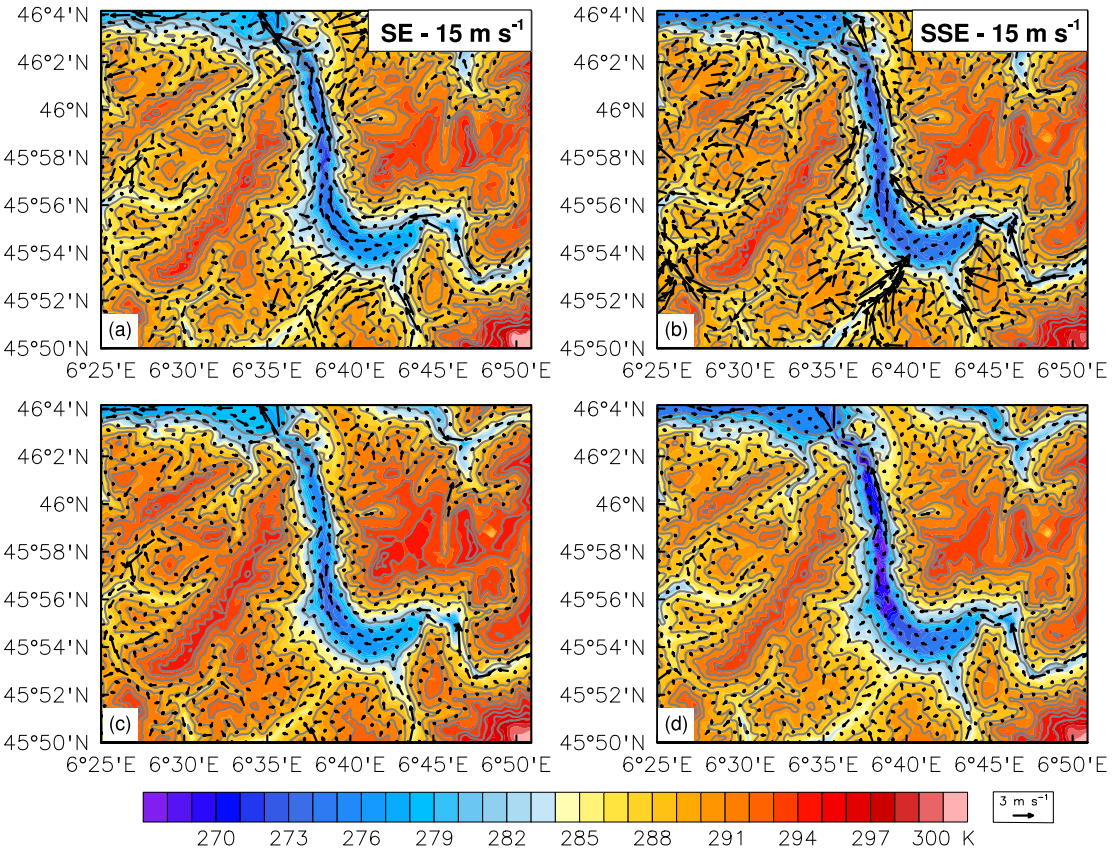

Figure V.9: Simulated wind and potential temperature fields at $z = 10$ m a.g.l. in WRF-R (top row) and WRF-I (bottom row) on 11 February 2015 at 1800 UTC (left column) and 12 February 2015 at 0600 UTC (right column). The speed and direction of the large-scale flow at $z = 6000$ m a.s.l. are indicated on the top right corner of the plots for WRF-R.

versely, the flow from MGV in WRF-I reverses above the near-surface only around 0000 UTC and the upper-part of the CAP cools steadily throughout the night as a result of radiative cooling (see Fig. V.8b, V.8d and V.8f). However, the lower part of the CAP displays a temporal evolution of wind speed and thermal structure similar to that in WRF-R, as can be inferred from the isentrope $\theta = 276$ K in Fig. V.8. This result suggests that the flow from MGV mostly controlled the increase in temperature around $z = 1000$ m a.s.l. between 0000 and and 0600UTC, and more generally the thermal structure of the upper-part of the CAP (see Fig. V.6f and Fig. V.4a), while the lower part of the CAP was mostly controlled by local processes.

At 0600 UTC, the near-surface flow in the part of the Passy Valley upstream of RS (see Fig. V.1b) is weak and almost stagnant in both WRF-R and WRF-I (see Fig. V.7b and V.7d). However, the near-surface temperature there is lower in WRF-I than in WRF-R, which explains the larger near-surface vertical gradient of potential temperature that develops in WRF-I when compared to WRF-R during the second part of the night (see Fig. V.4b).

V.4.3.b Sub-period P2b

During the sub-period P2b (from 11 February 2015 at 1200 UTC to 12 February 2015 at 1200 UTC) the evolution of the bulk thermal properties of the Passy Valley atmosphere are more similar in WRF-R and WRF-I than during P2a (see Fig. V.4). At 1800 UTC, the near-surface flows through MGV, CHMNX and STGV are down the tributaries and the near-surface flow in the Passy Valley is down-valley (see Fig. V.9a and V.9c). Hence, the near-surface flow and the flow in the upper-part of the CAP are in opposite directions (see Fig. V.5 and Sect. V.4.2).

The speed of the flow from MGV increases with time in WRF-R, reaching its maximum in the morning on 12 February 2015, while it remains constant in WRF-I (see Fig. V.9b and V.9d). The flow from CHMNX is weaker than that from MGV and comparable in WRF-R and WRF-I. In contrast to P2a, the near-surface temperature in the Passy Valley is similar in WRF-R and WRF-I during P2b (see also Fig. V.4b).

V.5 Mass and heat fluxes in and out of the valley

Sect. V.4.3 highlighted non-local controls of the large-scale flow on the CAP in the Passy Valley during the persistent stage (P2), in particular in determining the respective contributions of the tributary flows to the mass and heat budgets of the valley atmosphere. In this section, these contributions are quantified.

V.5.1 Mass budget

The mass budget of the Passy Valley atmosphere is performed over the PASSY control volume, defined in Sect. V.2.1. Assuming incompressibility, the mass budget reads

$$\sum_i \underbrace{\int_{A_i} \rho\, v_i\, n_i\, dS}_{M_i} = M_{\text{DS}} + M_{\text{MGV}} + M_{\text{CHMNX}} + M_{\text{STGV}} + M_{\text{TOP}} = 0, \tag{V.1}$$

where $A_i = A_{\text{DS}}$, A_{MGV}, A_{CHMNX}, A_{STGV}, are the lateral surfaces of the control volume (see the blue surfaces in Fig. V.1c), $A_i = A_{\text{TOP}}$ is the top surface at $z = z_m$, ρ is the air density, v_i is the wind component normal to the surface A_i orientated by the unit vector n_i (defined positive outwards).

The mass flux through DS is mostly out of the Passy Valley during P2. The only time period when there was a significant inflow into the valley through DS was between 1300 and 2000 UTC on 11 February 2015 because of the channelling of the large-scale flow, which will be discussed in more details later in the paper. As one may expect, DS is the main exit for the air mass within the valley (see Fig. V.10a). As long as DS

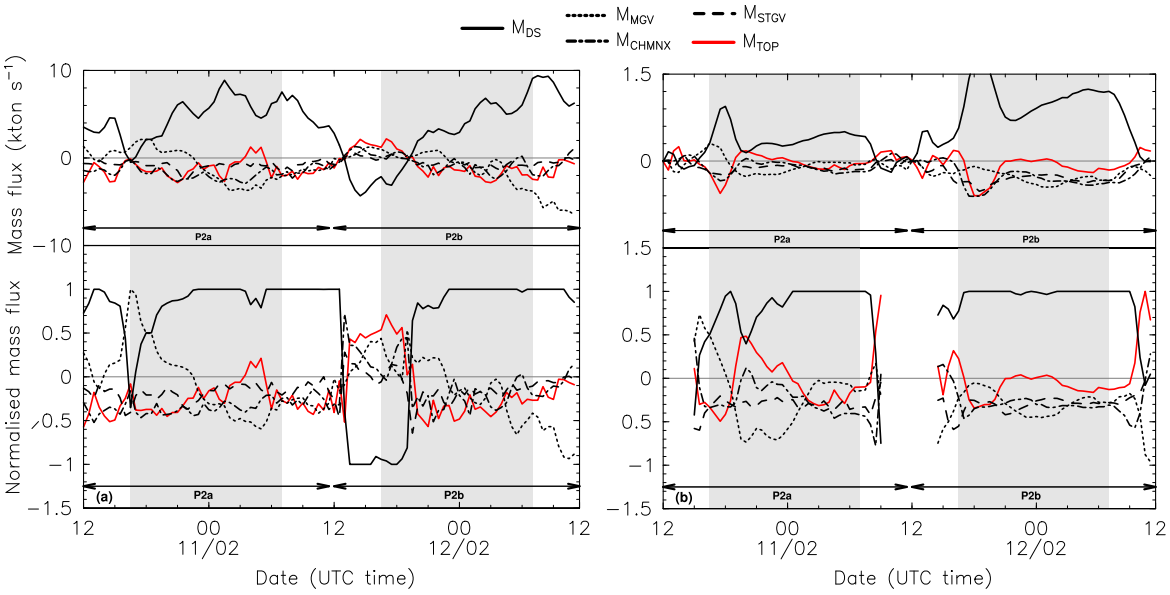

Figure V.10: Timeseries of the mass fluxes through DS (M_{DS}), MGV (M_{MGV}), CHMNX (M_{CHMNX}), STGV (M_{STGV}), vertically integrated from the ground surface to $z = z_m$, and through the top surface at $z = z_m$ (M_{TOP}) for the period from 10 February 2015 at 1200 UTC to 12 February 2015 at 1200 UTC in WRF-R (a) and WRF-I (b); see Fig. V.1b and V.1c for the location of the gates. The nighttime periods (from sunset to sunrise) are displayed as grey shading. The bottom panel shows the mass fluxes normalised by the total mass flux out of the Passy Valley. Positive and negative values of the mass flux correspond to a flux out of and into the Passy Valley, respectively.

acts as an exit, both CHMNX and STGV contribute an inflow into the valley, while the mass flux through MGV can be in or out of the valley. During P2a, M_{CHMNX} and M_{STGV} account for 35 and 18% of the total flow of mass out of the valley, respectively, when averaged during nighttime (from sunset to sunrise). When combined together, the flow from these tributaries provide about half of the mass flowing out of the valley at night during P2a. The other half is coming from M_{MGV} and/or M_{TOP}. $M_{\mathrm{MGV}} > 0$ (outflow) when the upper-level ridge passed over the valley (i.e. when the wind speed aloft decreased to its minimum value, see Fig. V.6a), and subsiding motions at the valley top contributes greatly to the inflow of mass into the valley. As the upper-level ridge moved away from the region (and the wind speed increases at upper-level, see Fig. V.6a), most of the air mass out of the valley flows through DS, and M_{TOP} decreases continuously while the flow through MGV reverses (M_{MGV} changes from positive to negative at about 2200 UTC). In the late night from 0300 to 0600 UTC, the inflow of mass from MGV exceeds that from CHMNX and STGV and the total mass originating from the tributaries exceeds that flowing through DS, resulting in a export of mass across the top of the valley volume.

The mass fluxes in WRF-I are one order of magnitude smaller than those in WRF-R (see Fig. V.10b). The contribution of M_{MGV} to the total flow of mass out of the valley

shows a similar temporal evolution in WRF-I and WRF-R, although the change of the flux from positive to negative at MGV occurs 4 to 5 hours earlier in WRF-I. This suggests that the mechanism controlling the direction of the flow at MGV is the same in WRF-I and WRF-R, despite the large difference in the speed of the flow. This point will be further analysed in Sect. V.5.2. The nighttime-averaged contribution to the total flow of mass out of the valley from CHMNX is smaller in WRF-I than in WRF-R (25% compared to 35%), because the down-valley flow at CHMNX is enhanced as a result of the channelling of the flow from the Sion valley.

During P2b, between 1300 and 2000 UTC the large-scale flow was channelled over the Swiss Plateau (see Fig. V.6b and Fig. V.5d), resulting in a strong inflow into the downstream part of the Passy Valley (see Fig. V.10a). This inflow through DS is mostly balanced by the outflow through MGV and the export of mass across the top of the valley volume. M_{DS} reverses from positive to negative at 2000 UTC when the large-scale flow rotates to south-southeasterly and so was in the down-valley direction. At this time, $M_{\mathrm{MGV}} > 0$ and M_{TOP}, M_{CHMNX} and M_{STGV} contribute equally to the total drainage out of the valley through DS and MGV. As the large-scale flow rotates to southerly, the flow at MGV reverses from up- to down-valley and strengthens, leading to a continuous increase of M_{MGV} during the course of the night and the associated suppression of vertical motions across the top of the valley volume. M_{CHMNX} decreases during the course of the night, contributing on average 15% of the total drainage out of the valley, compared to 35% during P2a. Conversely, the nighttime-averaged contribution to the total flow of mass out of the valley from STGV is 16% and comparable to that during P2a. This suggests that the flow through STGV is less sensitive to variations in the large-scale flow than those in CHMNX and MGV.

In WRF-I, each tributary contributes about 30% of the total drainage out of the Passy Valley through DS during P2b. Interestingly $M_{\mathrm{MGV}} < 0$ throughout P2b, as opposed to P2a. This can be explained as follows: since the CAP at 1200 UTC is much shallower than during P2a, and its top is below the height of MGV (see also Sect. V.5.2 and Fig. V.14a), there is no horizontal temperature contrast between RS and MGV and hence no thermally-driven up-valley flow from the Passy Valley to MGV.

The analysis presented so far is further developed by examining the vertical structure of the mass fluxes through DS. A significant fraction of the total drainage out of the Passy Valley occurs in the upper-part of the CAP as a result of the detrainment of the flow from the tributaries (see Fig. V.11a). The mass flux through DS in the lower part of the CAP is more variable with temporal oscillations between outflow (negative) and inflow (positive) in WRF-R. Such oscillations are also visible in WRF-I but only during P2b (see Fig. V.11b). These oscillations can be triggered either by those of thermally-driven flows or by internal gravity waves created by the detrain-

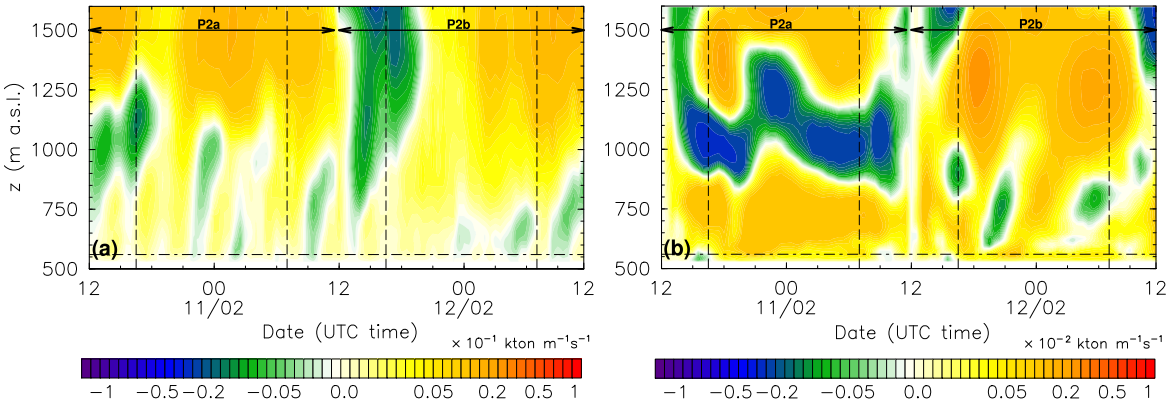

Figure V.11: Time-height plot of the mass flux through the downstream (DS) gate for the period from 10 February 2015 at 1200 UTC to 12 February 2015 at 1200 UTC in WRF-R (a) and WRF-I (b); see Fig. V.1b and V.1c for the location of the gate. The nighttime periods (from sunset to sunrise) are displayed as dashed vertical lines.

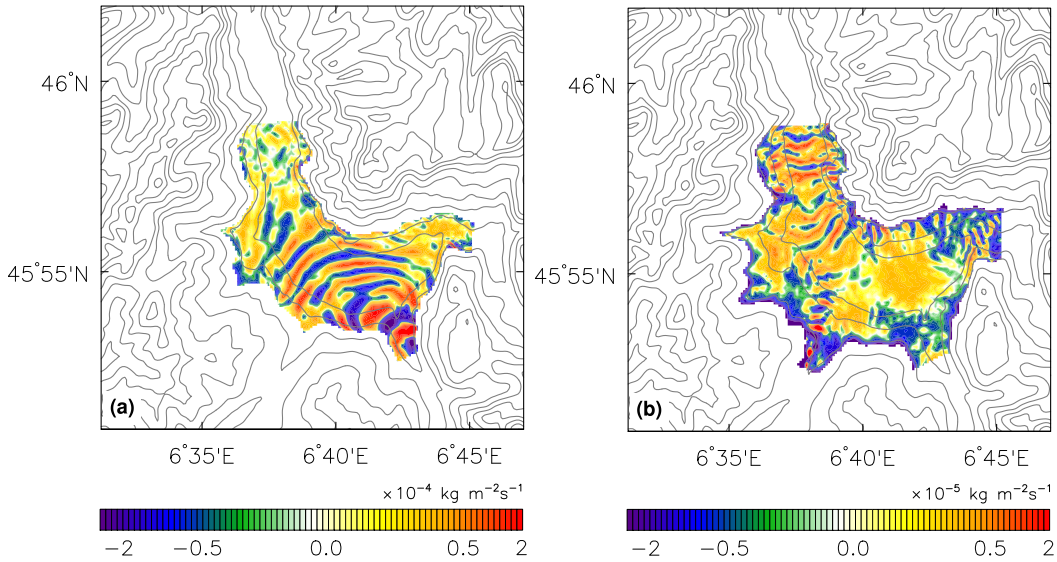

Figure V.12: Horizontal cross-sections (across the polygon defining the PASSY volume, see Fig. V.1b) of the vertical mass flux at the height of STGV on 10 February 2015 at 2200 UTC (during P2a) in WRF-R (a) and at the height of MGV on 11 February 2015 at 1900 UTC (during P2b) in WRF-I (b). Positive and negative values of the mass flux correspond to a flux out of and into the Passy Valley, respectively.

ment of the flow through the tributaries at the top of the CAP via a hydraulic jump [see for instance Largeron et al., 2013]. A closer inspection of Fig. V.11a and V.11b reveals that the slope of the contours associated with the oscillations with respect to the vertical is non zero, indicating that there is a phase propagation in the vertical. As a consequence, the hypothesis that oscillations could be triggered by those of thermally-driven flows can be rejected, as those are pure oscillations in time with no phase propagation [Largeron et al., 2013]. Horizontal cross-sections of the vertical mass flux at the height of STGV during P2a in WRF-R and at the height of MGV during P2b in WRF-I presented in Fig. V.12 for selected times elucidate the mecha-

nism behind the mass flux oscillations. In WRF-R the flow through STGV detrains at about $z = 1000$ m a.s.l., leading to the formation of internal gravity waves that propagate within the Passy Valley atmosphere (see Fig. V.12a). In WRF-I internal gravity waves are excited during P2b by the flow from MGV (see Fig. V.12b), and propagate downstream. The impact of these internal gravity waves on the near-surface drainage flows will be further examined in Sect. V.6.

V.5.2 Heat budget

The previous subsection revealed the key role of the inflows/outflows from the tributary valleys in the mass budget of the Passy Valley atmosphere during the persistent stage of the CAP and how those flows are affected by the large-scale flow. This section examines their role on the heat budget of the Passy Valley atmosphere.

The heat fluxes are computed from the non-linear advective term of the density-weighted volume-averaged heat budget equation over the PASSY control volume, that is, assuming incompressibility,

$$\begin{aligned} \mathrm{ADV} = \int_V \rho\, v_j \,\frac{\partial \theta}{\partial x_j}\, dV = \sum_i \int_{A_i} \rho\, \left(\theta'\, v_j\right)\, n_j\, dS = \\ H_{\mathrm{DS}} + H_{\mathrm{MGV}} + H_{\mathrm{CHMNX}} + H_{\mathrm{STGV}} + H_{\mathrm{TOP}}, \end{aligned} \tag{V.2}$$

where $\theta' = \theta - \overline{\theta}$ and $\overline{\theta}$ is the volume-averaged potential temperature in the PASSY volume [see for instance Lee et al., 2004], and A_j the lateral and top surfaces of the volume, defined in Sect. V.5.1. In order to quantify the contribution of advective processes to the heat budget of the valley atmosphere, the ADV term above is compared with the density-weighted volume-averaged total tendency, that is

$$\mathrm{TEND} = \int_V \rho\, \frac{\partial \theta}{\partial t}\, dV. \tag{V.3}$$

The effect of the heat fluxes through the tributaries on the thermal structure of the CAP is evaluated by investigating the temporal evolution of the CAP height, CAP_h, and the bottom height of the capping inversion, CI_h. CAP_h is defined as the maximum height where the vertical gradient of absolute temperature is positive and CI_h is defined as the height where the signed curvature of $\theta\,(z)$ presents a positive maximum. It should be noted that, during P2, when a capping inversion layer exists within the valley atmosphere, CAP_h is very close to the top height of this layer, so that the depth of the capping inversion d can be approximated as $d = \mathrm{CAP}_h - \mathrm{CI}_h$.

In WRF-R the temporal evolution of TEND during P2 follows that of the advection contribution ADV (see Fig. V.13a). TEND is largely controlled by ADV during P2a while it is close to zero during P2b (as a result of the balance between ADV and the

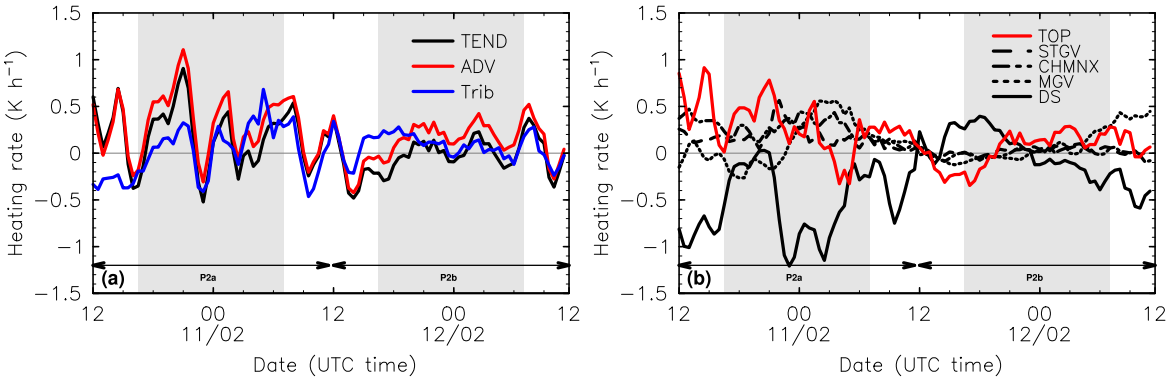

Figure V.13: (a) Timeseries of the density-weighted total potential temperature tendency (TEND), advection contribution (ADV) to the total tendency and that restricted to the tributaries (Trib, horizontal advection), averaged over the PASSY volume (see Fig. V.1b), for the period from 10 February 2015 at 1200 UTC to 12 February 2015 at 1200 UTC in WRF-R; (b) Timeseries of the horizontal advection contribution to the total tendency from DS, MGV, CHMNX and STGV (see Fig. V.1b). The nighttime periods (from sunset to sunrise) are displayed as grey shading.

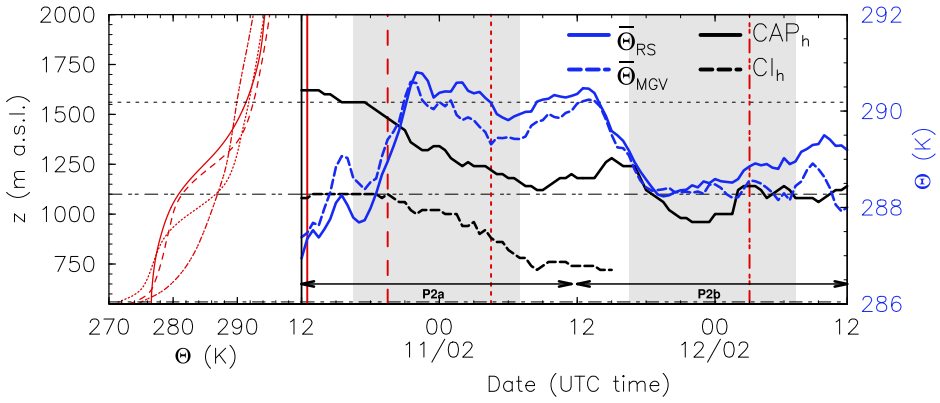

Figure V.14: Timeseries of the heights of the cold-air pool (CAP_h) and of the capping inversion (CI_h), and potential temperature at the RS and MGV sites (see Fig. V.1b), vertically-averaged in the height range $1150 < z < z_m = 1560$ m a.s.l ($\overline{\theta}_{RS}$ and $\overline{\theta}_{MGV}$, respectively), for the period from 10 February 2015 at 1200 UTC to 12 February 2015 at 1200 UTC in WRF-R. Note that there is no capping inversion after 1500 UTC on 11 February 2015. Dashed lines indicates the height of the valley floor at MGV (1100 m a.g.l.) and $z_m = 1560$ m a.s.l. (see Fig. V.1c). The nighttime periods (from sunset to sunrise) are displayed as grey shading.

contributions from turbulent heat and radiative flux divergences). The large variations in ADV during P2a are associated the variability of the advection contributions from the tributaries and top surface of the valley volume.

During the early night of P2a until 2200 UTC, when the flow through MGV is out of the valley volume (see Fig. V.10a), CAP_h decreases from $z = z_m$ to $z = 1300$ m a.s.l. principally as a result of warming of the upper-part of the CAP contributed by subsiding motions across the top surface of the valley volume (70%) and ADV through the other two tributaries, CHMNX and STGV (30%); see Fig. V.10b.

This result explains why later on the direction of the flow in MGV reverses from up- to down-valley. When it is up-valley, i.e. flowing from RS towards MGV, CI_h is about the height of the valley floor at MGV and $d \simeq 500$ m. Hence, the upper-part of the CAP above the height of the valley floor at MGV is colder at RS than at MGV (see Fig. V.14), leading to a pressure gradient between the two sites directed out of the valley. As warm air is advected in the upper-part of the CAP, the capping inversion sharpens (i.e. d decreases) and the temperature in the upper-part of the valley atmosphere becomes higher at RS than at MGV (see Fig. V.14), and the pressure gradient reverses to be directed into the valley.

As the flow through the tributaries strengthens during the course of the night of P2a, the heat flux through the tributaries increases. Most of the heat input (warming) through MGV, STGV and CHMNX is balanced by the heat export (cooling) through DS (see Fig. V.13a). From 0200 to 0600 UTC when the mass flux through the tributaries is maximum (see Fig. V.10a) and CAP_h and CI_h decrease continuously with time, ADV is mostly controlled by the heat flux through the tributaries (see Fig. V.13a and V.14). The analysis of the heat budget together with that of Fig. V.8 confirm that the upper-part of the CAP extending below CI_h is continuously displaced downstream out of the valley, and replaced by warm air through the tributary valleys (mainly MGV after 0200 UTC). The CAP displacement leads to a continuous decrease of CAP_h and CI_h during the course of the night. CI_h reduces to 150 m a.g.l. by 0900 UTC and the capping inversion is destroyed completely at 1500 UTC. This process is similar to the one associated with an impinging Föhn flow on a CAP, as described by Jaubert et al. [2005] and Flamant et al. [2006].

Turbulent mixing processes (for instance induced by internal gravity wave breaking or a hydraulic jump) in the upper-part of the CAP may be important to reduce locally the depth of the capping inversion d. The gradient Richardson number Ri at $z = 1000$ and 1100 m a.s.l. at the RS was found to be mostly larger than 1 during P2a and to fall below the critical value $Ri_c = 0.25$ only around 0130 and 0430 UTC (not shown), indicating that turbulent mixing played only a minor role in controlling the thermal structure of the upper-part of the CAP.

During P2b, the heat fluxes through the tributary valleys are generally weaker than during P2a (see Fig. V.13b). From 1200 to 2000 UTC the channelling of the large-scale flow into the valley through DS led to a substantial heat input (warming) in the upper-part of the CAP, balanced by the heat export (cooling) through the top surface of the valley volume (see the continuous decrease in potential temperature, averaged in the height range $1150 < z < z_m = 1560$ m a.s.l. in Fig. V.14). This heat export results from upward vertical motions induced by the convergence of the tributary flows that detrain in the upper-part of the CAP and of the channelled flow through DS. This leads to a further decrease of CAP_h. At 2000 UTC, H_{DS} and H_{TOP} change sign as was

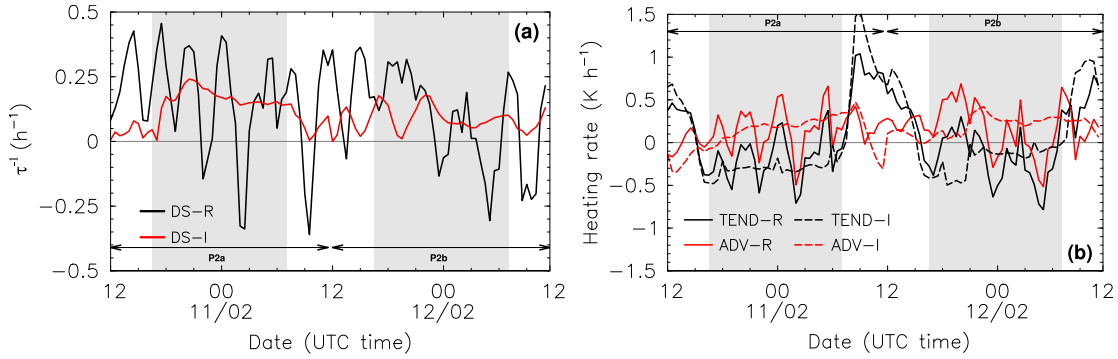

Figure V.15: (a) Timeseries of the inverse of the near-surface ($z < z_{100} = 100$ m a.g.l.) mass turnover time τ associated with the mass flux through the downstream (DS) gate (see Fig. V.1b) for the period from 10 February 2015 at 1200 UTC to 12 February 2015 at 1200 UTC in WRF-R and WRF-I. (b) Timeseries of the density-weighted total potential temperature tendency (TEND) and advection contribution (ADV) to the total tendency, averaged over the PASSY volume from the ground surface to $z = z_{100}$, for the period from 10 February 2015 at 1200 UTC to 12 February 2015 at 1200 UTC in WRF-R and WRF-I. The nighttime periods (from sunset to sunrise) are displayed as grey shading.

the case for the mass fluxes (see Fig. V.10a), becoming negative (cooling) and positive (warming), respectively. From this time on and until 1200 UTC, ADV is controlled by the interplay between subsiding motions at the valley top and heat fluxes through MGV and DS, which are modulated by the oscillations of the subsiding motions.

V.6 Factors controlling the near-surface inversion layer

The near-surface ($z < z_{100} = 100$ m a.g.l.) mass fluxes through DS in WRF-R and WRF-I are comparable (see Fig. V.11). Hence, it is instructive to compare their associated near-surface mass turnover time [see for instance Whiteman et al., 1996],

$$\tau = \frac{[\text{Mass}]^{z<z_{100}}}{M_{\text{DS}}^{z<z_{100}}}, \tag{V.4}$$

where $[\text{Mass}]^{z<z_{100}}$ is the mass of the PASSY control volume below $z = z_{100}$ and $M_{\text{DS}}^{z<z_{100}}$ is the mass flux through DS, vertically-integrated up to $z = z_{100}$. Although the dimension of τ is time, its sign depends on the direction of the flow through DS. If $\tau > 0$, the flow is out of the valley and τ measures the time required to renew the air mass within the the PASSY volume below $z = z_{100}$ through DS. Conversely, if $\tau < 0$ the flow through DS is into the valley and the near-surface air is stagnant within the valley. τ displays temporal oscillations with a period of approximately 3–4 hours (see Fig. V.15a), which are the signature of the internal gravity waves excited by the flow

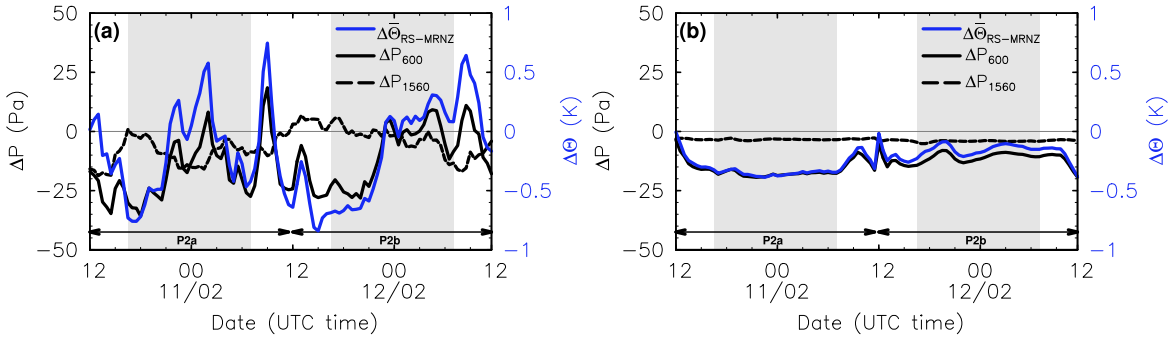

Figure V.16: Timeseries of the pressure difference at $z = 600$ m a.s.l. (ΔP_{600}) and at $z = z_m = 1560$ m a.s.l. (ΔP_{1560}), and difference in potential temperature, vertically averaged in the height range $600 < z < z_m = 1560$ m a.s.l. ($\Delta\overline{\theta}_{\text{RS-MRNZ}}$), between the RS and MRNZ sites (see Fig. V.1b) in WRF-R (a) and WRF-I (b). The nighttime periods (from sunset to sunrise) are displayed as grey shading.

through the tributary valleys. As pointed out in Sect. V.5.1, such oscillations are not present during P2a in WRF-I. The amplitude of the oscillations of τ in WRF-R is fairly large compared to its mean positive value during both P2a and P2b and makes τ to vary between positive (outflow) and negative (inflow) values. During P2a, the average value of τ over a period of oscillation decreases with time during the course of the night and the nighttime average is about 7 hours in both WRF-R and WRF-I. The similar trend of τ in WRF-R and WRF-I suggests that the near-surface drainage out of the valley is controlled by local thermally-driven flows but is modulated by the non-local control of the large-scale flow on the flows through the tributaries. The temporal evolution of τ during P2b differs in WRF-R and WRF-I. In WRF-R the average value of τ over a period of oscillation is about 4.5 hours before 2200 UTC and increases to more than 24 hours later on. By contrast, the nighttime average of τ in WRF-I in about 10 hours. This suggests that non-local controls of the large-scale flow are playing a role in the near-surface drainage during P2b in WRF-R.

Chemel et al. [2016] reported a systematic reduction in the observed PM_{10} (suspended particulate matter with aerodynamic diameters less than 10 μm) concentration in the Passy Valley between 2200 UTC and 0600 UTC during January and February 2015. Several mechanisms were hypothesised in order to explain the observed reduction in PM_{10} concentration at nighttime, including that thermally-driven drainage flows could export air out of the valley throughout the night. The analysis presented above indicates that the air mass in the near-surface atmosphere can be fully removed in a time-scale consistent with that observed by Chemel et al. [2016]. However, during P2b the stagnation of the air within the valley after 2200 UTC suggests that the drainage of the air out of the valley cannot be the sole explanation for the observed reduction in PM_{10} concentration at nighttime.

In order to elucidate the impact of non-local processes on the thermal structure

of the near-surface atmosphere above the valley floor, the tendency (TEND) and advection (ADV) terms of the heat budget (see Sect. V.5.2), averaged from the ground surface to $z = z_{100}$, are shown in Fig. V.15b. The temporal evolution and magnitude of both TEND and ADV during the morning and evening transitions (0700 to 0900 UTC and 1300 to 1500 UTC, respectively) is similar in WRF-R and WRF-I, indicating that local processes control the heat budget of the near-surface atmosphere during these transition periods. During P2a TEND and ADV display a similar trend in WRF-R and WRF-I during nighttime. During P2b, the trends are opposite: in WRF-R TEND and ADV decrease with time during the night while in WRF-I they increase. Note that as the consequence of the stagnation of the air mass in WRF-R in the late night during P2b, ADV fluctuates about zero. This difference between WRF-R and WRF-I during P2b is a result of the evolution of the large-scale flow. As the south-southeasterly large-scale flow strengthens during the course of the night, favouring channelling through MGV, subsidence of warm air at the top of the CAP reduces the horizontal temperature contrast between the valley centre and outside the valley towards MRNZ (see Fig. V.1b). This leads to a reduction in the near-surface pressure difference driving the down-valley flow between RS and MRNZ between 2100 and 0000 UTC (see Fig. V.16), leading to the stagnation of the near-surface air within the valley. This reduction is not as marked in WRF-I and the near-surface horizontal pressure difference between RS and MRNZ continues to drive a down-valley flow throughout the night (see Fig. V.16b).

V.7 Summary and conclusions

The purpose of the present work was to examine local and non-local controls on a persistent cold-air pool that formed in the Passy Valley in February 2015 using numerical model simulations. The Passy Valley is a region of truly complex terrain with steep slopes and three major tributary valleys, Megève, Saint-Gervais-les-Bains and Chamonix (see Sect. V.2.1). The numerical model simulations were performed using the Weather Research and Forecasting model at a horizontal-grid resolution of 111 m, carefully initialised (see Sect. V.2 for details on the design of the numerical model experiments) and found to realistically capture features of the persistent cold-air pool.

The cold-air pool formed in the evening on 9 February 2015 as a result of advection of warm air, associated with the passage of an upper-level ridge, above the Passy valley at the mean height of the terrain surrounding the valley, which set the height of the cold-air pool during its formation stage. The effects of the large-scale flow on the cold-air pool during its persistent stage, from 10 February 2015 at 1200 UTC to 12 February 2015 at 1200 UTC, was quantified by examining the mass and heat budget of the atmosphere at the valley scale and in the near-surface layer above the

valley floor (lowest 100 m). The horizontal mass and heat fluxes through the tributary valleys were quantified and compared to vertical fluxes across the valley top, in order to determine the role of the tributary flows during the persistent stage of the cold-air pool event.

The analysis showed that the thermal structure of the upper-part of the cold-air pool during the persistent stage, and in particular the height of the inversion, was controlled primarily by vertical advection at the valley top and from the flows through the tributary valleys. Conversely the near-surface atmosphere was mainly controlled by local processes, when the upper-level ridge moved over the Passy Valley, while it was strongly affected by the large-scale flow when the upper-level ridge moved away from the valley. More specifically, this transition in the large-scale flow led to a change of the direction of the flow in the Megève tributary valley, which substantially modified the dynamics and thermal structure of the Passy Valley atmosphere.

When the upper-level ridge passed over the Passy Valley (between 10 and 11 February 2015), the upper-part of the cold-air pool was found to be mostly controlled by the advection of warm air from the tributary valleys and vertical motions at the valley top. However, while the flow through the Chamonix and Saint-Gervais-les-Bains tributary valleys were down-valley (i.e. into the Passy Valley) throughout the night and supplied about 50% of the air mass that drained out of the valley, the flow through the Megève tributary valley was either up- or down-valley depending on the height of the cold-air pool with respect to the height of the tributary. As long as the height of the cold-air pool in the Passy Valley was about the height of the valley floor of the Megève tributary valley, the air was forced to flow out of the Passy Valley towards Megève, because of the thermally-induced horizontal pressure difference between the two valleys. The warm air advection through the Chamonix and Saint-Gervais-les-Bains tributary valleys and across the valley top decreased the cold-air pool height, which led to the reversal of the temperature difference between Passy and Megève, forcing a down-valley flow from Megève towards Passy. As this flow accelerated downslope, creating an hydraulic jump, it displaced the elevated capping inversion at the top of the cold-air pool towards the downstream part of the Passy Valley. The cold air was replaced by the warmer air transported by the tributary flow, thereby reducing progressively the height of the cold-air pool. The dynamics and thermal structure of the near-surface atmosphere above the valley floor was found to be almost decoupled from the upper-part of the cold-air pool and to be controlled by and large by local processes, although the flow was modulated by internal gravity waves generated by the hydraulic jump.

As the upper-level ridge moved away from the Passy Valley, the circulation above the Passy Valley was strongly ageostrophic, with a south-westerly flow over the Swiss Plateau, which was channelled into the Passy Valley through the downstream part of the valley towards Marnaz. However, the near-surface flow in the Passy Valley

remained down-valley. The heat fluxes through the tributary valleys were found to have a minor impact on the heat budget of the Passy Valley atmosphere, which was mostly controlled by the inflow of air through the downstream part of the valley and vertical advection at the valley top. As the south-southeasterly large-scale flow strengthened during the course of the night, favouring channelling through the Megève tributary valley, subsidence of warm air at the top of the cold-air pool reduced the temperature contrast between the valley centre and outside the valley towards Marnaz, leading to stagnant air over the valley floor.

The present work calls for a better characterisation of the controls of tributary flows and of varying large-scale flows on cold-air pooling. This would require an approach based on the climatology of the area to identify the prevalence of weather patterns. Future field campaigns should consider instrumenting the main tributary valleys and collecting long-term datasets to sample an extended range of synoptic forcings.

Acknowledgments

This work has been supported by a grant from LabEx Osug@2020 (Investissements d'avenir – ANR10LABX56). Numerical model simulations were performed using the UK national supercomputing facilities (ARCHER), accessed through the UK National Centre for Atmospheric Science (NCAS).

VI

Summary and Conclusions

VI.1 General conclusions

The aim of this thesis was to improve the understanding of physical processes governing the structure and evolution of the stable boundary layer in deep Alpine valleys under dry conditions and weak synoptic winds. The work used an integrated approach with idealised and real-case simulations. The numerical simulations were performed with the Weather Research and Forecast (WRF) model. The work contributes to an improved understanding of the effects of surrounding terrain (plains, valleys or tributaries) on the heat and mass budgets of the stable valley boundary layer. The following discussion responds to the research objectives outlined in Sect. II.5.

A valley opening on a plain represents the simplest model that allows for a three-dimensional valley-wind system to develop. In this simple framework, the interactions between thermally-driven flows and a developing cold-air pool was described and the effects on heat and mass budgets quantified (see Chapter III). Results were contrasted with those for an infinitely long valley (i.e. two-dimensional). A key point shown by the analysis is that downslope flows do not cease as soon as a three-dimensional along-valley flow can develop. In a two-dimensional valley, the speed of downslope flows decreases with time and so does their effect on the cooling processes of the valley boundary layer. In a three-dimensional valley two regimes can be identified: a transient regime, before the down-valley flow develops, followed by a quasi-steady regime, when the down-valley flow is fully-developed. The quasi-steady regime of the down-valley flow is characterised by a balance between the pressure force and advection in the along-valley direction. In this sense, the flow behaves as 'a flow in a pipe', with the cross-sectional area of the pipe set by the depth of the boundary layer (see Fig. VI.1a). The time for the quasi-steady regime to be reached is found to be proportional to the time-scale associated with the linear wave solution of the simplified along-valley flow equation derived by Egger [1990]. The coefficient of proportionality was found to be about 3, in agreement with what is suggested in the literature.

The development of a down-valley flow from the valley towards the plain changes

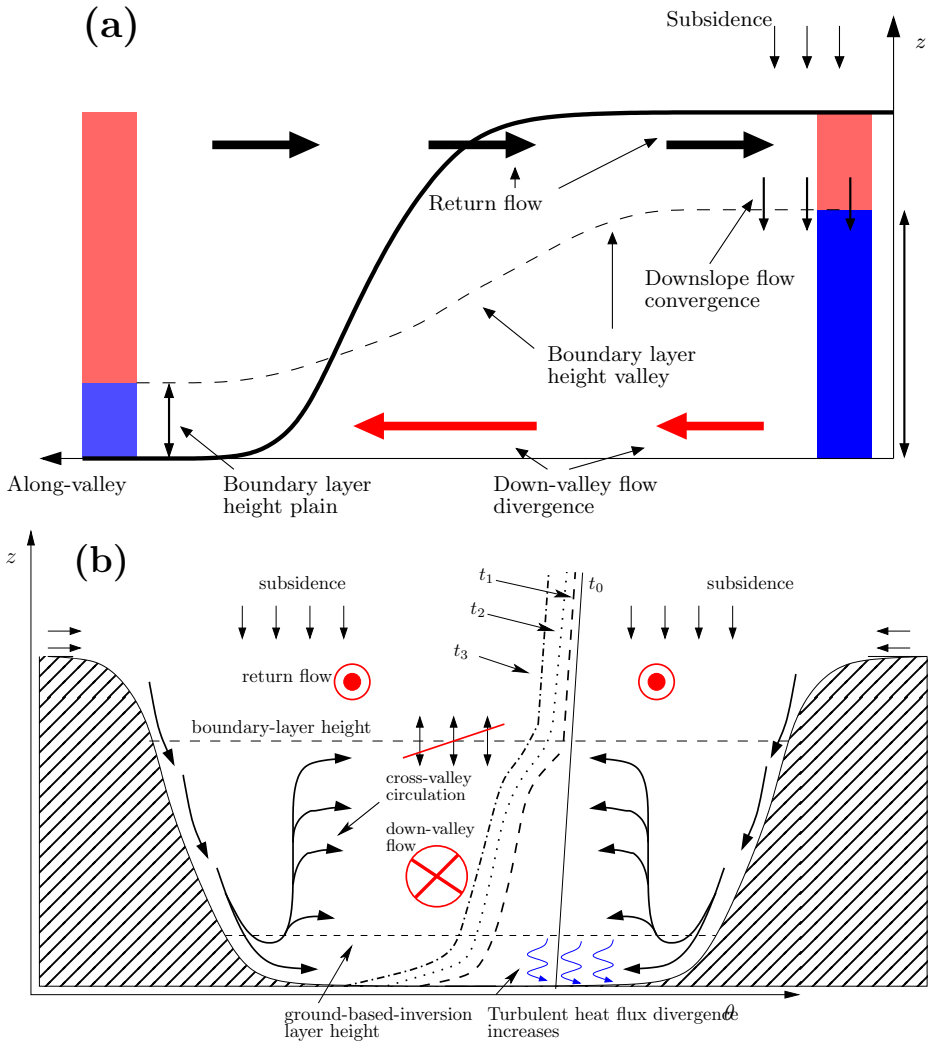

Figure VI.1: Schematic diagrams of **(a)** along-valley section showing the difference in the boundary-layer height between the plain (left) and the valley (right) which force the down-valley flow, with the main mechanisms coming into play in the mass budget of the valley; **(b)** cross-valley section showing the main phenomena and processes affected by the down-valley flow development and potential temperature profiles at times $t_1 < t_2 < t_3$ after that a quasi-steady regime is reached.

the downslope-flow-induced circulation and so the cooling processes within the valley. The along-valley divergence of the down-valley flow requires convergence of mass in the centre of the valley, thence vertical motions induced by the downslope flows convergence over the valley centre stops and a cross-valley circulation forms from the sidewalls towards the valley centre (see Fig. VI.1b). In the quasi-steady regime cooling rates were found to be uniform in the vertical direction for both the two-dimensional and three-dimensional valleys, above the strongly stratified ground-based inversion layer. Therefore the stability of the upper-part of the valley atmosphere hardly varied with time, and it was similar between the two-dimensional and three-dimensional valleys (see Fig. VI.1b). However, advection leads to a warming in the three-dimensional

valley and to a cooling in the two-dimensional valley. Considering volume-averaged quantities, the contribution from turbulent heat flux divergence increases by a factor of 3 compared to the two-dimensional valley, because of the development of the down-valley flow. In spite of this, the cooling due to this process was overtaken by the warming due to advection, and the cooling of the valley boundary layer in the three-dimensional valley was found to be about 3 times smaller than in the two-dimensional valley.

As a step towards modelling the complexities of real-world valleys, a system of two valleys was studied (see Chapter IV). Upstream valleys that open either on a wider valley (draining configuration) or on a narrower valley (pooling configuration) downstream were considered, and compared to the respective valley-plain configurations. A key result is that for all the configurations considered, a quasi-steady regime is reached associated with down-valley flows within the valley. However these flows are delayed and generally weaker for pooling and draining configurations, because of the reduced difference in the thermal structure of the atmosphere along the valley axis. As a result, the duration of the transient regime depends on the configuration, and it is found to increase for pooling and draining configurations when compared to the respective valley-plain cases. For pooling configurations it is the longest, and increases as the width of the downstream valley decreases. For strong pooling, the downstream valley can be colder than the upstream valley within the transient regime, thereby reversing the pressure gradient, causing up-valley flows from the downstream to the upstream valley. The impact on the cooling processes in the upstream valley largely depends on the regime and on the configuration of the valley system. During the transient regime, the volume-averaged cooling rate at the valley-scale is larger for pooling configurations compared to that for the respective valley-plain configuration (by more than 50 % for strong pooling). The enhanced cooling stems from the reduction of the warming contribution from both the vertical and along-valley heat fluxes. The along-valley heat flux in particular shows the greatest variations, because of the impact of pooling on the along-valley flows. For the strong pooling case, the along-valley heat flux can contribute to cool the upstream valley, because of the transport of cold air along the valley associated with the up-valley flow. In the quasi-steady regime, both along-valley and vertical heat fluxes contribute to the warming of the valley atmosphere, regardless of the configuration considered. For valley-plain and draining configurations the along-valley heat flux controls the warming contribution to the valley heat budget from advection, exporting colder air out of the upstream valley atmosphere. For pooling configurations, the along-valley heat flux is reduced and for strong pooling, it is almost negligible. The vertical heat flux increases compared to that for the respective valley-plain case (by a factor of 5 for strong pooling) but, in spite of this, the net contribution to the valley heat budget from advection is reduced for pooling configu-

rations. However, weaker down-valley flows also lead to a smaller cooling contribution from the surface sensible heat flux, as it is proportional to the wind speed close to the surface. It was found that in the quasi-steady regime the sum of the contributions from advection and surface sensible heat flux hardly varies between the different configurations, and the cooling rate of the upstream valley is almost independent of the configuration. A dimensionless form of the heat budget adapted from Whiteman et al. [1996] was introduced in order to quantify the fraction of the sum of surface sensible heat flux and radiative heat flux divergence that contribute to cool the valley atmosphere compared to advection, i.e. the cooling efficiency of the valley. The cooling efficiency increases for strong pooling compared to the respective valley-plain configuration, while it was found to decrease for the draining configuration. As a result of the effects on the cooling processes, draining and pooling configurations induce deeper and colder valley boundary layers compared to the respective valleys opening directly on a plain. This effect is particularly pronounced for the pooling configurations.

The role of the different mechanisms contributing to the mass budget of the valley atmosphere was quantified. When considering the valley boundary layer only, the mass budget of the valley is largely driven by a balance between the divergence of down-valley flows in the along-valley direction and the convergence of downslope flows at the top of the boundary layer (see Fig. VI.1b). The net contribution from downward vertical motions far from the slopes to the mass budget was found negligible. In this sense, the slope layer is a "preferred route" to follow for air masses in order to replace the air that drains out of the valley along the valley axis. When considering the scale of the valley plain circulation, the vertical mass flux at the top of the boundary layer is driven by an interplay between the along-valley convergence of the return flow, subsiding motions above the valley and horizontal convergent motions from the plateaux (see Fig. VI.1a). In a valley-plain configuration the contribution from the return flow balances the contribution from the other mechanisms. In pooling configurations, the deeper boundary layer leads to a deeper down-valley flow layer, with no return flow aloft. Hence, subsiding motions at the valley top and horizontal convergent motions from the plateaux solely contribute to the inflow of air through the slope layer at the top of the boundary layer.

Finally, a case-study of a persistent cold-air pool event in a deep Alpine Valley was analysed in order to quantify the effects of neighbouring valleys on the heat and mass budgets of the atmosphere of a real valley (see Chapter V). The episode occurred in a section of the Arve River Valley around the town of Passy (referred to in the present work as the Passy Valley) from 8 to 14 February 2015 during an intensive observation period (IOP) of the PASSY-2015 field campaign, characterised by weak wind speeds during the persistent stage of the event, but with varying direction from day to day. In order to determine the effect of the large-scale forcing on the dynamics

and thermodynamics of the boundary layer, the real-case simulation was contrasted with a *semi-idealised* simulation. This semi-idealised simulation used a real topography and land cover, but idealised initial and boundary conditions were specified.

The mass and heat fluxes from the tributary valleys, namely the Megève, Saint-Gervais-les-Bains and Chamonix Valleys, were quantified during the persistent stage of the event, from 10 February 2015 at 1200 UTC to 12 February 2015 at 1200 UTC. The contribution of these flows to the heat and mass budgets of the Passy Valley atmosphere were found to be variable from day to day, depending on the large-scale conditions. A key result is that the flows through the tributary valleys contributes significantly to the vertical thermal structure of the upper-part of the cold-air pool, while local thermally-driven flows were found to play a minor role in this layer. When the upper-level ridge passed over the Passy Valley during the persistent stage, that is between 10 and 11 February 2015, the continuous decrease of the height of the inversion and the destruction of the capping inversion at the top of the cold-air pool were found to be controlled by horizontal advection of warm air from the tributary flows and vertical warm air advection at the valley top. Mass fluxes in and out of the valley were found to be an order of magnitude larger for the real-case simulation than that for the semi-idealised simulation. This indicates that the large-scale conditions, even though characterised by relatively weak wind speed (< 15 m s^{-1} during the persistent stage), have an impact on the magnitude of these flows. The mass flux into the Passy Valley through the Saint-Gervais-les-Bains and Chamonix Valleys accounted for about 50 % of the total drainage out of the Valley and it was found to be comparable to the relative contribution of these two tributaries in the semi-idealised simulation. The direction of the flow in the Megève Valley was found to be sensitive to the height of the boundary layer in the Passy Valley with respect to that of the valley floor of the Megève Valley. When the cold-air pool was higher then the height of the valley floor of the Megève Valley, the atmosphere in the upper-part of the Passy Valley was found to be colder than the one in the tributary valley, thereby forcing the flow out of the Passy Valley. As the cold-air pool height decreased throughout the night between 10 and 11 February 2015, the reversal of the temperature difference led to a strong down-valley flow from the Megève Valley which dominated the heat and mass budgets of the Passy Valley atmosphere for the rest of the night. Even though the tributary flows largely impacted the upper-part of the cold-air pool when the upper-level ridge passed over the Passy Valley, the near-surface atmosphere was mainly controlled by local thermally-driven down-valley flows, with a modulation due to internal waves generated by the flow through the tributaries.

On the subsequent day, when the upper-level ridge moved away from the Passy Valley, during the first part of the night the circulation in the upper-part of the cold-air pool was found to be strongly affected by the channelling of the large-scale flow from

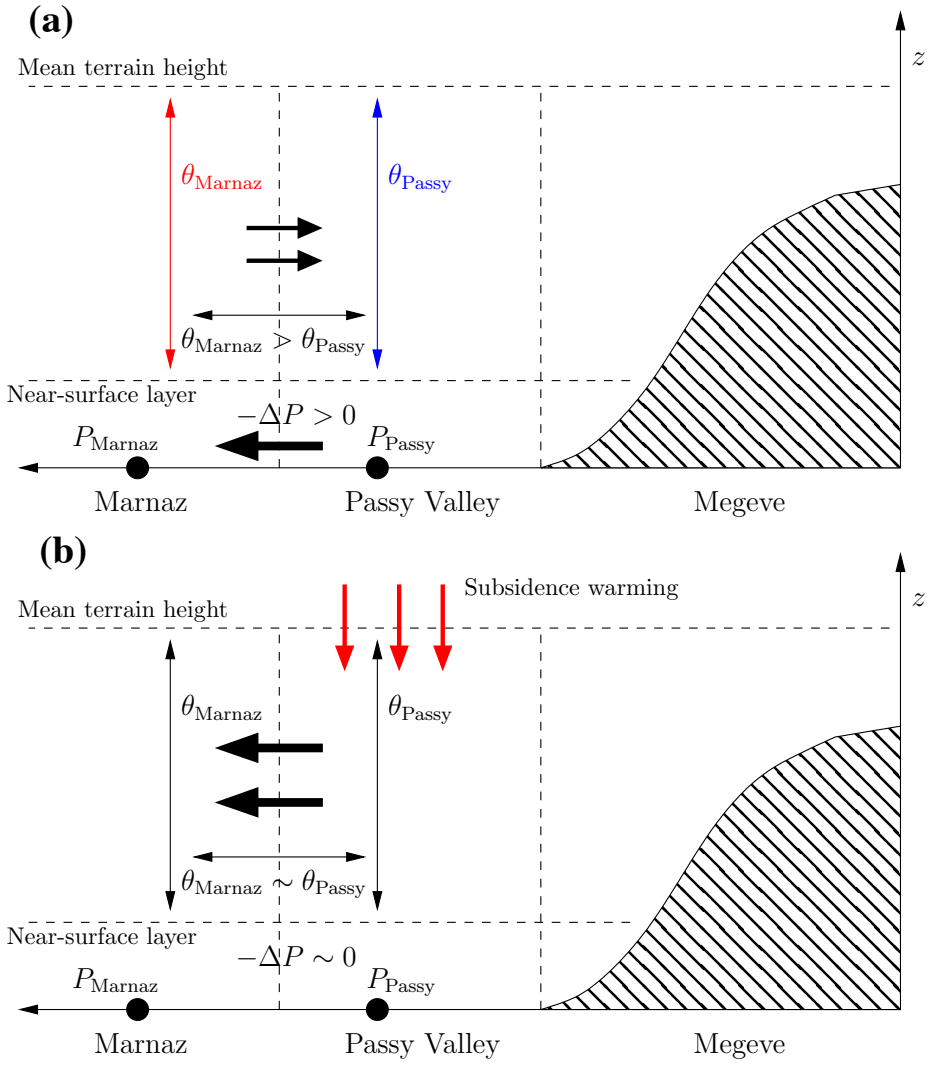

Figure VI.2: Schematic diagrams in a z-along-valley section of the controls on the near-surface atmosphere of the section of the Arve River Valley around the town of Passy when the upper-level ridge moved away from the Passy Valley; **(a)** during the first part of the night, the flow is channelled from Marnaz towards Megève in the upper-part of the valley, and the upper-part of the atmosphere is colder in the Passy Valley than in Marnaz, hence forcing thermally-driven down-valley flows in the near-surface atmosphere; **(b)** the temperature difference in the upper-part of the cold-air pool is reduced because of subsidence warming, thence the pressure difference at the surface is reduced and no down-valley flows form; the air is stagnant within the valley. See the text and Chapter V for details.

the near Swiss Plateau into the valley, with a minor effect of tributary flows on the heat budget of the valley atmosphere. The near-surface flow was down-valley (i.e. in the opposite direction of the flow in the upper-part of the cold-air pool), as a result of the positive near-surface pressure difference along the valley axis (see Fig. VI.2a). During the second part of the night, the air was found to be stagnant in the near-surface atmosphere, because of the reduction of the near-surface pressure difference forcing the down-valley flow. This reduction was primarily due to the strengthening of

the south-southeasterly large-scale flow, which led to subsidence warming at the top of the valley associated with the reversal of the flow out of the valley. This process led to a reduction of the horizontal temperature difference between the upper layer of the valley atmosphere and that outside of the valley (see Fig. VI.2b), thereby favouring stagnation close to the ground.

VI.2 Outlook

The general lesson learnt from this work is that the surrounding terrain can have profound impact on cold-air-pooling processes. This aspect requires further research, to provide a more complete understanding of the interactions between different elements of a mountain range. In the following a few ideas and concepts are developed for future research, on the basis of the conclusions, and limitations, of the present work.

The idealised simulations performed in the present work considered fully decoupled conditions associated to the formation of diurnal cold-air pools, that is the wind aloft was set to zero, and so no advection of warm/cold air aloft was considered. Process-level studies on persistent cold-air pools had focussed on their break-up due to turbulent erosion mechanisms [Lareau and Horel, 2015b]. There is a need for a better understanding of the link between cold-air pools, terrain features and wind aloft. A first question concerns the terrain features leading to the persistence of a cold-air-pool over multiple days during wintertime. For such episodes, the incoming radiative heating from the sun is usually insufficient to destroy the stable stratification that builds up from the ground and is enhanced 'from the top' because of warm-air advection aloft. Energetics models for real-case studies have been developed, neglecting advective processes or taking them into account using a simple functional dependency on the valley heat deficit [Largeron, 2010]. Leukauf et al. [2015] developed an energetic model for the time required to destroy completely a cold-air pool, which took into account heat transport processes associated with daytime thermally-driven up-slope flows. The analysis was restricted to a two-dimensional idealised valley, and the sensitivity to the radiative forcing was investigated. A step forward will be to quantify the dependency of cold-air pool persistence on the depth of the valley, given a certain warm-air advection aloft. This can be accomplished by means of idealised numerical simulations, varying systematically the non-dimensional depth of the valley, defined in Sect. II.3.2.a. As persistent cold-air pools usually develop in *deep* valleys a threshold value for the non-dimensional depth of the valley can be expected, above which the cold-air pool persists given a certain solar forcing throughout the day. An energetic model such as the one outlined by Leukauf et al. [2015] can be used, taking into account the heat exchanges associated not only with the valley flows, but also with the external flow.

Results of Chapter V for the Arve River Valley indicated that any scalar quantity (e.g. air pollutant, moisture) in the tributary valleys can be efficiently transported within the valley atmosphere, thereby impacting atmospheric composition in the valley. However, the analysis did not investigate the fraction of such quantity detrained over the near-surface inversion compared to that entrained close to the ground. Such quantification requires numerical simulations that track passive tracers. The design of these simulations should put particular emphasis on the emission inventory used. The experiments should be designed in order to quantify the contribution from the tributaries to the passive tracer concentration found at the valley bottom. This can be accomplished for instance, by switching off the emissions over the valley floor of the Arve River Valley, keeping only the emissions from the tributaries.

A

Valley heat deficit as a bulk measure of particulate air pollution in the Arve River Valley

---

The numerical simulations described in Chapter V covered only a fraction of the PASSY-2015 field campaign that was held in the Arve River Valley during the winter of 2014-2015. This appendix gives context for the detailed analysis presented in Chapter V, exploiting a dataset that extends over a two-months time period (January and February 2015), collected during the PASSY-2015 field campaign. The appendix focusses on the relationship between the bulk atmospheric stability (the valley heat deficit) and PM_{10} concentration within the valley at the diurnal and sub-diurnal time scales. This is realised using temperature profiles retrieved from a microwave radiometer, which sampled continuously the valley atmosphere throughout the two-months time period. The analysis of the measured cooling rate of the valley atmosphere allows us to propose a possible meteorological mechanism that may account for the sub-diurnal variability of PM_{10} concentration within the valley. This hypothesis was investigated by means of numerical simulations in the case-study presented in Chapter V.

This appendix is a reproduction of Chemel et al. [2016]. The candidate's contribution is 50 % of the study. The candidate contributed to the processing of the microwave radiometer temperature data and the interpretation of the results.

Abstract Urbanized valleys are particularly vulnerable to particulate air pollution during the winter, when ground-based stable layers or cold-air pools persist over the valley floor. We examine whether the temporal variability of PM_{10} concentration in the section of the Arve River Valley between Cluses and Servoz in the French Alps can be explained by the temporal variability of the valley heat deficit, a bulk measure

of atmospheric stability within the valley. We do this on the basis of temperature profile and ground-based PM_{10} concentration data collected during wintertime with a temporal resolution of one hour or finer, as part of the Passy-2015 field campaign conducted around Passy in this section of valley. The valley heat deficit was highly correlated with PM_{10} concentration on a daily time scale. The hourly variability of PM_{10} concentrations was more complex and cannot be explained solely by the hourly variability of the valley heat deficit. The interplay of the diurnal cycles of emissions and local dynamics is demonstrated and a drainage mechanism for observed nocturnal dilution of near-surface PM_{10} concentrations is proposed.

A.1 Introduction

Urbanized valleys often experience severe air pollution events during the winter, when a cold-air pool (CAP) lingers over the valley floor [e.g. Chazette et al., 2005; Malek et al., 2006; de Franceschi and Zardi, 2009; Gohm et al., 2009; Harnisch et al., 2009; Schnitzhofer et al., 2009; Silcox et al., 2012]. These CAPs are characterized by a strongly stratified ground-based temperature inversion, thereby suppressing vertical mixing of pollutants and decoupling the valley atmosphere from the generally stronger winds aloft, and can persist for multiple days, leading to an accumulation of pollution. These accumulations lead to PM_{10} (suspended particulate matter with aerodynamic diameters less than 10 μm) concentrations that exceed the daily average limit value of 50 μg m^{-3} required by the European Directive 2008/50/EC on ambient air quality and cleaner air for Europe not to be exceeded for more than 35 days in a calendar year. As an illustration of the extent of the problem, in Passy in the Arve River Valley in the French Alps, the number of days in a calendar year during which PM_{10} concentrations exceeded the daily average limit value of 50 μg m^{-3} has been greater than 35 days since the monitoring site was installed in 2007. This part of the Arve River Valley concentrates a mix of PM_{10} emission sources, including residential (wood) combustion, road transport with a major international route to Italy and industries, which contribute to elevated PM_{10} concentrations in stagnant CAPs. This problem is not isolated and is a major concern in complex terrain across the world [see for instance Green et al., 2015, for western US valleys], although legislation regarding pollution levels varies from country to country.

Previous works investigated relationships between wintertime particulate air pollution and meteorological variables in western US valleys. Silcox et al. [2012] related wintertime daily average $PM_{2.5}$ concentrations measured in the Salt Lake Valley, Utah, USA, during the Persistent Cold-Air Pool Study [PCAPS, Lareau et al., 2013a], to the valley heat deficit, a bulk measure of atmospheric stability within the valley, calculated using data from rawinsondes (RS) launched daily at 1200 UTC [0500 local time (LT)]

from the Salt Lake City International Airport. Daily average $PM_{2.5}$ concentrations were found well correlated and to increase with the valley heat deficit calculated at 0500 LT, which increased from day to day during persistent CAPs. The squared Pearson product–moment correlation coefficient r^2 was 0.61 (based on a linear regression of the data presented in their Fig. 3). However, this strong relationship manifested mostly as an association between low values of $PM_{2.5}$ concentrations and valley heat deficit.

Whiteman et al. [2014] extended this work and provided context for PCAPS by examining relationships between wintertime meteorological conditions and particulate air pollution in the Salt Lake Valley using data from twice-daily RS launched at 0000 and 1200 UTC (1700 and 0500 LT, respectively) from the Salt Lake City International Airport and daily average particulate air pollution measurements over a 40-year period from 1973 to 2003. A close association between $PM_{2.5}$ concentrations and valley heat deficit was found on winter, weekly and daily time scales, for the 15 winter seasons from 1998–1999 to 2012–2013 for which $PM_{2.5}$ concentration data were available. The correlation coefficient r^2 was 0.65 for daily average $PM_{2.5}$ concentrations for the winter seasons 1999–2000 to 2010–2011. Elevated $PM_{2.5}$ concentrations were found to be more likely to occur when snow cover was present, when surface pressure and column-mean valley relative humidity were high, and when column-mean valley temperature and wind speed were low. No statistically significant long-term trend in wintertime atmospheric stability within the valley could be detected in the 40-year record, indicating that the only option to improve air quality in such valleys is to consider stricter emission control strategies.

Green et al. [2015] examined relationships between daily average $PM_{2.5}$ concentrations and valley heat deficit, or differences between valley floor and ridge top temperatures, during wintertime in five western US valleys (Salt Lake City, Utah; Reno, Nevada; Boise, Idaho; Missoula, Montana; and Spokane, Washington). The valley heat deficit was calculated using data from twice-daily RS launched at 0000 and 1200 UTC (1700 and 0500 LT, respectively, for Salt Lake City, Boise and Missoula, and 1600 and 0400 LT, respectively, for Reno and Spokane) from nearby airports except for Missoula, where RS were not launched. For Missoula, differences between valley floor and ridge top temperatures were considered. $PM_{2.5}$ concentrations were highly correlated with valley heat deficit for all cities except Spokane, where the RS atmospheric profiles were not representative of the valley atmosphere. For all cities except Spokane, the correlation coefficient r^2 was greater for snow cover days than snow free days and was in the range 0.46–0.53. For a given valley heat deficit (or difference between valley and ridge top temperatures for Missoula) snow cover days experienced higher $PM_{2.5}$ concentrations than snow free days, mainly due to enhanced ammonium nitrate concentrations. This increase in ammonium nitrate concentrations is the result of increase secondary

formation under higher humidity and lower temperatures on snow cover days. This finding is consistent with that reported by Whiteman et al. [2014] that the probability of exceeding the daily average 35 μg m^{-3} US National Ambient Air Quality Standard in the Salt Lake Valley is roughly 4 times greater when there is snow cover present than when there is no snow cover. Weighting wintertime average $PM_{2.5}$ concentrations by the ratio of the specific winter average valley heat deficit to the long-term winter average valley heat deficit was found to reduce the winter-to-winter variability in $PM_{2.5}$ concentrations, allowing long-term trends to be more clearly identified so as to examine the effectiveness of emission control strategies.

The statistical relationships between daily average $PM_{2.5}$ concentrations and valley heat deficit reported by Silcox et al. [2012], Whiteman et al. [2014] and Green et al. [2015] are limited by the use of daily average values that cannot resolve shorter term variability. This study uses temperature profile and ground-based PM_{10} concentration data collected with a temporal resolution of one hour or finer, as part of the Passy-2015 field campaign conducted around Passy in the section of the Arve River Valley between Cluses and Servoz in the French Alps during the winter season 2014-2015 [Paci et al., 2015a,b; Staquet et al., 2015], characterized by typical wintertime meteorological conditions (not shown). We analyze the data to investigate

- whether conclusions from previous works as regards the relationships between daily average particulate air pollution and valley heat deficit are applicable to this section of the Arve River Valley;
- whether the hourly variability of PM_{10} concentrations in this section of the Arve River Valley can be explained by the hourly variability of the valley heat deficit.

The methodology is presented in Sect. A.2, results are presented and discussed in Sect. A.3, and conclusions are given in Sect. A.4.

A.2 Methodology

In the following the sites and instruments used in this work, namely a microwave radiometer (MWR) and PM_{10} monitor are described. The MWR data were collected during the main observation period of the Passy-2015 field campaign (from 10 January to 28 February 2015). We also use RS data collected during the intensive observation periods (IOPs) of the field campaign to compare to the MWR data.

A.2.1 Site

A topographic map of the section of the Arve River Valley between Cluses and Servoz in the French Alps is presented in Fig. A.1. LT is UTC+1 in the Arve River Valley

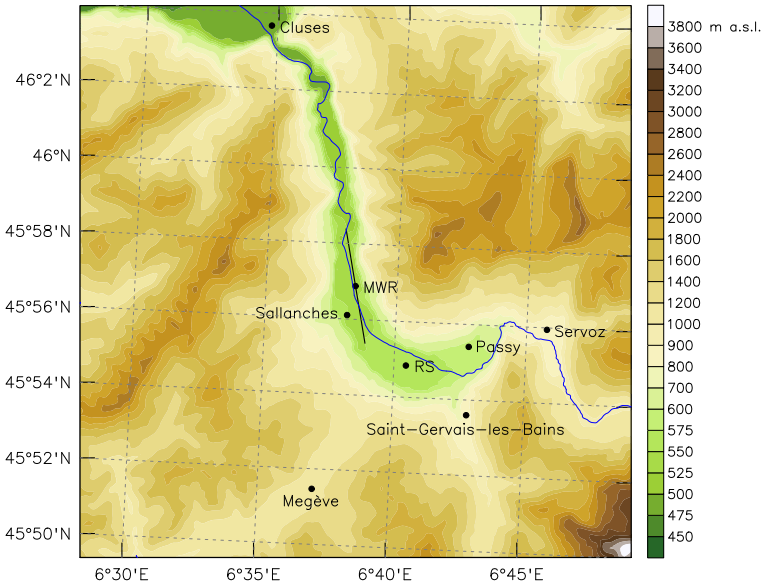

Figure A.1: Topographic map of the section of the Arve River Valley between Cluses and Servoz in the French Alps, displaying the terrain height (filled contours), Arve River (blue line) and location of the PM_{10} monitoring site in Sallanches, and of the rawinsonde (RS) and microwave radiometer (MWR) sites. The black line indicates the horizontal direction of the MWR beam, orientated 343° North.

Table A.1: Characteristics of the sites for the PM_{10} and meteorological measurements used in this paper and shown in Fig. A.1.

Site name	Latitude	Longitude	Elevation (m)	Instrument
Sallanches	45.93507	6.63556	542	TEOM™ FDMS
Rawinsondes (RS)	45.91400	6.67430	561	Rawinsonde
Microwave radiometer (MWR)	45.94800	6.64008	535	Microwave radiometer

during wintertime. The average times of sunrise and sunset above the horizon in this section of valley during the Passy-2015 field campaign main observation period were 0743 and 1743 LT, respectively.

This section of valley includes two major towns: Passy and Sallanches, with populations of 11,214 and 15,957 (2012 census), respectively. The valley-floor elevation decreases gradually down-valley from 588 m at Passy to 488 m at Cluses over a distance of 23 km, yielding an average slope of 0.25° between these two points. The width of the valley floor along this section of the valley increases gradually up-valley from just about 200 m at Cluses, where the valley presents a major constriction, to approximately 2,000 m near the location of the RS site, and hardly decreases from there towards the escarpment leading to Servoz. Table A.1 lists characteristics of the sites for the PM_{10} and meteorological measurements used in this paper and shown in Fig. A.1.

A.2.2 Instruments

A standard Thermo Scientific TEOM™ FDMS (Filter Dynamic Measurement System) sampler, maintained by the Air Rhône-Alpes air quality agency, provided routine hourly PM_{10} concentrations at an urban location in Sallanches.

A scanning Humidity And Temperature PROfiler (HATPRO), manufactured by Radiometer Physics GmbH, was deployed within the perimeter of the airfield in Sallanches. The HATPRO is a MWR measuring brightness temperatures for two 7-channel frequency reception bands: from 22.24 to 31.4 GHz and from 51 to 58 GHz. The first frequency band contains information on cloud liquid water content and the vertical profile of atmospheric absolute humidity, while the second frequency band contains information on the vertical profile of atmospheric temperature. A steerable paraboloid mirror, covered by a microwave transparent radome insures the focussing of the beam (width of 3°or less) and enables radiation from ±90°elevation to be received. The radome was continuously protected by a heated blower system to prevent the formation of dew and any condensation. The MWR was operated in a bilateral two-scan mode providing tropospheric profiles every 9–10 min, with elevation angles ±90.0°, ±42.0°, ±30.0°, ±19.2°, ±10.2°, ±5.4° above the horizon. The MWR beam was orientated 343° North (see Fig. A.1). An absolute system calibration, utilizing the built-in ambient temperature target and an external liquid-nitrogen-cooled radiometric target, was performed before the start of the Passy-2015 campaign. Further details on the technical specifications and calibration methods of the HATPRO are given by Rose et al. [2005].

In this work, we use temperature data retrieved from the measured brightness temperatures, following the combined elevation scanning and multiple frequency retrieval method described by Crewell and Löhnert [2007]. No long-term routine upper air observations are available for the section of the valley considered herein, so data from RS launched twice a day at 0000 and 1200 UTC (0100 and 1300 LT) at the WMO station 6610 at Payerne, Switzerland, during the period 1994-2014, were used to develop the retrieval algorithms. The station is located in the Broye River Valley between the Jura and Prealps mountain ranges (of mean height above the valley floor similar to that at the location of the MWR) at latitude 46.82°, longitude 6.95°(about 100 km north of the MWR site) and elevation 491 m (similar to that of the MWR site, see Table A.1), and has a climate and weather conditions typical of Alpine regions and so similar to that of the valley section considered herein. The retrieval algorithm uses simulated brightness temperatures at required frequencies and elevation angles derived from the pressure, temperature and humidity profiles from the long-term RS dataset via radiative transfer calculations [see for instance Crewell and Löhnert, 2007; Löhnert and Maier, 2012].

Temperature profiles retrieved from the MWR data were compared to the temperature profiles from the RS ascents, using Väisälä RS92 reusable radiosondes [Legain et al., 2013], launched at the RS site during the Passy-2015 IOPs. The RS temperature data were interpolated on the vertical levels of the retrieved MWR data. The time interval between two RS profiles varied from 1.5 to 12 h. Fig. A.2 displays times series of temperature profiles retrieved from the MWR data and from the RS ascents during the IOPs (IOP1 from 6 to 14 February 2015 and IOP2 from 17 to 20 February 2015) at the times of the RS launches. The overall temporal variability of the temperature profiles derived from the MWR data is comparable to that of the temperature profiles from the RS ascents. Accuracies reported in terms of root-mean-square-error (RMSE) for temperature for the HATPRO are typically between 0.4 and 0.8 K in the lowest 500 m a.g.l., gradually increasing with height to 1.2 K at 1,200 m a.g.l. and 1.7 K at 4,000 m a.g.l. [Löhnert and Maier, 2012]. Assuming that the atmosphere is horizontally homogeneous in the valley section, we can quantitatively compare the two datasets. This assumption will need to be evaluated in future work, for instance using results from numerical model simulations. The root-mean-square-differences calculated from the two datasets are 0.7 K below 500 m a.g.l., 1.1 K from 500 to 1,200 m a.g.l. and 1.7 K from 1,200 to 4,000 m a.g.l., which are comparable to the typical accuracies (RMSE) for the HATPRO. This result suggests that the vertical structure of the valley atmosphere in terms of temperature is similar above the MWR and RS sites. If this is the case, this indicates that the accuracy of the temperature profiles retrieved from the MWR data (based on long-term observations at Payerne) is as good as the typical accuracy for the HATPRO.

A.2.3 Bulk measure of atmospheric stability

In the analysis presented in Sect. A.3, we use extensively the heat deficit H [Whiteman et al., 1999b] as a bulk measure of atmospheric stability, defined by

$$H(z) = c_p \int_{h_0}^{z} \rho(z') \left[\theta(z) - \theta(z')\right] dz', \tag{A.1}$$

where $c_p = 1,005$ J kg^{-1} K^{-1} is the specific heat of air at constant pressure, $z - h_0$ is the height above ground level at $z = h_0$, and ρ and θ are the air density and potential temperature, respectively. The heat deficit is the heat (energy) per unit area (in J m^{-2}) required to bring a column of air of unit area and depth $z - h_0$ to the potential temperature at height z (and hence leading to a dry adiabatic lapse rate throughout the column). This method of determining a bulk measure of stability relies on a choice of integration height, as discussed in Sect. A.3.

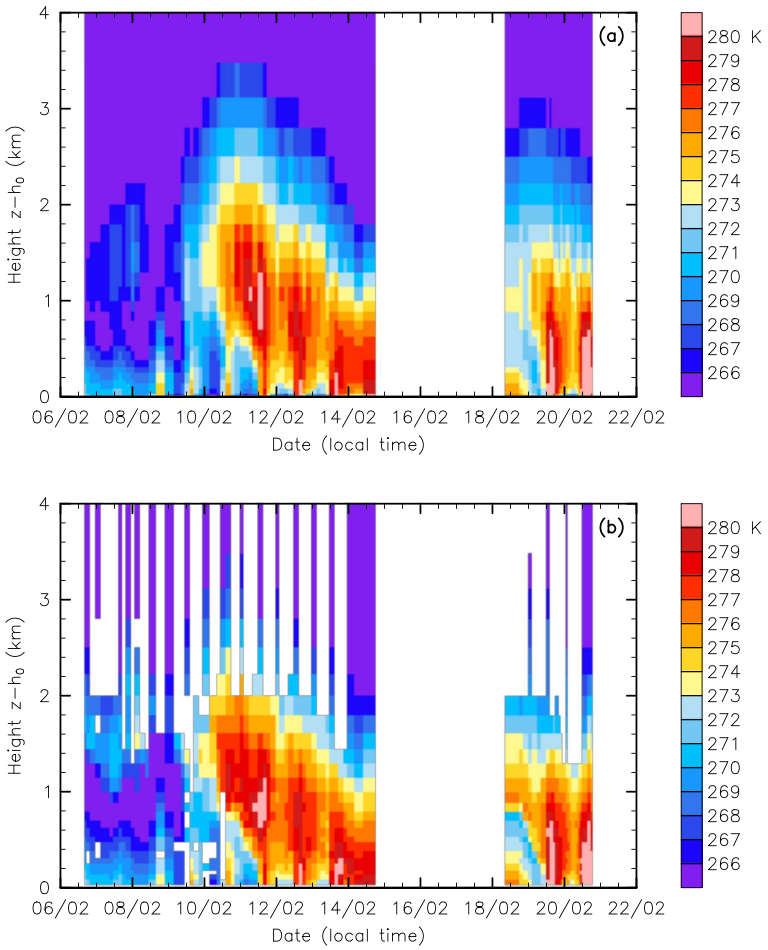

Figure A.2: Temperature profiles above ground level at $z = h_0$ at the location of the microwave radiometer (MWR) site (see Fig. A.1 and Table A.1), **(a)** retrieved from the MWR data and **(b)** from the rawinsonde (RS) ascents during the Passy-2015 intensive observation periods (IOPs) from 6 to 14 February 2015 (IOP1) and from 17 to 20 February 2015 (IOP2) at the times of the RS launches.

A.3 Results and discussion

A.3.1 Temporal variability of PM_{10} concentrations associated with the valley heat deficit

Since the focus of this work is on correlating ground-based PM_{10} concentrations to the heat deficit, we determined the height above ground level at which the correlation coefficient r^2 between the heat deficit and PM_{10} concentration at Sallanches during the Passy-2015 field campaign was maximum. The temperature derived from the MWR data was hourly averaged to correspond to the temporal resolution of the PM_{10} concentration measurements. The heat deficit was calculated to different integration heights at the location of the MWR site from the hourly average temperature profiles, assuming that the valley atmosphere is in hydrostatic balance, as is reasonable [see for instance Rampanelli et al., 2004b; Serafin and Zardi, 2011b; Arduini et al., 2016].

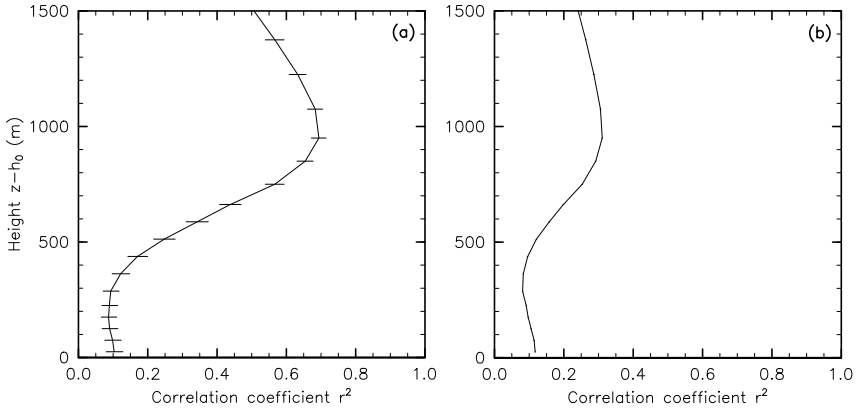

Figure A.3: Squared Pearson product–moment correlation coefficient r^2 between the heat deficit calculated for different integration heights z and PM_{10} concentration at Sallanches during the Passy-2015 field campaign main observation period (from 10 January to 28 February 2015) displayed as a function of height above ground level at $z = h_0$ at the location of the microwave radiometer site (see Fig. A.1 and Table A.1), on **(a)** daily and **(b)** hourly time scales. 95% confidence intervals, determined using the Fisher transformation, are shown as horizontal lines.

Fig. A.3 shows that the correlation coefficient r^2 increases with height reaching a maximum value for a height above ground level $z - h_0$ near $1,000$ m and decreases with height above, on both daily (midnight to midnight LT) and hourly time scales. The integration height corresponding to the maximum correlation is of the order of the mean height of the surrounding mountain ranges at the location of the MWR site (see Fig. A.1). This result is consistent with that reported by Whiteman et al. [2014] for the Salt Lake Valley, Utah, USA, and simply indicates that atmospheric stability above the bounding terrain is of decreasing significance for the trapping of pollutants in the valley. In the following the heat deficit integrated to this height will be referred to as valley heat deficit and denoted by H_v. The maximum correlation coefficient is significantly higher for the daily average values ($r^2 = 0.69$) than for the hourly average values ($r^2 = 0.31$). The correlation coefficient for the daily average values is comparable to those reported for US valleys, which are in the range 0.46–0.65 (see Sect. A.1) and for the Grenoble valley in the French Alps [$r^2 = 0.68$; Largeron, 2010; Largeron and Staquet, 2016b].

The time series and scatter plot of the daily average valley heat deficit and PM_{10} concentration at Sallanches during the Passy-2015 field campaign main observation period are presented in Fig. A.4. We note that all the five days when the daily average PM_{10} concentration exceeded the daily average limit value of 50 μg m^{-3} were associated with persistent CAPs [Whiteman et al., 2001b; Lareau et al., 2013a] as opposed to diurnal CAPs. Diurnal CAPs are destroyed the next day after sunrise by the growth of a convective boundary layer. In this work, we define persistent CAP events as CAP events triggered by an increase in the daily average valley heat deficit

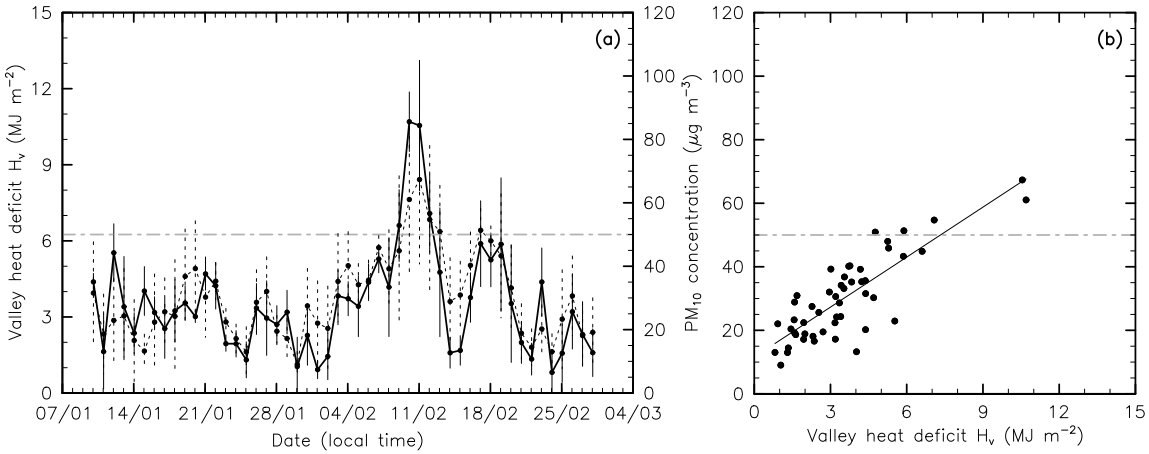

Figure A.4: **(a)** Time series of the daily average valley heat deficit (solid line) and PM_{10} concentration (dotted line) at Sallanches and **(b)** corresponding scatter plot, during the Passy-2015 field campaign main observation period (from 10 January to 28 February 2015). The grey horizontal line shows the the daily average limit value of 50 μg m^{-3}. The vertical solid and dotted lines on the time series indicate the range of hourly variations of the valley heat deficit and PM_{10} concentration, respectively. The solid line on the scatter plot shows the linear regression line.

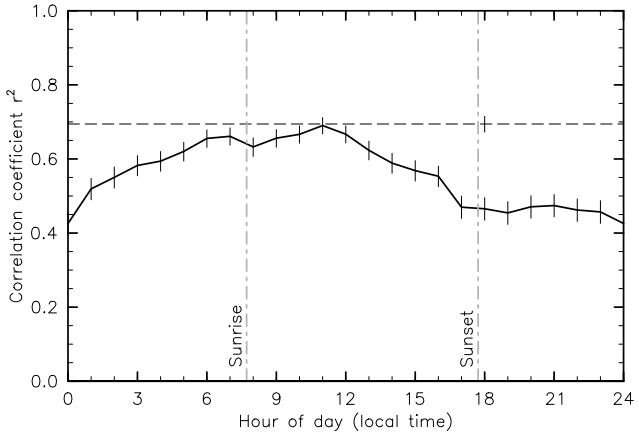

Figure A.5: Squared Pearson product–moment correlation coefficient r^2 between daily PM_{10} concentration and the valley heat deficit at Sallanches calculated for every hour of day (solid line), compared to that obtained by considering the daily average value (dashed line), during the Passy-2015 field campaign main observation period (from 10 January to 28 February 2015). 95% confidence intervals, determined using the Fisher transformation, are shown as black vertical lines. The grey vertical lines shows the average times of sunrise and sunset above the horizon during the period considered.

and lasting for as long as the daily average valley heat deficit is above that of the first day of the event. Persistent CAP events were observed during IOP1 (from 8 to 14 February 2015) and IOP2 (from 17 to 20 February 2015). The overall temporal variability of the daily average PM_{10} concentration is comparable to that of the valley heat deficit. There are fairly large hourly variations of both the valley heat deficit and PM_{10} concentration, as indicated by their ranges of variations in Fig. A.4a.

The studies by Silcox et al. [2012], Whiteman et al. [2014] and Green et al. [2015] used valley heat deficit values calculated at a particular time of day (either 0400 or 0500 LT). Considering another particular time of day might have led to different relationships between daily average PM_{10} concentration and valley heat deficit. To ascertain whether hourly variations of the valley heat deficit affect the correlation between daily average PM_{10} concentration and valley heat deficit, the correlation coefficients between daily PM_{10} concentration and the valley heat deficit calculated for every hour of day are shown in Fig. A.5 and compared to that obtained by considering the daily average value. The correlation coefficient r^2 calculated for every hour of day varies between 0.44 and 0.69. It is the highest and close to that calculated using the daily average valley heat deficit ($r^2 = 0.69$) at 1100 LT, and within 10% of that calculated using the daily average valley heat deficit during the morning hours from 0600 to 1300 LT. In order to maximize the variance of daily average PM_{10} concentration explained by the valley heat deficit calculated at a particular time of day, it is therefore more appropriate to calculate the valley heat deficit during these morning hours, in this valley and most likely in other valleys.

The time series and scatter plot of the hourly average valley heat deficit and PM_{10} concentration at Sallanches are presented in Fig. A.6. Not surprisingly, both the hourly valley heat deficit and PM_{10} concentration varies over a wide range of temporal scales. Given the spatial separation of measurement sites and various PM_{10} emission sources, and the time scales of processes involved in changing PM_{10} concentrations and distributing any changes (e.g. emissions, deposition, advection, mixing), out-of-phase variations will weaken direct correlation on an hourly time scale, where a change in one variable in one hour results in a later or slower change in PM_{10} concentration. In this sense the daily average is arguably a type of 'fuzzy' verification, integrating all sub-diurnal time scales. Single-time-per-day correlations would also be affected, but using all hours would suffer a so called 'double penalty', making them worse. The role of PM_{10} emissions and local dynamics on the hourly variability of PM_{10} concentrations will be examined in the following subsection of the paper.

We note that filtering the data around possible factors can lead to meaningless conclusions since the size of the dataset will be reduced. For example, washout and more generally scavenging by precipitation is effective in cleaning the polluted atmosphere. Large particles (with aerodynamic diameters greater than 1 μm) are most efficiently removed by washout. Hence, it is reasonable to hypothesize that low PM_{10} concentrations can be associated with washout, irrespective of the value of the valley heat deficit. Excluding the hours when precipitation occurred to eliminate such values does not reduce the scatter, leading to a similar correlation coefficient for the hourly average values ($r^2 = 0.32$ to be compared to $r^2 = 0.31$). Drawing randomly subsets of the data of the same size as that filtered for precipitation leads to correlation coef-

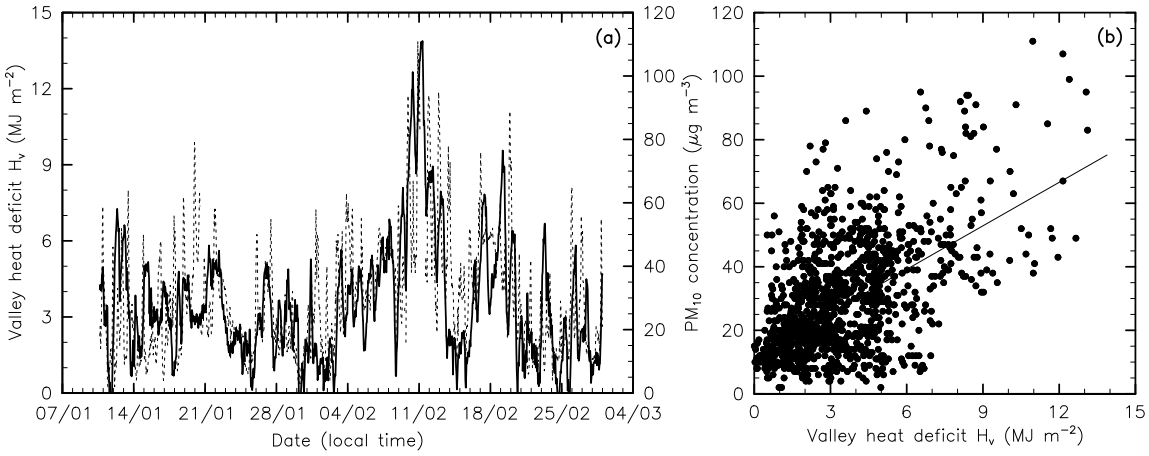

Figure A.6: **(a)** Time series of the hourly average valley heat deficit (solid line) and PM_{10} concentration (dotted line) at Sallanches and **(b)** corresponding scatter plot, during the Passy-2015 field campaign main observation period (from 10 January to 28 February 2015). The solid line on the scatter plot shows the linear regression line.

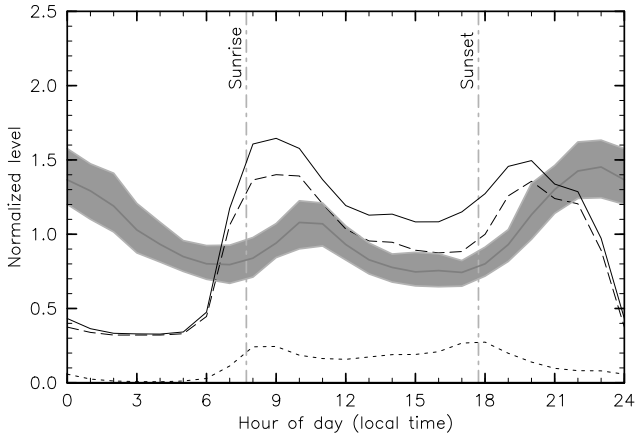

Figure A.7: Mean hour-of-day variation of PM_{10} concentration at Sallanches during the Passy-2015 field campaign main observation period (from 10 January to 28 February 2015), normalized by the mean value during this period (dark grey solid line), and diurnal profiles of PM_{10} emissions for the residential combustion (dashed line) and road transport (dotted line) source sectors, and both combined (black solid line), normalized by total PM_{10} emissions during the period considered. The 95% confidence interval for the mean hour-of-day variation of PM_{10} concentration, calculated through bootstrap re-sampling, is displayed as grey shading. The vertical lines shows the average times of sunrise and sunset above the horizon during the period considered.

ficients r^2 in the range 0.26–0.34. Hence, it is impossible to state the significance of the former change, or lack of, in r^2, except that it is within the bounds of error for the dataset.

A.3.2 Role of PM_{10} emissions and local dynamics on the hourly variability of PM_{10} concentrations

PM_{10} concentrations depend on PM_{10} emissions from various source sectors. The residential combustion and road transport source sectors are major source sectors for PM_{10} in the Arve River Valley in the French Alps (see Sect. A.1) with 61% of annual PM_{10} emissions from residential combustion (almost exclusively wood combustion) and 23% from road transport [estimated by Air Rhône-Alpes, 2014, for 2012]. Fig. A.7 shows the mean hour-of-day variation of PM_{10} concentration at Sallanches during the Passy-2015 field campaign main observation period, normalized by the mean value during this period, and diurnal profiles of PM_{10} emissions for the residential combustion and road transport source sectors, and both combined, normalized by total PM_{10} emissions during the period considered. These were obtained using typical hourly and monthly emissions factors for these source sectors in France from Schaap et al. [2005] and the contributions of these source sectors to total PM_{10} emissions estimated by Air Rhône-Alpes [2014], for 2012. We note that the diurnal pattern of road transport emissions in the Arve River Valley was slightly more complicated during the period considered because heavy good vehicles were banned from the roads in this section of the valley between 2200 LT on Saturdays to 2200 LT on Sundays and from 0700 to 1800 LT on Saturdays from 7 February to 8 March 2015. Moreover, the speed limit was lowered on motorways from 130 to 110 km h^{-1} during wintertime.

The diurnal emission patterns for both source sectors are bimodal with peaks representing morning and evening peaks for residential combustion and morning and afternoon traffic rush-hour peaks for road transport. When weighted by the percentage contributions of each source sector to total PM_{10} emissions during the period considered, the diurnal emission pattern remains bimodal but follows most closely that of residential combustion. It is evident that the mean hour-of-day variation of PM_{10} concentration follows the changes in PM_{10} emissions from the residential combustion and road transport source sectors combined, despite continued PM_{10} emissions. This 'double peak' profile for PM_{10} concentration is similar to those observed elsewhere in urbanized valleys with similar mix of PM_{10} emissions during wintertime [Trompetter et al., 2010, and references therein]. Reasons for the dilution of PM_{10} concentration observed between 1000 and 1700 LT (32% gradual decrease in 5 hours) and between 2300 and 0700 LT (45% gradual decrease in 8 hours) are explored in the following. It is worth noting that the source of dilution between 2300 and 0700 LT need not be as significant as that between 1000 and 1700 LT, since PM_{10} emissions are 2 to 3 times lower.

The *top* plot of Fig. A.8 shows the mean hour-of-day variation of hourly time rate of change of the potential temperature profile derived from the MWR data during the

Passy-2015 field campaign main observation period. The hourly time rate of change of the potential temperature of the near-surface layer changes from negative (i.e. cooling) to positive (i.e. warming) at 0900 LT, shortly after sunrise, and increases until 1300 LT. As a result, shallow, capped boundary-layer convection develops. The vertical gradient of potential temperature in the first 100 m above the ground surface decreases during this period (see the *bottom* plot of Fig. A.8), changing from positive (i.e. stable) to negative (i.e. unstable) shortly before 1300 LT, yielding a capped convective boundary layer of depth of at least 100 m at this time. Between 1400 and 1800 LT the hourly time rate of change of the potential temperature of the near-surface layer decreases, changing from warming to cooling at 1600 LT. This results in an increase of the near-surface vertical gradient of potential temperature, which changes from unstable to stable for the first 100 m around 1600 LT. Between sunset around 1800 LT and sunrise around 0800 LT the cooling rate of the near-surface layer decreases, while the near-surface vertical gradient of potential temperature continues to increase until midnight and then levels off until sunrise. This levelling off of the near-surface vertical gradient of potential temperature is associated with a progressive homogenization of the cooling rate in the vertical.

Arduini et al. [2016] found that, for an idealized alpine valley opening on a plain, the decrease of the cooling rate after the evening transition is associated with the development of the night-time valley-wind system, characterized by drainage winds. Hence, we hypothesize that cleaner air from nighttime drainage flows dilutes the lowest layers of the valley atmosphere as the CAP grows in depth. To check whether this explanation is plausible, let us assume that this section of the valley is trapezoidal, that the slope of the valley floor is constant and that the lowest layers of the valley atmosphere above the valley floor is of depth d. Because of these simplifications, the calculation presented below does not depend on d, and so let us set d to 10 m for an illustrative purpose. Estimates of the surface area and perimeter of the valley floor are 30 km^2 and 50 km, respectively. Hence, estimates of the volume and lateral surface area of this lowest layer are 0.3 km^3 and 0.5 km^2, respectively. Let us further assume that PM_{10} concentrations are horizontally homogeneous in the valley section. Hence, the 45% gradual decrease of PM_{10} concentration between 2300 and 0700 LT, observed in Fig. A.7, would require $0.3 \times 45\% = 0.135$ km^3 of clean air flowing through the lateral surface area of 0.5 km^2 in 8 hours, that is a wind speed in the order of 1 cm s^{-1}. If we restrict the inflow to the three major tributaries from Servoz, Saint-Gervais-les-Bains and Megève (see Fig. A.1), the lateral surface area reduces to approximately 0.03 km^2, leading to a wind speed in the order of 0.2 m s^{-1}. This scenario does not lead to absurd values, suggesting that nighttime drainage flows may be key to maintaining some degree of ventilation. Furthermore, vertical transport associated with such drainage flows could provide an additional mechanism for diluting

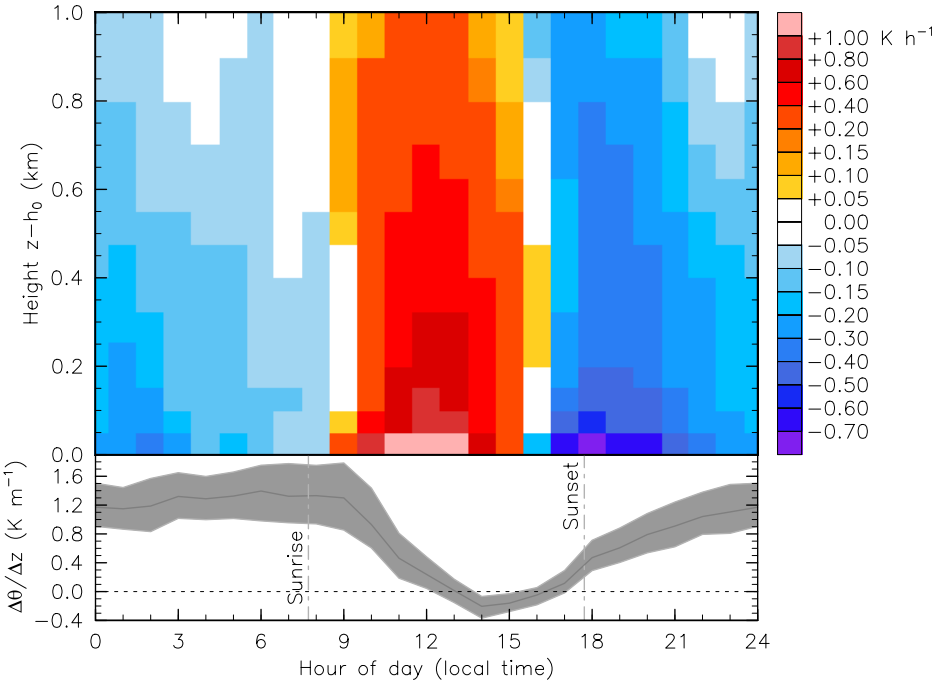

Figure A.8: The *top* plot displays the mean hour-of-day variation of hourly time rate of change of the potential temperature profile above ground level at $z = h_0$ at the location of the microwave radiometer site (see Fig. A.1 and Table A.1) during the Passy-2015 field campaign main observation period (from 10 January to 28 February 2015). Note that the colour scale is not linear. The *bottom* plot displays the mean hour-of-day variation of the vertical gradient of potential temperature in the first 100 m above the ground surface (dark grey solid line), denoted by $\Delta\Theta/\Delta z$, at the same location during the same period. The 95% confidence interval for the mean hour-of-day variation of $\Delta\Theta/\Delta z$, calculated through bootstrap re-sampling, is displayed as grey shading. The vertical lines shows the average times of sunrise and sunset above the horizon during the period considered.

near-surface PM_{10} concentrations. The importance of these mechanisms will need to be confirmed by results from numerical model simulations. Similar conclusions were reached from observations in the Kathmandu Valley, Nepal by Panday and Prinn [2009] and confirmed by results from numerical model simulations [Panday et al., 2009].

To summarize, the interplay of the diurnal cycles of emissions and local dynamics is as follows: PM_{10} concentrations increase sharply in the morning hours shortly before sunrise and until the onset of convection due to the increase of PM_{10} emissions from proximate sources, then is diluted vertically by shallow, capped boundary-layer convection (despite continued emission), increase sharply again when convection breaks down, and then is diluted by some removal process (hypothesized drainage winds) when PM_{10} emissions are minimum.

A.4 Conclusions

Analysis of temperature profile and ground-based PM_{10} concentration data collected with a temporal resolution of one hour or finer, as part of the Passy-2015 field campaign conducted around Passy in the section of the Arve River Valley between Cluses and Servoz in the French Alps during the winter season 2014-2015 led to the following main conclusions:

- The variance of daily average PM_{10} concentration explained by the daily average valley heat deficit during wintertime in this section of the Arve River Valley is consistent with that reported when correlating $PM_{2.5}$ concentration to the valley heat deficit calculated during the late night in US valleys by Silcox et al. [2012], Whiteman et al. [2014] and Green et al. [2015], and in the Grenoble valley in the French Alps by Largeron [2010] and Largeron and Staquet [2016b]. In addition, the correlation between daily average PM_{10} concentration and the valley heat deficit in this section of valley is found to be sensitive to the time when the valley heat deficit is calculated. It is more appropriate to calculate the valley heat deficit during the morning hours from 0600 to 1300 local time, when the correlation is comparable to that calculated using the daily average valley heat deficit. A similar result is expected for other valleys.

- The hourly variability of PM_{10} concentrations in this section of valley is more complex and cannot be explained solely by the hourly variability of the valley heat deficit. The diurnal cycle of near-surface PM_{10} concentration is affected by local PM_{10} emissions, atmospheric stability and the local dynamics of the valley atmosphere, as evidenced for other valleys [e.g. de Franceschi and Zardi, 2009; Gohm et al., 2009]. It is proposed that advection and mixing by nighttime drainage flows may be responsible for the decrease of near-surface PM_{10} concentration observed at night and that vertical mixing resulting from convection leads to a decrease of near-surface PM_{10} concentration in the morning (after the morning peak of PM_{10} emissions).

Analysis of additional observations collected during the Passy-2015 field campaign will help to understand and constrain the complex relationships between particulate air pollution and atmospheric conditions in this valley and other similar valleys. Analysis of numerical model simulations, along with these additional observations, will provide insights into the role of the local dynamics of the valley atmosphere on the spatial and temporal distribution of particulate air pollution in the valley.

Acknowledgments

We wish to thank the Bureau Municipal of Sallanches for providing access to the airfield in Sallanches and that of Passy for their kind support. The rawinsonde data were collected during the Passy-2015 field campaign, supported by the Agence de l'Environnement et de la Maîtrise de l'Énergie (ADEME) through the French program Les Enveloppes Fluides et l'Environnement (LEFE), and by Météo-France. The LEFE program is managed and coordinated by the Institut National des Sciences de l'Univers (INSU) du Centre National de la Recherche Scientifique (CNRS). The Passy-2015 field campaign was led by the Centre National de Recherches Météorologiques – Groupe d'étude de l'Atmosphère Météorologique (CNRM-GAME, UMR 3589 Météo-France and CNRS) while the Laboratoire des Ecoulement Géophysiques et Industriels (LEGI, UMR 5519 UJF/CNRS/Grenoble INP) was the coordinator of the LEFE project. Rawinsondes were funded by Météo-France and LEFE/ADEME, and the Väisälä sounding system was funded by CNRS-INSU and Météo-France and operated by the CNRM-GAME team GMEI/4M. The authors would like to acknowledge the National Centre for Atmospheric Science (NCAS) Atmospheric Measurement Facility (AMF) for the use of the microwave radiometer during this project. CC would like to thank W. E. Martin and B. J. Brooks for providing technical help with the operation and deployment of this instrument. The contribution by GA to this work was supported by a grant from LabEx Osug@2020 (Investissements d'avenir – ANR10LABX56). Finally, the authors thank one referee for valuable comments, which led to substantial improvements in this paper.

List of references

Adler B, Whiteman CD, Hoch SW, Lehner M (2012) Warm-air intrusion in Arizona's meteor crater. J Appl Meteorol Climatol 51:1010–1025 II.3.2.a

Air Rhône-Alpes (2014) PPA de la vallée de l'Arve: Impact du salage sur les concentrations de PM10. Tech. rep., Air Rhône-Alpes, France, 19 pp A.3.2

Arduini G, Staquet C, Chemel C (2016) Interactions between the night-time valley-wind system and a developing cold-air pool. Boundary-Layer Meteorol 161:49–72 III, IV.1, IV.4.1, IV.6.2, IV.7, V.1, A.3.1, A.3.2

Arduini G, Chemel C, Staquet C (2017) Energetics of deep alpine valleys in pooling and draining configurations. J Atmos Sci DOI 10.1175/JAS-D-16-0139.1, in press IV, V.1

Axelsen SL, van Dop H (2009) Large-eddy simulation of katabatic winds. Part 1: Comparison with observations. Acta Geophy 57:803–836 II.3.1.a

Baines PG (2008) Mixing in downslope flows in the ocean – plumes versus gravity currents. Atmos Ocean 46:405–419 III.4.1

Baker KR, Simon H, Kelly JT (2011) Challenges to modeling "cold pool" meteorology associated with high pollution episodes. Environ Sci Technol 45:7118–7119 III.1

Banta RM, Olivier LD, Neff WD, Levinson DH, Ruffieux D (1995) Influence of canyon-induced flows on flow and dispersion over adjacent plains. Theor Appl Climatol 52:27–42 II.3.1.b

Banta RM, Darby LS, Fast JD, Pinto JO, Whiteman CD, Shaw WJ, Orr BW (2004) Nocturnal low-level jet in a mountain basin complex. Part I: evolution and effects of local flows. J Appl Meteorol 43:1348–1365 II.3.1.b, II.4.2, III.1

Bell RC, Thompson RORY (1980) Valley ventilation by cross winds. J Fluid Mech 96:757–767 II.3.2.a

Billings BJ, Grubišic V, Borys RD (2006) Maintenance of a mountain valley cold pool: a numerical study. Mon Weather Rev 134:2266–2278 V.1

Bodine D, Klein PM, Arms SC, Shapiro A (2009) Variability of surface air temperature over gently sloped terrain. J Appl Meteorol Climatol 48:1117–1141 V.1

Bou-Zeid E, Meneveau C, Parlange M (2004) A scale-dependent Lagrangian dynamic model for large eddy simulation of complex turbulent flows. Phys Fluids 17, 025105, 10.1063/1.1839152 III.2.1

Burns P (2014) Interactions between downslope flows and a developing cold-air pool. Thesis, University of Hertfordshire, UK II.2

Burns P, Chemel C (2014) Evolution of cold-air-pooling processes in complex terrain. Boundary-Layer Meteorol 150:423–447 II.4.3, III.1, III.2.1, III.2.3, III.2.4, IV.3.3

Burns P, Chemel C (2015) Interactions between downslope flows and a developing cold-air pool. Boundary-Layer Meteorol 154:57–80 II.4.2, II.4.2, III.1, III.2.6, III.3.1, III.3.4, III.4.1, IV.1, IV.7, V.1

Catalano F, Cenedese A (2010) High-resolution numerical modeling of thermally driven slope winds in a valley with strong capping. J Appl Meteorol Climatol 49:1859–1880 II.4.2, III.1, III.6, IV.1

Chazette P, Couvert P, Randriamiarisoa H, Sanak J, Bonsang B, Moral P, Berthier S, Salanave S, Toussaint F (2005) Three-dimensional survey of pollution during winter in French Alps valleys. Atmos Environ 39:1035–1047 A.1

Chemel C, Burns P (2015a) Pollutant dispersion in a developing valley cold-air pool. Boundary-Layer Meteorol 154:391–408 II.3.3, IV.3.3

Chemel C, Burns P (2015b) Pollutant dispersion in a developing valley cold-air pool. Boundary-Layer Meteorol 154:391–408 III.6

Chemel C, Staquet C, Largeron Y (2009) Generation of internal gravity waves by a katabatic wind in an idealized alpine valley. Meteorol Atmos Phys 103:187–194 II.3.1.a

Chemel C, Arduini G, Staquet C, Largeron Y, Legain D, Tzanos D, Paci A (2016) Valley heat deficit as a bulk measure of wintertime particulate air pollution in the Arve River Valley. Atmos Environ 128:208–216 V.1, V.6, A

Chen F, Dudhia J (2001) Coupling an advanced land-surface/hydrology model with the Penn State/NCAR MM5 modeling system. Part I: model implementation and sensitivity. Mon Weather Rev 129:569–585 III.2.1, III.2.4, IV.3.1, V.2.3

Chrust MF, Whiteman CD, Hoch SW (2013) Observations of thermally driven wind jets at the exit of Weber Canyon, Utah. J Appl Meteorol Climatol 52:1187–1200 II.3.1.b

Clements CB, Archuleta J, Gudiksen PH (1989a) Experimental design of the 1984 ASCOT field study. J Appl Meteorol 28:405–413 II.2, V.1

Clements CB, Whiteman CD, Horel JD (2003) Cold-air-pool structure and evolution in a mountain basin: Peter Sinks, Utah. J Appl Meteorol 42:752–768 V.1

Clements WE, Archuleta JA, Hoard DE (1989b) Mean structure of the nocturnal drainage flow in a deep valley. J Appl Meteorol 28:457–462 II.3.1.b, II.4.2

Permanent Secretariat of the Alpine Convention (2015) Demographic changes in the Alps. Tech. Rep. 5, Permanent Secretariat of the Alpine Convention I.1

Coulter RL, Orgill M, Porch W (1989) Tributary fluxes into Brush Creek Valley. J Appl Meteorol 28:555–568 II.3.3, V.1

Coulter RL, Martin TJ, Porch WM (1991) A comparison of nocturnal drainage flow in three tributaries. J Appl Meteorol 30:157–169 II.3.3, V.1

Crewell S, Löhnert U (2007) Accuracy of boundary layer temperature profiles retrieved with multifrequency multiangle microwave radiometry. IEEE Trans Geosci Remote Sens 45:2195–2201 A.2.2

Cuxart J (2015) When can a high-resolution simulation over complex terrain be called LES? Front Earth Sci 3, 87, DOI 10.3389/feart.2015.00087 II.4, III.2.3

de Franceschi M, Zardi D (2009) Study of wintertime high pollution episodes during the Brenner-South ALPNAP measurement campaign. Meteorol Atmos Phys 103:237–250 II.2, II.3.1, A.1, A.4

De Wekker SFJ (2002) Structure and morphology of the convective boundary layer in mountainous terrain. Thesis, University of British Columbia II.1

De Wekker SFJ, Kossmann M (2016) Convective boundary layer heights over mountainous terrain – A review of concepts. Front Earth Sci 4:439–454 I.1

De Wekker SFJ, Whiteman CD (2006) On the time scale of nocturnal boundary layer cooling in valleys and basins and over plains. J Appl Meteorol Climatol 45:813–820 III.6

Deardorff JW (1980) Stratocumulus-capped mixed layers derived from a three-dimensional model. Boundary-Layer Meteorol 18:495–527 IV.3.1

Doran JC, Fast JD, Horel J (2002) The VTMX campaign. Bull Am Meteorol Soc 82:537–551 II.2

Dudhia J (1989) Numerical study of convection observed during the winter monsoon experiment using a mesoscale two-dimensional model. J Atmos Sci 46:3077–3107 III.2.1, IV.3.1

Durran DR (1990) Mountain waves and downslope winds. In: Blumen W (ed) Atmospheric processes over complex terrain, Meteorological Monographs, vol 23, no. 45, American Meteorological Society, 45 Beacon St., Boston, MA, USA, chap 4, pp 59–83 II.3.2.b

Egger J (1990) Observations of thermally developed wind systems in mountainous terrain. In: Blumen W (ed) Atmospheric processes over complex terrain, Meteorological Monographs, vol 23, no. 45, American Meteorological Society, 45 Beacon St., Boston, MA, USA, chap 3, pp 43–58 II.3.1.b, III.5, VI.1

Ekhart E (1948) De la structure thermique de l'atmosphere dans la montagne. La météorologie 4:3–26 II.1, II.1

Farr TG, Rosen PA, Caro E, Crippen R, Duren R, Hensley S, Kobrick M, Paller M, Rodriguez E, Roth L, Seal D, Shaffer S, Shimada J, Umland J, Werner M, Oskin M, Burbank D, Alsdorf D (2007) The Shuttle Radar Topography Mission. Rev Geophys 45, DOI 10.1029/2005RG000183 V.2.2

Fast JD, Darby LS (2004) An evaluation of mesoscale model predictions of down-valley and canyon flows and their consequences using doppler lidar measurements during VTMX 2000. J Appl Meteorol 43:420–436 II.4.2

Fast JD, Zhong S, Whiteman CD (1996) Boundary layer evolution within a canyonland basin. Part II: numerical simulations of nocturnal flows and heat budgets. J Appl Meteorol 35:2162–2178 II.4.3, IV.2.3, IV.9, IV.5.3

Flamant C, Drobinski P, Furger M, Chimani B, Tschannett S, Steinacker R, Protat A, Richner H, Gubser S, Häberli C (2006) Föhn/cold-pool interactions in the rhine valley during map iop 15. Q J R Meteorol Soc 132:3035–3058 II.4.4, V.1, V.5.2

Garratt JR (1992) The atmospheric boundary layer. Cambridge University Press, pp. 316 II.1, II.2

Geiger R (1965) The Climate Near the Ground. Harvard University Press, pp. 482 II.4.2

Gohm A, Harnisch F, Vergeiner J, Obleitner F, Schnitzhofer R, Hansel A, Fix A, Neininger B, Emeis S, Schäfer K (2009) Air pollution transport in an alpine valley: results from airborne and ground-based observations. Boundary-Layer Meteorol 131:441–463 II.3.1, A.1, A.4

Green MC, Chow JC, Watson JG, Dick K, Inouye D (2015) Effect of snow cover and atmospheric stability on winter $PM_{2.5}$ concentrations in western U.S. valleys. J Appl Meteorol Climatol 54:1191–1201 A.1, A.3.1, A.4

Grisogono B, Oerlemans J (2001) Katabatic flow: analytic solution for gradually varying eddy diffusivities. J Atmos Sci 58:3349–3354 II.3.1.a

Gross G, Wippermann F (1987) Channeling and countercurrent in the upper Rhine valley: Numerical simulations. J Climate Appl Meteor 26:1293–1304 II.3.2.c

Grubišić V, Doyle JD, Kuettner J, Dirks R, Cohn SA, Pan LL, Mobbs S, Smith RB, Whiteman CD, Czyzyk S, Vosper S, Weissmann M, Haimov S, Wekker SFJD, Chow FK (2008) The terrain-induced rotor experiment. Bull Am Meteorol Soc 89:1513–1533 II.2

Gudiksen PH, Shearer DL (1989) The dispersion of atmospheric tracers in nocturnal drainage flows. J Appl Meteorol 28:602–608 II.3.3, III.6

Gustavsson T (1995) A study of air and road¿surface temperature variations during clear windy nights. Int J Climatol 15.8:919–932 II.4.1

Haiden T, Whiteman CD, Hoch SW, Lehner M (2011) A mass flux model of nocturnal cold-air intrusions into a closed basin. J Appl Meteorol Climatol 50:933–943 II.4.2

Hall DK, Riggs GA, Salomonson VV (2006) MODIS/Terra Snow Cover 5-Min L2 Swath 500m, Version 5. Tech. rep., Boulder, CO, USA. NASA National Snow and Ice Data Center Distributed Active Archive Center, DOI 10.5067/ACYTYZB9BEOS V.2.2

Harnisch F, Gohm A, Fix A, Schnitzhofer R, Hansel A, Neininger B (2009) Spatial distribution of aerosols in the Inn Valley atmosphere during wintertime. Meteorol Atmos Phys 103:223–235 A.1

Heimann D, de Franceschi M, Emeis S, Lercher P, Seibert P (2007) Air pollution, traffic noise and related health effects in the alpine space: a guide for authorities and consulters. ALPNAP comprehensive report. Tech. rep., Universitá degli studi di Trento, Dipartimento di Ingegneria Civile e Ambientale, Trento, 335 pp II.2

Hoch SW, Whiteman CD, Mayer B (2011) A systematic study of longwave radiative heating and cooling within valleys and basins using a three-dimensional radiative transfer model. J Appl Meteorol Climatol 50:2473–2489 II.4, II.4.1

Holden JJ, Derbyshire SH, Belcher SE (2000) Tethered balloon observations of the nocturnal stable boundary layer in a valley. Boundary-Layer Meteorol 97:1–24 II.3, II.3.2.a, II.3.2.a

Holton JR (2004) An introduction to dynamic meteorology (4th edition). Elsevier Academic Press, Burlington, MA III.5

Hong SY (2010) A new stable boundary-layer mixing scheme and its impact on the simulated East Asian summer monsoon. Q J R Meteorol Soc 136:1481–1496 V.2.3

Jackson PL, Mayr G, Vosper S (2013) Dynamically-driven winds. In: Chow FK, De Wekker SFJ, Snyder BJ (eds) Mountain Weather Research and Forecasting: Recent Progress and Current Challenges, Springer Atmospheric Sciences, Springer, New York, NY, USA, chap 2, pp 121–218 II.3.2.b

Jaubert G, Bougeault P, Berger H, Chimani B, Flamant C, Häberli C, Lothon M, Nuret M, Vogt S (2005) Numerical simulation of meso-gamma scale features of föhn at ground level in the Rhine valley. Q J R Meteorol Soc 131:1339–1361 V.5.2

Jimenez P, Dudhia J, Gonzalez-Rouco J, J N, Montavez JP, Garcia-Bustamante E (2012) A revised scheme for the WRF surface layer formulation. Mon Weather Rev 140:898–918 III.2.5, IV.3.1

Katurji, Zhong (2012) The influence of topography and ambient stability on the characteristic of cold-air pools: a numerical investigation. J Appl Meteorol Climatol 51:1740–1749 II.4.3, III.1, III.6, IV.1

Kiefer MT, Zhong S (2011) An idealized modeling study of nocturnal cooling processes inside a small enclosed basin. J Geophys Res 116, D20127, DOI 10.1029/2011JD016119 II.4.2, IV.1, V.1

Kiefer MT, Zhong S (2013) The effect of sidewall forest canopies on the formation of cold-air pools: A numerical study. J Geophys Res Atmos 118:5965–5978 II.3.1.a

Klemp JB, Lilly DK (1975) The dynamics of wave-induced downslope winds. J Atmos Sci 32:320–339 II.3.2.b

Klemp JB, Dudhia J, Hassiotis J (2008) An upper gravity-wave absorbing layer for NWP applications. Mon Weather Rev 136:3987–4004 III.2.5

Kondo J, Kuwagata T, Haginoya S (1989) Heat budget analysis of nocturnal cooling and daytime heating in a basin. J Atmos Sci 46:2917–2933 II.4.3

Kossmann M, Sturman AP (2003) Pressure-driven channeling effects in bent valleys. J Appl Meteorol Climatol 42:151–158 II.4, II.5, II.3.2.c

Lareau N, Horel J (2015a) Dynamically induced displacements of a persistent cold-air pool. Boundary-Layer Meteorol 154:291–316 II.4.4, II.12, III.1

Lareau N, Crosman E, Whiteman CD, Horel JD, Hoch SW, Brown WOJ, Horst TW (2013a) The Persistent Cold-Air Pool Study. Bull Am Meteorol Soc 94:51–63 A.1, A.3.1

Lareau NP, Horel JD (2015b) Turbulent erosion of persistent cold-air pools: Numerical simulations. J Atmos Sci 72:1409–1427 II.3.2.a, II.4.4, II.4.4, V.1, VI.2

Lareau NP, Crosman E, Whiteman CD, Horel JD, Hoch SW, Brown WOJ, Horst TW (2013b) The persistent Cold-Air pool study. Bull Am Meteorol Soc 94:51–63 II.2, II.4.4, V.1

Largeron Y (2010) Dynamique de la couche limite atmosphérique stable en relief complexe. Application aux épisodes de pollution particulaire des vallées alpines. PhD thesis, Université de Grenoble, France, <tel-00606115> II.3.2.a, III.1, VI.2, A.3.1, A.4

Largeron Y, Staquet C (2016a) The atmospheric boundary layer during wintertime persistent inversions in the Grenoble valleys. Front Earth Sci 4, 70, DOI 10.3389/feart.2016.00070 II.3.2.a, II.4.4, V.1

Largeron Y, Staquet C (2016b) Persistent inversion dynamics and wintertime PM10 air pollution in alpine valleys. Atmos Environ 135:92–108 I.1, II.4.4, V.1, A.3.1, A.4

Largeron Y, Staquet C, Chemel C (2013) Characterization of oscillatory motions in the stable atmosphere of a deep valley. Boundary-Layer Meteorol 148:439–454 II.3.1.a, III.4.1, V.5.1

Lee T, Fukumori I, Tang B (2004) Temperature advection: Internal versus external processes. J Phys Oceanogr 34:1936–1944 IV.5.2, V.5.2

Legain D, Bousquet O, Douffet T, Tzanos D, Moulin E, Barrie J, Renard JB (2013) High-frequency boundary layer profiling with reusable radiosondes. Atmos Meas Tech 6:2195–2205 A.2.2

Lehner M, Whiteman CD, Hoch SW, Crosman ET, Jeglum ME, Cherukuru NW, Calhoun R, Adler B, Kalthoff N, Rotunno R, Horst TW, Semmer S, Brown WOJ, Oncley SP, Vogt R, Grudzielanek AM, Cermak J, Fonteyne NJ, Bernhofer C, Pitacco A, Klein P (2016) The metcrax II field experiment. Bull Am Meteorol Soc 97:217–235 II.2, II.3.2.a

Leukauf D, Gohm A, Rotach MW, Wagner JS (2015) The impact of the temperature inversion breakup on the exchange of heat and mass in an idealized valley: Sensitivity to the radiative forcing. J Appl Meteorol Climatol 54:2199–2216 VI.2

Livneh B, Xia Y, Mitchell KE, Ek MB, Lettenmaier DP (2010) Noah LSM snow model diagnostics and enhancements 11:721–738 V.2.2

Łobocki L (2014) Surface-layer flux-gradient relationships over inclined terrain derived from a local equilibrium, turbulence closure model. Boundary-Layer Meteorol 150:469–483 III.2.5

Löhnert U, Maier O (2012) Operational profiling of temperature using ground-based microwave radiometry at Payerne: prospects and challenges. Atmos Meas Tech 5:1121–1134, DOI 10.5194/amt-5-1121-2012 A.2.2

Long RR (1954) Some aspects of the flow of stratified fluids. II. Experiments with a two-fluid system. Tellus 6:97–115 II.3.2.b

Lu W, Zhong S (2014) A numerical study of a persistent cold air pool episode in the Salt Lake Valley, Utah. J Geophys Res Atmos 119:1733–1752 II.4.4, V.1, V.4.2

Lugauer M, Coauthors (2003) An overview of the VERTIKATOR project and results of alpine pumping. In: Proc. Int. Conf. on Alpine Meteorology, Brig, Switzerland, pp 129–132 II.2

Lundquist J, Pepin N, Rochford C (2008) Automated algorithm for mapping regions of cold-air-pooling in complex terrain. J Geophys Res 113, D22107, DOI 10.1029/2008JD009879 IV.1

Mahrt L (2014) Stably stratified atmospheric boundary layers. Ann Rev Fluid Mech 46:23–45 I.2

Malek E, Davis T, Martin RS, Silva PJ (2006) Meteorological and environmental aspects of one of the worst national air pollution episodes (January, 2004) in Logan, Cache Valley, Utah, USA. Atmos Research 79:108–122 I.1, A.1

Martinez D, Cuxart J, Cunillera J (2008) Conditioned climatology for stably stratified nights in the Lleida area. Tethys 5:13–24 II.3.1

McKee TB, O'Neal RD (1989) The role of valley geometry and energy budget in the formation of nocturnal valley winds. J Appl Meteorol 28:445–456 II.3.1, II.4.1, IV.1, IV.2.2, IV.7, V.1

McNider RT (1982) A note on velocity fluctuations in drainage flows. J Atmos Sci 39:1658–1660 II.3.1.a, III.4.1

Meløysund V, Leira B, Høiseth KV, Lisø KR (2007) Review – Predicting snow density using meteorological data 14:413–423 V.2.2

Meybeck M, Green P, Vörösmarty C (2001) A new typology for mountains and other relief classes – An application to global continental water resources and population distribution. Mountain Research and Development 21:34–45 I.1

Miguez-Macho G, Stenchikov GL, Robock A (2004) Spectral nudging to eliminate the effects of domain position and geometry in regional climate model simulations. J Geophys Res 109, D13104 V.2.3

Mlawer EJ, Taubman SJ, Brown PD, Iacono MJ, Clough SA (1997) Radiative transfer for inhomogeneous atmospheres: RRTM, a validated correlated-k model for the longwave. J Geophys Res 102, D14:16,663–16,682 III.2.1, IV.3.1, V.2.3

Moeng CH, Dudhia J, Klemp J, Sullivan P (2007) Examining Two-Way Grid Nesting for Large Eddy Simulation of the PBL Using the WRF Model. Mon Weather Rev 135:2295–2311 III.2.1, IV.3.2

Monti P, Fernando HJS, Princevac M, Chan WC, Kowalewski TA, Pardyjak ER (2002) Observations of flow and turbulence in the nocturnal boundary layer over a slope. J Atmos Sci 59:2513–2534 II.3.1.a

Morrison H, Curry JA, Khvorostyanov VI (2005) A new double-moment microphysics parameterization for application in cloud and climate models. Part I: Description. J Atmos Sci 62:1665–1677 V.2.3

Muller H, Whiteman CD (1988) Breakup of a Nocturnal Temperature Inversion in the Dischma Valley during DISKUS. J Appl Meteorol 27:188–194 IV.1

Nadeau DF, Pardyjak ER, Higgins CW, Huwald H, Parlange MB (2013) Flow during the evening transition over steep alpine slopes. Q J R Meteorol Soc 139:607–624 III.1

Neemann EM, Crosman ET, Horel JD, Avey L (2015) Simulations of a cold-air pool associated with elevated wintertime ozone in the Uintah basin, Utah. Atmos Chem Phys 15:135–151 V.1, V.2.2, V.2.3

Neff WD, King CW (1987) Observations of complex terrain flows using acoustic sounders: experiments, topography and winds. Boundary-Layer Meteorol 40:363–392 III.1

Neff WD, King CW (1989) The accumulation and pooling of drainage flows in a large basin. J Appl Meteorol 28:518–529 II.3.1.b, II.4.2, III.3.2

Noppler H, Fiedler F (2002) Mesoscale heat transport over complex terrain by slope winds ¿ a conceptual model and numerical simulations. Boundary-Layer Meteorol 104:73–97 II.4.3

Oke TR (1987) Boundary layer climates-2nd ed. Routledge, London II.8

Orlanski I (1975) A rational subdivision of scales for atmospheric processes. Bull Am Meteorol Soc 56:527–530 II.1

O'Steen LB (2000) Numerical simulation of nocturnal drainage flows in idealized valley-tributary system. J Appl Meteorol 39:1845–1860 II.3.3, III.1, V.1

Paci A, Staquet C, 43 co-authors (2015a) The Passy-2015 field experiment: an overview of the campaign and preliminary results. In: Proc. of the 33rd International Conference on Alpine Meteorology, Innsbruck, Austria V.1, A.1

Paci A, Staquet C, co-authors (2015b) The Passy-2015 field experiment: wintertime atmospheric dynamics and air quality in a narrow alpine valley. Atmos Chem Phys Discuss In preparation A.1

Paci A, Staquet C, et al (2016) La campagne passy-2015: dynamique atmosphérique et qualité de l'air dans la valleé de l'Arve. Pollution Atmosphérique 231-232:271–289, DOI 10.4267/pollution-atmospherique.5903 II.2

Palmer TN, Shutts GJ, Swinbank R (1986) Alleviation of a systematic westerly bias in general circulation and numerical weather prediction models through an orographic gravity wave drag parametrization. Q J R Meteorol Soc 112:1001–1039 I.1

Pan F, Smith RB (1999) Gap winds and wakes: SAR observations and numerical simulations. J Atmos Sci 56:905–923 II.3.1.b

Panday AK, Prinn RG (2009) Diurnal cycle of air pollution in the Kathmandu Valley, Nepal: Observations. J Geophys Res 114, D09305, DOI 10.1029/2008JD009777 II.3.1, II.3.3, A.3.2

Panday AK, Prinn RG, Schär C (2009) Diurnal cycle of air pollution in the Kathmandu Valley, Nepal: 2. Modeling results. J Geophys Res 114, D21308, DOI 10.1029/2008JD009808 II.3.3, A.3.2

Peltier WR, Clark TL (1979) The evolution and stability of finite-amplitude mountain waves. Part II: surface wave drag and severe downslope windstorms. J Atmos Sci 36:1498–1529 II.3.2.b

Petkovšek Z (1992) Turbulent dissipation of cold air lake in a basin. Meteorol Atmos Phys 47:237–245 II.4.4

Pinto JO, Parsons DB, Brown WOJ, Cohn S, Chamberlain N, Morley B (2006) Coevolution of down-valley flow and the nocturnal boundary layer in complex terrain. J Appl Meteorol Climatol 45:1429–1449 II.3.1.b, II.4.2, II.4.3, III.1

Porch WM, Fritz RB, Coulter RL, Gudiksen PH (1989) Tributary, valley and sidewall air flow interactions in a deep valley. J Appl Meteorol 28:578–589 II.3.3, II.3.3, V.1

Porch WM, Clements WE, Coulter RL (1991) Nighttime valley waves. J Appl Meteorol 30:145–156 II.3.1.b

Prandtl L (1952) Mountain and valley winds in stratified air. Hafner Publishing company, 422-425 II.3.1.a

Price JD, Vosper S, Brown A, Ross A, Clark P, Davies F, Horlacher V, Claxton B, McGregor JR, Hoare JS, Jemmett-Smith B, Sheridan P (2011) COLPEX field and numerical studies over a region of small hills. Bull Am Meteorol Soc 92:1636–1650 II.2

Princevac M, Hunt JCR, Fernando HJ (2008) Quasi-steady katabatic winds on slopes in wide valleys: hydraulic theory and observations. J Atmos Sci 65:627–643 II.3.1.a

Rampanelli G, Zardi D, Rotunno R (2004a) Mechanism of up-valley winds. J Atmos Sci 61:3097–3111 III.1, III.2.3, III.3.2, III.4.4, III.6, IV.1

Rampanelli G, Zardi D, Rotunno R (2004b) Mechanism of up-valley winds. J Atmos Sci 61:3097–3111 A.3.1

Reeves HD, Stensrud DJ (2009) Synoptic-scale flow and valley cold pool evolution in the western United States 24:1625–1643 II.4.4, V.1

Robinson DA, Kukla G (1985) Maximum surface albedo of seasonally snow-covered lands in the northern hemisphere. J Climate Appl Meteor 24:402–411 V.2.2

Rose T, Crewell S, Löhnert U, Simmer C (2005) A network suitable microwave radiometer for operational monitoring of the cloudy atmosphere. Atmos Res 75:183–200 A.2.2

Rotach MW, Wohlfahrt G, Hansel A, Reif M, Wagner J, Gohm A (2014) The world is not flat - implications for the global carbon balance. Bull Am Meteorol Soc 95:1021–1028 I.1, IV.1

Rotach MW, Gohm A, Lang MN, Leukauf D, Stiperski I, Wagner J (2015) On the vertical exchange of heat, mass, and momentum over complex, mountainous terrain. Front Earth Sci 3, 76, DOI 10.3389/feart.2015.00076 I.1, I.2

Rotunno R, Houze RA (2007) Lessons on orographic precipitation from the Mesoscale Alpine Programme. Q J R Meteorol Soc 133:811–830 I.1, I.2

Rotunno R, Lehner M (2016) Two-layer stratified flow past a valley. J Atmos Sci 73:4065–4076 II.3.2.a

Sakiyama SK (1990) Drainage flow characteristics and inversion breakup in two Alberta mountain valleys. J Appl Meteorol 67:1015–1030 II.3.1.b, IV.1

Sandu I, Beljaars A, Bechtold P, Mauritsen T, Balsamo G (2013) Why is it so difficult to represent stably stratified conditions in numerical weather prediction (NWP) models? Journal of Advances in Modeling Earth Systems 5:117–133 I.2

Schaap M, Roemer M, Sauter F, Boersen G, Timmermans R, Builtjes PJH, Vermeulen AT (2005) LOTOS-EUROS: Documentation. TNO-report B&O-A R 2005/297, TNO, The Netherlands, 40 pp A.3.2

Schmidli J (2013) Daytime heat transfer processes over mountainous terrain. J Atmos Sci 70:4041–4066 II.4.1, III.4.2, IV.1, IV.3.3

Schmidli J, Rotunno R (2010) Mechanism of along-valley winds and heat exchange over mountainous terrain. J Atmos Sci 67:3033–3047 II.4.1, II.4.3, III.1, III.3.2, IV.1, IV.2.4, IV.2.4, IV.6.2

Schmidli J, Rotunno R (2015) The quasi-steady state of the valley wind system. Front Earth Sci 3, 79, DOI 10.3389/feart.2015.00079 III.5, III.6

Schmidli J, Poulos GS, Daniels MH, Chow FK (2009) External influences on nocturnal thermally driven flows in a deep valley. J Appl Meteorol Climatol 48:3–23 II.3.2.c, III.1, V.2.2

Schmidli J, Billings B, Chow FK, De Wekker SFJ, Doyle J, Grubišić V, Holt T, Jiang Q, Lundquist KA, Sheridan P, Vosper S, Whiteman CD, Wyszogrodzki AA, Zängl G (2011) Intercomparison of mesoscale model simulations of the daytime valley wind system. Mon Weather Rev 139:1389–1409 III.1, III.2.2, III.2.3

Schnitzhofer R, Norman M, Wisthaler A, Vergeiner J, Harnisch F, Gohm A, Obleitner F, Fix A, Neininger B, Hansel A (2009) A multimethodological approach to study the spatial distribution of air pollution in an alpine valley during wintertime. Atmos Chem Phys 9:3385–3396 A.1

Serafin S, Zardi D (2011a) Daytime development of the boundary layer over a plain and in a valley under fair weather conditions: a comparison by means of idealized numerical simulations. J Atmos Sci 68:2128–2141 II.3.1.b, II.4.1, III.3.2

Serafin S, Zardi D (2011b) Daytime development of the boundary layer over a plain and in a valley under fair weather conditions: a comparison by means of idealized numerical simulations. J Atmos Sci 68:2128–2141 A.3.1

Serafin S, Zardi D (2015) An analytic solution for time-periodic thermally driven slope flows. Q J R Meteorol Soc 141:1968–1974 II.3.1.a

Silcox GD, Kelly KE, Crosman ET, Whiteman CD, Allen BL (2012) Wintertime $PM_{2.5}$ concentrations during persistent, multi-day cold-air pools in a mountain valley. Atmos Environ 46:17–24 A.1, A.3.1, A.4

Skamarock WC, Klemp JB, Dudhia J, Gill DO, Barker DM, Duda MG, Huang XY, Wang W, Powers JG (2008) A description of the Advanced Research WRF version 3. NCAR Technical Note NCAR/TN-475+STR, NCAR, Boulder, CO, 125 pp III.2.1, IV.3.1, V.2.3

Smith CM, Porté-Agel F (2014) An intercomparison of subgrid models for large-eddy simulation of katabatic flows. Q J R Meteorol Soc 140:1294–1303 III.2.1

Smith RB (1985) On severe downslope winds. J Atmos Sci 42:2597–2603 II.3.2.b

Staquet C, Paci A, 24 co-authors (2015) The Passy project: objectives, underlying scientific questions and preliminary numerical modelling of the Passy Alpine valley. In: Proc. of the 33rd International Conference on Alpine Meteorology, Innsbruck, Austria V.1, A.1

Stiperski I, Kavčič I, Grisogono B, Durran DR (2007) Including Coriolis effects in the Prandtl model for katabatic flows. Q J R Meteorol Soc 133:101–106 II.3.1.a

Stone GL, Hoard DE (1989) Low-frequency velocity and temperature fluctuations in katabatic valley flows. J Appl Meteorol 28:477–488 II.3.1.a

Stull RB (1988) An introduction to boundary layer meteorology. Kluwer Academic II.1

Tomasi E, Giovannini L, Zardi D, De Franceschi M (2014) High-resolution numerical simulations of wintertime atmospheric boundary layer processes in the Adige Valley during an ALPNAP project field campaign. In: Proc. of the 21st Symposium on Boundary Layers and Turbulence, Leeds, UK V.2.2

Trompetter WJ, Davy K P, Markwitz A (2010) Influence of environmental conditions on carbonaceous particle concentrations within new zealand. J Aerosol Sci 41:134–142 A.3.2

Vergeiner I, Dreiseitl E (1987) Valley winds and slope winds – Observations and elementary thoughts. Meteorol Atmos Phys 36:264–286 II.2, II.3.1, II.4.1, III.3.2, IV.1

Vinokur M (1980) On one-dimensional stretching functions for finite-difference calculations. NASA contractor report 3313, NASA, Washington, DC, USA, 56 pp III.2.3

Vosper SB, Brown AR (2008) Numerical simulations of sheltering in valleys: the formation of nighttime cold-air pools. Boundary-Layer Meteorol 127:429–448 II.3.2.a, II.4.1, III.1

Vosper SB, Hughes JK, Lock AP, Sheridan PF, Ross AN, Jemmett-Smith B, Brown AR (2014) Cold-pool formation in a narrow valley. Q J R Meteorol Soc 140:699–714 II.4.1, II.4.3, III.1, V.1

Vrhovec T (1991) A cold air lake formation in a basin – a simulation with a mesoscale numerical model. Meteorol Atmos Phys 46:91–99 V.1

Vrhovec T, Hrabar A (1996) Numerical simulations of dissipation of dry temperature inversions in basins. Geofizika 13:81–96 V.1

Wagner A (1932) Theorie und beobachtung der periodischen gebirgswinde. Gerlands Beitr Geophysi pp 408–449 II.4.1, II.10, IV.1

Wagner JS, Gohm A, Rotach MW (2015a) The impact of valley geometry on daytime thermally driven flows and vertical transport processes. Q J R Meteorol Soc 141:1780–1794 I.2, IV.1

Wagner JS, Gohm A, Rotach MW (2015b) Influence of along-valley terrain heterogeneity on exchange processes over idealized valleys. Atmos Chem Phys 15:6589–6603 I.2, IV.1

Weber RO, Kaufmann P (1998) Relationship of synoptic winds and complex terrain flows during the MISTRAL field experiment. J Appl Meteorol 37:1486–1496 II.3.2.c

Wei L, Zhaoxia P, Shigong W (2013) Numerical simulation of the life cycle of a persistent wintertime inversion over Salt Lake City. Boundary-Layer Meteorol 148:399–418 V.1

Weigel AP, Chow FK, Rotach MW, Street RL, Xue M (2006) High-resolution large-eddy simulations of flow in a steep Alpine valley. Part II: flow structure and heat budgets. J Appl Meteorol Climatol 45:87–107 II.4.1, III.1, III.4.2, III.6

Weigel AP, Chow FK, Rotach MW (2007) The effect of mountainous topography on moisture exchange between the surface and the free atmosphere. Boundary-Layer Meteorol 125:227–244 I.2

Weissmann M, Braun FJ, Gantner L, Mayr GJ, Rahm S, Reitebuch O (2005) The alpine mountain-plain circulation: Airborne doppler lidar measurements and numerical simulations. Mon Weather Rev 133:3095–3109 I.2

Whiteman CD (1982) Breakup of temperature inversions in deep mountain valleys: Part I. Observations. J Appl Meteorol 21:270–289 V.1

Whiteman CD (1986) Temperature inversion buildup in Colorado's Eagle valley. Meteorol Atmos Phys 35:220–226 II.3.1.b, II.4.2, II.9

Whiteman CD (1990) Observations of thermally developed wind systems in mountainous terrain. In: Blumen W (ed) Atmospheric processes over complex terrain, Meteorological monographs, vol 23, no. 45, American Meteorological Society, 45 Beacon St., Boston, MA, chap 2, pp 5–42 II.2, II.4.1, III.1, IV.1, IV.2.2, V.1

Whiteman CD (2000) Mountain meteorology: fundamentals and applications. Oxford University Press, pp. 355 II.3.1.b, II.3.2.c

Whiteman CD, Barr S (1986) Atmospheric mass transport by along-valley wind systems in a deep Colorado valley. J Climate Appl Meteor 25:1205–1212 II.3.1.b, II.3.3, III.6

Whiteman CD, Doran JC (1993) The relationship between overlying synoptic-scale flows and winds within a valley. J Atmos Sci 32:1669–1682 II.3.2.c

Whiteman CD, Zhong S (2008) Downslope flows on a low-angle slope and their interactions with valley inversions. Part I: observations. J Appl Meteorol Climatol 47:2023–2038 II.3.1.a, IV.3.3

Whiteman CD, Fritschen LJ, Orgill MM, Simpson JR (1989) Deep valley radiation and surface energy budget microclimates. Part I: radiation. J Appl Meteorol 28:414–426 II.4.1

Whiteman CD, McKee TB, Doran JC (1996) Boundary layer evolution within a canyonland basin. Part I: mass, heat, and moisture budgets from observations. J Appl Meteorol 35:2145–2161 II.3.3, II.3.3, II.4.3, IV.2.3, IV.2.3, IV.5.3, IV.7, V.6, VI.1

Whiteman CD, Bian X, Zhong S (1999a) Wintertime evolution of the temperature inversion in the Colorado Plateau Basin. J Appl Meteorol 38:1103–1117 V.4.1

Whiteman CD, Bian X, Zhong S (1999b) Wintertime evolution of the temperature inversion in the Colorado Plateau Basin. J Appl Meteorol 38:1103–1117 A.2.3

Whiteman CD, Zhong S, Bian X (1999c) Wintertime boundary layer structure in the Grand Canyon. J Appl Meteorol 38:1084–1101 II.4.4

Whiteman CD, Bian X, Sutherland JL (1999c) Wintertime surface wind patterns in the Colorado River valley. J Appl Meteorol 38:1118–1130 IV.4.2

Whiteman CD, Zhong S, Shaw WJ, Hubbe JM, Bian X, Mittelstadt J (2001a) Cold pools in the Columbia basin 16:432–447 II.2, II.4.4

Whiteman CD, Zhong S, Shaw WJ, Hubbe JM, Bian X, Mittelstadt J (2001b) Cold pools in the Columbia basin. Weath Forecasting 16:432–447 A.3.1

Whiteman CD, Haiden T, Pospichal B, Eisenbach S, Steinacker R (2004b) Minimum temperatures, diurnal temperature ranges, and temperature inversions in limestone sinkholes of different sizes and shapes. J Appl Meteorol 43:1224–1236 II.4.1

Whiteman CD, Muschinski A, Zhong S, Fritts D, Hoch SW, Hahnenberger M, Yao W, Hohreiter V, Behn M, Cheon Y, Clements CB, Horst TW, Brown WOJ, Oncley SP (2008) METCRAX 2006, meteorological experiments in arizona's meteor crater. Bull Am Meteorol Soc 89:1665–1680 II.2

Whiteman CD, Hoch SW, Lehner M, Haiden T (2010) Nocturnal cold-air intrusions into a closed basin: observational evidence and conceptual model. J Appl Meteorol Climatol 49:1894–1905 II.4.2, II.4.2

Whiteman CD, Hoch SW, Horel JD, Charland A (2014) Relationship between particulate air pollution and meteorological variables in Utah's Salt Lake Valley. Atmos Environ 94:742–753 I.1, A.1, A.3.1, A.3.1, A.4

Wicker LJ, Skamarock WC (2002) Time-splitting methods for elastic models using forward time schemes. Mon Weather Rev 130:2088–2097 III.2.1, IV.3.1

Wyngaard JC (2004) Toward numerical modeling in the "Terra Incognita". J Atmos Sci 61:1816–1826 II.4

Zängl G (2004) A reexamination of the valley wind system in the alpine Inn Valley with numerical simulations. Meteorol Atmos Phys 87:241–256 II.3.1.b, III.3.2

Zängl G (2005) Dynamical aspects of wintertime cold-air pools in an alpine valley system. Mon Weather Rev 133:2721–2740 II.2, V.1

Zangl G (2005) Formation of extreme cold-air pools in elevated sinkholes: An idealized numerical process study. Mon Weather Rev 133:925–941 II.4.1, III.1

Zängl G (2005a) Formation of extreme cold-air pools in elevated sinkholes: an idealized numerical process study. Mon Weather Rev 133:925–941 V.1, V.2.2

Zängl G (2005b) Wintertime cold-air pools in the bavarian danube valley basin: Data analysis and idealized numerical simulations. J Appl Meteorol 44:1959–1971 II.3.2.c, II.4.4, V.1

Zardi D, Whiteman CD (2013) Diurnal mountain wind systems. In: Chow FK, De Wekker SFJ, Snyder BJ (eds) Mountain weather research and forecasting: recent progress and current challenges, Springer atmospheric sciences, Springer, New York, NY, chap 2, pp 35–119 II.1, II.2, II.3.1, III.1, IV.4.2

Zhong S, Chow FK (2013) Meso- and fine-scale modeling over complex terrain: Parameterizations and applications. In: Chow FK, De Wekker SFJ, Snyder BJ (eds) Mountain weather research and forecasting: recent progress and current challenges, Springer atmospheric sciences, Springer, New York, NY, chap 10, pp 591–653 II.4

Zhong S, Whiteman CD, Bian X, Shaw WJ, Hubbe JM (2001) Meteorological processes affecting the evolution of a wintertime cold air pool in the columbia basin. Mon Weather Rev 129:2600–2613 II.4.4, II.4.4, V.1

Zhong S, Bian X, Whiteman CD (2003) Time scale for cold-air pool breakup by turbulent erosion. Meteorol Z 12:229–233 II.4.4, II.4.4, V.1

Zilitinkevich SS, Elperin T, Kleeorin N, Rogachevskii I, Esau I (2013) A hierarchy of energy- and flux-budget (EFB) turbulence closure models for stably-stratified geophysical flows. Boundary-Layer Meteorol 146:341–373 III.2.5